BEYOND-CMOS SPINTRONIC LOGIC AND FERROELECTRIC MEMORY

A Thesis
Presented to
The Academic Faculty

by

Sou-Chi Chang

In Partial Fulfillment
of the Requirements for the Degree
Doctor of Philosophy in the
School of Electrical and Computer Engineering

Georgia Institute of Technology
December 2016
Copyright © 2016 by Sou-Chi Chang

BEYOND-CMOS SPINTRONIC LOGIC AND FERROELECTRIC MEMORY

Approved by:

Professor Azad Naeemi, Advisor
School of Electrical and Computer Engineering
Georgia Institute of Technology

Professor Jeffrey Davis
School of Electrical and Computer Engineering
Georgia Institute of Technology

Professor Saibal Mukhopadhyay
School of Electrical and Computer Engineering
Georgia Institute of Technology

Professor David Citrin
School of Electrical and Computer Engineering
Georgia Institute of Technology

Professor Phillip First
School of Physics
Georgia Institute of Technology

Date Approved: September 29, 2016

To my family, who taught me how to live

and

To my advisors, who taught me how to think

ACKNOWLEDGEMENTS

I would like to thank my advisor Prof. Azad Naeemi for giving me this opportunity to join his group and pursue my dream of studying nanoelectronics. In the past four years, Prof. Naeemi gave me immense freedom in research, and his broad-mindedness as well as enthusiasm in learning new things inspired me to become a better researcher. Perhaps the most important lesson I learned from Prof. Naeemi is his openness. He always keeps his office door open and welcomes every wild idea I had in my mind. If any of research in my PhD years becomes useful in the future, full credit should be given to Prof. Naeemi.

I would also like to thank Prof. Ming-Jer Chen at National Chiao Tung University and Prof. Jasprit Singh at University of Michigan for teaching me the fundamental of electronic transport in semiconductors. What I learned from you has given me a firm background to explore more exciting solid-state devices. It was one of my wonderful memories for being a student of all my advisors and I will definitely miss it in the future.

I would like to thank Prof. Jeffrey Davis, Prof. Saibal Mukhopadhyay, Prof. David Citrin, and Prof. Phillip First for serving my committee members. I would also like to thank our previous and current group members (Prof. Shaloo Rakheja, Dr. Vachan Kumar, Dr. Ahmet Ceyhan, Phillip Bonhomme, Dr. Chenyun Pan, Alex Cardwell, Sourav Dutta, Victor Huang, Nickvash Kani, Javaneh Mohseni, Rouhollah Mousavi, Ramy Nashed, Divya Prasad, Chia-Sheng Hsu, and Yu-Ching Liao) for their support and discussion, and I believe their names will continuously be mentioned in the area of nanoelectronics.

My special thanks go to Dr. Ian Young, Dr. Dmitri Nikonov, and Dr. Sasikanth

Manipatruni at Intel Components Research. I very much appreciate all the support and valuable guidance you gave during my PhD years.

My most personal thanks go to my family, my father Hsien-Chang Chang, my mother Ching-Lien Kao, my sister Wen-Ting Chang, and my wife Wen-Chen Yeh, for their sacrifices and all the love that they have given to me. The completion of this thesis would be impossible without your support. Finally, I would like to thank my family, friends, and my advisors again for giving me this wonderful journey and this thesis is dedicated to all of you.

TABLE OF CONTENTS

DEDICATION . . . . **iii**

ACKNOWLEDGEMENTS . . . . **iv**

LIST OF TABLES . . . . **x**

LIST OF FIGURES . . . . **xii**

I INTRODUCTION **1**

1.1 CMOS Scaling 3

1.1.1 Physical Limits 4

1.1.2 Power Limits 5

1.1.3 Technology Limits 7

1.1.4 Potential Solutions to Beyond-CMOS Technology 7

1.2 Ferromagnetism 8

1.2.1 Models of Ferromagnetic Materials 9

1.2.2 Spin Currents and Spin Relaxation 11

1.2.3 Spin-transfer Torque and Magnetic Dynamics 12

1.2.4 Magnetic Domain Walls 19

1.2.5 Temperature Effects 21

1.3 Ferroelectricity 22

1.3.1 Polarization-Electric field Hysteresis Loop 23

II SCALING LIMITS ON ALL-SPIN LOGIC **25**

2.1 Overview 25

2.2 All-spin Logic 25

2.3 Mathematical Models 26

2.4 Results and Discussion 29

2.4.1 Dipole Interaction 29

2.4.2 Leakage Currents 35

2.4.3 Shunt Path 37

2.5 Summary 37

III SILICON INTERCONNECTS FOR ALL-SPIN LOGIC 39

3.1 Overview 39

3.2 Silicon Spin Interconnects 39

3.3 Spin Injection 42

3.3.1 Tunneling Interface 42

3.3.2 Non-magnetic Channel 46

3.3.3 Results and Discussion 47

3.4 Spin Interconnects 57

3.4.1 Spin Transport and Magnetization Dynamics 57

3.4.2 Results and Discussion 62

3.5 Summary 69

IV COPPER AND ALUMINUM INTERCONNECTS FOR ALL-SPIN LOGIC 72

4.1 Overview 72

4.2 Copper and Aluminum Spin Interconnects 72

4.3 Mathematical Models 73

4.4 Results and Discussion 77

4.4.1 Spin currents and Injection Efficiency 77

4.4.2 Delay and Energy Performance 82

4.5 Summary 87

V DOMAIN WALL INTERCONNECTS FOR ALL-SPIN LOGIC 90

5.1 Overview 90

5.2 Domain Wall Interconnects 90

5.3 Mathematical Models 92

5.3.1 Switching Device 94

5.3.2 One-dimensional Landau-Lifshitz-Gilbert Equation 95

5.3.3 Domain Wall Transport 98

5.4 Results and Discussion 99
5.4.1 Domain Walls at Boundaries 100
5.4.2 Delay, Energy, and Material Targets 101
5.4.3 Thermal Fluctuations 109
5.4.4 Summary 109
VI LOW-POWER SPIN VALVE/DOMAIN WALL LOGIC 111
6.1 Overview 111
6.2 Spin Valve/Domain Wall Logic 111
6.3 Mathematical Models 116
6.4 Results and Discussion 119
6.4.1 Logic Non-reciprocity 121
6.4.2 Buffer, Inverter, 3-input Majority Gate, and DW/Spin current Transducer 125
6.4.3 Comparison to NLSVs and CMOS Circuits 127
6.5 Summary 131
VII ELECTRORESISTANCE IN FERROELECTRIC TUNNEL JUNCTIONS 132
7.1 Overview 132
7.2 Ferroelectric Tunnel Junctions 132
7.3 Mathematical Models 135
7.3.1 FTJ without Non-polar Dielectric 136
7.3.2 FTJ with Non-polar Dielectric 138
7.3.3 FE Hysteresis Loop 140
7.3.4 Tunneling Currents 141
7.4 Results and Discussion 143
7.4.1 Comparison with Experimental *I*-*V* Characteristics 143
7.4.2 Interface Termination Effects on TER 147
7.4.3 FTJs with CoO_x 151
7.5 Summary 152

VIII CONCLUSION AND OUTLOOK **155**
8.1 Conclusion 155
8.1.1 Spintronic Logic 155
8.1.2 Ferroelectric Memory 156
8.2 Future Work 157
8.2.1 Magnetoelectric Logic 158
8.2.2 Magnetostrictive Spin-transfer Torque Logic 159
8.2.3 Antiferromagnetic Spintronics 161
8.2.4 Switching Dynamics in Ferroelectric Tunnel Junctions 163
APPENDIX A — IMPORTANT DERIVATIONS AND JUSTIFICATION IN CHAPTER V **165**
APPENDIX B — IMPORTANT DERIVATIONS AND EQUIVALENT SPIN CIRCUITS IN CHAPTER VI **174**
APPENDIX C — IMPORTANT DERIVATIONS IN CHAPTER VII **179**
REFERENCES **184**

LIST OF TABLES

1 Simulation parameters for all-spin logic (ASL) in Section 2.4. L_c, L_g, I_c, M_s, $K_{u,z}$, and α are the channel length, shunt path, input current, saturation magnetization, material anisotropy energy density, and damping coefficient, respectively. 30

2 Oxide parameters used in Fig. 21. 4 eV and 4.05 eV are used for the work function of an FM metal, Φ_F, and the electron affinity of Si, χ_s, respectively. By assuming that the energy band diagram is aligned according to the bulk properties of each layer, the interface barrier heights ϕ_1 and ϕ_2 are defined as $\Phi_F - \chi$ and $\chi_s - \chi$, respectively. . . 51

3 Parameters for the interface conductance matrix and the LLG equation. L_m, W_m, and t_m are the length, width, and thickness of the nanomagnet, respectively. 65

4 Simulation parameters for tunneling currents. m^*, χ, Φ, and E_f are the effective mass, electron affinity, work function, and Fermi energy of the material [186]. The effective mass of the FM metal, Cu, and Al are assumed to be equal to m_0, where m_0 is the free electron mass. Fermi energy and exchange energy splitting of the ferromagnet (in units of eV) are 2.25 and 2.15, respectively [45]. 77

5 Parameters of the nanomagnet, interface conduction matrix, and interconnect for all the delay and energy simulations [141, 13]. L_m, W_m, and t_m are the length, width, and thickness of the nanomagnet, respectively. W_{int} and t_{int} are the width and thickness of the interconnect, respectively. 83

6 Simulation parameters for ASL. The transport parameters of the Cu channel are obtained from the compact model developed in Ref. [176]. Note that the imaginary part of mixing conductance is assumed to be zero for the FM metal/NM metal interface. 104

7 Simulation parameters for the FM interconnect. Note that no material anisotropy in the transverse direction is assumed ($K_{u,y} = K_{u,z} = 0$). . . 104

8 Simulation parameters in this section. ρ and β are the resistivity and spin polarization of conductivity for permalloy, respectively. $l_{sf,\parallel}$ and $l_{sf,\perp}$ are longitudinal and transverse spin relaxation lengths of permalloy, respectively. l_{FM}, w_{FM}, and t_{FM} are the length, width, and thickness of FM wires, respectively. l_{NM}, w_{NM}, and t_{NM} are the length, width, and thickness of the NM channel, respectively. $G_{\uparrow\uparrow}$, $G_{\downarrow\downarrow}$, and $G_{\uparrow\downarrow}$ are majority, minority, and mixing interface conductances, respectively. 121

9 A performance comparison between schemes based on SVs and NLSVs. 200μA is applied to both structures to simulate inverters, and the shunt path in the NLSV is 30nm. The delay (τ) is defined as the total time required for DW creation in the beginning of the FM wire and DW automotion to the end of the FM wire. E is the switching energy. . . 130

10 A performance comparison for a majority gate using the proposed devices (Fig. 60) and the low-power (LP) CMOS switches (F=15nm, 2018 technology node in the 2013 edition of ITRS [165]). E, τ, and $Area$ are the switching energy, critical delay, and required circuit area, respectively. The spacing between FM interconnects is assumed to be 20nm. A 3-input majority gate function is given as $O = AB + BC + CA$, where A, B, C are the inputs and O is the output. In the CMOS implementation, a 3-input majority gate is composed of three 2-input NAND and one 3-input NAND gates, which require at least 18 CMOS digital switches with routing interconnects in different metal layers to minimize the area. 131

LIST OF FIGURES

1 Potential energy profile in the source-to-drain direction to illustrate the drain-induced barrier lowing (DIBL) effect in a scaled CMOS transistor. 4

2 Potential energy profile in the source-to-drain direction to illustrate direct quantum-mechanical tunneling as the channel length becomes too short. 5

3 Static (black square) and dynamic (red circle) power density versus channel length [169]. 6

4 Comparison between the band structures of a FM transition metal using different approximations [178]. (a) Local spin density approximation (LSDA), (b) Stoner model, and (c) s-d model. 11

5 Schematic of the origin of spin-transfer torques (STTs) in FM metals. The yellow arrows represent the direction of the magnetic moment. . 13

6 Schematic of a macrospin under the effects of the effective field, the damping, and the STT. A field-like (FL) torque is also include; however, it is usually ignored in metallic layers. The easy axis is assumed to be in the z direction. 18

7 Schematic of two different types of magnetic domain walls (DWs) in an FM thin-flim wire. (a) Transverse wall (TW), and (b) vortex wall (VW). 21

8 Schematic of a typical polarization-electric field hysteresis loop for a good FE material. P_s is the spontaneous polarization, E_c is the coercive field strength, and ϵ_{FE} is a constant that represents the linear response of non-switchable dipoles to the applied electric field. 24

9 Factors limiting scaling of all-spin logic: dipole coupling between the input and the output magnets, the leakage current from the output, and the shunt path acting as a spin sink [26]. 27

10 Equivalent spin circuit for ASL with current sources at both input and output. The inset shows a resistor network for a current source on the magnet [26]. 28

11 Self-consistent scheme for ASL dynamics. $H_{dipole,21}$ is the dipole field imposed on the output (denoted as 2) from the input magnet (denoted as 1), and vice versa [26]. 29

12 (a) and (c) Magnetization dependence on time for the input (top) and the output (bottom) magnets without and with dipole fields, respectively. Thermal noise fields are not included in both (a) and (c). (b) and (d) are the delay distributions due to the noise over 1000 stochastic simulations without and with dipole fields, respectively [26]. 31

13 (a) and (c) Delay vs. channel length under different magnitudes of the injection current in ASL and material anisotropies. Data with and without dipole fields are shown. (b) and (d) Average delay and standard deviation (over 100 stochastic simulations) vs. channel length corresponding to the cases shown in (a) and (c), respectively [26]. . . 33

14 (a) and (c) Delay vs. channel length under different saturation magnetizations and volumes of the magnets. Data with and without dipole fields are shown. (b) and (d) Average delay and standard deviation (over 100 stochastic simulations) vs. channel length corresponding to the cases shown in (a) and (c), respectively [26]. 34

15 (a) Delay vs. channel length with and without the leakage current. Both positive and negative leakage currents are shown. (b) average delay with the standard deviation (over 100 stochastic simulations) vs. channel length with positive and negative leakage currents. The dipolar interaction is ignored. [26] 36

16 Average delay and energy with the standard deviation (over 100 stochastic simulations) vs. shunt path. The channel length is 120 nm. [26] . 37

17 Schematic of a Si interconnect for ASL. The receiving magnet is assumed to form an Ohmic contact with the interconnect. Spin injection from the input magnet, spin transport through the channel, and stochastic magnetization dynamics of the receiving magnet are key elements to describe the operation of a Si all-spin interconnect [29]. . . 40

18 Schematic of the semi-infinite FM/oxide/Si structure and its energy band diagram, $U(z)$, for spin injection analysis. The blue and black lines are the band diagrams for up-spin and down-spin electrons, respectively [29]. The tunneling current is calculated by the non-equilibrium Green's function (NEGF) method, and the spin drift-diffusion equation is used to handle spin transport in the channel. Both mechanisms are connected through interface spin accumulation, μ_{s0}. $E_{c\uparrow}$ and $E_{c\downarrow}$ are the majority and minority band of the magnet, respectively. E_F is the Fermi energy of the magnet. ΔE_f is the exchange splitting in the magnet. ϕ_1 and ϕ_2 are the barrier heights at the FM/oxide and oxide/Si interface, respectively. ΔE_t is the band splitting in the oxide. V_{TL} is the voltage across the tunneling region. V_s is the surface band bending of the Si channel. At the oxide/Si interface, the chemical potentials of the majority and minority carriers, $\mu_\uparrow$ and $\mu_\downarrow$, respectively, are split according to μ_{s0}. 43

19 (a) Spin current density and (b) spin polarization of current versus the voltage across the tunneling region under different doping densities of the channel in the presence and absence of ISA [29]. The simulation parameters are given as follows: $\phi_1 = 2.6$ eV, $\phi_2 = 2.6$ eV, $E_F = 2.25$ eV, $\Delta E_f = 2.15$ eV, $\Delta E_t = 0$ eV, $m^* = 0.2m_0$, and $\epsilon = 10\epsilon_0$. The oxide thickness is 0.5 nm. (c) and (d) are the energy band diagrams illustrating spin polarization of the current increases when the voltage and doping density increase, respectively. The yellow arrows represent additional majority carriers tunneling through the junction, which increases both spin current density and spin polarization of the current. 48

20 (a) Spin current density and (b) spin polarization of current versus the voltage across the tunneling region under different FM/oxide interface barrier heights in the presence and absence of ISA [29]. The simulation parameters are given as follows: $N_d = 5 \times 10^{18}$ cm^{-3}, $\phi_2 = 2.6$ eV, $E_F = 2.25$ eV, $\Delta E_f = 2.15$ eV, $\Delta E_t = 0$ eV, $m^* = 0.2m_0$, and $\epsilon = 10\epsilon_0$. The oxide thickness is 0.5 nm. (c) The energy band diagram illustrating spin polarization of the current increases when the ϕ_1 decreases. The yellow arrow represents additional majority carriers tunneling through the junction, which increases both spin current density and spin polarization of the current. 50

21 (a) Spin current density and (b) spin polarization of the current versus voltage across the tunneling region under different oxide thicknesses in the presence and absence of ISA [29]. The simulation parameters are given as follows: $N_d = 5 \times 10^{18}$ cm^{-3}, $\phi_1 = 2.3$ eV, $\phi_2 = 2.6$ eV, $E_F = 2.25$ eV, $\Delta E_f = 2.15$ eV, $\Delta E_t = 0$ eV, $m^* = 0.2m_0$, and $\epsilon = 10\epsilon_0$. 52

22 (a) Spin current density and (b) spin polarization of the current versus voltage across the tunneling region under different oxide materials in the presence and absence of ISA [29]. The simulation parameters are given as follows: $N_d = 5 \times 10^{18}$ cm^{-3}, $E_F = 2.25$ eV, $\Delta E_f = 2.15$ eV, and $\Delta E_t = 0$ eV. The parameters for each insulator are given in Table 2. The oxide thickness is 0.5 nm. 53

23 Spin current density and spin polarization of the current versus the exchange splitting [29]. The simulation parameters are given as follows: $N_d = 5 \times 10^{18}$ cm^{-3}, $\phi_1 = 2.3$ eV, $\phi_2 = 2.6$ eV, $E_F = 2.25$ eV, $\Delta E_t = 0$ eV, $m^* = 0.2m_0$, and $\epsilon = 10\epsilon_0$. The oxide thickness is 0.5 nm. 54

24 Spin current density and spin polarization of the current versus band splitting of the insulator, ΔE_t [29]. The simulation parameters are given as follows: $N_d = 5 \times 10^{18}$ cm^{-3}, $E_F = 2.25$ eV, $\phi_1 = 2.3$ eV, $\phi_2 = 2.6$ eV, $m^* = 0.2m_0$, and $\epsilon = 10\epsilon_0$. The oxide thickness is 0.5 nm. 55

25 Spin current density and spin polarization of the current versus the oxide/Si interface barrier height, ϕ_2. The inset shows a larger ϕ_2 results in a smaller Schottky barrier height [29]. The simulation parameters are as follows: $N_d = 5 \times 10^{18}$ cm^{-3}, $\phi_1 = 2.3$ eV, $E_F = 2.25$ eV, $\Delta E_f = 2.15$ eV, $\Delta E_t = 0$ eV, $m^* = 0.2m_0$, and $\epsilon = 10\epsilon_0$. The oxide thickness is 0.5 nm. 58

26 Comparison between the stochastic LLG solver and the analytical expression for $< \phi^2 >$ (the inset is for τ_{sw}) [29]. 63

27 (a) Switching time and (b) energy versus doping density for different channel lengths [29]. The injected spin current is constant and equal to 3.8×10^{10} A/m^2. The solid lines represent the average value of five data points for each set of parameters. The same representation is used in Figs. 28 to 31. 64

28 (a) Switching time and (b) energy versus channel length for different doping densities [29]. The injected spin current is constant and equal to 3.8×10^{10} A/m^2. 66

29 (a) Switching time and (b) energy versus channel length for different values of interface tunneling resistance [29]. The doping density of the channel is 4.78×10^{19} cm^{-3} and R_0 is 6.4×10^{-12} $\Omega\cdot$ m^2. 67

30 (a) Switching time, (b) energy, and (c) energy-delay product (EDP) versus applied voltage for different channel lengths [29]. The doping density of the channel is 4.78×10^{19} cm^{-3}. 69

31 (a) Switching time, (b) energy, and (c) energy-delay product (EDP) versus applied voltage for different sizes of the receiving nanomagnet [29]. The interconnect length is 1 μm and the doping density of the channel is 4.78×10^{19} cm^{-3}. 70

32 (a) Switching components connected by ASL-type interconnects [28]. The blue rectangles are the nanomagnets and the dark gray rectangles are insulating spacers. The arrows show the electrical currents. The dark gray arrows indicate the redundant electrical current paths increasing power dissipation. The light green arrow shows the electrical current with which a considerable fraction of spin current is shunted directly to the ground. (b) Switching components connected by CSV-like interconnects, where the losses resulting from the charge currents in the shunt path of the interconnect and those in the previous ASL switch are eliminated. The yellow rectangle is the tunneling oxide. The initial magnetic unit vectors of the transmitting and receiving nanomagnets are assumed to be $[-1, 0, 0]$ and $[1, 0, 0]$, respectively. 74

33 The energy band diagram of the FM metal/oxide/NM metal structure [28]. $E_{f,FM}$ and $E_{f,NM}$ are Fermi energies of the ferromagnet and normal metal, respectively. $E_{c\uparrow}$ and $E_{c\downarrow}$ are conduction band edges for up-spin and down-spin electrons, respectively. ΔE is the exchange energy splitting. Φ_1 and Φ_2 are interface barrier heights at the ferromagnet/oxide and oxide/normal metal interfaces, respectively. eV_a is the difference in Fermi level between the ferromagnet and normal metal due to the applied voltage. 76

34 (a) Spin current and (b) injection efficiency versus the applied voltage for Cu, Al, and Si [28]. The insulator thickness is 0.5 nm. The work function of the ferromagnet is 4 eV. Al_2O_3 is used as a tunneling barrier. Since the Si channel is highly degenerate, the effect of spin accumulation on the spin currents is ignored [29]. Inset (i) and (ii) in (b) show the effect of the Schottky barrier and work function of the metal on the energy band diagram. 78

35 Spin current and injection efficiency versus the applied voltage with different (a) interface barrier heights, Φ_1, (b) oxide thicknesses, and (c) oxide materials [28]. For (a), the tunneling effective mass is $0.2m_0$, Φ_2 is 3.2 eV, and the oxide thickness is 0.5 nm. For (b), Φ_1 is 2.55 eV, the tunneling effective mass is $0.2m_0$, and Φ_2 is 3.2 eV. For (c), the work function of the ferromagnet is 4 eV, Cu is used as an interconnect, and 0.5 nm is used as the oxide thickness. 80

36 Spin current and injection efficiency versus the exchange energy splitting/ Fermi energy ratio [28]. 81

37 Delay and energy versus the interconnect length under a fixed bias voltage [28]. In this case, SRLs of Cu and Al are about 202 nm and 512 nm, respectively. The applied voltage is 0.1 V. For each set of parameters, five simulations are done to estimate the random fluctuations due to the thermal noise. The same estimation is also used for Figs. 38 and 39. 84

38 (a) Delay, energy and (b) energy-delay product versus the applied voltage for 400 nm-long Cn and Al interconnects [28]. 86

39 Energy versus the interconnect length under the same magnetic response for SV-like and Cu ASL (light green diamond) interconnects [28]. The structures of ASL and SV-like interconnects are shown in Fig. 32. For SV-like interconnects, the channel materials include Cu (blue circle), Al (red triangle), and Si (black square). 88

40 Schematics of all-spin logic (ASL) interconnects using automotion of domain walls (DWs) and creation of DWs using ASL [25]. The Cartesian coordinate used for the calculations of interconnects is also defined. 92

41 Schematics illustrating the difference between interconnects based on spin-transfer-torque switching and automotion of DWs [25]. The ferromagnetic metals are represented by blue rectangles with black arrows. The red arrows represent the direction of electrical current. 93

42 The numerical procedure for modeling DW interconnects for ASL [25]. 94

43 The circuit representation of ASL connected by FM wires for modeling DW creation [25]. The red, blue, and light yellow bars represent the conductance of the contact, FM metal/NM metal interface, and NM transport channel, respectively. 96

44 The comparison between the DW created by ASL/1-D LLG in a 600 nm interconnect and Walker's trial solutions [195]. The Walker's trial parameters: $\phi = 1.32$ radian and $\chi = 50$ nm [25]. 99

45 The time evolution of the magnetization at the end of the interconnect for (a) DW reflection ($\alpha = 0.01$) and (b) DW disappearance ($\alpha = 0.1$) [25]. The domain wall is located near the boundary initially and moves toward the edge due to automotion. 102

46 (a) The effects of phase and Gilbert damping coefficient at the end of the interconnect on the DW reflection and disappearance. Red lines represent the DW is reflected, and blue lines represent the DW is destroyed at the end [25]. The interconnect length is 400 nm and the DW is located at $z = 360$ nm initially. The Gilbert damping coefficient changes from 0.01 to 0.1 for $z = 360$ nm to $z = 400$ nm, and is set to be 0.01 for the rest of the wire. Note that if ϕ is exactly $\pi/2$ or 0, the domain walls have zero speed. (b) Schematics for illustrating high and low energy DW configurations in the in-plane ferromagnetic interconnect. The green arrow represents the direction of material anisotropy. The red region is where the damping coefficient is changed in Fig. 46(a). 103

47 The delay and energy versus the interconnect length. The current source for ASL is 0.5 mA [25]. For the ferromagnetic interconnect, the saturation magnetization is 1×10^6 A/m and damping coefficient is 0.01. The infinite delay represents no DW reaching the end of the interconnect. 105

48 The delay and energy versus the magnitude of the ASL current supply for (a) 100 nm and (b) 400 nm interconnects [25]. The parameters for the interconnects are the same as those shown in Fig. 47. 107

49 The effects of (a) Gilbert damping coefficient ($I_c = 0.5$ mA) and (b) saturation magnetization on the delay (the interconnect length is 100 nm) [25]. 108

50 The thermal noise effects ($T = 300$ K) on the domain wall displacement using automotion with different damping coefficients (a) $\alpha = 0.01$ and (b) $\alpha = 0.001$ [25]. The interconnect length is 400 nm with saturation magnetization being equal to 1×10^6 A/m ($I_c = 1$ mA). 110

51 Schematic of the proposed computing element, comprising a lateral metallic SV and two FM interconnects, where DW automotion is used to update the magnetization of the wire. The damping mechanism in the region bounded by dashed lines is stronger than that in the rest to enhance the logic non-reciprocity, which is also optimized by sizing the input and output contact areas (or varying L_{input} and L_{output}). The blue, gray, and yellow colors designate FM, insulating, and NM materials, respectively. The yellow arrow represents the magnetization orientation in the wire. The magnetizations pointing to $+x$ and $-x$ are defined as 1 and 0, respectively. 112

52 The schematic of a three-inputs majority gate under the proposed scheme. An AND or an OR gate can be realized by setting one of the inputs as a control terminal. 115

53 An equivalent spin circuit of a single device shown in Fig. 51. Blue, yellow, and mixed blue/yellow bars stand for FM materials, NM materials, and FM/NM interfaces, respectively. Black and red arrows stand for spin currents flowing into the FM materials and charge current sources, respectively. Dashed and solid bars represent shunt and series conductances, respectively. 117

54 Time evolution of average magnetizations of FM wires for the input (top) and the output (bottom) in an SV inverter with different damping coefficients at the end of the wire. 120

55 Time evolution of average magnetizations of FM wires for the input (top) and the output (bottom) in an SV inverter with different input contact lengths. The damping coefficient at the end of FM interconnect is set to be 0.18 for Figs. 55 to 63. 122

56 Time evolution of average magnetizations of FM wires for the input (top) and the output (bottom) in an SV inverter with different output contact lengths. 123

57 Time evolution of average magnetizations of FM wires for the input (top) and the output (bottom) in an SV inverter under different magnitudes of driving current. 124

58 Time evolution of average magnetizations of FM wires for the input (top) and the output (bottom) in an SV device with initial parallel alignment under positive and negative driving currents. 126

59 Time evolution of average magnetizations of FM wires for the input (top) and the output (bottom) in an SV device with initial anti-parallel alignment under positive and negative driving currents. 126

60 Time evolution of average magnetizations of FM wires in a 3-input majority gate based on SVs for the three inputs and the output (bottom). -100μA is applied at each input. The input and output contact lengths are 40 and 20nm, respectively. 127

61 Time evolution of average magnetizations of FM wires for the input (top) and the output (bottom) in a NLSV inverter with different output contact lengths. 128

62 Time evolution of average magnetizations of FM wires for the input (top) and the output (bottom) in a NLSV inverter with different input contact lengths. 129

63 Time evolution of average magnetizations of FM wires for the input (top) and the output (bottom) in a NLSV inverter under different magnitudes of driving current. 129

64 Schematics of FTJs in the (a) absence and (b) presence of a non-polar DE layer between the FE and metal electrode. M_1 and M_2 are top and bottom metal electrodes, respectively. 135

65 Schematics of electrostatic potential profiles due to (a) applied electric field, (b) built-in field, and (c) depolarization field for FTJs with (bottom panel) and without (top panel) a non-polar DE layer between the FE and top metal electrode. 138

66 Schematics of energy band diagrams at a bias voltage V_a, satisfying $\mu_2 - \mu_1 = eV_a$, for FTJs (a) without and (b) with a non-polar DE layer between the FE and metal electrode. Arrows in the FE represent the direction of the electric polarization. 142

67 (a) Comparison between FTJ (Co/BTO/LSMO) experimental data [32] and simulation results using the following band diagram parameters: $t_{FE} = 2$ nm, $\phi_1 = \phi_2 = 7.15$ eV, $E_{F1} = E_{F2} = 6.5$ eV, $\epsilon_1 = 2.5$, $\epsilon_2 = 9.8$, $\lambda_1 = 0.5 \times 10^{-10}$ m [233], $\lambda_2 = 1 \times 10^{-10}$ m [233], $m^* = 0.8m_0$. (b) Simulated FE hysteresis loop for FTJ (Co/BTO/LSMO) experiments [32] ($V_c \sim \pm 3$ V, $\epsilon_{FE} \sim 15$, and $P_r \sim 0.3$ C/m^2) with the following LK parameters: $\gamma = 10^{-2}$ m sec/F, $\alpha_1 = -2.77 \times 10^7$ m/F, $\alpha_{11} = -5.35 \times 10^8$ m^5/C^{2}F, and $\alpha_{111} = 6.4 \times 10^9$ m^9/C^{4}F. 144

68 (a) Comparison between FTJ (Au/PVDF/W) experimental data [218] and simulation results using the following band diagram parameters: $t_{FE} = 2$ nm, $\phi_1 = 6.76$ eV, $\phi_2 = 6.7$ eV, $E_{F1} = E_{F2} = 6.5$ eV, $\epsilon_1 = 6.5$, $\epsilon_2 = 20$, $\lambda_1 = 0.75 \times 10^{-10}$ m [65], $\lambda_2 = 0.45 \times 10^{-10}$ m [94], $m^* = 0.1m_0$. (b) Simulated FE hysteresis loop for FTJ (Au/PVDF/W) experiments [218] ($V_c \sim \pm 1$ V, $\epsilon_{FE} \sim 4.4$, and $P_r \sim 0.18$ C/m^2) with the following LK parameters: $\gamma = 1.5 \times 10^{-3}$ m sec/F, $\alpha_1 = -1.38 \times 10^9$ m/F, $\alpha_{11} = -2.67 \times 10^{10}$ m^5/C^{2}F, and $\alpha_{111} = 8 \times 10^{11}$ m^9/C^{4}F. 146

69 Energy band diagrams at 0.1 V for both polarization states with two different effective contact ratios: (a) 1.98 and (b) 0.49. The dark blue and the green correspond to the polarization states pointing to the top and bottom contacts, respectively. Red dash lines represent chemical potentials at both contacts. 149

70 TER at $V_a = 0.1$ V and effective contact ratio versus top contact (a) dielectric constant and (b) screening length. TER and effective contact ratios are defined as $\frac{I_\uparrow}{I_\downarrow}$ and $\frac{\lambda_1 \epsilon_2}{\lambda_2 \epsilon_1}$, respectively. 150

71 (a) Energy band diagrams at 0.1 V for high/low resistance states in an FTJ with a CoO_x buffer layer at the interface. ϕ_c for high and low resistance states are 6.6 and 0.1 eV, respectively. (b) Comparison with experimental data [115] using various ϕ_c for high and low resistance states and different writing voltages. In addition to $t_{DE} = 0.6$ nm, $t_{FE} = 1$nm, ϕ_1 and ϕ_c, the simulation parameters are the same as those in Fig. 67. 153

72 The proposed computational scheme using the magnetoelectric (ME) effects: (a) a single device, (b) two devices in cascade using a two-phase clocked circuit, and (c) a three-input majority gate [27]. The beige, green, and blue regions represent the metal contact, the ferroelectric (FE), and the ferromagnet (FM), respectively. The green and yellow arrows show the direction of the electric polarization of the FE and the magnetization of the FM, respectively. Under this scheme, logic 1 and 0 are represented by either voltage polarity or direction of the magnetization. A positive voltage and the magnetization pointing to the $+x$ direction stand for 1, and a negative voltage and the magnetization pointing to the $-x$ direction stand for -1. One of the possible setups for magnetization initialization is also shown. 160

73 Schematic of clocked magnetostrictive STT logic, which may further reduce the STT switching energy with the help of magnetostriction. Red, blue, grey and yellow bars represent piezoelectric, FM, insulating, and NM materials, respectively. V_1 and V_2 are applied voltages with different clock cycles. 161

74 Schematic of superfluid spin transport through an AFM insulator predicted in Ref. [213], where the input and the output are electrically isolated but magnetically well coupled and may be potentially useful in the application of spin logic. Note that spin accumulation at the input/AFM insulator interface is generated by the SHE through $J_{c,in}$. 162

75 (a) The magnetization profile for a DW in a wire. (b) The corresponding demagnetization field using Eq. 58 and Eq. 67 and material anisotropy field using Eq. 57. The wire dimension is $400 \times 20 \times 2$ nm^3 with $M_s = 1 \times 10^6$ A/m and $K_{u,z} = 1.2 \times 10^5$ joule/m^3. 172

76 Comparisons between the numerical solver for the 1-D LLG equation and the analytical expressions for DW transport in Chapter V. C under (a) an external magnetic field, (b) in-plane spin currents, and (c) out-of-plane spin currents. The DW motion due to transverse shape anisotropy (automotion) is included in all the figures above as a reference. Note that for (c), the out-of-plane spin currents cannot be too large since in such a case, either the DW is destroyed or spin waves are created, and the analytical models fail to describe the transport. ±z in (c) represents ±z spin polarization of currents. 173

77 A simple SV structure that is used to derive Eq. 142. 176

78 An equivalent spin circuit for a 3-input majority gate. The color definition is the same as that shown in the main text. 177

79 An equivalent spin circuit for a NLSV. The color definition is the same as that shown in the main text. 178

80 Schematics of illustrating the electron wave vector in the spherical coordinate and the NEGF approach to FTJs without and with a non-polar DE layer between the FE and metal electrode. 181

CHAPTER I

INTRODUCTION

Over the past four decades, the exponential increase in the computing power of microchips has been the consequence of the relentless scaling of complementary metal-oxide-semiconductor (CMOS) integrated circuits based on Moores law [156]. While it is expected that this trend extends for at least another 10 years, active research in the field of the beyond-CMOS technology is underway in pursuit of low-power logic and non-volatile circuits [165, 164]. One of the most explored beyond-CMOS options is spintronics, where the electron spin is used as a computational state variable. Among many proposed spintronic devices, digital computing using lateral metallic non-local spin valves (NLSVs) with spin-transfer torque (STT) effects [8], also known as all-spin logic (ASL), has drawn significant attention due to ultra-low voltage operation, non-volatility, higher logical efficiency, high density integration, and availability of a complete set of Boolean functions [142]. However, to realize ASL integrated circuits, device scalability is extremely important since for advanced technology nodes, a microprocessor typically comprises billions of digital switches. Furthermore, the large dynamic power associated with STT-driven magnetization switching also becomes an issue for ASL to become a viable beyond-CMOS technology option. Therefore, it is of interest to (i) identify the scaling limits of the ASL [26], (ii) explore several ways to reduce or eliminate these scaling limits [28, 29, 25], and (iii) even improve the energy efficiency of the scaled ASL components.

On the other hand, in addition to spintronics, where ferromagnetism has been

widely used to manipulate and store bits [178], recently ferroelectricity has also attracted significant interest because of its promising potential in technological applications [48]. Ferroelectric materials can be used to represent binary data as well, since their spontaneous polarization can be switched directly by applying an electric field. Recent experimental and theoretical work show that ferroelectricity can still survive down to a few nanometers [62, 135, 216, 188, 69], in which electronic transport is mainly dominated by quantum-mechanical tunneling. Therefore, a device composed of a thin ferroelectric (FE) layer sandwiched by two metallic electrodes, also known as a ferroelectric tunnel junction (FTJ), is proposed to generate giant tunneling electorsistance (TER), which is typically a few orders of magnitude larger than tunneling magnetoresistance (TMR) in magnetic tunnel junctions (MTJs) [224]. Hence, it is also of interest to have a deep and systematic understanding of the transport properties of FTJs and explore any possible technique to further improve TER for FTJs as beyond-CMOS non-volatile logic or memory components.

With these goals in mind, this thesis is organized as follows. First, in Chapter II, scaling limits on ASL are investigated theoretically. Next, in Chapters III and IV, novel structures to interconnect ASL using Si, Cu, and Al as channel materials are explored to loosen these scaling limits. Furthermore, to completely get rid of the energy associated with interconnects, Chapter V proposes a new concept in which automotion of magnetic domain walls (DWs) along ferromagnetic (FM) wires are used to propagate digital signals for ASL. By combining all the advantages from the structures shown in Chapters II to V, a new scheme, where digital computing is performed using STTs in spin valves (SVs) and DW automotion in FM wires, is presented in Chapter VI. For beyond-CMOS non-volatile components using the FE, Chapter VII shows an original theoretical approach based on quantum mechanics and thermodynamics that can well describe experimental I-V characteristics in various FTJs, and also explain the controversy in inverse TER observed from different groups.

Chapter VIII concludes the thesis and also discusses the outlook for both spintronic and FE non-volatile logic and memory in the beyond-CMOS era.

Overall, this thesis is aimed at (i) exploring novel device and interconnect concepts for energy-efficient STT-driven spintronic logic, and (ii) understanding electronic transport in FTJs as non-volatile memories in the beyond-CMOS era. Before we dive into the details of each chapter, in the rest of Chapter I, an overview of CMOS scaling is given to highlight the motivation of this thesis, and to present the background knowledge for both ferromagnetism and ferroelectricity that may help readers understand this thesis better.

1.1 CMOS Scaling

The goal of CMOS scaling (or Moore's law) is to improve the performance of a microchip without significantly increasing the fabrication cost. In the past few decades, CMOS scaling has followed the famous scaling theory (or constant-field scaling) proposed by Robert Dennard in 1972, which states that when the device size is reduced by a scaling factor of S (~ 0.7 [161]) in each new technology generation, the channel length (L_{ch}), the oxide thickness (t_{ox}), the bias voltage (V_{bias}), and the doping density (N_d) have to be adjusted accordingly by the same factor [49]. In other words, for each generation, the channel length, the oxide thickness, the bias voltage, and the doping density become $S \times L_{ch}$, $S \times t_{ox}$, $S \times V_{bias}$, and N_d/S, respectively. The device performance will also be improved as the device is scaled. For example, the switching speed of a CMOS transistor becomes faster as the channel length is shorter due to the reduction of the electron traveling time from the source to the drain. However, recently, there are some challenges that significantly prevent CMOS transistors from further scaling down, and these challenges can be viewed from three different aspects, including physical, power, as well as technology limitations [79]. In the following, limitations from each aspect are discussed briefly.

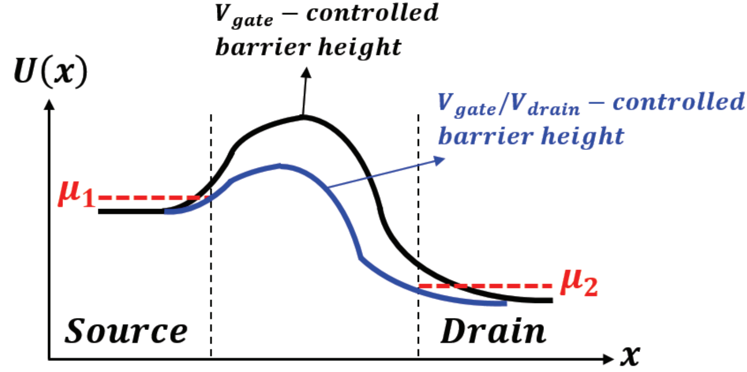

Figure 1: Potential energy profile in the source-to-drain direction to illustrate the drain-induced barrier lowing (DIBL) effect in a scaled CMOS transistor.

1.1.1 Physical Limits

Physical limits in general refer to the factors that prevent CMOS transistors from scaling as their physical size is reduced. For an ideal CMOS switch, the gate terminal should be able to fully control the energy barrier between the source and the drain. When a switch is on, the barrier height is reduced by the gate voltage through the electrostatic field; thus, most of electrons can be injected thermionically from the source to the drain and contribute the current flow. On the contrary, when a device is off, the barrier height is large. In such a case, only few electrons can cross the barrier and almost no current flow is established. However, due to the increase of the drain capacitor, as the channel of a CMOS transistor is reduced to pursue a higher switching speed, not only the gate but also the drain terminal can control the barrier. This is illustrated in Fig. 1, where the barrier height is further reduced in the presence of the drain voltage in a short channel device. This phenomenon is known as drain-induced barrier lowing (DIBL) [161], and its direct effect on the device performance is the increase of subthreshold leakage currents. Consequently, to reduce DIBL, the gate capacitor is increased by reducing the oxide thickness, which causes an increase in the leakage current due to direct quantum-mechanical tunneling from the gate to the channel. Also, the mobility degradation due to remote scattering from

doped polycrystalline silicon becomes more pronounced as the oxide becomes thinner [36, 35]. As a result, to achieve a large gate capacitor, the high$-k$ dielectric based on Hf and Zr has replaced SiO_2 [160]. Recently, non-planar structures such as FinFET have been used to further enhance the gate-to-channel control [85]. Unfortunately, no matter how strong the gate control is enhanced, as the channel length is reduced to the region in which direct tunneling from the source to the drain occurs [111], a CMOS transistor cannot work as a switch anymore as illustrated in Fig. 2. DIBL can also be mitigated by increasing the channel doping density, which is also one of the scaling rules in Dennard's theory. However, in heavier doped channels, several side effects such as mobility degradation due to impurity scattering, band-to-band tunneling [160], gate-induced drain leakage [77] negatively affect both performance and functionality of the CMOS device.

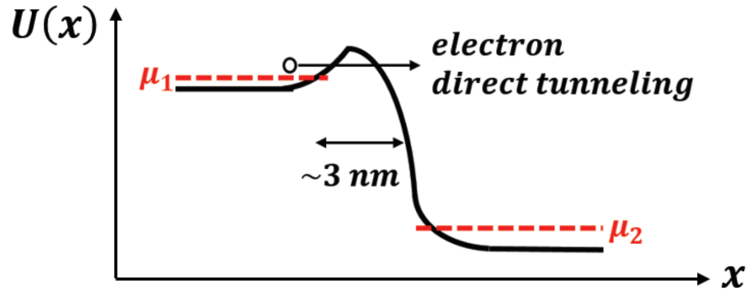

Figure 2: Potential energy profile in the source-to-drain direction to illustrate direct quantum-mechanical tunneling as the channel length becomes too short.

1.1.2 Power Limits

As mentioned in Dennard's scaling theory, V_{bias} needs to be scaled in each generation. To have large enough on-currents, the threshold voltage (V_{th}) has to be also scaled with V_{bias}. However, the reduction of V_{th} leads to more pronounced subthreshold leakage currents, which significantly increases the static power dissipation. It is found that the leakage currents can be increased by 10 times if the reduction of V_{th} is about 85mV [161]. Also, based on the analysis of the CMOS NAND noise margin, the

scaling of V_{bias} stops at ~ 0.5V to keep logic state consistency in the worst case [136]. In digital integrated circuits (ICs), the power dissipation density can be divided into two types: dynamic power density and static power density [63]. The former is due to the switching devices, and the latter results from leakage currents of the non-switching devices. Because the switching frequency increases in a smaller device and V_{bias} has stopped scaling in recent technology generation, the dynamic power density has been increasing in each generation. Consequently, to suppress the power density below the limit that can be removed, the operating frequency now remains almost constant in each advanced technology. On the other hand, the static power density is also raised rapidly in each generation due to the increasing subthreshold leakage currents. Fig. 3 shows that as the device dimension is reduced below a certain size (e.g. 10nm), the static power will finally surpass the dynamic one. In such a case, a microchip will still dissipate a significant amount of energy even in the stand-by mode.

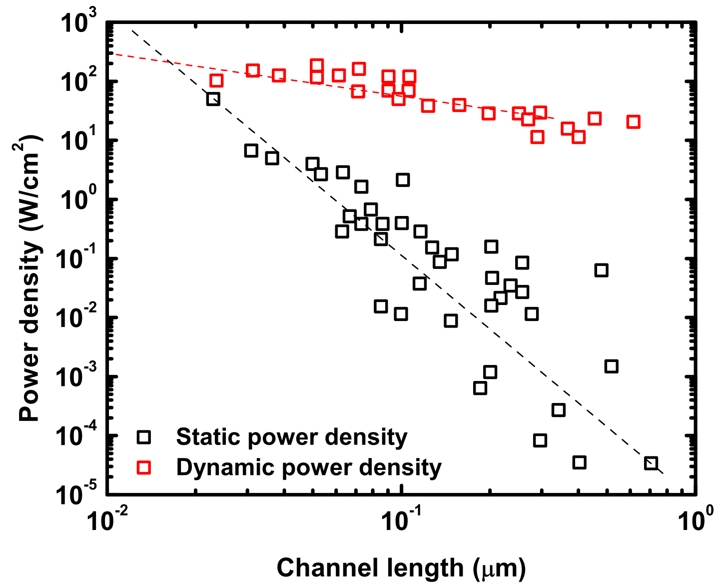

Figure 3: Static (black square) and dynamic (red circle) power density versus channel length [169].

1.1.3 Technology Limits

CMOS transistors are typically fabricated by patterning them on a wafer using lithography with masks. The resolution of a lithography system, CD, can be roughly estimated by the Rayleigh equation given as

$$CD \sim k\frac{\lambda}{NA}, \tag{1}$$

where k is the lithography constant depending on the process control, λ is the lithography wavelength, and NA is the numerical aperture of the focusing optics, describing the focusing strength of the projection system. As a result, a shorter lithography wave length is desirable to obtain higher resolution. The 248nm lithography wave length combined with optical approximity correction (OPC) helped CMOS technology scale successfully from 0.18μm to 0.13μm [207]. State-of-art 193nm ultraviolet (UV) lithography has been widely used in current advanced CMOS patterning. For future scaled CMOS technology (e.g. 7nm), extreme ultraviolet (EUV) lithography ($\lambda \sim 13.5$nm) may be required. However, the most challenging issue with the EUV patterning is the high cost and low throughput. In addition to pursue a shorter lithography wavelength, the multiple pattering technique has also been used to further enhance the feature density of manufacturing ICs [106, 238].

1.1.4 Potential Solutions to Beyond-CMOS Technology

To address the issues mentioned above, lots of alternative devices have been proposed, which can be roughly divided into two main categories [165, 164]. One is still using the electron charge to represent digital bits (i.e. charging and discharging a capacitor) such as Tunnel FETs, which can potentially reach the subthreshold swing (SS) lower than 60mV/dec [6]. Another is using alternative state variables such as the electron spin and electric polarization to implement digital logic mainly because of their non-volatility. Here, devices using ferromagnetism (or electron spin) and ferroelectricity (or electric polarization) are particularly interesting because they may

enable zero static power dissipation. However, for STT-driven devices such as ASL, the power associated with the magnetization switching is much larger than that for CMOS switches. In Ref. [142], it has been shown that the switching energy in ASL can be comparable to or even lower than that in a CMOS transistor if some material and interface parameters can be achieved in the future; however, so far, it is still unclear how to realize such materials. Therefore, instead of playing with the material parameters, part of this thesis is to reduce the switching energy in STT-driven devices by engineering the device structure. In the following, some key concepts in both ferromagnetism and ferroelectricity that will be used throughout this thesis are mentioned.

1.2 Ferromagnetism

Ferromagnetism occurs as electrons in materials become spontaneously spin-polarized. Since spintronic logic covered in this thesis is mainly based on transition FM metals such as iron, cobalt, nickel, and their alloys, here the origin of ferromagnetism in these materials are briefly reviewed [212, 178].

In transition metals, spontaneous spin polarization of electrons is induced by the competition between atomic-like exchange interaction and inter-atomic hybridization. The former prefers to align spins, and spin polarization is reduced by the latter. The atomic-like exchange interaction can be understood easily from Hund's rules, which describe how nearly degenerate atomic levels are filled by electrons to minimize the energy. From Hund's first rule, it is known that in isolated atoms, to maximize the spin polarization, electrons with one spin direction are put into partially filled atomic orbitals before those with the opposite spin direction. The energy lowing from this process is to reduce the Coulomb repulsion between electrons with the same spin by keeping them further apart, which is basically the Pauli exclusion principle. As a result, based on Hund's first rule, non-zero spin angular momentum in isolated

atoms is established by those partially filled orbitals. Note that in addition to spin angular momentum, non-zero orbital angular momentum can also contribute magnetic moments of isolated atoms. On the other hand, it is well-known that energy bands in solids are formed due to hybridization of electronic states in the neighboring atoms. During band formation, magnetic moments are suppressed mainly by (i) quenching the orbital component of the magnetic moment through breaking spherical symmetry for the environment of each atom, and (ii) avoiding electrons moving from low-energy filled bands to high-energy unoccupied bands. Consequently, most solids do not show ferromagnetism except for those with tightly bound 4f-orbitals, where the hybridization is too weak to suppress spin polarization. However, due to partially filled 3d-orbitals, the transition metals have both strong exchange splitting and hybridization. The exchange splitting shifts the band of majority carriers lower than that of minority carriers to stabilize ferromagnetic states, which can be considered as the compensation of kinetic energy associated with moving electrons from low-energy filled band states to high-energy unoccupied band states. Based on the physics mentioned above, several models that describe ferromagnetism in FM transition metals are introduced.

1.2.1 Models of Ferromagnetic Materials

The most sophisticated model that accurately describes much of the key physics in FM transition metals is based on the local spin density approximation (LSDA) [123, 76, 101], where hybridization is treated exactly and the atomic-like exchange interaction is handled under mean-field theory. The LSDA approximation is able to successfully describe many properties such as magnetic moments in FM metals without any fitting parameters. The fundamental degrees of freedom in this approach are electron and spin densities, which are calculated by wave functions. However, so far, no formal justification has been shown for using LSDA wave functions as real

functions; therefore, these wave functions are now served as a good approximation to real wave functions in most cases.

There are also two simplified models that are often used to describe FM metals. One is known as the free-electron Stoner model, and another is known as the s-d model. The free-electron Stoner model assumes that there are two bands in an FM metal, and one is for up-spins and another is for down-spins. There exists a relative shift in the energy gap between the two bands due to the exchange splitting, and both bands have a free-electron dispersion given as

$$E\left(k\right)=\frac{\hbar^2k^2}{2m_0}+\frac{\sigma_z\Delta}{2}, \tag{2}$$

where E is the electron energy, $\hbar$ is the reduced Planck constant, k is the electron wave vector, σ_z is the Pauli spin matrix, Δ is the exchange splitting, and m_0 is the free electron mass. Sometimes m_0 is replaced by the effective mass m^* to obtain a better fit to the experimental results [45]. In the s-d model, "s" and "d" stand for delocalized conduction electronic states and localized magnetic states, respectively. The localized magnetic states are assumed to be weakly coupled to the "s" states through the interaction given as $-JS \cdot s$ with J being the interaction strength, S being the local moment of each d electron shell, and s being the spin density of conduction electrons. Fig. 4 shows a comparison between band structures under the LSDA, free-electron Stoner, and s-d approximations for an FM transition metal [178]. From Fig. 4, it can be seen that the realistic band structure of an FM metal is far more complicated than the parabolic shapes assumed in the Stoner model, and the d electrons are not localized as assumed in the s-d model due to the strong hybridization within the d bands and of the d bands with s bands. However, even though both models are not able to describe the full band structure of an FM metal that can be calculated under the LSDA approximation, they are extremely useful to illustrate the essential physics behind an FM metal, describe the experimental results by adjusting a few fitting parameters, and sometimes estimate the performance of a device where

FM metals are involved. As will be shown later, the Stoner model is used to describe spin injection from an FM metal into a non-magnetic semiconductor or metal [28, 29] due to its successful agreement with experimental results in MTJs by varying simply a few material parameters such as the interface barrier and effective mass [45].

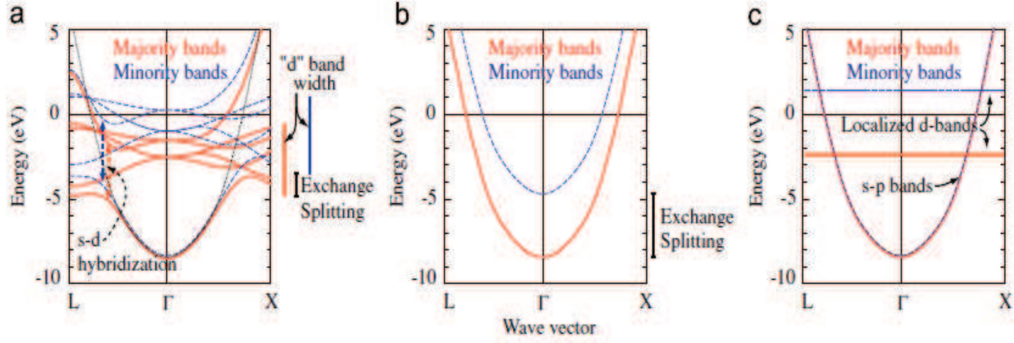

Figure 4: Comparison between the band structures of a FM transition metal using different approximations [178]. (a) Local spin density approximation (LSDA), (b) Stoner model, and (c) s-d model.

1.2.2 Spin Currents and Spin Relaxation

From the band structure models introduced above, spin-polarized currents can be understood as a result of different band structures for majority and minority electronic states in an FM metal. In other words, thanks to spin-dependent electronic properties in an FM metal, a magnetic layer can act as a spin filter and thus spin currents are generated. Using Cr/Fe multilayers as an example, as electrons are injected from Cr into Fe, down spins have a higher probability to transmit through the thin film than up ones due to different interface and defect scattering induced by the spin-dependent band structure [230]. Consequently, the electrons flowing out of the Fe layer become spin-polarized in the direction of down spins in the Cr/Fe/Cr structure. Furthermore, as spin-polarized currents flow into a non-magnetic material such as Cu or Si, spin polarization of the current can only persist on the scale of the spin relaxation length, which is typically a few hundreds of nm in Cu [176] and about several microns in

Si [131]. Spin relaxation in general is referred to a process that brings the non-equilibrium spin-polarized electrons back to the equilibrium in a material. Therefore, since NM materials are not spin-polarized under equilibrium, the spin relaxation length in NM materials can be considered as a characteristic length in which the spin polarization of the current can be preserved. Beyond this length scale, the spin orientation in currents is mostly destroyed through a significant dephasing process induced by both phonon and impurity scattering [176]. Spin currents, I_s, are typically defined as

$$I_s = I_\uparrow - I_\downarrow \tag{3}$$

with $I_\uparrow$ and $I_\downarrow$ being currents comprising up- and down-spin electrons, respectively. The spin polarization in currents, P, is usually defined as spin currents normalized to charge currents given as

$$P = \frac{I_s}{I_c} = \frac{I_\uparrow - I_\downarrow}{I_\uparrow + I_\downarrow}, \tag{4}$$

where I_c is the charge current. Spin currents in this thesis play an important role in propagating spin information between FM metals. Note that the magnetic moment and spin density vector are always in the opposite direction. Interestingly, people typically define that the FM metal magnetized to the "up (down)" direction is due to the "spin-up (spin-down)" electrons in spintronic devices for convenience, and this convention will also be followed while calculating the spin current. Consequently, as will be shown later, the STT term in the differential equation for the magnetization dynamics (see Eq. 10) is written in terms of the magnetic-moment flow, which is the the spin current defined above.

1.2.3 Spin-transfer Torque and Magnetic Dynamics

In any material system, a STT is present as long as the flow of spin angular momentum is not uniform. For example, consider a spin current flowing into a single-domain

FM thin film, whose magnetic moment is not collinear with that of the spin current. Due to the filtering process, the spin current flowing out of the thin film must have the same magnetic moment as the FM material. As a result, to generate the difference in the magnetic moment between two spin flows, it is required for the FM thin film to absorb a portion of spin angular momentum carried by incident electrons. During this process, the FM material reorients the spin direction of the flowing electrons by exerting a torque on them. Because the conservation of spin angular momentum is approximately valid in FM metals, the magnetization of the FM material also experiences an equal and opposite torque from the conducted electrons. The latter is also know as the STT, and its magnitude can be typically calculated either by considering (i) the mutual precession of the flowing spin and the magnetization during their interaction [78] or (ii) the net change in spin currents before and after experiencing STTs [178]. Fig. 5 illustrates the physical origin of a STT in FM metals.

Figure 5: Schematic of the origin of spin-transfer torques (STTs) in FM metals. The yellow arrows represent the direction of the magnetic moment.

As illustrated in Fig. 5, it can be seen that as long as the magnitude of STT is strong enough, the magnetization of an FM metal can be aligned with the incident electron spin, and this switching magnetization dynamics is typically described by micromagnetics, which is a phenomenological and also efficient approach to model magnetism on a mesoscopic length scale [19, 59]. Note that micromagnetics is not aimed to describe the dynamics of atomic magnetic moments, but rather taking the continuum limit, and it has become popular mainly because the magnetic devices of interest are usually much larger than the atomic length. In such a case, calculations based on the atomic scale are extremely time-consuming and thus become impractical.

Here, several key concepts in micromagnetics are reviewed briefly, and the macrospin approximation, which is widely used to investigate the magnetization dynamics, is also discussed.

In magnetic systems, the magnetization tends to align with an effective field, which in general varies with the space, and typically is contributed by four different sources, including the external applied magnetic field, magnetocrystalline anisotropy, micromagnetic exchange, and the magnetostatic field. For each contribution, there is the free energy associated with it, and the corresponding field is simply the functional derivative of the free energy with respect to the magnetization given as

$$\vec{H}(\vec{r}) = \frac{-1}{\mu_0 M_s} \frac{\partial F}{\partial \vec{m}(\vec{r})}, \tag{5}$$

where μ_0 is the free space permeability, M_s is the saturation magnetization, F is the free energy contributed by each source, $\vec{m}$ is the magnetic unit vector at each domain, and $\vec{r}$ is the position vector. Magnetocrystalline anisotropy mainly results from the spin-orbit coupling, and the magnetization will tend to align with certain lattice directions. The free energy of this material anisotropy in general has different mathematical forms depending on the lattice structure of the material. In FM materials, the micromagnetic exchange interaction tends to align the magnetizations of the neighboring domains in the same direction to reach low-energy configurations. The magnetostatic field is a highly non-uniform and non-local effect, which results from the magnetic field generated by the magnetization (or magnetic dipole) of each domain. Mathematically, the total free energy including four contributions can be written as

$$\begin{aligned} F &= -\mu_0 M_s \int d^3 r H_{ext} \cdot \vec{m}(r) - K_u \int d^3 r \left(\hat{n} \cdot \vec{m}(r)\right)^2 \\ &\quad + A \int d^3 r \left(\left(\frac{\partial \vec{m}}{\partial x}\right)^2 + \left(\frac{\partial \vec{m}}{\partial y}\right)^2 + \left(\frac{\partial \vec{m}}{\partial z}\right)^2 \right) \\ &\quad - \frac{\mu_0 M_s^2}{8\pi} \int d^3 r \int d^3 r' \vec{m}(\vec{r}) \cdot \frac{3\left(\vec{m}\left(\vec{r'}\right) \cdot \vec{x}\right)\vec{x} - \vec{m}\left(\vec{r'}\right)|\vec{x}|^2}{|\vec{x}|^5}, \end{aligned} \tag{6}$$

where H_{ext} is the external applied magnetic field, M_s is the saturation magnetization, $\vec{x} = \vec{r} - \vec{r'}$, A is the exchange constant, and K_u is the material anisotropy energy density. By using the definition shown in Eq. 5, the corresponding effective magnetic field is given as

$$\begin{aligned} \vec{H}(\vec{r}) &= \vec{H_{ext}} + \frac{2K_u}{\mu_0 M_s}\hat{n}\left(\hat{n} \cdot m\left(\vec{r}\right)\right) + \frac{2A}{\mu_0 M_s}\nabla^2 \vec{m} \\ &+ \frac{M_s}{4\pi}\int d^3r' \frac{3\left(\vec{m}\left(\vec{r'}\right) \cdot \vec{x}\right)\vec{x} - \vec{m}\left(\vec{r'}\right)|\vec{x}|^2}{|\vec{x}|^5}. \end{aligned} \quad (7)$$

As mentioned previously, since micromagnetics is attempted to describe magnetization dynamics on the mesoscopic length scale, the atomic exchange discussed in the band structure of FM metals is not explicitly shown in the above expressions. Instead, the atomic exchange effect is implicitly included by the following constraints: (i) $\vec{m}$ is a unit vector, and (ii) the magnitude of the magnetization is equal to the saturation magnetization.

In the absence of STTs, as the magnetization is not in equilibrium, it will precess around the effective field, which may depend on time. If there is no process that dissipates the system energy, this precession will last forever and the magnetization distribution remains on the same energy surface. The equation of motion for the magnetic precession is given as

$$\frac{\partial \vec{m}}{\partial t} = -\gamma\mu_0\left(\vec{m} \times \vec{H_{eff}}\right), \quad (8)$$

where γ is the gyromagnetic ratio ($\gamma = 17.6 \times 10^{10}$ tesla^{-1}s^{-1}). To account for the energy dissipation, a phenomenological damping term is introduced into Eq. 8 [70] and the equation becomes

$$\frac{\partial \vec{m}}{\partial t} = -\gamma\mu_0\left(\vec{m} \times \vec{H_{eff}}\right) + \alpha\left(\vec{m} \times \frac{\partial \vec{m}}{\partial t}\right), \quad (9)$$

where α is known as Gilbert damping coefficient, which can be calculated by including both intrinsic and extrinsic physical processes [185, 148]. The dominant intrinsic

process for FM semiconductors [198] and transition metals [71] can be described by the Kambersky damping model based on electron-hole pair generation [107]. Note that as FM materials are in contact to NM metals, there is also a well-known phenomenon called spin pumping that also contributes the damping. Spin pumping in general refers to a process where spin currents are injected into NM metals through the magnetization precession in FM materials [221, 155, 81].

To account for the STT in the magnetization dynamics, in practice, Eq. 9 is modified by assuming that $\frac{\partial \vec{m}}{\partial t}$ is directly proportional to the STT and given as [141]

$$\frac{\partial \vec{m}}{\partial t} = -\gamma\mu_0 \left(\vec{m} \times \vec{H_{eff}}\right) + \alpha \left(\vec{m} \times \frac{\partial \vec{m}}{\partial t}\right) - \frac{\vec{m} \times \left(\vec{I_s} \times \vec{m}\right)}{eN_s} \tag{10}$$

with I_s being the net spin current flowing into the FM metal, e being the elementary charge, and N_s being the number of Bohr magnetons inside the magnet, defined as $\frac{2M_sV}{\gamma\hbar}$, where V is the volume of an FM metal. However, the direct insertion of STT into Eq. 10 requires some discussion because some subtle physics is involved in this step. The main assumption of Eq. 10 is that all of the transverse spin components absorbed by the FM metal are used to reorient the magnetization, instead of other processes such as the excitation of short-wavelength spin wave modes or being transferred to the atomic lattice. Nevertheless, this assumption is still a good approximation to explain most of the present-day STT experiments. Furthermore, in a more strict sense, not only spin but also orbital angular momentum can affect the magnetization. In other words, the total angular momentum and the magnetization should be written as $\vec{s} + \vec{l}$ and $\frac{-\mu_B\left(2\vec{s}+\vec{l}\right)}{\hbar}$, respectively, where $\vec{s}$ as well as $\vec{l}$ are spin and orbital angular momentum density vectors, respectively and μ_B is the Bohr magneton. However, in an FM metal, it is a good first-order approximation to ignore the orbital contribution since the orbital moments are significantly suppressed by strong hybridization of d electrons, and thus Eq. 10 is used in most STT analyses for metallic multilayers.

Another approximation that is often used in STT analyses is known as the macrospin approximation, basically assuming that the magnetization of an FM material is spatially uniform during its motion and thus can be treated as a macrospin. The macrospin approximation is able to caputre some fundamental physics in STT-driven dynamics. For example, the threshold for the onset of the precession states and the magnetization switching can be estimated accurately by the macrospin approximation [158]. However, in some recent experiments, it has been shown that the STT-driven switching is far more complicated than that described under the macrospin approximation [1]. Therefore, here a brief discussion on the limitations of the macrospin approximation is given.

As mentioned above, the macrospin approximation basically assumes that there exists only one domain in an FM material, and no multi-domain structure will be formed under any excitation. The critical size of a single-domain FM body can be estimated by the energy minimization between the exchange energy and the magnetostatic energy. If only the exchange effect is considered, a single-domain state is preferred as the size of an FM metal is scaled down to the exchange length, defined as $l_{exch} = \sqrt{\frac{2A}{\mu_0 M_s^2}}$. This critical length can be further increased if the FM material has magnetocrystalline anisotropy that also stabilizes the uniform magnetization. However, the actual critical length can only be determined through numerical simulations, and is typically about $(4-8)\, l_{exch}$ with l_{exch} being 5nm for most FM materials [178]. Therefore, the upper bound of a single-domain FM body is about 40nm, which is much smaller than most of the STT studies and explains the failure of the macrospin description in some experiments. Interestingly, there still exists some cases where the macrospin approximation is a fairly good approach even though the sample size is far larger than the critical dimension. This result can be mainly attributed to the following two reasons. First, the critical length mentioned above is determined by the magnetic configuration with the lowest energy. Since this length is estimated simply

from the static configuration, it cannot be used to predict if the transition from a single- to a multi-domain state occurs during the magnetization reversal, in which an energy barrier is typically required to be overcome. Second, the critical length is valid only for the geometry having the same order of magnitude in the x, y, and z directions (e.g. cubes). For an FM thin film that is often used in STT-driven devices, its thickness is much smaller than the lateral dimensions, and the balance between both exchange and magnetostatic energies may change, leading to a larger critical length. As a result, for any given device geometry, it is necessary to perform full-scale micromagnetic simulations to see if the macrospin approximation is reasonable. So far, it has been demonstrated that the macrospin approach can quantitatively explain some experimental results in the structure involving multilayer nanopillars due to a very small dimension where a STT is applied [158]. Part of devices and interconnects introduced in this thesis only allow STTs exerted on a small FM region and thus are also modeled by the macrospin approximation. On the other hand, any size of point contact structure is not suitable for the macrospin approximation because of the strong exchange effect from extended magnetic layers [181, 182].

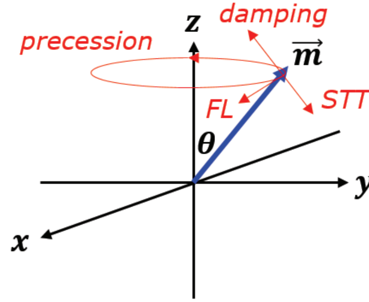

Figure 6: Schematic of a macrospin under the effects of the effective field, the damping, and the STT. A field-like (FL) torque is also include; however, it is usually ignored in metallic layers. The easy axis is assumed to be in the z direction.

There are several important STT-driven modes that can be described by Eq. 10 under the macrospin approximation. A macrospin under the effects of the effective field, the damping, and the STT is illustrated in Fig. 6. Consider that the initial

magnetic moment is slightly tilted away from the easy axis (z-axis in Fig. 6) due to thermal noise fluctuations or the applied magnetic field, without any STT and the damping effects, the magnetic moment will precess around the effective field in a circle. To reduce the total energy, the damping tends to push the magnetic moment back to the easy axis. As a result, in the absence of STTs, the magnetic moment under a damping process will follow a spiral path with the decreasing precession angle and move toward the easy axis. As a STT is exerted on the macrospin, depending on the direction of the current flow, its direction can be either the same or opposite to that of damping torque. If the STT is in the same direction to the damping, it basically increases the effective damping process in an FM material. On the other hand, if the STT is in the opposite direction to the damping, there are three modes that can be excited depending on if the point of instability is passed. First, if the magnitude of the STT is smaller than the damping, meaning that the instability point is not passed, similar precession back toward the easy axis mentioned above occurs, and is also known as the damped motion. Next, as the precession angle is increased by the greater STT and finally crosses the instability point, dynamic equilibrium, also known as stable precession, can be achieved if the damping torque increases with the precession angle faster than the STT. Finally, if the damping is always smaller than the STT after crossing the instability point, the precession angle can be increased to 180°, and this dynamics is the famous magnetization switching, which will be extensively applied to the devices and interconnects introduced in this thesis.

1.2.4 Magnetic Domain Walls

As the size of FM metals in the device becomes larger than the critical length (i.e. interconnects), magnetic domains are established to lower the total energy described by Eq. 5. At different device scales, the dominant interaction is also different. For example, the micromagnetic exchange is short-ranged and tends to align nearby spins,

the magnetocrystalline anisotropy is also short-ranged and orients spins to some particular lattice directions, and the magnetostatic interaction is long-ranged and prefers anti-parallel alignment for distant parts of the FM material. Note that the magnetostatic interacton is mainly determined by the sample shape (as known as shape anisotropy) and is much weaker than the exchange effect on the short-range scale. As a result, due to the magnetostatic effect, as the sample becomes larger, the resulting configuration is typically broken into several domains and creates some specific magnetic patterns under equilibrium. The transition regions between different domains are known as magnetic domain walls, where the magnetization rotates from one domain's orientation to another's. The length of the transition region (or the length of DWs), l_{DW}, is determined by the competition between magnetocrystalline anisotropy and exchange interaction given as $\sqrt{\frac{A}{K_u}}$. A wider transition region reduces the exchange energy but increases the magnetocrystalline energy. In soft FM materials such as Permalloy (Py), since the material anisotropy is very weak, the DW length is determined by shape and exchange interactions. In a thin-film FM wire, there exists two common DW structures depending on the sample size. One is called the transverse wall (TW), and another is called the vortex wall (VW). Fig. 7 shows the spin structures of the two different walls. In the TWs, the exchange energy is minimized by putting free poles at the edge. As the width and thickness of the wire increase, the magnetostatic energy increases, and in such a case, a VW is preferred since the free poles can be minimized at the expense of increasing the exchange energy. Reference [147] has shown that for Py, the boundary between the TW and the VW is about $t \cdot w = 60l_{exch}^2$ with t and w being the thickness and the width of the FM wire, respectively. For FM interconnects introduced in this thesis, $t \cdot w$ is roughly $2 \times 20\text{nm}^2$, which is much smaller than $60l_{exch}^2$ and thus only TWs in FM wires are considered in this thesis.

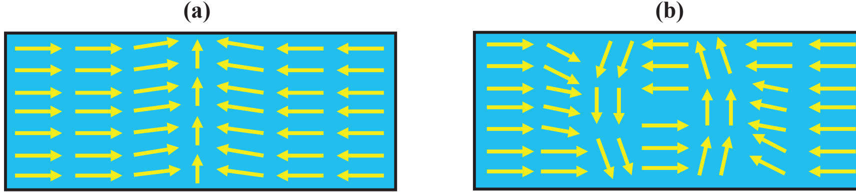

Figure 7: Schematic of two different types of magnetic domain walls (DWs) in an FM thin-flim wire. (a) Transverse wall (TW), and (b) vortex wall (VW).

1.2.5 Temperature Effects

As the temperature is deviated from zero Kelvin, spin transport (or spin relaxation length) is degraded due to the increasing scattering rates (e.g. phonon) [176]. On the other hand, at room temperature, it is required to consider the effect of thermal random fields on the magnetization dynamics, especially as the size of FM materials becomes smaller. This is mainly because the magnitude of the thermal random field, ν, is increased with the reducing dimension and can be mathematically expressed as

$$\nu = \sqrt{\frac{2\alpha k_B T}{\mu_0^2 \gamma M_s V}}, \tag{11}$$

where k_B the Boltzmann constant and T is the temperature. Also, the current threshold for the onset of the magnetization switching and the time required to reverse the magnetization are both significantly modified under thermal fluctuations. Typically thermal fluctuations allow the magnetization switching to occur at the currents below the critical threshold estimated in the absence of thermal field, and also result in a switching time distribution rather than a single value [28]. Furthermore, thermal noise plays a pivotal role in the non-volatility of the small STT-driven devices. As the FM devices become smaller, the barrier height between the two low-energy magnetic states is reduced, and thus spins can easily get reversed with simply thermal excitations. Under the macrospin approximation, in a FM material that has strong magnetocrystalline anisotropy, the energy barrier, E_b, is given as [29]

$$E_b = K_u V. \tag{12}$$

On the contrary, If the FM material has weak material (magnetocrystalline) anisotropy such as Py, the shape (magnetostatics) anisotropy is dominated for the energy barrier given as [23]

$$E_b = (N_{yy} - N_{zz}) \frac{\mu_0 M_s^2 V}{2}, \tag{13}$$

where N_{yy} as well as N_{zz} are the demagnetization tensors in the easy plane.

1.3 Ferroelectricity

There are two basic requirements for a material to be considered as an FE material. One is that a material should have spontaneous polarization under equilibrium, and another is that the direction of polarization can be reversed by an applied electric field. Ferroelectricity may occur if a dielectric reaches the condition called polarization catastrophe, meaning that the polarization becomes very large even at a very small applied electric field. Mathematically, the condition of polarization catastrophe can be shown by considering a dielectric with the susceptibility, χ_D. At a small applied electric field (E_D), the polarization (P_D) is simply proportional to E_D and can be written as $P_D = \chi_D E_D$. As the polarization becomes larger, the dipoles in a dielectric can also contribute the total electric field. As a result, the polarization now becomes $P_D = \chi_D (E_D + \lambda_D P_D)$, where λ_D is a proportionality constant for the field induced by the dipoles, and P_D can be expressed as $P_D = \frac{\chi_D}{(1-\lambda_D \chi_D)} E_D$. Consequently, polarization catastrophe occurs as $\lambda_D \chi_D$ is close to 1 since the polarization can be extremely large even at a very small applied electric field [112]. Physically, if an ion in a dielectric is slightly moved away from its equilibrium site under an applied electric field, the force due to an ion-induced electric field increases much faster than the elastic force, which tends to move the ion back to its equilibrium site. As a result, an asymmetric shift in the equilibrium position of the ions occurs and a permanent dipole moment (or spontaneous polarization) is established. This type of FE phase is also known as displacive transitions (in contrast to order-disorder transitions) since

in this picture, the ferroelectricity is originated from the ionic displacement. The oxides with perovskite structures such as $BaTiO_3$ and $PbTiO_3$ are well known examples of displacive transitions [40]. In particular, recently barium titanate ($BaTiO_3$) has drawn significant attention since its ferroelectricity can still be preserved as the thickness is reduced to a few nanometers, which enables the experimental demonstration of a switch based on polarization-dependent tunneling (or an FTJ) - an existing conceptual idea since 1971 [55].

1.3.1 Polarization-Electric field Hysteresis Loop

The most relevant property of an FE material to this thesis is the polarization-electric field hysteresis loop. This is because, as will be shown in Chapter VII, in an FTJ, the current is determined by the polarization-dependent energy band diagram, which follows the FE hysteresis loop closely. As a result, here, some background knowledge about the FE hysteresis loop is given.

In general, the experimental measurement of an FE hysteresis loop can be well described by a thermodynamic model based on Landau theory, even though this approach is fully macroscopic, meaning that the atomic displacement mentioned above is not captured. The success of Landau theory can be attributed to the fact that the postulated free energy is close to the realistic free energy of an FE material [64]. Landau theory says that the free energy of a system can be expanded in terms of the order parameter, which is the polarization in an FE material (or the magnetization in an FM metal). As a result, the free energy, G, corresponding to the phase transition from the paraelectric to the FE, is given as

$$G = \alpha_{FE} P_{FE}^2 + \beta_{FE} P_{FE}^4 + \cdots \, , \tag{14}$$

where α_{FE} and β_{FE} are the expansion coefficients and P_{FE} is the polarization. Note that α_{FE} is temperature-dependent and typically can be written as $a_{FE}\,(T - T_0)$ with a_{FE} being a constant and T_0 being the Curie temperature. In Eq. 14, only even terms

exist since the free energy is assumed to be identical as the polarization is switched. If the polarization reversal can also considered as a phase transition, the total free energy including the contribution of an applied electric field ($E_{applied}$) is given as

$$G = \alpha_{FE} P_{FE}^2 + \beta_{FE} P_{FE}^4 + \cdots - E_{applied} P_{FE}, \tag{15}$$

and the dynamics of the order parameter can be described by

$$\gamma_{FE} \frac{\partial P_{FE}}{\partial t} = -\frac{\partial G}{\partial P_{FE}}, \tag{16}$$

where γ_{FE} is the viscosity coefficient. Eq. 16 is known as Landau-Khalatnikov equation (also see Eq. 88) and will be used to reproduce the measured FE hysteresis loop from different FE thin films in Chapter VII. Fig. 8 shows schematically a typical polarization-electric field relation measured from a good FE material, which is characterized by the spontaneous polarization, the strength of coercive field, and the linear response of non-switchable dipoles. As will be shown in Chapter VII, with proper expansion coefficients, Fig. 8 can be well described by the LK equation.

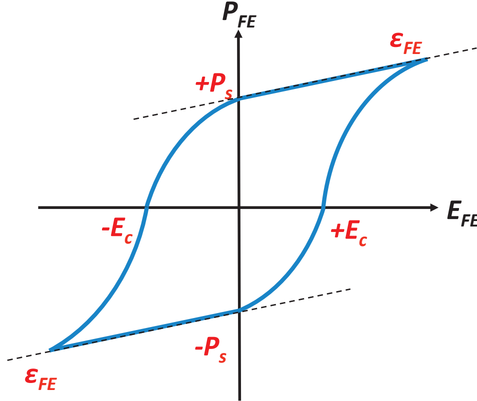

Figure 8: Schematic of a typical polarization-electric field hysteresis loop for a good FE material. P_s is the spontaneous polarization, E_c is the coercive field strength, and ϵ_{FE} is a constant that represents the linear response of non-switchable dipoles to the applied electric field.

CHAPTER II

SCALING LIMITS ON ALL-SPIN LOGIC

2.1 Overview

The focus of this chapter is to explore the potential issues that may affect the performance and functionality of ASL as its dimension is scaled. Therefore, in this chapter, scaling limits on ASL are studied theoretically using spin circuit theory and the stochastic Landau-Lifshitz-Gilbert (LLG) equations under the macrospin approximation. It is found that as ASL circuits are scaled, the device delay increases significantly due to a stronger dipole coupling between the input and the output magnets. The effect of the dipole interaction can be mitigated by increasing the input current and by using smaller magnets with stronger material anisotropy and weaker saturation magnetization. Furthermore, the presence of the leakage current modifies the device delay. Finally, both delay and energy of ASL increase dramatically as the shunt path is shortened.

2.2 All-spin Logic

Manipulating the electron spin as a computational variable has been one of the most promising candidates in the field of beyond complementary metal-oxide-semiconductor (CMOS) computing [165, 164]. Among many proposed spintronic devices, digital computing using metallic non-local spin valves (see Fig. 9), also known as ASL, has drawn significant attention due to ultra-low voltage operation, non-volatility, and availability of a complete set of Boolean functions [8]. In ASL, spins are injected into the channel through a charge current path from the magnet to the ground. This spin injection creates the spin accumulation underneath the input magnet, which leads to

the spin diffusive current along the channel. As spins reach the end of the channel, a STT is exerted onto the output magnet. As long as the STT is strong enough, the magnetic state at the output can be controlled by that at the input. Consequently, either *COPY* or *INVERT* operation can be realized by a single ASL device [8]. Interestingly, making ASL smaller can enhance the STT exerted on the output, since less spin-flip scattering occurs while spins diffuse toward the end [226]. This contributes to ASL circuits becoming more energy-efficient as the channel length is shortened. However, there are three issues coming up in scaled ASL, illustrated in Fig. 9, which will make the device fail if the current pulse is not adjusted accordingly: (i) As the input and output magnets become closer, the dipole interaction between magnets rather than the STT will dominate the output switching. (ii) When cascading ASL devices, there is an unwanted leakage current in the channel due to the voltage driving the next stage. This leakage current becomes larger as the channel length is reduced, and output switching time will suffer. (iii) The reduction in the shunt path makes fewer spins reach the end of the channel since most of spins flow into the ground directly; thus, ASL will become less energy-efficient or cannot even realize functions properly. The following sections aim to explore these scaling effects on ASL. Note that the width of the channel can also be shortened to make ASL smaller; however, the spin relaxation length will be impaired due to more sidewall/grain boundary scattering inside the channel [176]. As a result, the easy axis of the magnet is designed to be in the direction of the channel width (the z axis in Fig. 9) to minimize spin-flip scattering due to the dimensional scaling.

2.3 Mathematical Models

To estimate the spin current flowing through ASL, circuit models for spin transport in the NM material and ferromagnet/normal metal interface are used [141, 13]. The equivalent circuit for a single ASL device, including the effects of the driving current

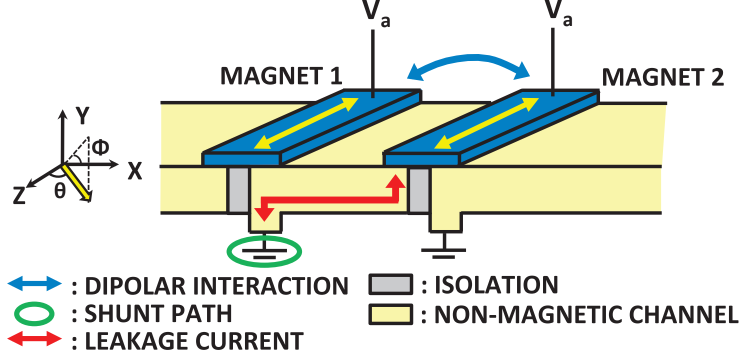

Figure 9: Factors limiting scaling of all-spin logic: dipole coupling between the input and the output magnets, the leakage current from the output, and the shunt path acting as a spin sink [26].

at the next stage, is shown in Fig. 10, and the corresponding conductance matrix, **G**, can be obtained by applying the standard nodal analysis (see [25] as an example).

The voltage vector including both charge and spin components, V, is obtained using the linear Ohmic relation given as

$$V = \mathbf{G}^{-1} I \tag{17}$$

with I being the current vector representing charge and spin currents at each node defined as follows:

$$I = [I_1 \quad N \quad N \quad N \quad N \quad I_2]^T, \tag{18}$$

where $I_1 = [I_{ASL} \quad 0 \quad 0 \quad 0]$, $I_2 = [I_{leakage} \quad 0 \quad 0 \quad 0]$, and $N = [0 \quad 0 \quad 0 \quad 0]$. Note that I_{ASL} and $I_{leakage}$ are calculated using a simple resistor network shown in the inset of Fig. 10. The spin currents flowing into the input and output magnets can be estimated using the voltage vector across the magnet, and will be the input parameters to the equation of the magnetization dynamics as mentioned below.

The magnets in ASL are often designed to be small enough so that the magnetic response can be in the range of nanoseconds. As a result, the magnets here are assumed to be single-domain, and the corresponding magnetization dynamics follows the LLG

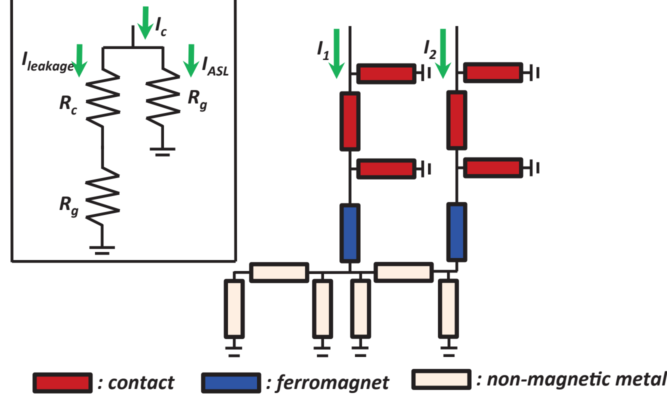

Figure 10: Equivalent spin circuit for ASL with current sources at both input and output. The inset shows a resistor network for a current source on the magnet [26].

equation including the STT term [141, 201] (see Eq. 10) under the macrospin approximation [210]. The effective magnetic field in the LLG equation includes the material anisotropy, self-demagnetization [10], thermal noise [20], and the dipole effect [108]. Due to the non-uniform nature of dipole interaction, the average dipole field acting on the magnet is evaluated by numerically integrating all the dipole components over the volume of the cubic shape [108]. Note that the field-like torque is incorporated into the imaginary part of interface mixing conductance, which typically is close to zero at the ferromagnet/normal metal interface [13]. The stochastic LLG equation is solved numerically using the midpoint method [29]. Fig. 11 illustrates how spin circuits and LLG equations are coupled for ASL under the dipole interaction. Since both interface conductance and dipole field depend on the magnetic orientation of the magnet, simultaneously solving LLG equations and spin circuits is required to describe the full magnetization dynamics of the input and output magnets. Note that the dipole field acting on the output is calculated using the magnetization of the input, and vice versa.

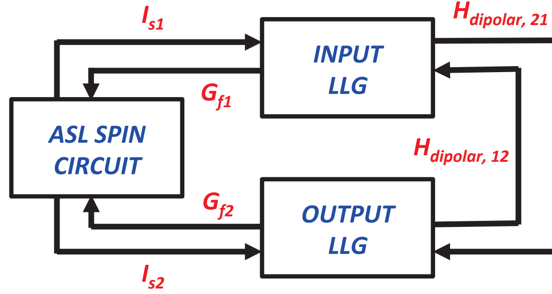

Figure 11: Self-consistent scheme for ASL dynamics. $H_{dipole,21}$ is the dipole field imposed on the output (denoted as 2) from the input magnet (denoted as 1), and vice versa [26].

2.4 Results and Discussion

In the following simulations, unless stated otherwise, the magnet size, shown in Table 1 along with typical material parameters, is chosen to be 120nm×20nm×2nm. This corresponds to the demagnetization-induced energy barrier of $70k_BT$ at room temperature, enough to ensure a reasonable magnetic retention time [210]. The spin transport parameters of Cu in [176] are used to include the dimensional scaling effects on spin relaxation. For simplicity, the input and output magnets are assumed to be in-plane magnetized for all the simulations. The out-of-plane magnetized magnets are also of interest because of the high thermal stability and the low switching current. However, the mathematical approach used here is quite general and thus can be applied to explore the same scaling factors in the out-of-plane case.

2.4.1 Dipole Interaction

In ASL, the input magnet creates stray field affecting the magnetization dynamics of the output magnet, and vice versa. The strength and direction of the stray field mainly depend on the distance and magnetizations of the magnets. Let us first examine the ASL operation without stray fields. Fig. 12(a) shows the magnetization dynamics in ASL without dipole fields, and it is found that the input can be copied into the output as long as spin injection is performed at the input [8]. Note that the

Table 1: Simulation parameters for all-spin logic (ASL) in Section 2.4. L_c, L_g, I_c, M_s, $K_{u,z}$, and α are the channel length, shunt path, input current, saturation magnetization, material anisotropy energy density, and damping coefficient, respectively.

Symbol	Value	Unit
L_c	45	nm
L_g	30	nm
I_c	-3	mA
M_s	10^6	A·m^{-1}
$K_{u,z}$	0	joule·m^{-3}
α	0.01	-

switching time (delay) is defined by the moment when m_z crosses zero. Furthermore, as the thermal field is added in Fig. 12(b), the delay is fluctuating over simulation runs and distributed within a certain range. When dipole coupling between magnets is included, as shown in Fig. 12(c), the delay becomes longer and the input magnetization dynamics is also modified. This is because the presence of dipole fields acts like an additional anisotropy to the magnet, making the STT to become relatively weaker. Also, the delay distribution due to the noise becomes broader as shown in Fig. 12(d), since the noise becomes more pronounced in the magnetization dynamics. The same trends are also observed in the *INVERT* operation since the dipole fields induced by the magnetization reversal are similar.

The scaling limit imposed by the dipole coupling can be seen in (a) and (c) of Figs 13 and 14. As the magnets are far apart, the delay including dipole fields is almost the same as that without dipole coupling. However, as the channel length is reduced, the delay increases significantly due to greater dipole fields between magnets. Also, a stronger dipole interaction broadens the delay distribution in the short channel as shown in (b) and (d) of Figs. 13 and 14. Note that as the channel length is longer, delay fluctuations also become greater since the STT is weaker due to more spin relaxation in the channel.

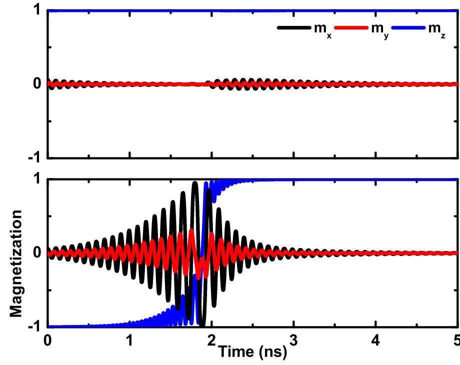

(a)

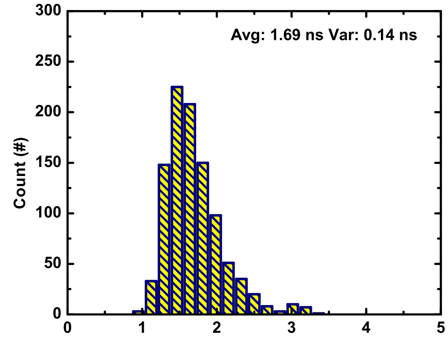

(b)

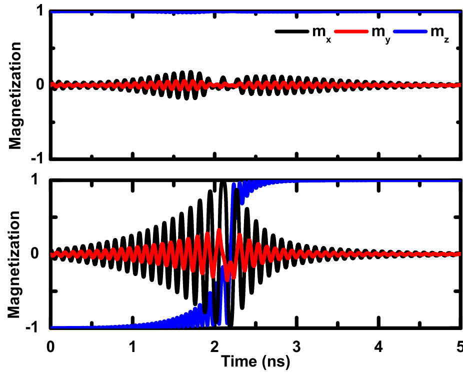

(c)

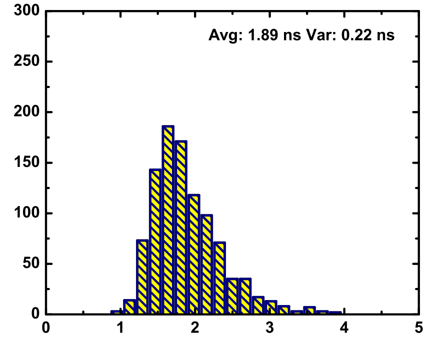

(d)

Figure 12: (a) and (c) Magnetization dependence on time for the input (top) and the output (bottom) magnets without and with dipole fields, respectively. Thermal noise fields are not included in both (a) and (c). (b) and (d) are the delay distributions due to the noise over 1000 stochastic simulations without and with dipole fields, respectively [26].

To mitigate the dipole effect in scaled ASL, the most straightforward way is increasing the current to make the output mainly dominated by STTs. Fig. 13(a) shows the increase in the delay due to dipole fields is shorter when the current flowing into ASL is greater. Furthermore, it is shown in Fig. 13(b) that thermal fluctuations are significantly reduced under a stronger current. Therefore, reducing the effect of dipole coupling in ASL can be realized at the expense of the higher switching energy. Another way to reduce the dipole effect is by adding material anisotropy to the magnets. As illustrated in Figs. 13(c) and (d), when the channel is shortened, the delay with stronger material anisotropy does not increase as much compared to that without uniaxial anisotropy, and the delay fluctuations due to the noise are also suppressed.

From Figs. 13(a) to (d), it is seen that the increasing STT with respect to the magnet would be a more efficient way to minimize the dipole effect compared to modifying anisotropy. Rather than injecting larger currents into ASL, using a magnet with a smaller saturation magnetization (M_s) also enhances the STT without consuming additional energy. Also, the dipole field produced by a magnet becomes weaker if M_s is smaller [108]. Note that since the energy barrier (EB) is proportional to the square of M_s (see Eq. 13), one needs to make sure that the magnet stability is still maintained while reducing Ms. In Figs. 14(a) and (b), where EBs (k_BT) are 70, 45, and 35 for M_s ($\frac{A}{m}$) being 10^6, 8×10^5, and 7×10^5, respectively, it is shown that by reducing M_s, the increase of delay due to the dipole coupling is almost eliminated, and the delay fluctuations are greatly suppressed. Furthermore, in addition to M_s, making the magnet size smaller can also increase the role of STT, and again one has to ensure non-volatility in ASL while scaling the magnets. As expected, Figs. 14(c) and (d) show the increase in the delay and the broadening of the delay distribution are both greatly mitigated in the short channel. The EBs (k_BT) in Figs. 14(c) and (d) are 70, 55, and 40 for the largest volume to the smallest one, respectively.

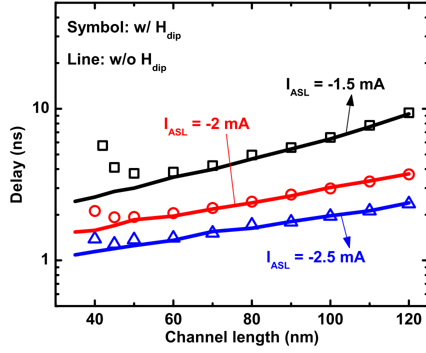

(a)

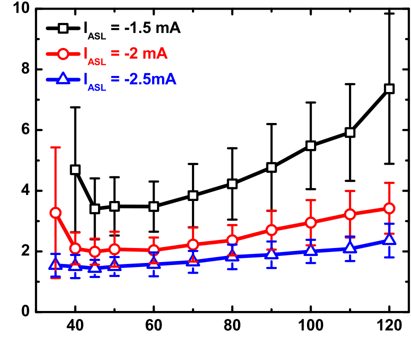

(b)

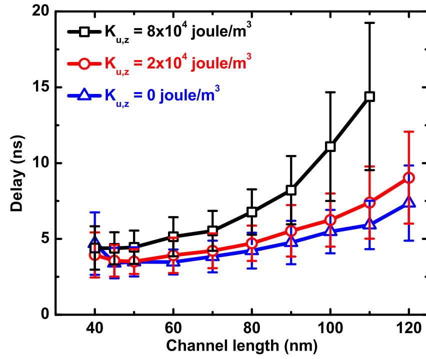

(c)

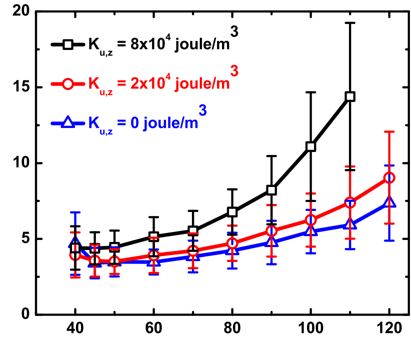

(d)

Figure 13: (a) and (c) Delay vs. channel length under different magnitudes of the injection current in ASL and material anisotropies. Data with and without dipole fields are shown. (b) and (d) Average delay and standard deviation (over 100 stochastic simulations) vs. channel length corresponding to the cases shown in (a) and (c), respectively [26].

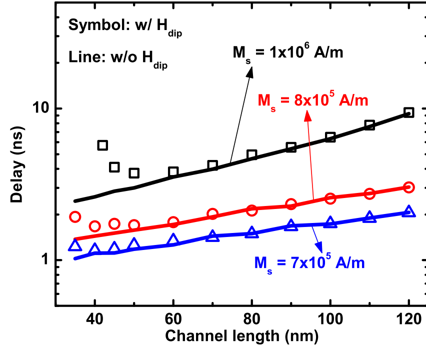

(a)

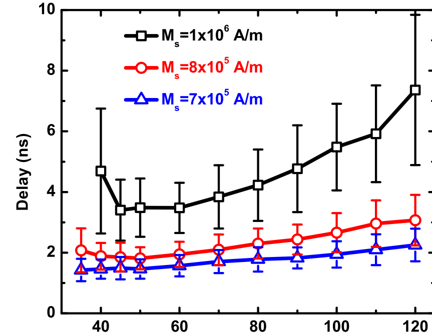

(b)

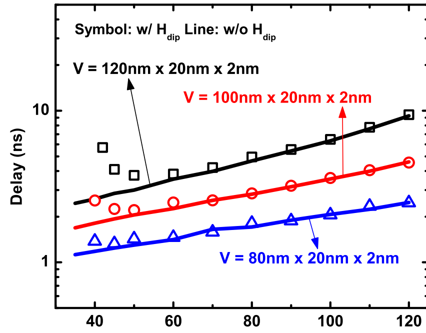

(c)

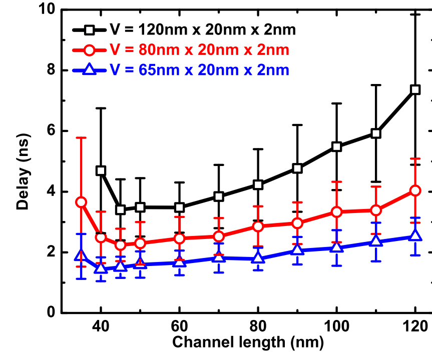

(d)

Figure 14: (a) and (c) Delay vs. channel length under different saturation magnetizations and volumes of the magnets. Data with and without dipole fields are shown. (b) and (d) Average delay and standard deviation (over 100 stochastic simulations) vs. channel length corresponding to the cases shown in (a) and (c), respectively [26].

2.4.2 Leakage Currents

For a single ASL device, the output is mainly controlled by the input through one-way diffusion of spins. However, for a complex circuit involving multiple ASL devices [23], the input and output are not well-isolated since there is a leakage current flowing from the output to the input as illustrated in Fig. 9. As a result, the output switching is not only determined by the input but also depends on the direction of the leakage current.

In Fig. 15(a), it is shown that positive and negative current sources at the output decrease and increase the delay, respectively. This can be explained by either spin injection or extraction is performed at the output. If a negative current is applied at the output (the opposite spins with respect to those at the input are injected into the channel), the spin polarization along the channel and the STT are reduced; thus, the delay is increased. Note that Fig. 15 is for the COPY operation with the initial anti-parallel configuration; however, the trend remains the same for the INVERT operation with the initial parallel configuration because the input current is simply reversed. Also, it can also be seen in Fig. 15(a) that the delay does not increase significantly as ASL is scaled even though the leakage current is increased in a short channel. This is because the delay is more sensitive to the STT close to the critical current. Thus, despite the fact that the leakage current is reduced in a longer channel, the change in delay is still comparable to that in the short channel. Furthermore, as shown in Fig. 15(b), the delay fluctuations with a negative leakage current is wider than those with a positive one due to the reduced STT.

To eliminate the leakage currents, it was proposed to electrically separate each stage from the next and to use dipole coupling to transfer information between stages [90]. However, it is difficult to obtain an error-free magnetization reversal through mutual dipole fields due to the mixing between damping and precessional dynamics [108]. Thus, alternatively, using interconnects based on DW automotion can reduce

the leakage and is suitable for ASL scaling [25]. To completely remove the leakage, a simple spin valve (SV) with a tunneling barrier can be used to cascade ASL devices [29, 28]. However, the function provided by an ASL device after an SV stage is limited since the same voltage is shared by both ASL and SV devices.

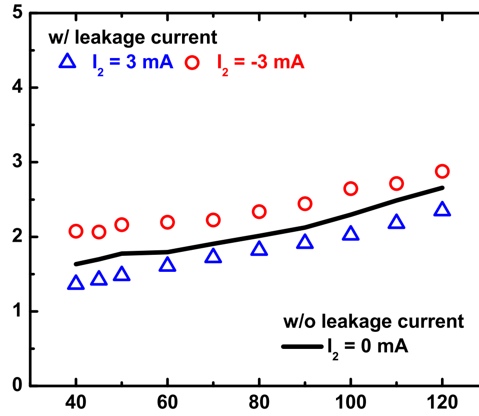

(a)

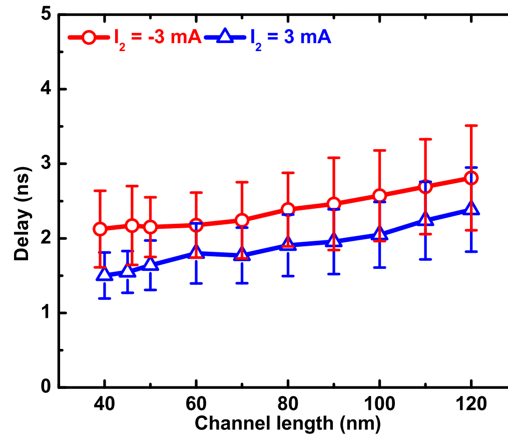

(b)

Figure 15: (a) Delay vs. channel length with and without the leakage current. Both positive and negative leakage currents are shown. (b) average delay with the standard deviation (over 100 stochastic simulations) vs. channel length with positive and negative leakage currents. The dipolar interaction is ignored. [26]

2.4.3 Shunt Path

Figure 16 shows that delay, energy and thermal fluctuations increase as the shunt path becomes shorter. This is mainly because most of spins are injected directly into the ground rather than contributing to the STT at the end. A larger delay results in a larger switching energy since a longer current pulse is required. Note that in real integrated circuits, shunt paths may not be scaled correspondingly with the devices since typically a global ground is shared by all the devices in a chip though long interconnects.

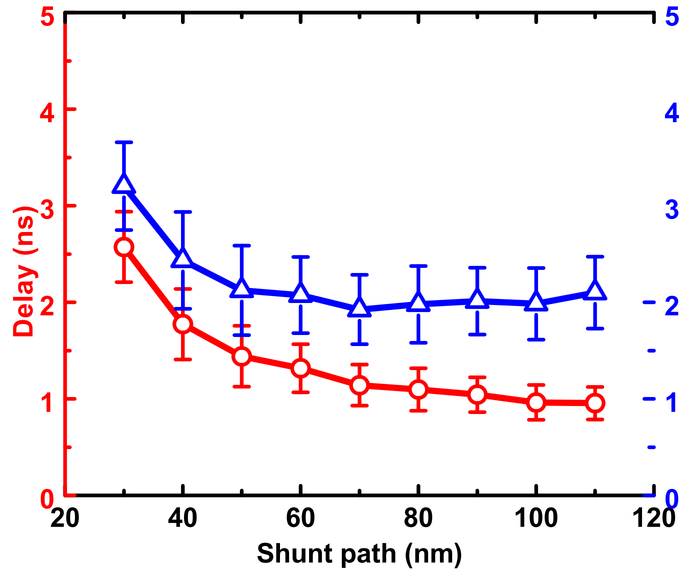

Figure 16: Average delay and energy with the standard deviation (over 100 stochastic simulations) vs. shunt path. The channel length is 120 nm. [26]

2.5 Summary

In this chapter, the effects of dipole coupling, leakage currents, and the shunt path which may limit scaling of ASL have been explored [26]. It was found that operation of in-plane Permalloy-based ASL can be preserved at the expense of switching time and energy at channel length of > 30nm. In the next two chapters, a novel interconnect

structure based on a simple SV with a tunneling barrier at the input is presented to improve the energy efficiency of ASL circuits. Si as the channel material is discussed in Chapter III, and Chapter IV focuses on Cu and Al-based interconnects.

CHAPTER III

SILICON INTERCONNECTS FOR ALL-SPIN LOGIC

3.1 Overview

In this chapter, a Si spin interconnect for all-spin logic is analyzed by a comprehensive physical model including spin injection, spin transport, and stochastic magnetization dynamics. It is shown that the spin current density and spin polarization of the current can be improved by changing material properties, interface conditions, and structure dimensions. Furthermore, with the help of an electric field, spin information can preserve and propagate between magnets in a highly doped μm-scale Si channel. Different from metallic all-spin logic, instead of the short spin relaxation length, the main constraint of a Si spin interconnect is the high bias voltage required to minimize the energy-delay product. The minimum energy-delay product and corresponding bias voltage can be reduced significantly by downscaling the nanomagnet. This improvement in the magnetic response allows Si to provide a compatible low-power interconnect technology to metallic all-spin logic.

3.2 Silicon Spin Interconnects

As mentioned in the previous chapter, a lateral non-local spin valve configuration with a metallic spin channel, also known as ASL, provides a low resistive current path and is suitable for logic devices [8, 9]. However, any emerging device technology needs to be complemented with compatible interconnects; otherwise, the energy, delay, and circuitry for signal conversion will be prohibitive. Spin logic devices can potentially outperform CMOS logic devices in terms of the energy-delay product if proper improvements in nanomagnet material properties are achieved [142]. However,

the short spin relaxation length of metallic channels will severely increase the energy dissipation of the spin interconnects. At room temperature, metallic spin channels such as Cu and Al are constrained as they suffer from spin relaxation lengths as short as a few hundred nanometers. The problem is compounded for smaller channel widths [176]. Hence, it is of great interest to pursue alternate spintronic channel materials.

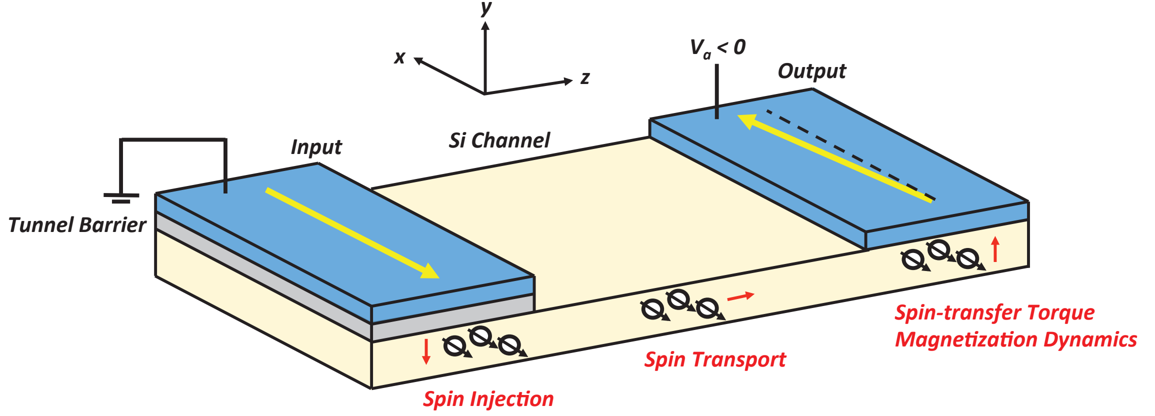

Figure 17: Schematic of a Si interconnect for ASL. The receiving magnet is assumed to form an Ohmic contact with the interconnect. Spin injection from the input magnet, spin transport through the channel, and stochastic magnetization dynamics of the receiving magnet are key elements to describe the operation of a Si all-spin interconnect [29].

Silicon, the cornerstone of CMOS technology, can preserve electron spin polarization over a distance of several microns [127, 131] and even longer under an applied electric field. This promising feature makes Si a strong candidate in the application of spin communication. Figure 17 shows the structure of the proposed Si all-spin interconnect, in which the logic directionality is obtained by the tunnel barrier inserted only at the transmitter side [45]. Along the channel, the spin signal is accelerated by an electric field and stored into the output magnet by the STT effect through the spin current [201]. In this chapter, a comprehensive physical model, including spin injection, spin transport, and stochastic magnetization dynamics, is provided to explore the possibility of Si as interconnects for ASL.

Electrical spin injection into n-type Si has been successfully demonstrated in experiments at both low [197, 191, 227, 102] and room temperature [44, 96, 132]. From a theoretical point of view, initially spin injection was treated by assuming that both spin current and spin accumulation are continuous at the junction, and found that spin polarization of the current depends on conductivities of the magnet and channel (the so-called conductivity mismatch problem) [100, 192, 193, 239]. Meanwhile, it was concluded that a substantial discontinuity of spin accumulation due to selective interface conductance significantly improves spin polarization of the current [180, 240, 58]. Selective conductance of spins from Fe/Co/Fe electrodes via MgO is well described by symmetry-dependent filtering [21]. However, a material system to inject spins from an FM metal into Si through a thin oxide is yet to be fully understood. Recently, while spin injection into GaAs through Al_2O_3 has been studied [39], spin polarization of the FM and spin-back flow process, which can be attributed to spin accumulation at the oxide/semiconductor interface [57, 15, 95], are not taken into account. Hence, this paper focuses on non-symmetry dependent spin injection via metallic tunneling oxides. To study this phenomenon, a transport model, accounting for the effect of direct quantum tunneling combined with current-dependent interface spin accumulation (ISA), is built up to examine the impact of the material properties and structure dimensions on spin currents and spin polarization of the current. The non-equilibrium Greens function (NEGF) method [149, 46] with the single band effective mass Hamiltonian is used to describe quantum tunneling due to its successful agreement with experimental data in MTJs by adjusting a few material parameters such as the interface barrier and effective mass [45]. We note that detailed experimental effort to elucidate the nature of spin injection into silicon interconnects are essential to develop an accurate picture. Our injection models can be calibrated to these experiments to further assist spin device/interconnect development. In particular, optical spin spectroscopy [74, 119], non-local spin injection into silicon [44, 191, 227], and

spin pumping with inverse spin Hall effect in semiconductors [93, 184] can provide essential parameters.

To explore the possibility of Si interconnects for ASL, the injection model is then combined with spin transport and magnetization dynamics to obtain the switching time, switching energy, and EDP of an Si all-spin interconnect. While using Si as a channel for spin communication has been proposed in Ref. [50], the spin orientation in the transmitter is detected by charge currents flowing through spin-up and spin-down receiving magnets instead of the spin-transfer torque switching. Therefore, the potential of Si in the ASL configuration still needs to be clarified.

3.3 Spin Injection

In this section, a physical model for injecting spins from an FM metal into a Si channel with the effect of interface spin accumulation is presented. Based on this model, the dependences of the spin current and spin polarization of the current on the FM metal, insulating oxide, and semiconducting channel are discussed.

3.3.1 Tunneling Interface

Unlike metals, the efficiency of electrically injecting spins from the FM metal into the Si channel is extremely low due to conductivity mismatch. To overcome this problem, a thin oxide layer as a tunnel barrier is introduced between the FM metal and the channel. To simplify the problem, the semi-infinite layered structure shown in Fig. 18 is used to capture essential physics of spin injection instead of a full interconnect. Here we assume spin accumulation in the non-magnetic channel is due to direct tunneling of spin-polarized electrons in the FM metal. In other words, in the following analysis, spin-flipping scattering and trap-assisted tunneling originating due to imperfect interface conditions or the poor quality of the oxide [220] are ignored.

The current due to electrons tunneling from the FM metal into the Si channel is calculated by the NEGF formalism. For the tunneling region, the Green's function,

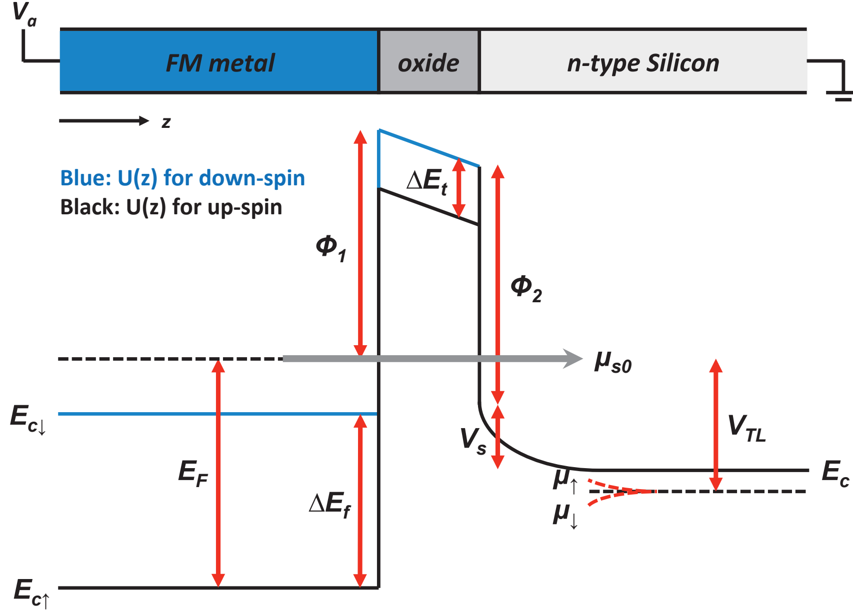

Figure 18: Schematic of the semi-infinite FM/oxide/Si structure and its energy band diagram, $U(z)$, for spin injection analysis. The blue and black lines are the band diagrams for up-spin and down-spin electrons, respectively [29]. The tunneling current is calculated by the non-equilibrium Green's function (NEGF) method, and the spin drift-diffusion equation is used to handle spin transport in the channel. Both mechanisms are connected through interface spin accumulation, μ_{s0}. $E_{c\uparrow}$ and $E_{c\downarrow}$ are the majority and minority band of the magnet, respectively. E_F is the Fermi energy of the magnet. ΔE_f is the exchange splitting in the magnet. ϕ_1 and ϕ_2 are the barrier heights at the FM/oxide and oxide/Si interface, respectively. ΔE_t is the band splitting in the oxide. V_{TL} is the voltage across the tunneling region. V_s is the surface band bending of the Si channel. At the oxide/Si interface, the chemical potentials of the majority and minority carriers, $\mu_\uparrow$ and $\mu_\downarrow$, respectively, are split according to μ_{s0}.

$\mathbf{G}$, is defined as

$$\mathbf{G} = [E\mathbf{I} - \mathbf{H} - \mathbf{\Sigma_L} - \mathbf{\Sigma_R}]^{-1}, \tag{19}$$

where E is the total electron energy, $\mathbf{I}$ is an identity matrix whose size depends on the number of grid points used in the numerical calculation, $\mathbf{H}$ is the single band effective mass Hamiltonian, and $\mathbf{\Sigma_{L(R)}}$ is the self-energy of the left (right) contact, which is assumed to be the quasi-equilibrium region of the FM metal (Si channel). Since the structure is three-dimensional (3-D), the total electron energy can be written as

$$E = E_{\parallel}(z) + E_{\perp}(z) + U(z), \tag{20}$$

where z is the direction of the current flow (see Fig. 17), $E_{\parallel}$ is the longitudinal energy, $E_{\perp}$ is the transverse energy, and U is the FM metal/oxide/Si energy band diagram defined in Fig. 18, which is obtained by solving Poisson equation under the Thomas-Fermi approximation. By assuming that θ is the angle between the electron motion and the electric field (in the z direction), and both total electron energy and transverse wave vector, k_t, are unchanged during the transport, the transverse energy is given as

$$E_{\perp}(z) = \frac{\hbar^2 k_t^2}{2m^*(z)} = \frac{m^*(z_1)[E - U(z_1)]\sin^2\theta}{m^*(z)}, \tag{21}$$

where z_1 is the location where electrons are injected and $m^*(z)$ is the effective mass profile for the tunneling region. Note that at the interface, the effective mass is assumed to be the average of adjacent layers [46].

The one-dimensional (1-D) single band effective mass Hamiltonian operator is written as

$$\hat{H} = -\frac{\hbar^2}{2}\frac{1}{\partial z}(\frac{1}{m^*(z)}\frac{\partial}{\partial z}) + \frac{\hbar^2 k_t^2}{2m^*(z)} + U(z), \tag{22}$$

and the corresponding tridiagonal matrix in the finite difference scheme is given as

$$\mathbf{H} = \begin{cases} H_{n,n} = t_{n-1} + t_{n+1} + \frac{\hbar^2 k_t^2}{2m^*(z_n)} + U(z_n), \\ H_{n,n+(-)1} = -t_{n+(-)1}, \end{cases} \tag{23}$$

where t_n is the coupling strength between the nearest grid points given as $\hbar^2/2m^*(z_n)a^2$, n is an integer from 1 to N, N is the number of grid points used in the numerical calculation, and a is the distance between the nearest grid points. The self-energy under open boundary conditions is given as

$$\mathbf{\Sigma_{L(R)}} = \begin{cases} \Sigma_{i,j} = -te^{ik_\parallel a}, & \text{for } i = j = 1(N) \\ \Sigma_{i,j} = 0, & \text{otherwise,} \end{cases} \tag{24}$$

where $t = \hbar^2/2m^*(z_{1(N)})a^2$ and $k_\parallel a = \cos^{-1}(1 - E_\parallel(z_{1(N)})/2t)$ for the left (right) contact. From Eqs. (19) to (24), Green's function can be calculated, and the transmission coefficient through the junction at the given energy and transverse wave vector is given as

$$T(E, k_t) = trace(\mathbf{\Gamma_L G \Gamma_R G^\dagger}), \tag{25}$$

where $\mathbf{\Gamma_{L(R)}}$ is the broadening function of the left (right) contact given as $i(\mathbf{\Sigma_{L(R)}} - \mathbf{\Sigma^\dagger_{L(R)}})$, and $\mathbf{G}^\dagger$ is the conjugate transport of the Green's function. The tunneling current density is then calculated by the Landauer formula given as

$$J = -\frac{e}{Ah}\int \partial E \sum_{k_t} T(E, k_t)[f_L(E) - f_R(E)], \tag{26}$$

where e is the elementary charge, A is the cross-sectional area, h is the Planck constant, and $f_{L(R)}$ is the Fermi-Dirac distribution function of the left (right) contact given as $f_{L(R)}(E) = 1/[1 + \exp(\frac{E-\mu_{L(R)}}{k_B T})]$, in which $\mu_{L(R)}$ is the chemical potential of the left (right) contact. The majority and minority current densities, denoted as $J_\uparrow$ and $J_\downarrow$, respectively, are calculated using the corresponding energy band diagram in the Hamiltonian. As mentioned in Chapter I, the spin current density, J_s, and the charge current density, J_c, are defined as $J_\uparrow - J_\downarrow$ and $J_\uparrow + J_\downarrow$, respectively. The spin polarization of the current is the spin current density normalized to the charge current density.

3.3.2 Non-magnetic Channel

The spin density, n_s, in the NM material is described by the 1-D spin drift-diffusion equation [239, 240] given as

$$L_s^2 \frac{\partial^2 n_s}{\partial z^2} + L_e \frac{\partial n_s}{\partial z} - n_s = 0, \tag{27}$$

where $L_s = \sqrt{D_n \tau_s}$ is the spin diffusion length, $L_e = \mu_n \tau_s \mathbf{E}$ is the spin drift length, τ_s is the spin relaxation time, D_n and μ_n are the electron diffusion coefficient and mobility, respectively, and $\mathbf{E}$ is the electric field along the channel. By assuming that all the donors are ionized at room temperature, the electric field can be roughly estimated by Ohm's law given as $\mathbf{E} = J/eN_d\mu_n$, where N_d is the doping density of the channel. To handle the degenerate semiconductor, the spin density and spin accumulation, μ_s, are linked through the Joyce-Dixon approximation [103] given as

$$\mu_s \simeq \frac{k_B T}{2} \ln(\frac{1 + \frac{n_s}{N_d}}{1 - \frac{n_s}{N_d}}) + k_B T \frac{n_s}{\sqrt{8} N_c}, \tag{28}$$

where k_B is the Boltzmann constant, T is the operating temperature, and N_c is the conduction band effective density. In the channel, both drift and diffusion transport mechanisms contribute to the spin current given as

$$J_s = eD_n \frac{\partial n_s}{\partial z} + e n_s \mu_n \mathbf{E}. \tag{29}$$

The boundary conditions are (i) the spin current at the beginning of the channel, which corresponds to the tunneling current, and (ii) zero spin accumulation (or spin density) at the end of the channel due to the semi-infinite structure. For spin transport parameters such as spin relaxation time and mobility, the compact model developed in Ref. [177] and the measured data reported in Ref. [121] are used to account for the effect of doping density.

At the oxide/Si interface, since spin accumulation, which depends on the tunneling current, modifies chemical potentials of majority and minority carriers and leads to a

change in injected spin current, a self-consistent solution to the NEGF formalism and the spin drift-diffusion equation is necessary to study spin injection. Note that spin accumulation at the FM metal/oxide interface is negligible compared with that at the oxide/Si interface due to large density of states in the FM metal [14]. Furthermore, electrons are assumed to be free from scattering while traveling through the space-charge region. This approximation is valid especially for a highly doped channel, which is desired for interconnects due to low resistive current paths. The procedure for obtaining a self-consistent solution is as follows: (i) for both majority and minority carriers, calculate the tunneling current without any modification of the chemical potential due to spin accumulation at the oxide/Si interface; (ii) use the tunneling spin current to solve the spin drift-diffusion equation and obtain the channel spin accumulation profile, from which interface chemical potentials are updated as follows:

$$\mu_{\uparrow(\downarrow)} = \mu_R + (-)\mu_{s0}, \tag{30}$$

where $\mu_{\uparrow(\downarrow)}$ and μ_{s0} are the modified chemical potential of majority (minority) carriers and spin accumulation at the oxide/Si interface, respectively; (iii) re-calculate the tunneling current based on new chemical potentials. The iteration between (ii) and (iii) continues until the interface spin accumulation converges.

3.3.3 Results and Discussion

As mentioned above, the injected spin current changes with spin accumulation at the oxide/Si interface. To be more precise, ISA decreases and increases the transport energy range of interest for majority and minority carriers, respectively, leading to the reduction of the spin current and spin polarization of the current [57, 15, 95]. ISA becomes significant only when it is comparable to the transport energy range of interest. Thus, figures 19 to 22 show that the reduction of the spin current due to ISA becomes important especially at a small voltage. This is because at low voltages, a small shift in the voltage leads to a large increase in the current magnitude,

which results in significant spin accumulation at the interface. Furthermore, in the low bias region, large spin currents and lightly doped channels make the reduction more pronounced due to increased ISA. However, for the spin current density with a reasonable switching response (in the order of 10^{10} A/m^2 for soft magnets), because the corresponding transport energy range of interest is usually much larger than ISA, this reduction can be considered as a second-order effect.

(a)

(b)

(c)

(d)

Figure 19: (a) Spin current density and (b) spin polarization of current versus the voltage across the tunneling region under different doping densities of the channel in the presence and absence of ISA [29]. The simulation parameters are given as follows: $\phi_1 = 2.6$ eV, $\phi_2 = 2.6$ eV, $E_F = 2.25$ eV, $\Delta E_f = 2.15$ eV, $\Delta E_t = 0$ eV, $m^* = 0.2m_0$, and $\epsilon = 10\epsilon_0$. The oxide thickness is 0.5 nm. (c) and (d) are the energy band diagrams illustrating spin polarization of the current increases when the voltage and doping density increase, respectively. The yellow arrows represent additional majority carriers tunneling through the junction, which increases both spin current density and spin polarization of the current.

Spin injection depends largely on the surface band bending near the oxide/Si interface (often called Schottky barrier). In Figs. 19(a) and (b), it is found that a larger voltage and a heavier doped channel result in higher spin currents and spin polarization of the current. This can be explained by the energy band diagram shown in Figs. 19(c) and (d), illustrating a larger voltage and higher doping density reduce the effect of the Schottky barrier, leading to higher tunneling probability and allowing more majority carriers tunneling through the junction. Furthermore, it can be seen in Figs. 20(a) and (b) that having a smaller FM metal/oxide interface barrier improves spin injection. This can be attributed to the fact that for a smaller FM metal/oxide barrier, the Schottky barrier height decreases as shown in Fig. 20(c); therefore, the tunneling probability increases and more majority carriers can tunnel through the junction, resulting in larger spin currents and spin polarization of the current. In general, a FM metal with the smaller work function has a lower interface barrier and is appropriate for efficient spin injection [154].

Figure 21(a) shows that a thinner oxide leads to a larger spin current because tunneling probability increases as the thickness decreases; however, spin polarization of the current weakly depends on the oxide thickness as shown in Fig. 21(b) since (i) the oxide discussed here has no intrinsic spin selectivity to provide additional spin polarization to the FM electrode, and (ii) the Schottky barrier does not change too much with the oxide thickness. Furthermore, at a small applied bias, a thinner oxide suffers from more serious reduction due to ISA so spin polarization of the current decreases. Nevertheless, for the spin interconnect, this reduction is not important because the voltage across the tunneling region is typically large enough to provide the spin current for switching the magnet. At a higher bias, the thinner oxide leads to higher spin polarization of the current. Note that the effect of metal induced gap states (MIGS) for the FM metal/oxide interface is not taken into account here [129]; that is, the FM metal/oxide interface barrier maintains a constant value for different

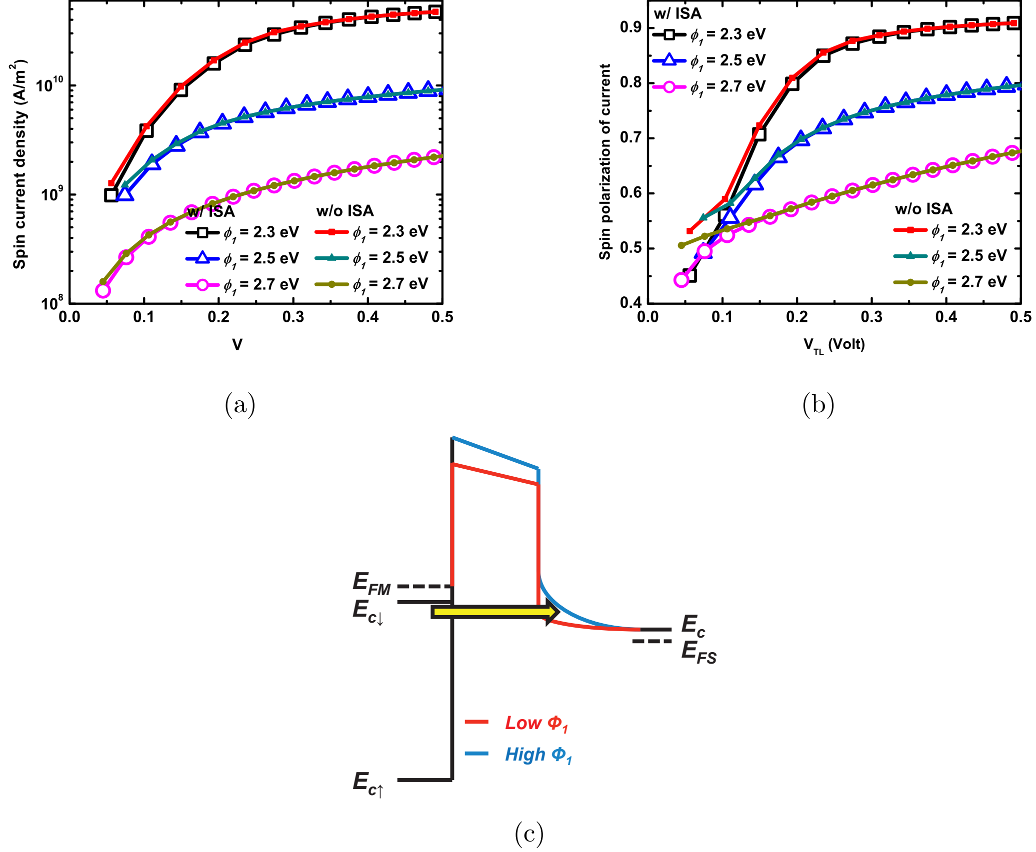

(a) (b)

(c)

Figure 20: (a) Spin current density and (b) spin polarization of current versus the voltage across the tunneling region under different FM/oxide interface barrier heights in the presence and absence of ISA [29]. The simulation parameters are given as follows: $N_d = 5 \times 10^{18}$ cm^{-3}, $\phi_2 = 2.6$ eV, $E_F = 2.25$ eV, $\Delta E_f = 2.15$ eV, $\Delta E_t = 0$ eV, $m^* = 0.2m_0$, and $\epsilon = 10\epsilon_0$. The oxide thickness is 0.5 nm. (c) The energy band diagram illustrating spin polarization of the current increases when the ϕ_1 decreases. The yellow arrow represents additional majority carriers tunneling through the junction, which increases both spin current density and spin polarization of the current.

oxide thicknesses.

Using different oxides as a tunneling barrier also has a significant impact on spin injection. This is because each oxide has its own tunneling effective mass and interface barriers, which gives distinct transmission properties. Figure 22 shows how spin currents and spin polarization of the current change when Al_2O_3, HfO_2, and SiO_2 are used as tunneling barriers. The parameters for each oxide are given in Table 2 [186]. Since spin polarizations of the current for different oxides are similar, the oxide with high electron affinity and low tunneling effective mass is desired for injecting high spin currents.

Table 2: Oxide parameters used in Fig. 21. 4 eV and 4.05 eV are used for the work function of an FM metal, Φ_F, and the electron affinity of Si, χ_s, respectively. By assuming that the energy band diagram is aligned according to the bulk properties of each layer, the interface barrier heights ϕ_1 and ϕ_2 are defined as $\Phi_F - \chi$ and $\chi_s - \chi$, respectively.

	Al_2O_3	HfO_2	SiO_2
m^* (m_0)	0.2	0.2	0.5
χ (eV)	1.45	2.55	0.95
ϵ (ϵ_0)	10	20	3.9

The exchange effect in an FM metal plays an important role in spin injection. A smaller exchange energy means more minority carriers exist in an FM metal. This reduces spin polarization of an FM metal and impairs spin injection quantities as shown in Fig. 23. Hence, an FM metal with high spin polarization is desirable for injecting spin into an NM channel. Note that the interface barrier height may be modified by using different FM electrodes due to the change of the interface conditions and work function; therefore, the benefit of high spin-polarized electrode might be shadowed due to an increase of the barrier height at the FM metal/oxide interface. Furthermore, an oxide with intrinsic spin selectivity can also improve spin injection because majority and minority carriers in an FM metal see different potential energy

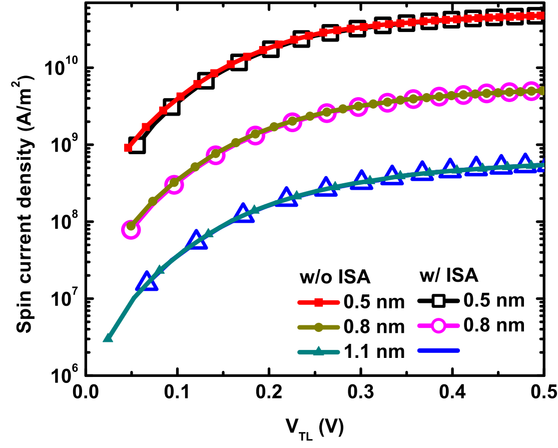

(a)

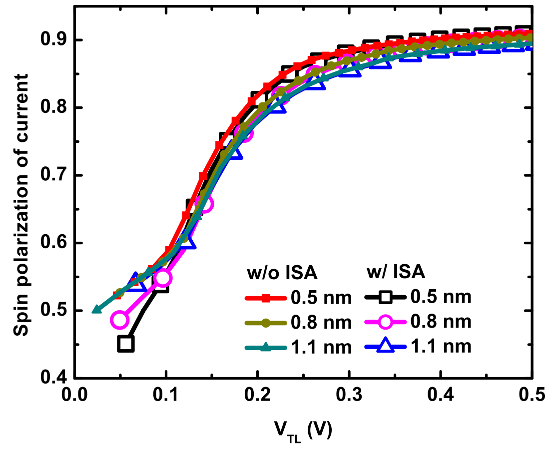

(b)

Figure 21: (a) Spin current density and (b) spin polarization of the current versus voltage across the tunneling region under different oxide thicknesses in the presence and absence of ISA [29]. The simulation parameters are given as follows: $N_d = 5\times10^{18}$ cm^{-3}, $\phi_1 = 2.3$ eV, $\phi_2 = 2.6$ eV, $E_F = 2.25$ eV, $\Delta E_f = 2.15$ eV, $\Delta E_t = 0$ eV, $m^* = 0.2m_0$, and $\epsilon = 10\epsilon_0$.

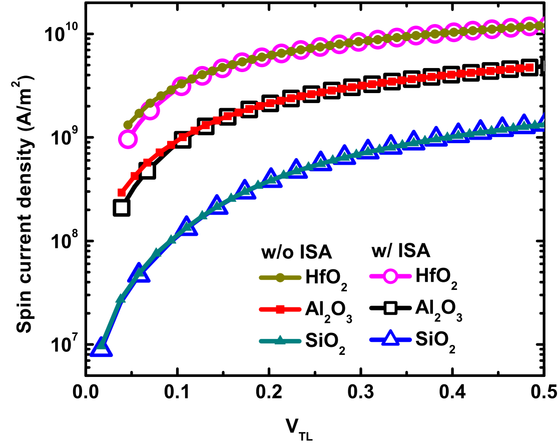

(a)

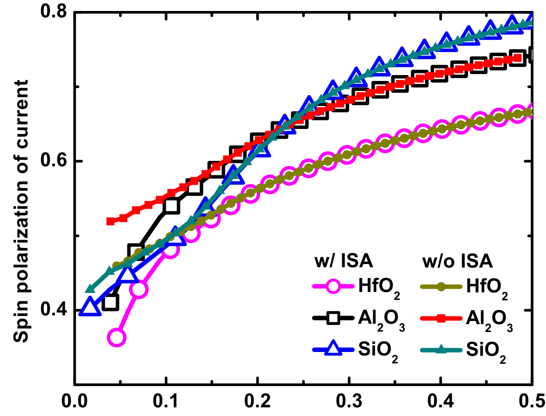

(b)

Figure 22: (a) Spin current density and (b) spin polarization of the current versus voltage across the tunneling region under different oxide materials in the presence and absence of ISA [29]. The simulation parameters are given as follows: $N_d = 5 \times 10^{18}$ cm^{-3}, $E_F = 2.25$ eV, $\Delta E_f = 2.15$ eV, and $\Delta E_t = 0$ eV. The parameters for each insulator are given in Table 2. The oxide thickness is 0.5 nm.

profiles while traveling through the oxide. In Fig. 24, the band splitting, ΔE_t, is used to represent additional spin polarization provided by the tunneling barrier. Increasing ΔE_t means more minority carriers are blocked; thus, better spin injection is attained. This filtering effect is more obvious as the number of majority and minority carriers in the magnet become close, which implies that for a magnet with high spin polarization, the spin selectivity of the oxide may not offer a significant improvement to spin injection. Note that this simple model only gives a qualitative explanation for improving spin injection using the spin-selective oxide. For a real spin-filtering oxide like MgO, an atomistic approach in calculating the band structures of the FM metal and the oxide is required to accurately model the transport properties [187].

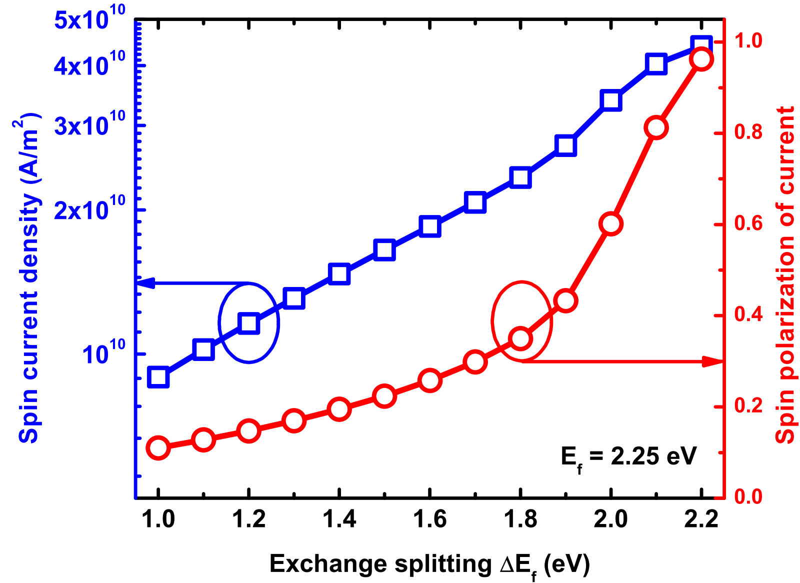

Figure 23: Spin current density and spin polarization of the current versus the exchange splitting [29]. The simulation parameters are given as follows: $N_d = 5 \times 10^{18}$ cm^{-3}, $\phi_1 = 2.3$ eV, $\phi_2 = 2.6$ eV, $E_F = 2.25$ eV, $\Delta E_t = 0$ eV, $m^* = 0.2m_0$, and $\epsilon = 10\epsilon_0$. The oxide thickness is 0.5 nm.

In reality, there may exist some accumulated charges (either positive or negative) at the imperfect oxide/Si interface, and the interface barrier height (ϕ_2 shown in Fig.

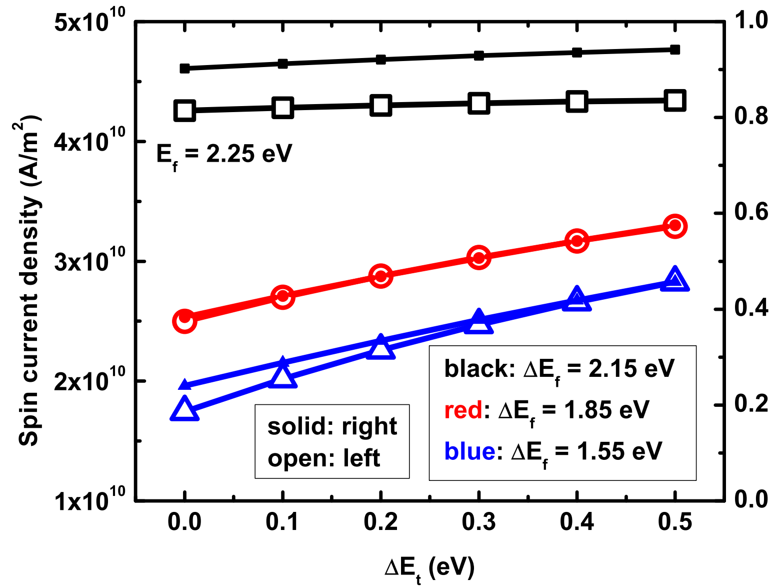

Figure 24: Spin current density and spin polarization of the current versus band splitting of the insulator, ΔE_t [29]. The simulation parameters are given as follows: $N_d = 5 \times 10^{18}$ cm^{-3}, $E_F = 2.25$ eV, $\phi_1 = 2.3$ eV, $\phi_2 = 2.6$ eV, $m^* = 0.2m_0$, and $\epsilon = 10\epsilon_0$. The oxide thickness is 0.5 nm.

18) is no longer simply determined by the work function difference between the oxide and Si. The barrier height at the oxide/Si interface affects spin injection in a significant way, since a larger barrier height, which decreases the Schottky barrier, allows more majority carriers tunneling through the junction and increases the spin current density and spin polarization of the current as shown in Fig. 25. Consequently, the reduced Schottky barrier (such as Cs treated Si surface [96]) is desired for efficient spin injection. However, the accumulated charges at the interface may degrade spin injection due to the increasing spin-flipping process even though the Schottky barrier is reduced. This is because when a Schottky barrier is lower, the electric field difference at the oxide/Si interface becomes larger, meaning more net charges accumulated from defects at the interface. A defect with net spin may produce spin-dependent scattering and degrade spin injection. However, in the case of Cs treated Si surface, the improvement offered by the reduction in the Schottky barrier height seems to outweigh any degradation caused by extra spin flippings at the interface based on experimental results in Ref. [96].

Spin injection into Si has a strong non-linear dependence on the applied bias due to the nature of the tunneling mechanism. The spin quantities increase with the voltage and finally almost saturate as shown in Figs. 19 to 22. This is because as a bias voltage becomes larger, more and more majority carriers can tunnel through the junction, leading to an improvement in spin injection as we mentioned previously. However, as the voltage keeps increasing, the contribution to the current from increased majority carriers becomes negligible since their energies are far below the Fermi energy and the corresponding transmission coefficient is too small; therefore, the spin quantities gradually saturate. As a result, due to these non-linear relations between spin quantities and the applied voltage, injecting large spin currents with high spin polarization can be realized at the small bias voltage. Note that the spin currents calculated in Ref. [186] are slightly larger than those we calculate here. The

difference may result from the approximations made in the Tsu-Esaki model [222], which assumes the transverse effective mass is independent of the spatial coordinate so that the longitudinal energy is also conserved during the transport. However, for a more realistic situation considered in this work, the FM metal, oxide, and Si usually have different transverse dispersion relations and only the total energy is conserved. Moreover, the difference becomes larger at a smaller voltage due to ISA, which has also been ignored in Ref. [186]. Nevertheless, the dependences of spin polarization of currents on material and dimension parameters in Ref. [186] are similar to those in the absence of ISA shown in this paper. In Ref. [39], the impacts of doping density, interface barrier, and Schottky barrier on spin polarization of currents are not consistent with those shown here. This discrepancy may be from the fact that spin polarization of an FM metal in Ref. [39] is simply described by the splitting of chemical potentials at the FM metal/oxide interface, instead of the exchange energy splitting used in this chapter.

3.4 Spin Interconnects

In this section, the spin injection model is extended by including spin transport through the channel and magnetization dynamics of the output magnet to describe the full operation of a Si all-spin interconnect. Through this model, the impacts of the interconnect parameters such as channel length and doping density on the switching behavior and power dissipation are quantified.

3.4.1 Spin Transport and Magnetization Dynamics

To understand the switching behavior of a full Si all-spin interconnect, it is necessary to incorporate spin transport of the channel and output nanomagnet dynamics into the spin injection model mentioned in the previous section. Spin currents and spin accumulation at the end of the channel depend on the Si/output magnet interface conductance, which is a function of the angular position in the nanomagnet and can

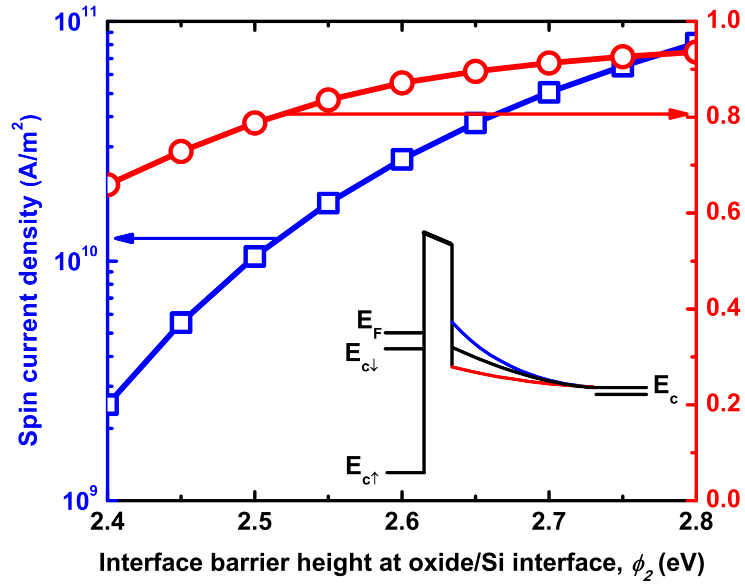

Figure 25: Spin current density and spin polarization of the current versus the oxide/Si interface barrier height, ϕ_2. The inset shows a larger ϕ_2 results in a smaller Schottky barrier height [29]. The simulation parameters are as follows: $N_d = 5 \times 10^{18}$ cm^{-3}, $\phi_1 = 2.3$ eV, $E_F = 2.25$ eV, $\Delta E_f = 2.15$ eV, $\Delta E_t = 0$ eV, $m^* = 0.2m_0$, and $\epsilon = 10\epsilon_0$. The oxide thickness is 0.5 nm.

be described by a 4×4 matrix $\mathbf{G_{int}}$ given as [141, 13]

$$\mathbf{G_{int}}(\vec{m}) = \mathbf{R}^{-1}(\vec{m})\mathbf{G_{int}}(\hat{x})\mathbf{R}(\vec{m}) \tag{31}$$

where $\mathbf{G_{int}}(\hat{x})$ is the interface conductance matrix with nanomagnet magnetization being in the x direction (the easy axis)

$$\begin{bmatrix} G_{\uparrow\uparrow} + G_{\downarrow\downarrow} & G_{\uparrow\uparrow} - G_{\downarrow\downarrow} & 0 & 0 \\ G_{\uparrow\uparrow} - G_{\downarrow\downarrow} & G_{\uparrow\uparrow} + G_{\downarrow\downarrow} & 0 & 0 \\ 0 & 0 & 2\mathrm{Re}(G_{\uparrow\downarrow}) & 2\mathrm{Im}(G_{\uparrow\downarrow}) \\ 0 & 0 & -2\mathrm{Im}(G_{\uparrow\downarrow}) & 2\mathrm{Re}(G_{\uparrow\downarrow}) \end{bmatrix} \tag{32}$$

and $\mathbf{R}(\vec{m})$ is the rotation matrix

$$\begin{bmatrix} 1 & 0 & 0 & 0 \\ 0 & r_{22} & r_{23} & r_{24} \\ 0 & r_{32} & r_{33} & r_{34} \\ 0 & r_{42} & r_{43} & r_{44} \end{bmatrix}. \tag{33}$$

For the expressions above, $\vec{m}$ is the magnetic moment unit vector of the output magnet, and $G_{\uparrow\uparrow}$, $G_{\downarrow\downarrow}$, and $G_{\uparrow\downarrow}$ are majority, minority, and mixing interface conductances, respectively. The elements in the rotation matrix are defined as follows:

$$\begin{bmatrix} r_{22} & r_{23} & r_{24} \end{bmatrix} = \hat{X} = \hat{m_r} \tag{34}$$

$$\begin{bmatrix} r_{32} & r_{33} & r_{34} \end{bmatrix} = \hat{Y} = -\frac{\hat{X} \times \hat{x}}{|\hat{X} \times \hat{x}|} \tag{35}$$

$$\begin{bmatrix} r_{42} & r_{43} & r_{44} \end{bmatrix} = \hat{Z} = \hat{X} \times \hat{Y}. \tag{36}$$

Equation (32) implies that spin accumulation at the end of the channel is not only contributed by the injected spin current but also by the mixing conductance at the Si/output magnet interface. For simplicity, the components in $\mathbf{G_{int}}(\vec{m})$ for heavily doped Si to magnet are assumed to be similar to those at a metal to magnet interface.

The current density and voltage vector across the interface are linked through $\mathbf{G_{int}}(\vec{m})$ according to Ohm's law given as [141]

$$\vec{J} = \mathbf{G_{int}}(\vec{m})\vec{V} \tag{37}$$

where $\vec{J} = [J_c \ J_{sx} \ J_{sy} \ J_{sz}]$ and $\vec{V} = [V \ V_{sx} \ V_{sy} \ V_{sz}]$. Note that J_c here is the same as the tunneling current injected from an FM metal due to charge conservation. By assuming that the spin voltage (or spin accumulation) in the nanomagnet is negligible, the spin accumulation vector at the end of the Si channel can be written as

$$\hat{\mu_s} = -e(V_{sx}\hat{x} + V_{sy}\hat{y} + V_{sz}\hat{z}). \tag{38}$$

Equation (38) serves as one of the boundary conditions for the spin drift-diffusion equation in the x, y, and z directions. In general, for an arbitrary magnetic moment of the receiving magnet, the spin tunneling current has to be solved self-consistently with the spin drift-diffusion equation and the interface conductance matrix due to ISA. However, as mentioned in the previous section, for a reasonable switching response, ISA can be ignored so that the NEGF method is decoupled from the spin drift-diffusion equation. Note that since spin accumulation at the end of the NM channel is initially unknown, iteration between the spin drift-diffusion equation and the interface conduction matrix with self-consistency is still required to obtain the spin current entering the output nanomagnet.

The phenomenological equation (or LLG equation) describing the receiving nanomagnet is given in Eq. 10, where $\vec{H_{eff}}$ includes material anisotropy, shape anisotropy, and thermal random noise [141]. Implicit in the LLG equation is that the magnitude of the magnetic moment remains constant as mentioned in Chapter I. Mathematically, the internal field can be written as

$$\vec{H_{eff}} = \vec{H_u} + \vec{H_s} + \vec{H_t}. \tag{39}$$

By assuming the easy axis is in the x direction, the material anisotrophy field is given

as

$$\vec{H}_u = (\frac{2K_u}{\mu_0 M_s} m_x)\hat{x} \tag{40}$$

where K_u is the material anisotropy energy density. The shape anisotropy field, coming from demagnetization inside the magnet, is given as

$$\vec{H}_s = -M_s(N_x m_x \hat{x} + N_y m_y \hat{y} + N_z m_z \hat{z}) \tag{41}$$

where N_x, N_y, and N_z are the components of the demagnetization tensor which depend on the geometry of the magnet [10]. Thermal noise in the nanomagnet manifests as fluctuations in the internal anisotropy field [19]. At room temperature, a Gaussian white noise is used to model the thermal field, acting isotropically on the nanomagnet and is written as

$$\vec{H}_t = H_x\hat{x} + H_y\hat{y} + H_z\hat{z} = \sqrt{\frac{2\alpha k_B T}{\mu_0^2 \gamma M_s V}}(\frac{\partial W_x}{\partial t}\hat{x} + \frac{\partial W_y}{\partial t}\hat{y} + \frac{\partial W_z}{\partial t}\hat{z}) \tag{42}$$

where W_x, W_y, and W_z are three independent Wiener processes in the x, y, and z directions, respectively. The distribution of the thermal field satisfies the following conditions:

$$< H_i(t) >= 0, \tag{43}$$

and

$$< H_i(t)H_j(t') >= \frac{2\alpha k_B T}{\mu_0^2 \gamma M_s V}\delta(t-t')\delta_{ij}. \tag{44}$$

The stochastic LLG equation in Eq. 10 is numerically solved by the midpoint method in the sense of Stratonovich calculus [43]. Note that with all the internal fields mentioned above, the fluctuation due to the thermal noise follows

$$< \phi^2 >= \frac{k_B T}{\mu_0 M_s V[|\vec{H}_u| - M_s(N_{xx} - N_{yy})]} \tag{45}$$

where ϕ is the angle between the magnetic moment unit vector and the easy axis under no spin current, and $< >$ means the average value. Figure 26 is a validation of the stochastic LLG solver using (45) and the switching time under a simple demagnetization field pointing in the out-of-plane direction given as [210]

$$\tau_{sw} = \frac{\tau_0 \ln(\frac{\pi}{\phi_0})}{(\frac{I}{I_c} - 1)} \tag{46}$$

where τ_0 is a fitting parameter, ϕ_0 is the initial angle of the magnet given as $\sqrt{k_B T / 2E_b}$, I is the current entering the magnet, and I_c is the critical current for magnetization reversal given as

$$I_c = \frac{2e}{\eta\hbar}(2\alpha E_b)(1 + \frac{|\vec{H}_s|}{2|\vec{H}_u|}). \tag{47}$$

where η is spin polarization of the current. As shown in Fig. 26, because of the increasing importance of the thermal noise effect, the results from the stochastic solver start to deviate more from the curve obtained from the analytical expressions as the barrier height and the input current decrease.

The magnetization dynamics for a Si all-spin interconnect is realized in the following procedure: (i) in the beginning, the tunneling spin current, served as one of the boundary conditions for the spin drift-diffusion equation, is calculated by the NEGF formalism; (ii) the spin drift-diffusion equation and the interface conduction matrix are solved self-consistently to obtain the spin current entering the receiving magnet; (iii) with the torque from the spin current, the LLG solver is used to evaluate the magnetic moment at the next time step. An iteration between (ii) and (iii) establishes the time evolution of the magnetic moment unit vector for the receiving nanomagnet.

3.4.2 Results and Discussion

Using the full model described above, the impacts of the doping density, channel length, interface resistance, and applied bias on the switching response of the interconnect are investigated. Quantities used to characterize the performance of an

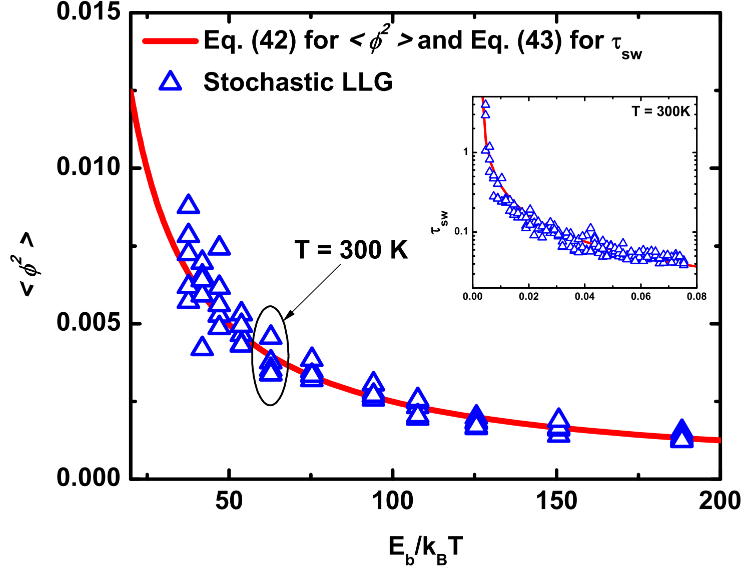

Figure 26: Comparison between the stochastic LLG solver and the analytical expression for $< \phi^2 >$ (the inset is for τ_{sw}) [29].

interconnect are the switching time, τ_{sw}, switching energy, E_{sw}, and energy-delay product (EDP). A fast switching response with the low energy is desirable for a high performance interconnect. The EDP is usually used to compromise the switching speed and the energy if their trends are opposite. The input pulse duration is assumed to be equal to the switching time even though promising strategies of the STT switching exist [166]. Therefore, the switching energy and EDP can be considered as a worst-case situation here. The EDP is given as

$$EDP = E_{sw}\tau_{sw} = IV\tau_{sw}^2 \tag{48}$$

where $E_{sw} = IV\tau_{sw}$ and V is the voltage across the interconnect. The parameters used for the receiving magnet are listed in Table 3 [13, 142].

In the following simulations, initially the magnetic moments of the input and output magnets are assumed to be in the negative and positive x directions, respectively, so the switching time is defined as the magnetic moment of the output magnet in the

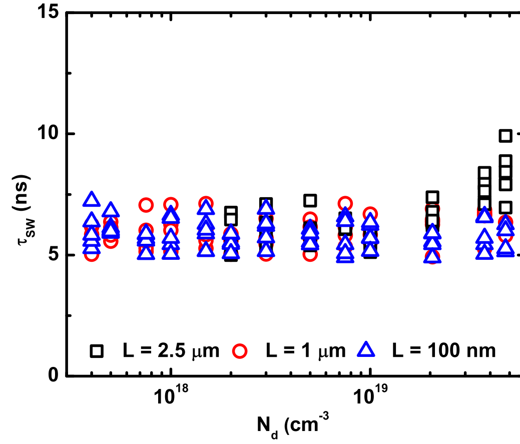

(a)

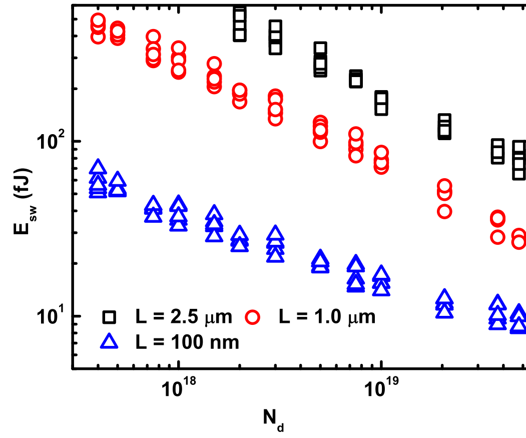

(b)

Figure 27: (a) Switching time and (b) energy versus doping density for different channel lengths [29]. The injected spin current is constant and equal to 3.8×10^{10} A/m^2. The solid lines represent the average value of five data points for each set of parameters. The same representation is used in Figs. 28 to 31.

Table 3: Parameters for the interface conductance matrix and the LLG equation. L_m, W_m, and t_m are the length, width, and thickness of the nanomagnet, respectively.

Symbol	Value	Units
μ_0	$4\pi \times 10^{-7}$	joule·A^{-2}·m^{-1}
γ	17.6×10^{10}	tesla^{-1}·s^{-1}
M_s	2.5×10^{5}	A·m^{-1}
α	0.0021	-
L_m	75.7	nm
W_m	37.8	nm
t_m	3	nm
K_u	6×10^{4}	joule·m^{-3}
$G_{\uparrow\uparrow}$	0.6×10^{15}	Ω^{-1}·m^{-2}
$G_{\downarrow\downarrow}$	0.2×10^{15}	Ω^{-1}·m^{-2}
Re($G_{\uparrow\downarrow}$)	5.5×10^{15}	Ω^{-1}·m^{-2}
Im($G_{\uparrow\downarrow}$)	1.5×10^{13}	Ω^{-1}·m^{-2}

x direction changes from 1 to -1. To show the fluctuation of the thermal noise, five simulations are done for each set of parameters. In Figs. 27 and 28, it is shown that the switching time can be independent of both channel length and doping density for a μm-scale channel because the electric field improves the effective spin relaxation length significantly. As a result, the switching energy can be reduced by increasing the doping density without sacrificing the speed. However, if the channel becomes highly degenerate, the electric field cannot compensate the loss of spin relaxation time due to more impurity scattering [53], and the switching time will start to increase with the doping density. Since spin information is carried by the charge current, the switching energy increases with the channel length.

The switching time can be reduced by improving the magnetic response of the nanomagnet, which can be done by engineering interface tunneling resistance such as changing the work function of the FM metal and the electron affinity of the oxide as

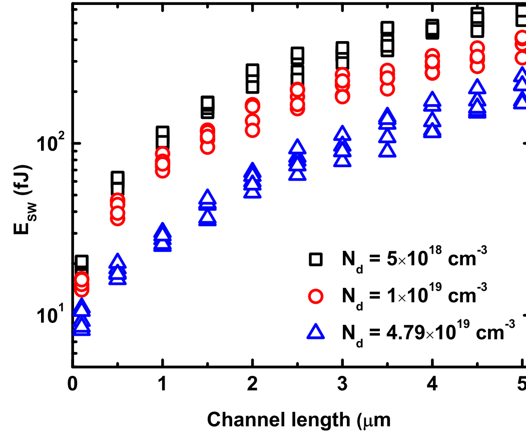

(a)

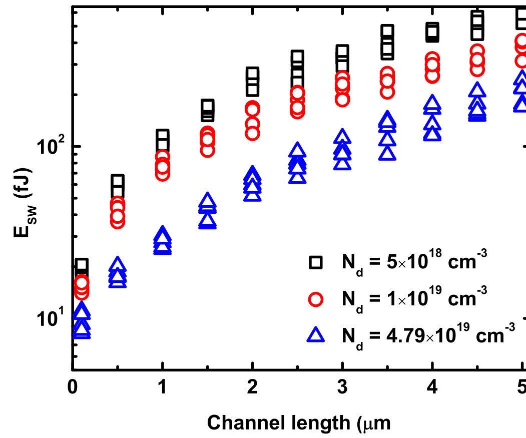

(b)

Figure 28: (a) Switching time and (b) energy versus channel length for different doping densities [29]. The injected spin current is constant and equal to 3.8×10^{10} A/m^2.

mentioned in the previous section. As shown in Fig. 29, a lower interface tunneling resistance gives faster switching time due to a larger STT exerted onto the magnet. However, a high switching energy is required for low interface tunneling resistance because of a large voltage drop across the channel.

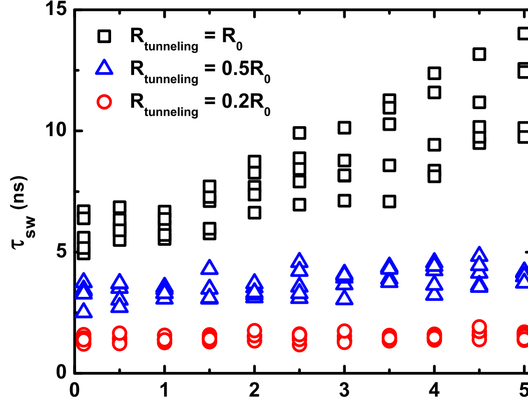

(a)

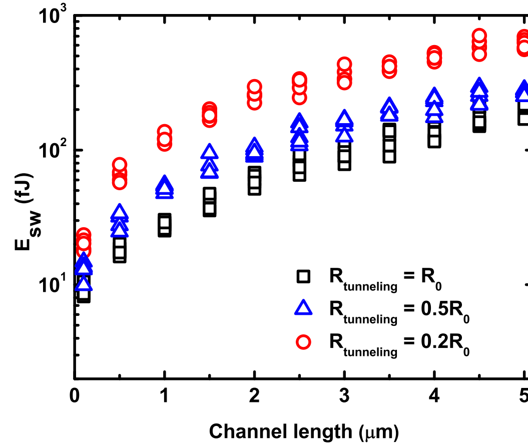

(b)

Figure 29: (a) Switching time and (b) energy versus channel length for different values of interface tunneling resistance [29]. The doping density of the channel is 4.78×10^{19} cm^{-3} and R_0 is 6.4×10^{-12} $\Omega\cdot$ m^2.

Another way to improve the magnetic response is to increase the applied voltage. Figure 30 shows that the switching time becomes shorter as the applied bias increases.

However, a large applied bias, which is responsible for a high switching energy, is needed for a long channel to provide enough currents for switching the magnet. As a result, unlike metallic ASL, instead of the short spin relaxation length, the major limit of the Si spin interconnect is a high applied bias due to the resistive μm-scale channel. For the spin communication in the GHz applications, the required voltage is at least larger than 2 V for a 2.5 μm-long channel. Moreover, there exists an optimum voltage to obtain the lowest EDP since the switching time and energy have opposite trends with the applied bias. As shown in Fig. 30, the optimal voltages are about 0.3 V, 1 V, and 3 V for the channel lengths equal to 100 nm, 1 μm, and 2.5 μm, respectively. The large optimal voltage for the lowest EDP is also a critical constraint to the applications of long Si spin interconnects.

The problem of a large optimal applied voltage can be mitigated by downscaling the receiving nanomagnet. In Fig. 31, the optimal voltage for the lowest EDP is significantly reduced as the magnet becomes smaller because the switching response is largely improved. The EDP is also reduced since both switching time and energy are decreased by downscaling the magnet. Note that at room temperature, the thermal noise plays an important role in the interconnect performance. Figures 27 to 30 show that the fluctuations due to the thermal noise become more pronounced especially for a long highly doped channel and at a small applied bias since the STT is weaker. Reducing the size of the magnet not only improves the EDP but also reduces the fluctuations induced by random noise (see Fig. 31). Note that downscaling the magnet reduces the energy barrier, E_b, which determines how long the magnet can retain its state in the absence of the spin current; therefore, the short life time for maintaining the magnetic state may cause an issue in a non-volatile interconnect if the magnet becomes too small. However, in a logic circuit, it is not necessary that all devices and interconnects are non-volatile for non-volatile circuits. For instance, one can envision a non-volatile circuit in which only the inputs and outputs of each

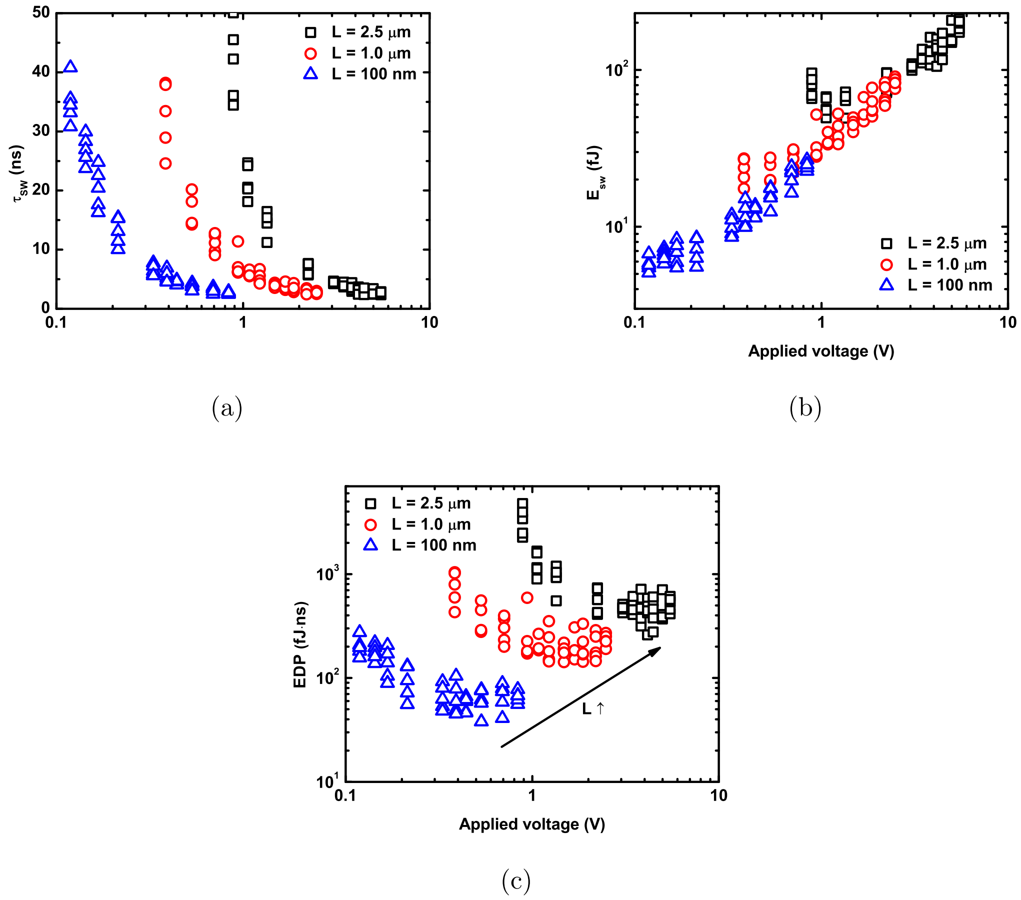

Figure 30: (a) Switching time, (b) energy, and (c) energy-delay product (EDP) versus applied voltage for different channel lengths [29]. The doping density of the channel is 4.78×10^{19} cm^{-3}.

pipeline state are non-volatile.

3.5 Summary

To sum up, in this chapter, a comprehensive physical model of the Si interconnect for ASL is developed. Using this model, spin injection and the switching response of a Si all-spin interconnect are analyzed. In the first part of this chapter, it is shown that to efficiently inject large spin currents, the nanomagnet should have high spin polarization and a low work function, the oxide layer needs to be thin and to have a high electron affinity, a small tunneling effective mass, and intrinsic spin selectivity,

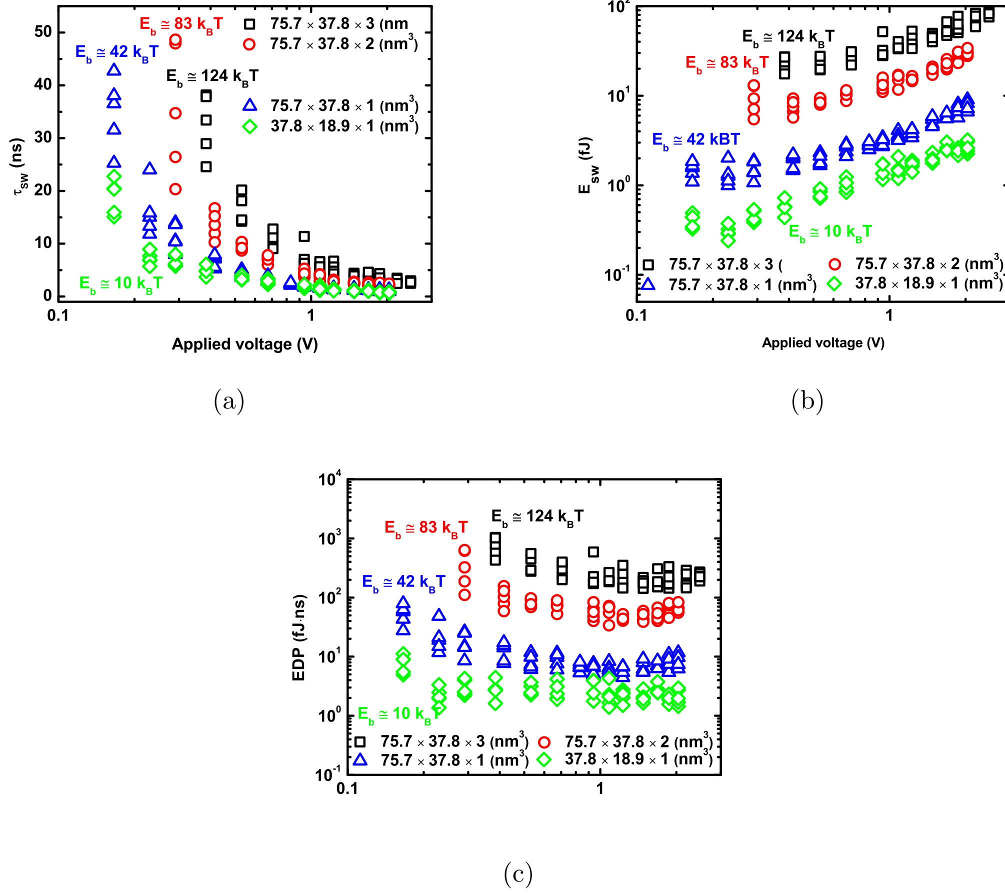

Figure 31: (a) Switching time, (b) energy, and (c) energy-delay product (EDP) versus applied voltage for different sizes of the receiving nanomagnet [29]. The interconnect length is 1 μm and the doping density of the channel is 4.78×10^{19} cm^{-3}.

the oxide/Si interface barrier height should be large, and the Si channel needs to be heavily doped. Because of the strong non-linear relations between the applied bias and spin injection quantities, it is possible to inject large spin currents with high efficiency at the small voltage.

In the second part of this chapter, the impacts of the Si channel length, doping density, interface tunneling resistance, and applied bias on the switching response are discussed. An electric field along the channel improves the effective spin relaxation length significantly and enables spin information propagate through a highly doped μm-scale interconnect without too much degradation. An increase in the applied

voltage lowers the interconnect delay at the price of a higher energy per switching operation. As a result, there exists an optimal voltage that minimizes the EDP of a Si spin interconnect. The impact of downscaling the sizes of the nanomagnets on the switching time and energy of Si spin interconnects has been quantified, and it has been demonstrated that size scaling is quite effective in improving the potential performances of these μm-scale interconnects.

CHAPTER IV

COPPER AND ALUMINUM INTERCONNECTS FOR ALL-SPIN LOGIC

4.1 Overview

Similar to the previous chapter, in this chapter, a simple spin-valve (SV) configuration combined with STT-driven switching is also used as an energy-efficient interconnect structure for ASL. However, instead of Si, interconnects using Cu and Al as channel materials are considered and analyzed based on physical models for spin injection, spin transport, and magnetization dynamics. The results indicate the proposed metallic interconnects dissipate less energy as compared to ASL interconnects based on the non-local spin-valve configuration. Compared to a similar spin interconnect with a Si channel, the spin currents and injection efficiencies are predicted to be higher since no Schottky barrier is formed at the interface of metals like Cu or Al with an insulator. Because of the longer spin relaxation length in Al as compared to Cu, the delay and energy dissipation are lower when Al is used especially at longer lengths where signal loss becomes important. While metallic spin interconnects are faster and more energy-efficient in short lengths because of their smaller resistances and higher spin injection efficiencies, they are outperformed by spin interconnects with Si channels at long lengths because the spin relaxation lengths in Si can be as long as many micrometers whereas in metals they are limited to a few hundred nanometers.

4.2 Copper and Aluminum Spin Interconnects

In ASL, as shown in Fig. 32(a), electrons carrying spin information diffuse through the channel and exchange their angular momentum with the target nanomagnet [201].

The in-built non-reciprocity is achieved by putting the ground location close to the transmitter [202]. Both *COPY* and *INVERT* operations can be realized by ASL, meaning that it can be used as a switch or an interconnect. However, this ASL configuration is not energy-efficient to be used as an interconnect because (i) a big fraction of spins injected by the transmitter into the channel directly flow into the ground. (ii) From the receiver to the ground, there are still redundant current paths increasing power dissipation, which becomes significant as the interconnect length or number of nanomagnets in the previous stage increases. Consequently, to overcome the problems mentioned above, the interconnect shown in Fig. 32(b) is used for ASL. In this structure, the spin signal from the previous ASL stage is copied using an SV configuration combined with the STT-driven switching. For the case of metallic channels (e.g. Cu or Al), the non-reciprocity is realized by inserting a thin oxide at the transmitter side [45]. If the channel is semiconducting (e.g. Si), the non-reciprocity is maintained by an electric field across the channel [29], and a tunneling barrier at the transmitter is still required to overcome the so-call conductivity mismatch problem [192, 180]. The higher energy efficiency of this structure is achieved by (i) eliminating the redundant current paths in the previous ASL stage, and (ii) no loss of injected spin due to lack of shunt path to the ground. Thus, it is of great interest to understand how to design this SV-like interconnect for ASL. In this chapter, our emphasis is on the interconnects made of metallic channels such as Cu and Al. The design and analysis for the semiconducting channel such as Si have already been discussed in the previous chapter [29].

4.3 Mathematical Models

In this section, a physical model to study spin injection, spin transport and stochastic magnetization dynamics in metallic SV-like interconnects is presented.

The analysis of the metallic spin interconnect can be divided into three parts: spin

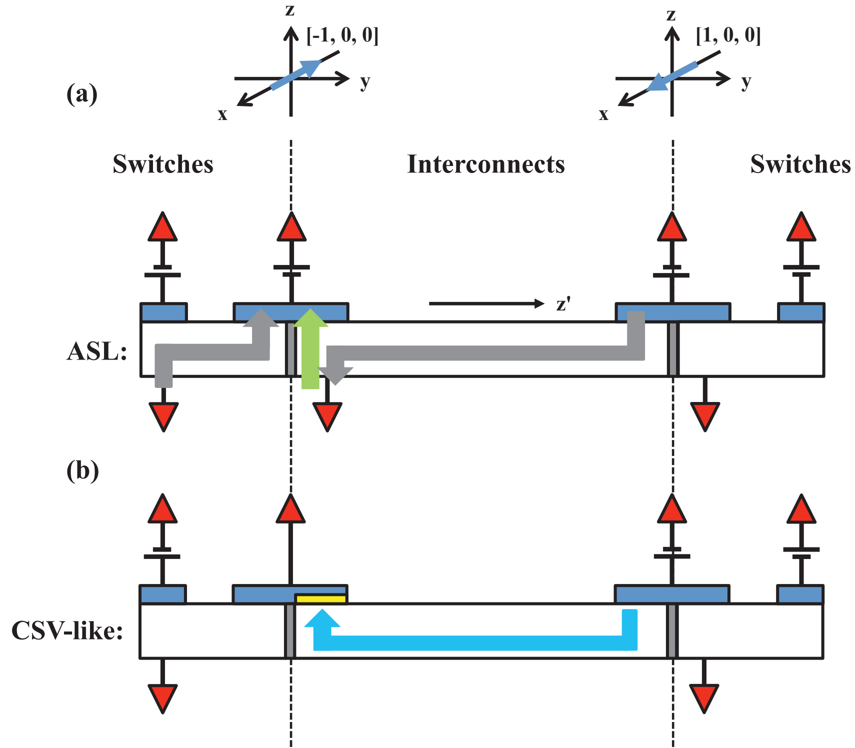

Figure 32: (a) Switching components connected by ASL-type interconnects [28]. The blue rectangles are the nanomagnets and the dark gray rectangles are insulating spacers. The arrows show the electrical currents. The dark gray arrows indicate the redundant electrical current paths increasing power dissipation. The light green arrow shows the electrical current with which a considerable fraction of spin current is shunted directly to the ground. (b) Switching components connected by CSV-like interconnects, where the losses resulting from the charge currents in the shunt path of the interconnect and those in the previous ASL switch are eliminated. The yellow rectangle is the tunneling oxide. The initial magnetic unit vectors of the transmitting and receiving nanomagnets are assumed to be $[-1, 0, 0]$ and $[1, 0, 0]$, respectively.

injection, spin transport, and magnetization dynamics. Here spin injection is realized by electrons tunneling from the FM metal into the NM metal since a thin oxide is used at the transmitter side to achieve non-reciprocity. The tunneling currents in this chapter are calculated using the NEGF method based on a single-band effective mass Hamiltonian [46]. Because of the strong screening effect in metals, these injected spin-polarized electrons travel through the channel mainly via the diffusion mechanism, which can be well-described by the spin diffusion equation [226]. Once electrons reach the end of the channel, they try to change the magnetization of the receiving magnet by the STT. The magnetic response of the nanomagnet under the STT from out-of-plane spin currents and effective field including material anisotropy, shape anisotropy, and thermal noise is given by solving the LLG equation [141]. The random noise field is treated as three independent Wiener processes in the x, y, and z direction and the resulting stochastic LLG equation is numerically solved by the midpoint method in the sense of Stratonovich calculus [43].

The mathematical details of the tunneling currents and LLG equation have been given in the previous chapter [29]. Here we only stress some key points which are distinct from those in Si as follows: (i) The potential energy profile of FM metal/oxide/NM metal shown in Fig. 33 lacks a Schottky barrier due to a strong screening effect in metallic materials. This energy band diagram is used to calculate the Green's function, transmission coefficient, and tunneling currents. (ii) The effects of spin accumulation on tunneling currents can be ignored in both FM and NM metals due to the large density of states in metallic materials [14]; thus, spin tunneling currents can be given by solving the NEGF method directly rather than self-consistently with the spin diffusion equation. (iii) Instead of the spin drift-diffusion equation [239, 240], the spin diffusion equation is used to describe spin transport in the channel given by

$$\frac{\partial^2 \mu_{s,i}(z')}{\partial z'^2} = \frac{\mu_{s,i}(z')}{L_{sf}^2} \tag{49}$$

where $\mu_s(z')$ is the spin accumulation profile along the NM channel, L_{sf} is the spin diffusion length, and i represents either the x, y, or z direction. The spin current profile, $J_s(z')$, in the NM channel is given as

$$J_{s,i}(z') = \sigma \frac{\partial \mu_{s,i}(z')}{\partial z'} \tag{50}$$

where σ is conductivity of the NM metal. The boundary conditions for the channel are spin tunneling currents and spin currents at the end of the channel, which are obtained by solving Eqs. (49) and (50), as well as the interface conductance matrix [13] simultaneously. Note that spin accumulation in the receiving nanomagnet is assumed to be zero.

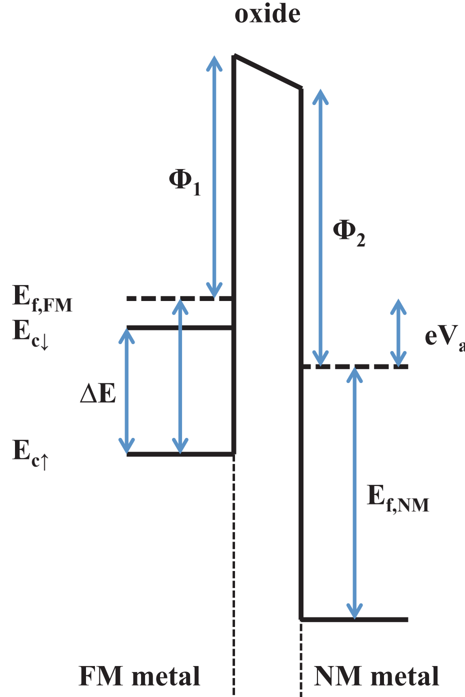

Figure 33: The energy band diagram of the FM metal/oxide/NM metal structure [28]. $E_{f,FM}$ and $E_{f,NM}$ are Fermi energies of the ferromagnet and normal metal, respectively. $E_{c\uparrow}$ and $E_{c\downarrow}$ are conduction band edges for up-spin and down-spin electrons, respectively. ΔE is the exchange energy splitting. Φ_1 and Φ_2 are interface barrier heights at the ferromagnet/oxide and oxide/normal metal interfaces, respectively. eV_a is the difference in Fermi level between the ferromagnet and normal metal due to the applied voltage.

4.4 *Results and Discussion*

In this section, we use the model mentioned in the previous section to study Cu and Al as channel materials in the SV-like interconnect structure and compare them with Si. The effects of different channel materials on spin injection, delay, and energy of the interconnect are discussed. We also show SV-like configuration is more energy-efficient than ASL in the use of interconnects.

4.4.1 Spin currents and Injection Efficiency

Spin injection plays an important role in determining the performance of the interconnect. The efficiency of spin injection is defined as injected spin currents normalized to the electrical currents. Larger injected spin currents give a faster magnetic response of the receiving nanomagnet, and higher injection efficiency reduces the power dissipation needed for injecting spin. Due to a thin oxide, a dominant transport mechanism of spin injection into the interconnect is the tunneling process. The parameters for the spin injection calculation are summarized in Table 4.

Table 4: Simulation parameters for tunneling currents. m^*, χ, Φ, and E_f are the effective mass, electron affinity, work function, and Fermi energy of the material [186]. The effective mass of the FM metal, Cu, and Al are assumed to be equal to m_0, where m_0 is the free electron mass. Fermi energy and exchange energy splitting of the ferromagnet (in units of eV) are 2.25 and 2.15, respectively [45].

	Al_2O_3	HfO_2	SiO_2
m^* (m_0)	0.2	0.2	0.5
χ (eV)	1.45	2.55	0.95
	Cu	Al	
Φ (eV)	4.65	4.28	
E_f (eV)	7	11.6	

Figure 34 shows spin tunneling currents and injection efficiencies versus the applied bias. It is found that the tunneling currents into Cu and Al are significantly larger

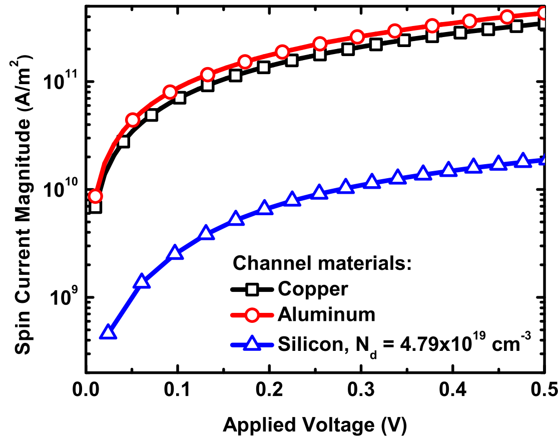

(a)

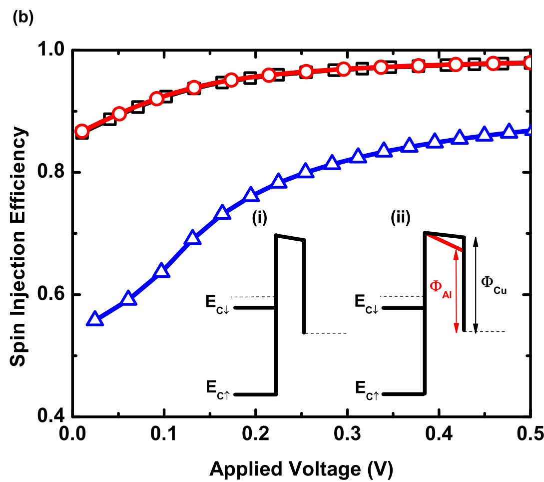

(b)

Figure 34: (a) Spin current and (b) injection efficiency versus the applied voltage for Cu, Al, and Si [28]. The insulator thickness is 0.5 nm. The work function of the ferromagnet is 4 eV. Al_2O_3 is used as a tunneling barrier. Since the Si channel is highly degenerate, the effect of spin accumulation on the spin currents is ignored [29]. Inset (i) and (ii) in (b) show the effect of the Schottky barrier and work function of the metal on the energy band diagram.

than those into Si. This is because there is no Schottky barrier at the oxide/metal interface to reduce the tunneling probability. Moreover, the existence of a Schottky barrier in a semiconducting channel can also explain higher injection efficiencies into the metal. A larger Schottky barrier blocks more majority carriers in the ferromagnet and thus spin injection efficiencies are reduced in Si. Spin tunneling currents into Al are only slightly larger than those into Cu even though the difference in their work functions is about 0.4 eV. This is because only electrons with the energies considerably higher than the Fermi energy of the ferromagnet experience the change of the barrier height (Φ_2 in Fig. 33). Since the Fermi-Dirac distribution decays exponentially for energies a few kT above the Fermi energy, the dependence of the current magnitude on the barrier height is weak. For spin injection efficiencies, Cu and Al are close since no Schottky barrier exists at the interface of either metal to introduce an additional spin selectivity.

In Fig. 35, we study the impact of changes in the FM metal/oxide interface barrier height (Φ_1 in Fig. 33), oxide thickness, and oxide material on spin currents and injection efficiencies. It is found that the spin current is larger if Φ_1, oxide thickness, and tunneling effective mass are lowered, which is because of an increased tunneling probability. In general, Φ_1 can be changed significantly by using the ferromagnet with a different work function, an oxide with a different electron affinity, and by having surface charges at the ferromagnet/oxide interface. However, spin injection efficiency is weakly dependent on these parameters, since there is no Schottky barrier in the metallic system to introduce an additional spin selectivity. An oxide with certain spin preference such as MgO can also potentially improve spin injection efficiencies [21]. For simplicity, only oxides without any intrinsic spin selectivity are considered in this paper. Note that large spin injection efficiencies in Figs. 34 and 34 ($> 80\%$) are because we use a highly spin-polarized ferromagnet such as the CoFeB alloy, where the Fermi energy and exchange energy splitting are close [45], as a spin injector in

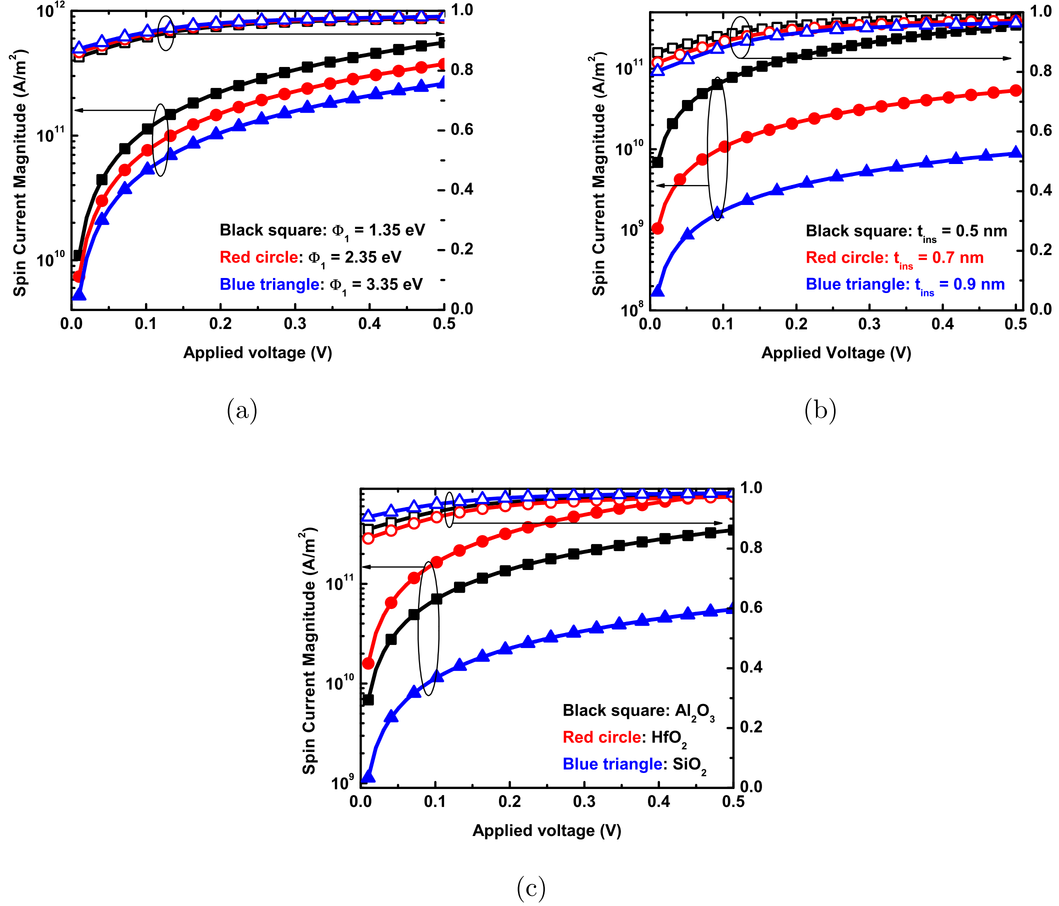

Figure 35: Spin current and injection efficiency versus the applied voltage with different (a) interface barrier heights, Φ_1, (b) oxide thicknesses, and (c) oxide materials [28]. For (a), the tunneling effective mass is $0.2m_0$, Φ_2 is 3.2 eV, and the oxide thickness is 0.5 nm. For (b), Φ_1 is 2.55 eV, the tunneling effective mass is $0.2m_0$, and Φ_2 is 3.2 eV. For (c), the work function of the ferromagnet is 4 eV, Cu is used as an interconnect, and 0.5 nm is used as the oxide thickness.

the simulations.

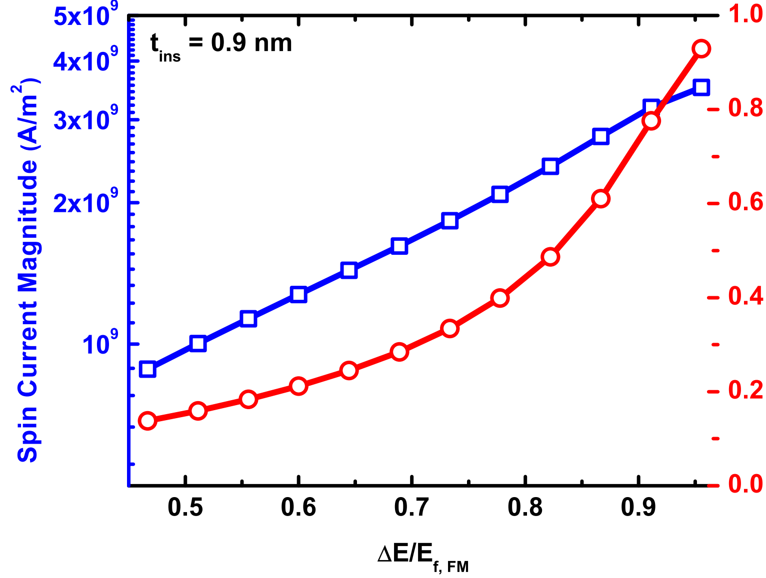

Figure 36: Spin current and injection efficiency versus the exchange energy splitting/ Fermi energy ratio [28].

Figure 36 shows in metals, both spin currents and injection efficiencies increase with the spin polarization of the FM metal. This is because a higher spin polarization gives more majority carriers contributing tunneling currents. From Figs. 35 and 36, we know that spin injection efficiencies into a metallic channel are mainly determined by spin-polarized electrons in the FM metal, rather than the oxide and interface barrier. This particular trend in normal metals agrees with experiments for spin-polarized tunneling into a superconducting metal, where the injection efficiency is also given by the net polarization of the electrons in the FM metal [151]. However, to the best of our knowledge, experiments for spin-polarized tunneling into a normal metal is still lacking, and our hope is that more experiments on the ferromagnet/oxide/normal metal structure can be stimulated by this new interconnect structure to explore the underlying physics more.

4.4.2 Delay and Energy Performance

The energy dissipation of the interconnect, E_{int}, is given as

$$E_{int} = IV\tau_{int} \tag{51}$$

where I is the electrical current flowing through the interconnect, V is the total applied bias across the interconnect, and τ_{int} is the delay time spin information needs to be written into the receiver. In the following simulations, since the transit time of electrons traveling through the channel is much smaller than the responding time of the magnet, the delay time is defined when the magnetization of the receiving nanomagnet in the x direction changes from 1 to 0. Note that the initial magnetic unit vectors of the transmitting and receiving nanomagnets are assumed to be $[-1, 0, 0]$ and $[1, 0, 0]$, respectively (see Fig. 32).

The delay and energy depend on how many spin-polarized electrons can transfer their angular momentum with the receiving nanomagnet. High injected spin currents give a strong spin signal at the beginning of the interconnect; however, how far these spins can propagate depends on the spin relaxation length (SRL) of the channel. In general, SRLs in metals are mainly determined by spin relaxation time and diffusion coefficient, which are strong functions of scattering mechanisms. As a result, to account for the effects of scatterings on spin transport parameters, compact models developed in Ref. [176] are used. The imperfection of the metallic interconnect is considered by grain-boundary reflectivity (R), average separation of the grain boundaries (d), and sidewall specularity (p). Simulations parameters for the nanomagnet, interface conduction matrix, and interconnect are summarized in Table 5. Furthermore, at room temperature, the thermal noise plays an important role in the magnetic response; therefore, we run the simulations five times for the same set of parameters to roughly estimate the thermal fluctuations. Note that a large number of simulations are still required to obtain the accurate noise variance.

Table 5: Parameters of the nanomagnet, interface conduction matrix, and interconnect for all the delay and energy simulations [141, 13]. L_m, W_m, and t_m are the length, width, and thickness of the nanomagnet, respectively. W_{int} and t_{int} are the width and thickness of the interconnect, respectively.

Symbol	Value	Units
M_s	2.5×10^5	$\text{A}\cdot\text{m}^{-1}$
α	0.0021	–
L_m	37.8	nm
W_m	18.9	nm
t_m	1	nm
K_u	6×10^4	$\text{joule}\cdot\text{m}^{-3}$
$G_{\uparrow\uparrow}$	0.6×10^{15}	$\Omega^{-1}\cdot\text{m}^{-2}$
$G_{\downarrow\downarrow}$	0.2×10^{15}	$\Omega^{-1}\cdot\text{m}^{-2}$
$\text{Re}(G_{\uparrow\downarrow})$	5.5×10^{15}	$\Omega^{-1}\cdot\text{m}^{-2}$
$\text{Im}(G_{\uparrow\downarrow})$	0.015×10^{15}	$\Omega^{-1}\cdot\text{m}^{-2}$
W_{int}	18.9	nm
t_{int}	37.8	nm
p	0	–
R	0.3	–
d	18.9	nm

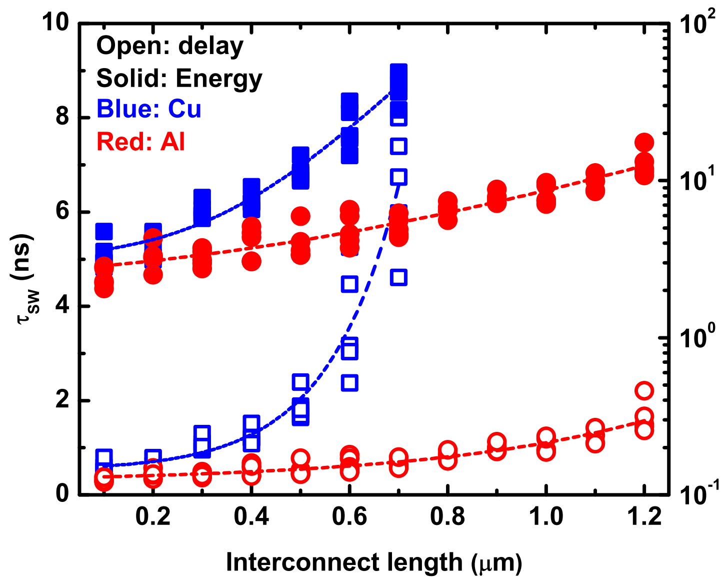

Figure 37: Delay and energy versus the interconnect length under a fixed bias voltage [28]. In this case, SRLs of Cu and Al are about 202 nm and 512 nm, respectively. The applied voltage is 0.1 V. For each set of parameters, five simulations are done to estimate the random fluctuations due to the thermal noise. The same estimation is also used for Figs. 38 and 39.

In Fig. 37, the delay and energy are plotted versus the interconnect length for Cu and Al as channel materials. It can be seen that both delay and energy increase with the interconnect length. This can be explained by more electrons lose their initial spin polarization in a longer channel due to spin relaxation. In Cu, due to a shorter SRL, the delay and energy increase much faster than those in Al. Also, thermal fluctuations become more pronounced in a longer channel because of a weaker STT from spin currents. From Fig. 37, we can see that a 700 nm-long Cu interconnect suffers from serious thermal noise fluctuations.

To mitigate thermal noise fluctuations, the most straightforward way is to enhance the STT on the receiving nanomagnet using a larger applied bias. The delay, energy, and EDP versus the applied bias are given in Fig. 34, where the channel length is chosen to be 400 nm, which is the typical length of local interconnects [165, 164]. The EDP is defined as the product of delay and energy. From Fig. 38, it is found that less thermal fluctuations and the smaller delay are obtained at the expense of higher power dissipation. Furthermore, with the same bias voltage, Al turns out to be a better option than Cu as the channel material due to a faster magnetic response and lower energy dissipation. Since the delay and energy have opposite trends with respect to the voltage, the EDP is often used to find out the optimal voltage. However, unlike Si, there is no optimal voltage that minimizes the EDP in the metallic channel. This is because the delay decreases rapidly when the spin current is small, and for the short interconnect, the spin current entering into the receiving magnet is mainly determined by spin injection. Since injected spin currents in a metallic channel are much larger than those in a Si channel, the decrease in the delay can be compensated by an increase in the spin current, making the EDP almost independent of the voltage. Thus, the optimal voltage for a metallic spin interconnect can be determined by the system requirements such as delay, energy, or noise tolerance.

Figure 39 shows the energy dissipation for Cu, Al, and Si SV-like interconnects

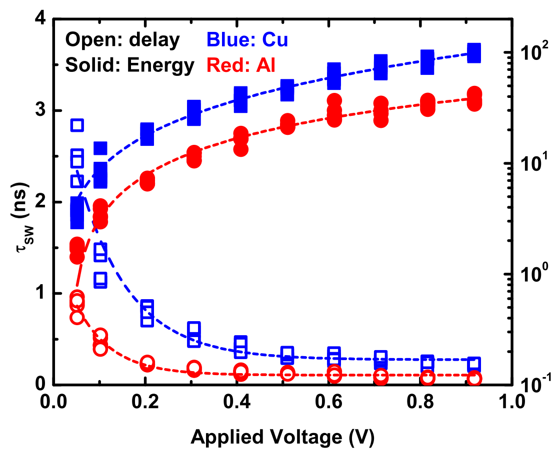

(a)

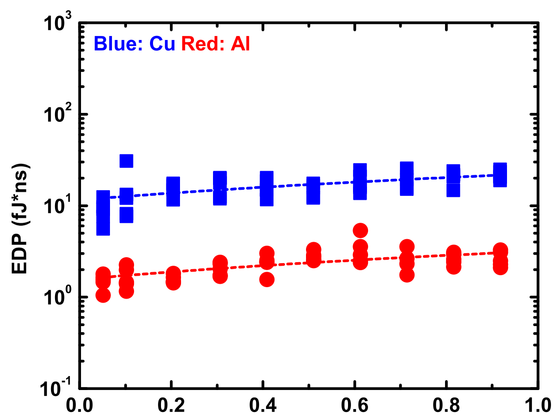

(b)

Figure 38: (a) Delay, energy and (b) energy-delay product versus the applied voltage for 400 nm-long Cn and Al interconnects [28].

as a function of the channel length. As a reference, the energy dissipation of a Cu ASL interconnect (see Fig. 32(a)) is also shown. Here only the energy dissipation corresponding to the interconnect (the middle section between the dashed lines in Fig. 32) has been plotted. The circuit models developed in Ref. [12] are used to simulate the Cu ASL interconnect. The delay in Si interconnects is obtained at the optimal applied bias that minimizes the EDP [29]. From Fig. 39, it is found that metallic channels consume less power in a short interconnect due to a low resistive current path; however, in a long μm-scale interconnect, the energy dissipated by the metallic channel increases rapidly because of short SRLs. Therefore, since SRLs in metals are restricted to hundreds of nanometers, metals like Cu and Al are suitable for the use of short local interconnects. The Si channel is a better option for longer interconnects since it has longer spin relaxation time and its SRL can be further improved by an electric field [177]. The same trend can also be deduced from the analytical expressions in Ref. [28]. Furthermore, in the same figure, it is also shown that the SV-like configuration turns out to be a more energy-efficient interconnect structure than its ASL counterpart. The real energy saving offered by SV-like interconnects is even higher since we have ignored the extra energy dissipation caused by the redundant current paths in the previous ASL stage.

4.5 Summary

In this chapter, a simple SV structure with STT-driven switching has been used as a more energy-efficient interconnect for ASL. Using Cu and Al as channel materials, the interconnect is analyzed through a comprehensive set of physical models including spin injection, spin transport, and stochastic magnetization dynamics. For spin injection, it is predicted that due to lack of a Schottky barrier at the oxide/NM metal interface, significantly higher spin injection efficiencies can be achieved with metals

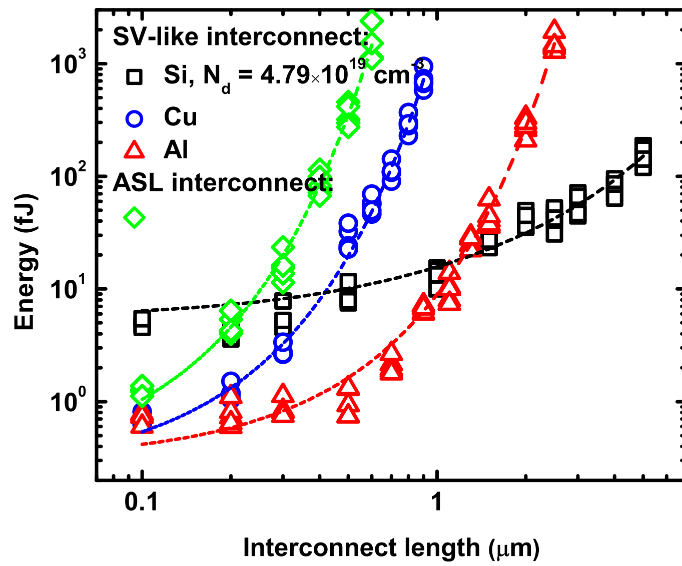

Figure 39: Energy versus the interconnect length under the same magnetic response for SV-like and Cu ASL (light green diamond) interconnects [28]. The structures of ASL and SV-like interconnects are shown in Fig. 32. For SV-like interconnects, the channel materials include Cu (blue circle), Al (red triangle), and Si (black square).

like Cu and Al. Moreover, spin polarization in an FM metal is the main factor determining the spin injection efficiency in the FM metal/oxide/NM metal structure. This is very different from the case with Si channel, where injection efficiency depends largely on interface barriers. For the delay and energy dissipation, Al outperforms Cu due to its longer SRL, and both Al and Cu are better than the Si channel in local short interconnects due to low resistance of metallic structures. However, in the application for longer interconnects, Si is a more promising candidate due to its long spin relaxation time and the possibility of using an electric field to improve its spin relaxation length. In metallic interconnects like Cu and Al, the energy dissipation increases rapidly as the channel length goes beyond hundreds of nanometers.

CHAPTER V

DOMAIN WALL INTERCONNECTS FOR ALL-SPIN LOGIC

5.1 Overview

In this chapter, a novel interconnect concept based on automotion of magnetic DWs is presented. The proposed interconnect is analyzed using a comprehensive numerical model including an equivalent circuit for ASL operations [141], the 1-D LLG equation for domain wall creation, reflection, and disappearance at the boundaries. Analytical expressions for domain wall transport [195, 217, 140] along the wire are also presented. From the model, it is found that the reflection of the domain wall can be eliminated by using a material with high Gilbert damping coefficient at the end, the energy dissipation can be independent of the interconnect length, and domain wall displacement and energy dissipation can be further improved using a material with a low damping factor and saturation magnetization. Furthermore, the interconnect reliability is also studied by applying the thermal random noise analysis on the dynamics of domain walls, and it is found that thermal fluctuations can have a significant impact on the interconnect performance; thus, the interconnect with a low Gilbert damping factor is desired to suppress the thermal noise effects.

5.2 Domain Wall Interconnects

For ASL, interconnects have been studied using a lateral simple SV with STT switching using copper, aluminum, and silicon as channel materials in Chapters III and IV [29, 28]. It is shown that the energy of the interconnect is significantly reduced by eliminating the shunt path in ASL. Also, depending on the length of the interconnect,

the energy can be minimized by choosing a metallic or semiconducting channel due to different spin relaxation lengths [176, 177] and the electric field effect [239]. However, no matter what structure or material is used, spin tunneling injection is still required to create spin polarization in the NM semiconducting channel or maintain the reciprocity of the metallic interconnect. To avoid this charge to spin conversion, it is intuitive to use FM wires as interconnects, where the spin information can be stored and propagate directly. A magnetic DW is the transition region between magnetic domains in the FM material. As a result, it is of interest to explore the possibility of DWs as interconnects for ASL.

Despite the fact that a DW can be moved over a significant distance by an external magnetic field [195], in-plane spin current [11, 134, 243, 237], or out-of-plane spin current [114], it still requires an additional energy to create a magnetic field or electrical current associated with spin torque on the interconnect. Recently, automotion of DWs has been demonstrated [34], and it is shown that due to intrinsic transverse anisotropy, which is mainly due to demagnetization inside the wire, a DW can travel a long distance with a high velocity ($\sim$ 1k m/s) by simply transforming its shape. The concept of spintronic interconnects using automotion of DWs has been proposed in [167]. However, in terms of energy, it has an obvious advantage over the existing proposed interconnects [29, 28], where the charge current flowing through the channel is always required to carry spin information. Therefore, this chapter aims at clarifying the potential of DW automotion as interconnects for ASL.

The interconnect structure is shown in Fig. 40, where the logic stages are connected by an FM interconnect which is uniformly magnetized initially. The DW is created and propagates automatically once the previous logic stage finishes the computation. The energy for the interconnect is simply that required for DW creation, which is exactly the same as that used in logic computation in the previous device stage; therefore, this configuration is particularly interesting compared to those based

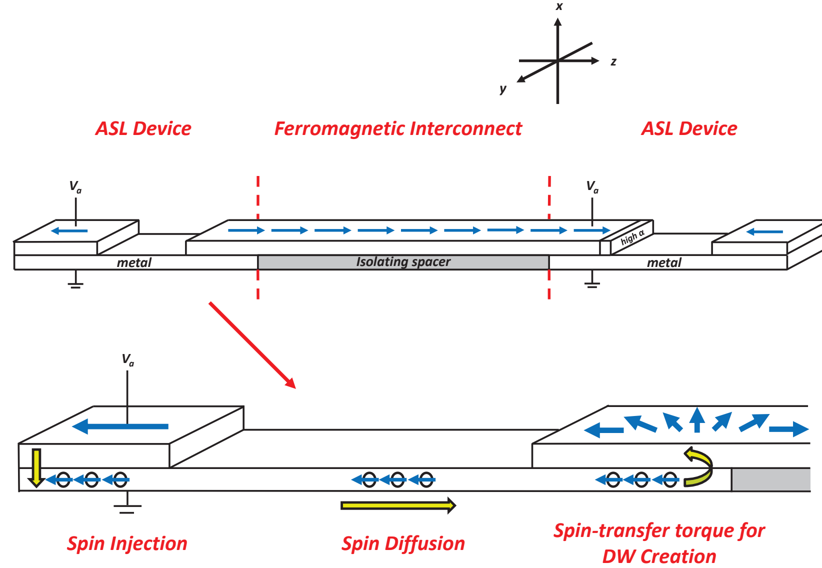

Figure 40: Schematics of all-spin logic (ASL) interconnects using automotion of domain walls (DWs) and creation of DWs using ASL [25]. The Cartesian coordinate used for the calculations of interconnects is also defined.

on STT switching since there is no extra power consumption for data transmission in the interconnect as illustrated in Fig. 41. Note that a leakage current path through the interconnect exists, and the resulting STT may either improve or degrade the DW transport depending on the functionality of ASL. However, this leakage current is typically negligible because of the relatively high resistance of the very thin (∼2 nm) FM interconnect compared to NM metallic wires in ASL. For simplicity, in this chapter, a single inverter or a buffer is used for the device stage, which in general can be a more complex function such as a majority gate [163, 23].

5.3 Mathematical Models

To analyze the proposed interconnect scheme shown in Fig. 40, it is necessary to appropriately describe the operation of ASL, DW creation, reflection, and disappearance at the edges, and DW displacement in the channel. Fig. 42 shows the numerical procedure for modeling the DW interconnect for ASL. Since, at each time step, spin

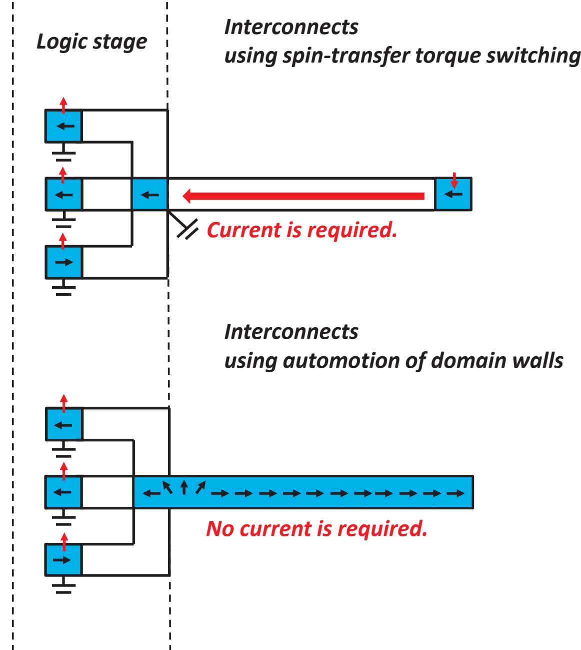

Figure 41: Schematics illustrating the difference between interconnects based on spin-transfer-torque switching and automotion of DWs [25]. The ferromagnetic metals are represented by blue rectangles with black arrows. The red arrows represent the direction of electrical current.

currents for creating the DW depend on ASL/interconnect interface resistance, which is determined by the magnetization of the wire, simultaneously solving the ASL equivalent circuit and 1-D LLG equation is required to model the DW creation. Once a DW is created at the beginning of the interconnect, it can be well-described by two important parameters in the Walker's trial form [195] as we will show later, the displacement (χ) and phase (ϕ) of the DW. The analytical expression for DW transport is used to estimate how far the DW can move automatically in the channel. Finally, as the DW approaches the end of the wire, the magnetization distribution of the interconnect is plugged back into the 1-D LLG equation to see whether the DW is either reflected or destroyed. Note that analytical DW transport equations only work in the absence of random noise fluctuations. Hence, when discussing the thermal noise effects on DW dynamics, the LLG equation is required to be solved throughout the interconnect. In this section, the mathematical formalism of the ASL, 1-D

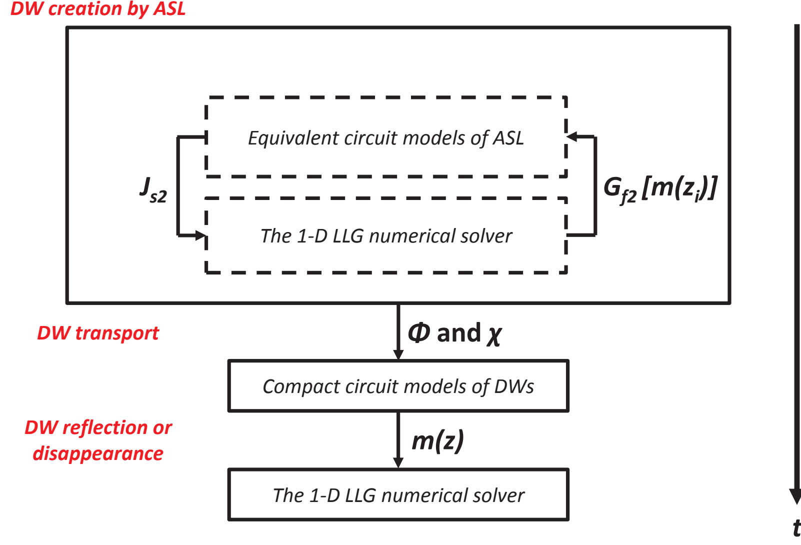

Figure 42: The numerical procedure for modeling DW interconnects for ASL [25].

LLG equation, and DW transport models are presented, and the comparison in DW transport between the analytical expressions and numerical simulations can be found in Appendix A.

5.3.1 Switching Device

The ASL structure is shown in the device part of Fig. 40. In ASL, the spin-polarized electrons, injected by local charge currents, diffuse through the channel and insert STTs onto the FM interconnect. If a STT is strong enough, the magnetization in the region where spin current is present will be reversed, and a DW is created. To model the operation of ASL, the circuit representations of spin transport in the non-magnetic channel and ferromagnet/normal metal interface [141, 13] are used, and the equivalent circuit of ASL with the interconnect on which spin currents are applied is shown in Fig. 43. The corresponding circuit conduction matrix, $\mathbf{G}$, is obtained by applying the nodal analysis on the circuit (see Appendix A) and defined as

$$\{V\} = \mathbf{G}^{-1}\{I\}, \tag{52}$$

where $\{V\}$ and $\{I\}$ are the voltage and current vectors representing charge and spin components at each node. The current vector only has one non-zero component representing the source of charge currents. Note that parallel interface conduction matrices are used to describe multiple domains in the FM interconnect, where the exchange effect is accounted for by the 1-D LLG equation. The magnitude of spin currents at the end of ASL is also affected by the magnetization profile of the wire; therefore, at each time step, once the magnetization of the wire is updated, the corresponding voltage vector at each node can be calculated from Eq. 52, and spin currents responsible for creating a DW are also known using the following equation:

$$I_{ij} = G\left(V_i - V_j\right), \tag{53}$$

where I_{ij} is the 4×1 current vector flowing from the node i to the node j; therefore, the current density used in the 1-D LLG equation for DW creation is given as

$$J_s = \frac{1}{A_{in}}\left[\sum_{k=1}^{N} I_{ij}(\vec{m}_k)\right] \tag{54}$$

with A_{in} being the cross-sectional area at the ASL/wire interface and k is the index for each domain. Note that J_s changes with time during the DW creation because of the magnetization reversal in the beginning of the channel.

5.3.2 One-dimensional Landau-Lifshitz-Gilbert Equation

The magnetization dynamics of the wire is governed by the LLG equation. Since here the structure we are interested in is a wire, where typically the width and thickness are much smaller than the length, the magnetization in the cross-sectional area is assumed to be uniform; therefore, instead of 3-D micromagntic simulations [167], the 1-D LLG equation is used to capture the essential physics of DWs in a FM interconnect [217].

The 1-D LLG equation under the effects of an external magnetic field, spin-torque

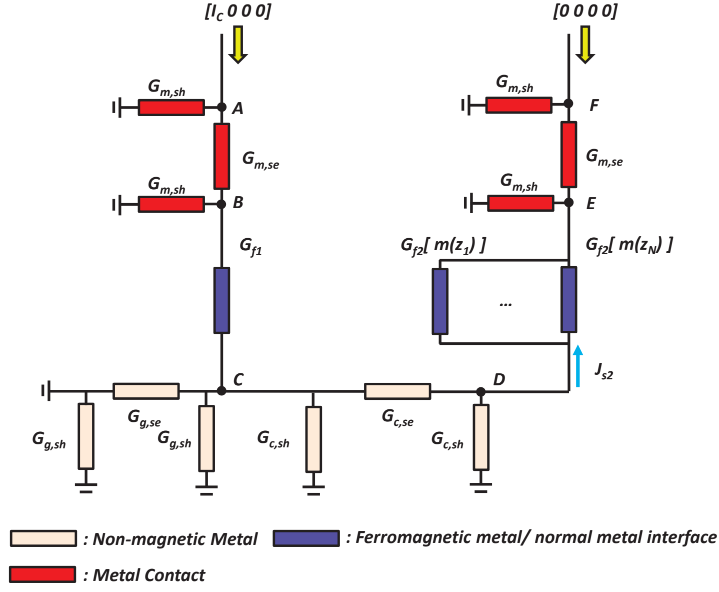

Figure 43: The circuit representation of ASL connected by FM wires for modeling DW creation [25]. The red, blue, and light yellow bars represent the conductance of the contact, FM metal/NM metal interface, and NM transport channel, respectively.

from in-plane and out-of-plane spin currents is given as

$$\begin{aligned}\frac{\partial \vec{m}}{\partial t} &= -\gamma\mu_0(\vec{m}\times\vec{H_{eff}}) + \alpha(\vec{m}\times\frac{\partial \vec{m}}{\partial t}) - \gamma a_J[\vec{m}\times(\vec{m}\times\vec{p})] - u_J(\frac{\partial \vec{m}}{\partial z}) \\ &\quad +\beta u_J(\vec{m}\times\frac{\partial \vec{m}}{\partial z}),\end{aligned} \tag{55}$$

where γ is the gyromagnetic coefficient, α is the Gilbert damping coefficient, μ_0 is the free space permeability, $\vec{m}$ represents the unit vector of the magnetization of each domain, and $\vec{H_{eff}}$ is the effective magnetic field including the uniaxial anisotropy field, $\vec{H_u}$, demagnetization field, $\vec{H_d}$, exchange interaction, external magnetic field, $\vec{H_{ex}}$, and thermal random field, $\vec{H_{th}}$, defined as

$$\vec{H_{eff}} = \vec{H_u} + \vec{H_d} + \frac{2A}{\mu_0 M_s}\frac{\partial^2 \vec{m}}{\partial z^2} + \vec{H_{ex}} + \vec{H_{th}}, \tag{56}$$

where M_s is the saturation magnetization, A is the exchange constant, and $\vec{H_u}$, $\vec{H_d}$,

$\vec{H_{ex}}$, and $\vec{H_{th}}$ are given as

$$\vec{H_u} = \frac{2K_{u,x}}{\mu_0 M_s} m_x \hat{x} + \frac{2K_{u,y}}{\mu_0 M_s} m_y \hat{y} + \frac{2K_{u,z}}{\mu_0 M_s} m_z \hat{z}, \quad (57)$$

$$\vec{H_d}(z_i) = -M_s \left[\sum_j N_{x,ij} m_x(z_j) \hat{x} + \sum_j N_{y,ij} m_y(z_j) \hat{y} + \sum_j N_{z,ij} m_z(z_j) \hat{z} \right], \quad (58)$$

$$\vec{H_{ex}} = H_{ex,x} \hat{x} + H_{ex,y} \hat{y} + H_{ex,z} \hat{z}, \quad (59)$$

$$\vec{H_{th}}(z_i) = \sqrt{\frac{2\alpha k_B T}{\mu_0^2 \gamma M_s V_D}} \left[\frac{\partial W_x(z_i)}{\partial t} \hat{x} + \frac{\partial W_y(z_i)}{\partial t} \hat{y} + \frac{\partial W_z(z_i)}{\partial t} \hat{z} \right], \quad (60)$$

where k_B is the Boltzmann constant, T is the temperature, V_D is the volume of each domain, and W is the Weiner process. The thermal random fields are assumed to be isotropic, spatially and temporally uncorrelated and satisfy the following relations [175]

$$\langle H_{th}(z_i, t) \rangle = 0, \quad (61)$$

$$\langle H_{th,a}(z_i, t) H_{th,b}(z_j, t') \rangle = \frac{2\alpha k_B T}{\mu_0^2 \gamma M_s V_D} \delta_{ab} \delta(z_i - z_j) \delta(t - t') \quad (62)$$

with $\langle \cdot \rangle$ denoting the ensemble average, and a, b being indices labeling cartesian components. Note that the demagnetization field at each time step has spatial dependence and is calculated using the entire magnetization profile along the wire with the demagnetization tensor including magnetostatic interactions between magnetic domains [162, 153]. In Eq. 55, a_J is the coefficient for the Slonczewski torque defined as

$$a_J = \frac{\hbar J_{s,out-of-plane}}{2etM_s}, \quad (63)$$

where $J_{s,out-of-plane}$ is the magnitude of out-of-plane spin current density, t is the thickness of the wire, and e is the elementary charge. Note that the field-like torque is incorporated into the imaginary part of the mixing conductance in the interface conductance matrix, which is negligible at the normal metal/ferromagnet interface [13]. For torque due to in-plane spin currents, μ_J and βu_J represent the strengths of the adiabatic and non-adiabatic processes, respectively, where β is typically in the

range between 0.01 to 0.1 for different types of the DW [54], and u_J is given as

$$u_J = -\frac{\mu_B J_{s,in-plane}}{eM_s}, \tag{64}$$

where μ_B is the Bohr magneton, and $J_{s,in-plane}$ is the magnitude of in-plane spin current density. In this chapter, a perfect FM strip with no specific pinning site is assumed. In practice, extrinsic pinning may exist along the interconnect due to local defects or line-edge roughness that may impair the DW automotion. However, these extrinsic factors could be significantly reduced or even completely eliminated as the technology advances; thus, this chapter aims at the intrinsic properties of an ASL interconnect using the DW automotion. The numerical procedure of solving Eq. 55 is provided in Appendix A.

5.3.3 Domain Wall Transport

Fig. 44 shows the Walker's trial form [195] can fit the DW created by ASL well in the absence of thermal fluctuations; therefore, instead of solving the 1-D LLG equation for the entire wire, the analytical expressions based on Walker's trial solutions are used to capture the DW transport in the interconnect. The standard approach [195, 217, 140] is followed to derive the analytical expressions for DW transport, and the detailed derivation can be found in Appendix A. Note that the derived expressions here not only include transverse anisotropy (automotion) but also an external magnetic field, in-plane and out-of-plane spin currents to be consistent with Eq. 55.

The equations of motion for DW transport in the channel are given as

$$\left(1+\alpha^2\right)\frac{\partial \chi}{\partial t} = \frac{-\gamma\Delta(K_x - K_y)\sin 2\phi}{QM_s} + (1+\alpha\beta)\,\mu_J + \frac{\gamma\Delta p a_J}{Q} + \frac{\gamma\Delta\alpha\mu_0 H_{ex}}{Q} \tag{65}$$

$$\left(1+\alpha^2\right)\frac{\partial \phi}{\partial t} = \frac{\alpha\gamma(K_x - K_y)\sin 2\phi}{M_s} + \frac{(\beta-\alpha)\,Q}{\Delta}\mu_J - \gamma p\alpha a_J + \gamma\mu_0 H_{ex}, \tag{66}$$

where Q is the topological charge distinguishing the type of the DW (+1: head-to-head and -1: tail-to-tail), H_{ex} is the magnitude of an applied magnetic field in the z direction, p is either 1 or -1, representing z or -z spin polarization, respectively, Δ is

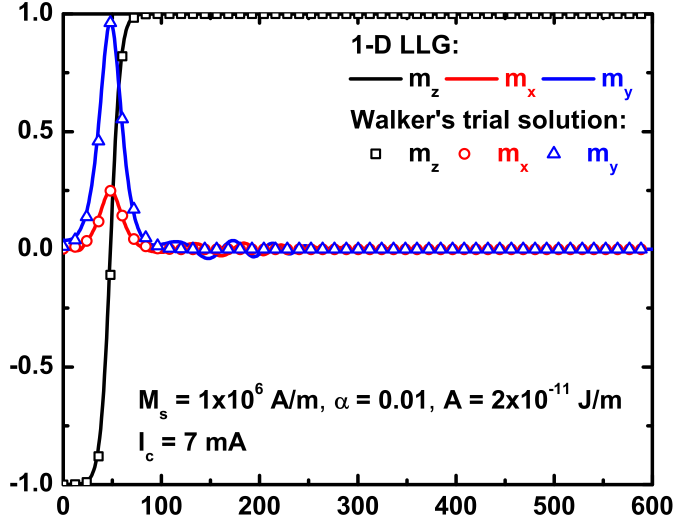

Figure 44: The comparison between the DW created by ASL/1-D LLG in a 600 nm interconnect and Walker's trial solutions [195]. The Walker's trial parameters: $\phi =$ 1.32 radian and $\chi = 50$ nm [25].

the domain wall thickness, and K_i includes uniaxial and shape anisotropy with the form given as $\frac{1}{2}\mu_0 M_s^2 N_i - K_{u,i}$. An important assumption here is that the demagnetization tensor, N_i, is independent of the space and only determined by the geometry [10]; therefore, the approximate demagnetization field, $\vec{H}_d'$, is simply given as

$$\vec{H}_d' = -M_s(N_x m_x \hat{x} + N_y m_y \hat{y} + N_z m_z \hat{z}). \tag{67}$$

The justification of using Eq. 67 in the equations of motion for DW transport is provided in Appendix A. In the following section, Eqs. 65 and 66 are used to study DW transport along the interconnect after a DW is created.

5.4 Results and Discussion

In this section, the comprehensive numerical model mentioned in Section 5.3 (see Fig. 42) will be used to study ASL interconnects based on the automotion of the DW. First, we focus on how to avoid DW reflection at the end of the interconnect,

which is an undesired feature in transmitting information. Next, the delay and energy of DW automotion interconnects in the ASL configuration are quantified. The performance of DW automotion interconnects can be optimized by adjusting the strength of transverse anisotropy and Gibert damping coefficient. Finally, the effects of thermal noise on interconnect reliability are discussed. Note that all the interconnects simulated in this section are in-plane magnetized initially since a higher wall velocity can be obtained from in-plane DWs [167]. A perpendicularly-magnetized wire is interesting as well since ASL using perpendicular magnetization anisotropy (PMA) magnets potentially has higher thermal stability and lower switching current [234]. However, the design aspects discussed in this section for an in-plane wire is general and thus also adaptable to the PMA one.

5.4.1 Domain Walls at Boundaries

After a DW is created by ASL, it moves toward the end of the interconnect automatically due to transverse anisotropy. For the purpose of the interconnect, the magnetization of the wire has to be completely reversed when the DW reaches the end, which is possible if the DW is destroyed as it is close to the boundary; however, in some cases, instead of being destroyed at the edge, the DW is reflected and the magnetization of the wire is recovered as the DW moves backward. This is an undesired feature for the use of the interconnect since the transmitting signal is coming back; therefore, it is of interest to understand the DW reflection so that a proper structure can be designed to make the DW disappear at the end of the interconnect.

Fig. 45 shows the time evolution of the magnetization at the end of the interconnect for the cases that the DW is reflected and destroyed. For the reflection, the DW with an opposite phase, which is responsible for a negative velocity, is recreated at the end of the channel as the DW reaches the boundary. On the other hand, if there is no enough energy for the DW to reform, through the damping mechanism, the DW

will gradually disappear at the end of the channel.

Fig. 46(a) shows the DW energy is a key parameter to determine the transient behavior of the DW at the end of the interconnect. In Fig. 46(a), a DW with a given phase is initially located near the boundary and it moves toward the end automatically due to transverse anisotropy. It is found that with a higher damping coefficient, the DW tends to disappear at the end since most of energy is dissipated during the transport. Also, with a constant damping coefficient, the DW in a lower energy configuration (see Fig. 46(b)) prefers to disappear at the end. However, the control of the DW phase reaching the end is quite difficult since it depends on both injected spin currents from ASL and DW transport in the channel; hence, high damping materials [138] incorporated at the end of the interconnect as shown in Fig. 40 are recommended to prevent DWs from being reflected.

5.4.2 Delay, Energy, and Material Targets

After knowing that the DW will disappear at the end using high damping materials, the delay of the interconnect can be defined as

$$DELAY = \tau_c + \tau_t, \tag{68}$$

where τ_c is the time for ASL creating the DW in the interconnect, and τ_t is the time for the DW traveling to the end of the channel. The energy of the entire structure is given as

$$ENERGY = I_c V \tau_p, \tag{69}$$

where I_c is the charge current supply on ASL, V is the voltage on the transmitting magnet of ASL, and τ_p is the pulse duration of the current supply. Note that the current source can be turned off once the DW is formed in the interconnect; thus, for the lowest energy operation, τ_p would be equal to τ_c, which will vary due to different current sources; however, for simplicity, here the pulse duration is set to be 1 ns in all the simulations. The simulation parameters are summarized in Tables 6 and 7.

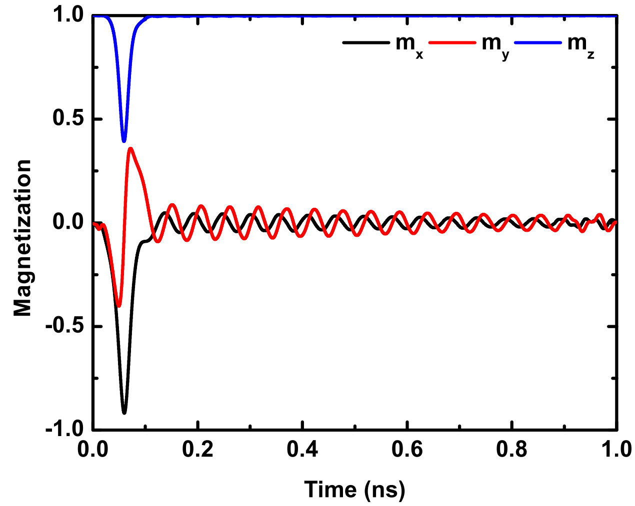

(a)

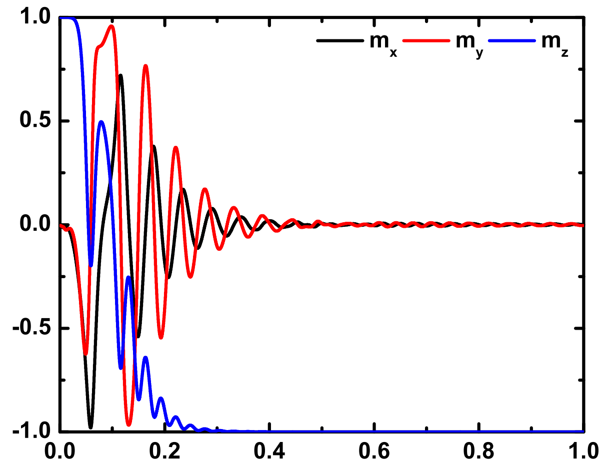

(b)

Figure 45: The time evolution of the magnetization at the end of the interconnect for (a) DW reflection ($\alpha = 0.01$) and (b) DW disappearance ($\alpha = 0.1$) [25]. The domain wall is located near the boundary initially and moves toward the edge due to automotion.

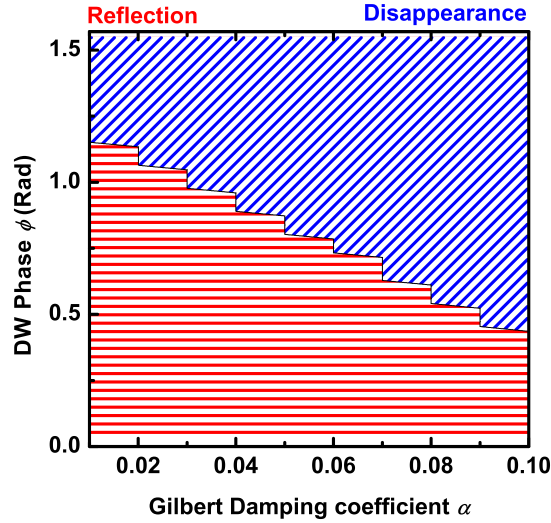

(a)

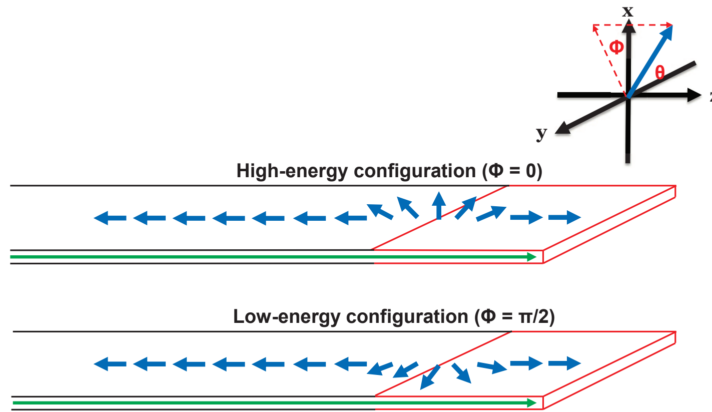

(b)

Figure 46: (a) The effects of phase and Gilbert damping coefficient at the end of the interconnect on the DW reflection and disappearance. Red lines represent the DW is reflected, and blue lines represent the DW is destroyed at the end [25]. The interconnect length is 400 nm and the DW is located at $z = 360$ nm initially. The Gilbert damping coefficient changes from 0.01 to 0.1 for $z = 360$ nm to $z = 400$ nm, and is set to be 0.01 for the rest of the wire. Note that if ϕ is exactly $\pi/2$ or 0, the domain walls have zero speed. (b) Schematics for illustrating high and low energy DW configurations in the in-plane ferromagnetic interconnect. The green arrow represents the direction of material anisotropy. The red region is where the damping coefficient is changed in Fig. 46(a).

Table 6: Simulation parameters for ASL. The transport parameters of the Cu channel are obtained from the compact model developed in Ref. [176]. Note that the imaginary part of mixing conductance is assumed to be zero for the FM metal/NM metal interface.

Symbol	Value	Unit
Length for the ground path, L_g	30	nm
Width for the ground path, W_g	20	nm
Thickness for the ground path, t_g	20	nm
Channel length, L_c	100	nm
Channel width, W_c	20	nm
Channel thickness, t_c	20	nm
Surface specularity, p	1	–
Grain boundary reflectivity, R	0.1	–
Majority interface conductance, $G_{\uparrow\uparrow}$	0.6×10^{15}	$\Omega^{-1}\cdot\mathrm{m}^{-2}$
Minority interface conductance, $G_{\downarrow\downarrow}$	0.2×10^{15}	$\Omega^{-1}\cdot\mathrm{m}^{-2}$
Mixing interface conductance, $G_{\uparrow\downarrow}$	5.5×10^{15}	$\Omega^{-1}\cdot\mathrm{m}^{-2}$

Table 7: Simulation parameters for the FM interconnect. Note that no material anisotropy in the transverse direction is assumed ($K_{u,y} = K_{u,z} = 0$).

Symbol	Value	Unit
Free space permeability, μ_0	$4\pi \times 10^{-7}$	joule$\cdot$A$^{-2}\cdot$m^{-1}
Gyromagnetic ratio, γ	17.6×10^{10}	tesla$^{-1}\cdot$s^{-1}
Saturation magnetization, M_s	$0.25/1 \times 10^6$	A$\cdot$m^{-1}
Gilbert damping coefficient, α	0.001/0.007/0.01	–
Exchange constant, A	2×10^{-11}	joule$\cdot$m^{-1}
Uniaxial anisotropy energy density, $K_{u,x}$	1.2×10^5	joule$\cdot$m^{-3}
Interconnect length, L_{int}	$100 - 1000$	nm
Interconnect width, W_{int}	20	nm
Interconnect thickness, t_{int}	2	nm

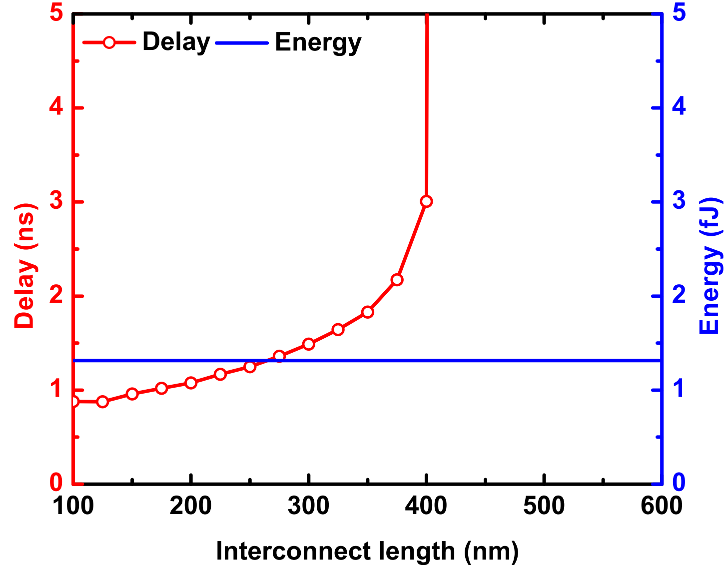

Figure 47: The delay and energy versus the interconnect length. The current source for ASL is 0.5 mA [25]. For the ferromagnetic interconnect, the saturation magnetization is 1×10^6 A/m and damping coefficient is 0.01. The infinite delay represents no DW reaching the end of the interconnect.

Fig. 47 shows the energies needed for different interconnect lengths are the same. This is because the required energy for the interconnect is simply to create the DW, instead of driving the DW. Due to shape anisotropy, the DW is able to move automatically along the interconnect without consuming any energy. Note that the delay does not linearly increase with the interconnect length since due to the damping process, the DW velocity becomes slower as the DW travels through the wire. Therefore, if the interconnect is too long for a DW to reach the end, the delay becomes infinite.

The current source in ASL plays an important role in determining the interconnect performance. Fig. 48(a) shows with different magnitudes of the current supply, the delay changes in an oscillating behavior. This can be explained by the fact that the initial phase of the DW depends on the injected spin current in a similar fashion, which is also observed in 3-D micromagnetic simulations [167]. Since the DW velocity has the sinusoidal dependence on the phase, a faster velocity is not necessarily obtained

from a stronger current. Therefore, even though the time for DW creation increases as the current magnitude is reduced, there is no guarantee for obtaining a shorter delay using a stronger current. Furthermore, in Fig. 48(a), we can see that when the current is low enough, the delay becomes infinite since within the current pulse, the spin torque from ASL is not strong enough to create the DW that moves properly. Thus, there exists a minimum energy for operating the interconnect. However, in Fig. 48(b), in the case of longer interconnects, the delay also becomes infinite as the current increases. This is because the initial DW phase created by ASL fails to provide enough velocity that drives the DW to the end of the interconnect. In such a case, the DW stops in the middle of the interconnect and the delay becomes infinite. As a result, choosing a proper biasing current working for different interconnect lengths is critically important for interconnects using automotion of DWs.

To mitigate the DW-stopping issue in longer interconnects, as shown in Fig. 49(a), a FM material with a lower Gilbert damping coefficient [73, 3] is suggested since in such a case, the DW can preserve its velocity longer and travel over a reasonable distance for the use of interconnects. On the other hand, in Fig. 49(b), the energy of the interconnect can be further reduced by using a material with a lower saturation magnetization since the DW can be created with the lower current. However, the delay does not necessarily increase with saturation magnetization since both DW creation time and initial DW velocity depend on the magnitude of STT. Furthermore, saturation magnetization also affects how DW velocity changes in the channel. Therefore, instead of saturation magnetization, reducing damping mechanisms in the interconnect will be a more efficient way to improve the displacement. Moreover, the energy performance can be further improved by using a metallic channel in ASL with a longer spin relaxation length, e.g., a channel with smaller grain boundary reflectivity and larger surface specularity, since the minimum charge current in ASL required to create a DW can be reduced.

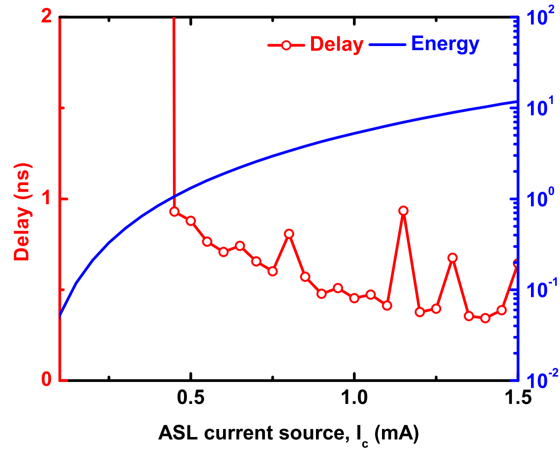

(a)

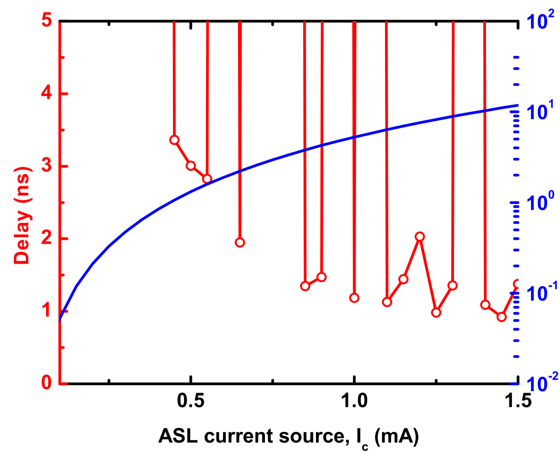

(b)

Figure 48: The delay and energy versus the magnitude of the ASL current supply for (a) 100 nm and (b) 400 nm interconnects [25]. The parameters for the interconnects are the same as those shown in Fig. 47.

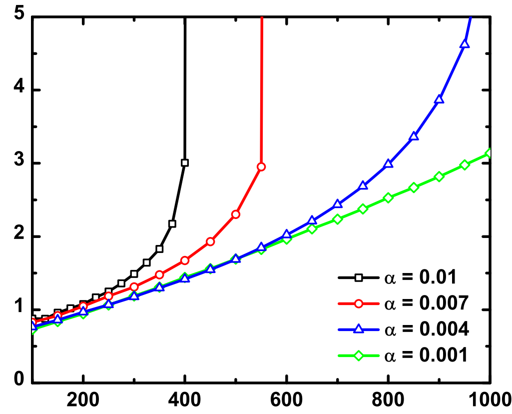

(a)

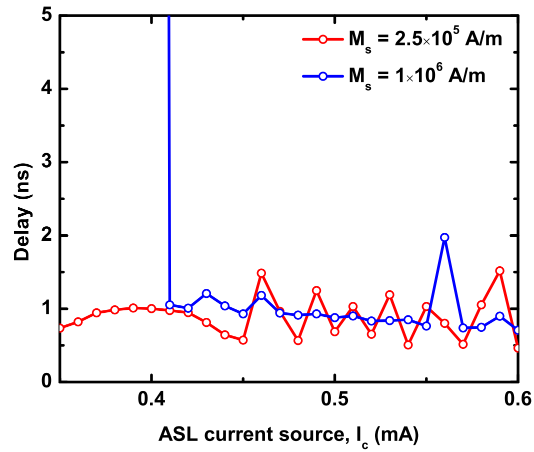

(b)

Figure 49: The effects of (a) Gilbert damping coefficient (I_c = 0.5 mA) and (b) saturation magnetization on the delay (the interconnect length is 100 nm) [25].

5.4.3 Thermal Fluctuations

At room temperature, thermal fluctuations on magnetization dynamics inside the interconnect is inevitable; therefore, it is of interest to study how DW automotion is influenced by the thermal noise. Fig. 50(a) shows that the DW automotion is strongly dependent on the thermal noise. This is mainly because the fluctuating DW phase due to the noise changes the velocity as the DW travels through the interconnect; thus, the trajactory of the DW displacement in time can largely deviate from that without the noise. This large deviation can impair the reliability of the interconnect significantly since the DW can reach the end of the wire with quite different delays. The similar constraint can be also be observed in interconnects based on STT switching [29, 28], where the delay distribution becomes wider as the interconnect length increases or the applied voltage is reduced. As a result, to reduce the noise effect on DW automotion, an interconnect with low Gilbert damping is recommended since the magnitude of the thermal field can be reduced, and the deviation from the noiseless situation is largely suppressed using a low damping channel as shown in Fig. 50(b).

5.4.4 Summary

In this chapter, interconnects for ASL using automotion of DWs are proposed to make ASL circuits more energy-efficient, and are analyzed using a hybrid physical solver including ASL equivalent circuits, 1-D LLG equation, and equations of motion for DW transport. Through the model, the reflection of the DW is eliminated by adding a layer with a high damping coefficient at the end of the FM interconnect. The energy and delay are also studied. It is found that the delay of the interconnect using DW automotion can be independent of the length; furthermore, the interconnect performance can be improved by reducing both saturation magnetization and damping coefficient along the channel, and the reliability can be also enhanced by a low damping channel.

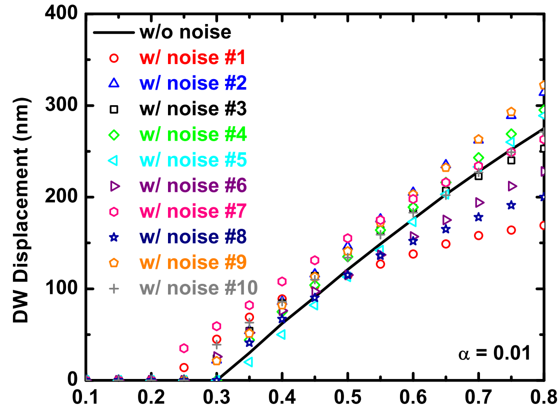

(a)

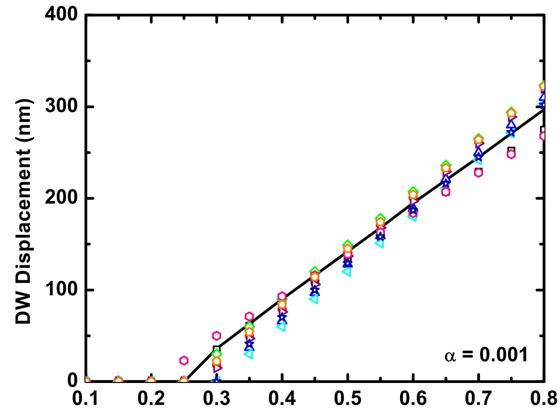

(b)

Figure 50: The thermal noise effects ($T = 300$ K) on the domain wall displacement using automotion with different damping coefficients (a) $\alpha = 0.01$ and (b) $\alpha = 0.001$ [25]. The interconnect length is 400 nm with saturation magnetization being equal to 1×10^6 A/m ($I_c = 1$ mA).

CHAPTER VI

LOW-POWER SPIN VALVE/DOMAIN WALL LOGIC

6.1 Overview

By combining all the advantages of the structures discussed from Chapter III to V, in this chapter, a novel scheme for non-volatile digital computation is proposed using STTs and automotion of magnetic DWs [30]. The basic computing element is composed of a lateral SV with two FM wires served as interconnects, where DW automotion is used to propagate the information from one device to another. The non-reciprocity of both device and interconnect is realized by sizing different contact areas at the input and the output as well as enhancing the local damping mechanism. The proposed logic is suitable for scaling due to a high energy barrier provided by a long FM wire. Compared to the scheme based on non-local spin valves (NLSVs) in Chapter V, the devices can be operated at lower current density due to utilizing all injected spins for local magnetization reversals, and thus improve both energy efficiency and resistance to electromigration. This device concept is justified by simulating a buffer, an inverter, and a 3-input majority gate with comprehensive numerical simulations, including spin transport through the FM metal/NM metal interfaces as well as the NM channel and stochastic magnetization dynamics inside FM wires. In addition to digital computing, the proposed framework can also be used as a transducer between DWs and spin currents for higher wiring flexibility in the interconnect network.

6.2 Spin Valve/Domain Wall Logic

Spintronics, a field of switching magnetization using variety of sources [87], has recently been one of the most promising candidates in the beyond CMOS computing

[165], as power dissipation due to leakage currents in present-day integrated circuits increases with device density, doubling approximately every two years according to the Moore's law [156]. The major advantage of encoding digital information into magnetic states is their non-volatility, which eliminates the delay and energy required to save and fetch the data when a microprocessor is put in a *sleep* state, with power off. It thus loosens the power constraints in a microprocessor. In most of the proposed spin-based logic devices [165], the bit is represented by the magnetization of a single-domain ferromagnet, and the communication between bits is realized using either spin currents [8, 247], the dipolar coupling [47, 41], or spin wave propagation between magnetoelectric cells [113, 52]. However, no matter how well the data is preserved while bits are transmitted, the data retention time is degraded as the device size is scaled due to the lowering of the energy barrier of the magnet [210]. Hence, it is of interest to seek an alternative magnetic structure in digital computing, where bits can be retained longer in the path of scaling.

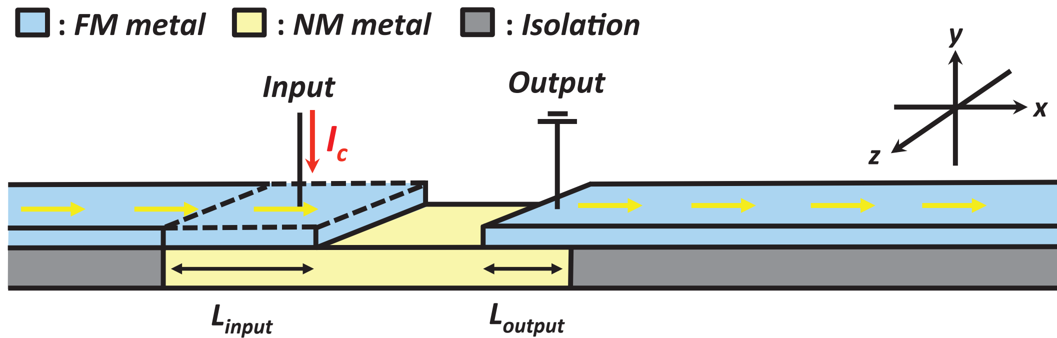

Figure 51: Schematic of the proposed computing element, comprising a lateral metallic SV and two FM interconnects, where DW automotion is used to update the magnetization of the wire. The damping mechanism in the region bounded by dashed lines is stronger than that in the rest to enhance the logic non-reciprocity, which is also optimized by sizing the input and output contact areas (or varying L_{input} and L_{output}). The blue, gray, and yellow colors designate FM, insulating, and NM materials, respectively. The yellow arrow represents the magnetization orientation in the wire. The magnetizations pointing to $+x$ and $-x$ are defined as 1 and 0, respectively.

Using FM nanowires to store bits in digital logic can provide better non-volatility

than using a single-domain magnet due to a higher energy barrier of the wire. Some spin-based devices have been proposed to realize computation by controlling the location of the magnetic DW in the FM wire using in-plane spin currents [42, 17]. However, those devices need highly resistive MTJs to convert the magnetic signal to the electrical one. The latter is used to drive magnetization switching in the next stage for a more complex logic function. On the other hand, the general concept of using FM wires as interconnects has been proposed, in which the shape-anisotropy-driven DW motion, also known as DW automotion [34], is used to update the bit inside the wire [167]. Recently, devices in the form of NLSVs connected by FM wires based on automotion of DW has been proposed due to full metallic structures and the possibility of energy-free propagation of DW once it is created [25]. In contrast, in NLSVs, only a part of injected spins contribute a STT to DW creation in the interconnect, and the STT becomes much weaker as the shunt path in the device is reduced [26]. As a result, a lateral simple SV with a tunneling barrier is suggested to eliminate the shunt path and simultaneously maintain the non-reciprocity [28, 29]. While the device is able to fully use injected spins for information processing, it still has some drawbacks due to the fact that a tunneling barrier, that is required to maintain the non-reciprocity [45] or overcome conductivity mismatch [180], is highly resistive. As a result, in this chapter, to further reduce the device resistance while all the injected spins are used to manipulate the magnetization, a metallic SV with FM interconnects based on DW automotion is proposed as a basic element for digital computing (Fig. 51). Unlike typical applications such as magnetic field sensors and random access memories (RAM), where the asymmetry of SVs is achieved by either making one magnet thicker than another or having the exchange bias provided by an antiferromagnet on one of the magnets, here the logic non-reciprocity is realized by sizing different contact areas of the input and the output as well as locally enhancing the damping process underneath the input contact.

Figure 51 shows the device structure, comprising a simple metallic SV with two FM wires as interconnects. A voltage is applied across the metallic channel. Since the resistance of the FM wire is much higher than that of the NM channel thanks to its small thickness, almost all of the current flows into the NM channel rather than the FM wire. When a negative voltage is applied at the input, electrons with spin polarization collinear to the magnetization underneath the input contact are injected into the NM channel. Because of strong screening effects inside the normal metal, injected spins travel through the channel mainly by diffusion [226]. As spin-polarized electrons reach the end of the metallic channel, a STT is exerted onto the FM region under the output contact. As long as the magnitude of STT is well above the threshold for local magnetization reversal and within a certain range, a DW with a $+x$ velocity can be created in the beginning of the wire [167]. The DW would propagate toward the end of the FM wire due to intrinsic shape anisotropy [34]. Therefore, the bit is written from the input to the output and passed to the next stage through the interconnect. Furthermore, at the output, while a DW is generated by the input, electrons with spin polarization anti-parallel to the magnetization underneath the output contact are accumulated at the interface and diffuse back to the input. Thus, there is also a STT exerted on the FM region at the input. To reduce STT effects on the input for non-reciprocity, the damping mechanism at the input is set to be stronger than the rest of the interconnect, making the input's response to STT weaker. Note that local highly-damped regions may be realized by intentionally increasing the impurity concentration (e.g. Nd) at the end of the FM wire [138]. Making the input highly damped can also ensure that the DW can disappear at the end of the wire and thus no data reflection occurs in the interconnect [25]. In addition to the local enhancement of damping coefficient, the non-reciprocity can also be further improved by varying charge current density at both input and output, which strongly influence the magnitude of STT in the device (see Appendix B for analytical derivations). On

the other hand, if the voltage polarity is reversed, the STT experienced by the output is due to back-diffusive spin-polarized electrons from the input interface. Since spin polarization of these electrons is anti-parallel to the input magnetization, the bit is inverted as it is written into the output.

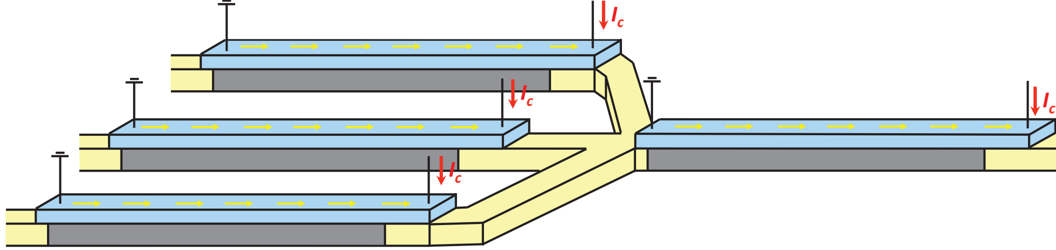

Figure 52: The schematic of a three-inputs majority gate under the proposed scheme. An AND or an OR gate can be realized by setting one of the inputs as a control terminal.

To sum up, the device is switched to lower-energy parallel and anti-parallel configurations as negative and positive voltages are applied, respectively. This feature is of interest in digital computing since the bit can be encoded into the magnetization, and non-inverting logic or inverting logic can be realized using the same structure by simply changing the supply voltage polarity. The device operation can be understood by making an analogy to a simple SV with one layer fixed and another layer free. Here a "quasi-fixed" layer is achieved by both reducing the STT applied at the input and the input's response to STT. In addition, a 3-input majority gate is also of interest since majority logic is more efficient for implementing combinatorial logic (fewer gates required). An AND or an OR gate can be realized by setting one of the inputs as a control terminal [163]. Figure 52 shows a 3-input majority gate implementation using the proposed scheme. Similar to Ref. [163], the magnetization underneath the output contact is controlled by the net spin polarization of current flowing into the output, which is mainly determined by the majority of the inputs. Note that for a 3-input majority gate, if magnetizations of the inputs are not identical (e.g. two inputs are in the $+x$ direction and one input is in the $-x$ direction), the net STT

at the output is not simply the sum over all the contributions from the inputs. In fact, the net spin torque is weakened under non-identical inputs because there are some currents directly flowing from one input to another due to different resistances of the signal paths (e.g. parallel and anti-parallel configurations result in low and high resistances, respectively).

6.3 Mathematical Models

To model the proposed scheme as shown in Fig. 51, spin circuit theory is used to describe spin transport through NM and FM metals as well as their interfaces [13, 141, 24]. Note that in this chapter, at the NM/FM interface, the perpendicular spin component is simply dependent on spin accumulation at the NM side [125, 24], instead of that across FM/NM interface assumed in Ref. [141]. For FM nanowires, the magnetization dynamics is captured by the stochastic LLG equation. Similar to Ref. [25] (or Chapter V), a self-consistent numerical iteration between spin circuits and the LLG equation is required to describe the time evolution of the system. In this section, the theoretical approach to model the proposed scheme is presented in detail.

An equivalent circuit of a single device is given in Fig. 53, where $[G_{NM,se}]$ and $[G_{NM,sh}]$ are the series and shunt conductances of the NM material, respectively, $[G_{FM,se}]$ and $[G_{FM,sh}]$ are the series and shunt conductances of the FM material, respectively, $[G_{int,se}]$ and $[G_{int,sh}]$ are series and shunt conductances at the FM/NM interfaces, respectively, L_p, L_c, and t_{FM} are the contact length, channel length, and thickness of FM wires, respectively, and $\vec{m_1}$ as well as $\vec{m_2}$ are the magentizations at the input and output, respectively. Note that all the conductances in Fig. 53 are 4×4 matrices, and $[G_{int,se}]$, $[G_{int,sh}]$, $[G_{FM,se}]$, as well as $[G_{FM,sh}]$ vary with the local magnetization and thus are space-dependent. The number of FM and interface sub-circuits at both input and output is determined by the size of the contacts (i.e. L_{input}

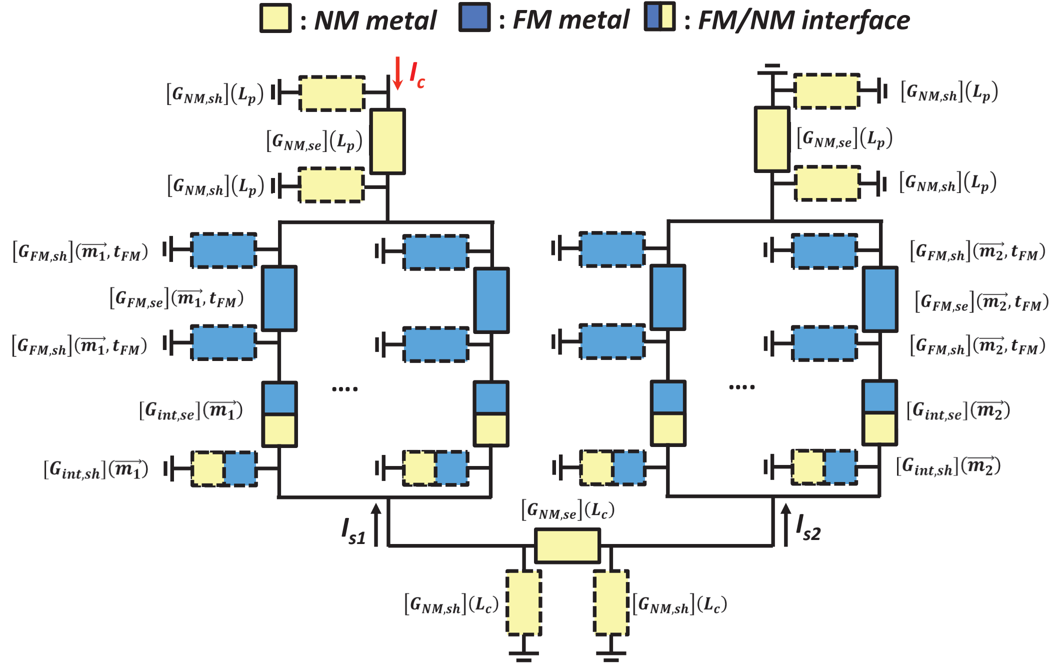

Figure 53: An equivalent spin circuit of a single device shown in Fig. 51. Blue, yellow, and mixed blue/yellow bars stand for FM materials, NM materials, and FM/NM interfaces, respectively. Black and red arrows stand for spin currents flowing into the FM materials and charge current sources, respectively. Dashed and solid bars represent shunt and series conductances, respectively.

and L_{output} in Fig. 51). The detailed mathematical expressions of these conductance matrices can be found in Refs. [141, 24]. In this chapter, the interface shunt conductance is only required at the side where a STT is present [24], rather than both sides assumed in Refs. [23, 203]. This is because from both experimental and theoretical studies, the transverse spin component can only penetrate some typical FM metals (e.g. Fe, Co, and Py) less than 1nm [248, 205, 225]. However, in some weak FM metals such as CuNi, the transverse spin component may appear at both sides of the FM thin film, and thus a more sophisticated expression for the interface transport is required [124]. The overall conductance matrix for a single device, $[G]_{4N\times 4N}$, can be obtained using a nodal analysis similar to Ref. [25], where a set of equations are established by the fact that the net current at each node is zero and satisfies the following equation:

$$[I]_{4N\times 1} = [G]_{4N\times 4N} \, [V]_{4N\times 1} \,, \tag{70}$$

where $[I]_{4N\times 1}$ and $[V]_{4N\times 1}$ are current and voltage column vectors describing charge and spin components for all the nodes in the circuit, N is the total number of nodes in the circuit, and the index 4 includes one charge component and three spin elements in the x, y, and z directions. By multiplying the inverse matrix of $[G]_{4N\times 4N}$ at both sides of Eq. 5, the charge and spin voltages at each node can be obtained. And the nodal current vector, $[I_{ij}]$, including both charge and spin components flowing from the i to the j node, is given as

$$[I_{ij}]_{4\times 1} = [G_{ij}]_{4\times 4} \left([V_i]_{4\times 1} - [V_j]_{4\times 1}\right) , \tag{71}$$

where $[G_{ij}]_{4\times 4}$ is the conductance with $[I_{ij}]_{4\times 1}$ flowing through, and $[V]_{4\times 1}$ is the nodal voltage vector having both charge and spin components. Thus, spin currents flowing into the input and the output of a single device can be calculated by solving the nodal equations of the equivalent circuit shown in Fig. 53. To evaluate the magnetic responses of the wires, spin currents flowing into the FM wires at both input and

output, calculated from the spin circuit, become the inputs to the stochastic LLG equation given in Eq. 10. Note that here I_s is the average spin current flowing into the FM wires, and $\vec{H_{eff}}$ is the effective magnetic field including material anisotropy, $\vec{H_m}$, shape anisotropy, $\vec{H_s}$, exchange interaction, and thermal random noise, $\vec{H_{th}}$, and given as follows:

$$\vec{H_{eff}} = \vec{H_m} + \vec{H_s} + \frac{2A}{\mu_0 M_s}\frac{\partial^2 \vec{m}}{\partial x^2} + \vec{H_{th}}, \tag{72}$$

where all the internal fields are defined the same as those in Ref. [25], and A is the exchange constant. Note that since the width and the thickness of FM wires are quite small, magentizations in both y and z directions are assumed to be uniform and thus the exchange field is only dependent on the x direction. From Refs. [167, 25], it has been shown that this assumption describes DW automotion well in terms of some important quantities of interconnect such as DW velocity and driving currents for DW creation compared to full micromagnetic simulations. Once the magnetization of the wire is updated after solving the LLG equation, the FM and FM/NM interface conductance matrices will also be changed accordingly due to their dependence on the local magnetizations. Hence, the new spin circuit has to be solved iteratively to obtain the updated spin currents flowing into the wire, and a self-consistent numerical solution between the spin circuit and the LLG equation establishes a complete dynamics of a single device. Similarly, a 3-input majority gate can be simulated using the equivalent circuit shown in Appendix B with the LLG equations for FM wires.

6.4 Results and Discussion

In this section, the proposed concept is justified using the numerical scheme mentioned in the preceding section by investigating the logic non-reciprocity, and a buffer, an inverter, as well as a 3-input majority gate are simulated. To explore the potential of the proposed device, its performance is also compared with NLSV and CMOS counterparts. In the following simulations, the in-plane magnetized wire is used due

to a faster DW velocity compared to the out-of-plane one [167]. The wire length is chosen as 300nm for typical local interconnects [165], and the mesh size is 2nm. The magnetic wires are modeled with the material parameters of permalloy, in which material anisotropy is weak and thus the energy barrier is mainly determined by shape anisotropy. Furthermore, Cu is used as the non-magnetic material and the length is chosen as 70nm, which can be further reduced to improve the energy efficiency as long as the dipole coupling between the input and the output FM wires is weak enough [26]. Note that Cu transport parameters such as resistivity and spin relaxation length are obtained through the compact model developed in Ref. [176] by assuming that the specularity (p) and reflectivity (R) of the wire are 1 and 0.1, respectively. If not stated otherwise, for simplicity, the applied current pulse is set to be 1.5ns to drive a single device. However, thanks to DW automotion, the current can be turned off to save energy immediately after a DW is created in the beginning of the wire. Simulations parameters not mentioned above are summarized in Table. 8.

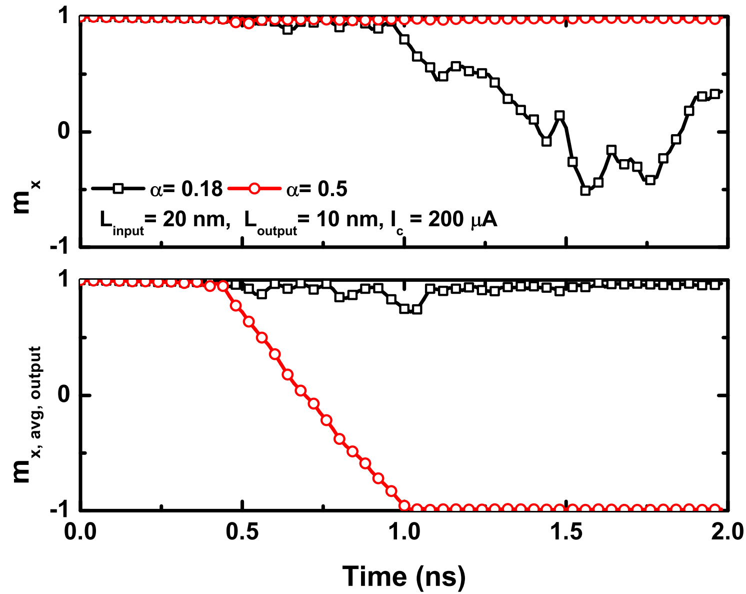

Figure 54: Time evolution of average magnetizations of FM wires for the input (top) and the output (bottom) in an SV inverter with different damping coefficients at the end of the wire.

Table 8: Simulation parameters in this section. ρ and β are the resistivity and spin polarization of conductivity for permalloy, respectively. $l_{sf,\parallel}$ and $l_{sf,\perp}$ are longitudinal and transverse spin relaxation lengths of permalloy, respectively. l_{FM}, w_{FM}, and t_{FM} are the length, width, and thickness of FM wires, respectively. l_{NM}, w_{NM}, and t_{NM} are the length, width, and thickness of the NM channel, respectively. $G_{\uparrow\uparrow}$, $G_{\downarrow\downarrow}$, and $G_{\uparrow\downarrow}$ are majority, minority, and mixing interface conductances, respectively.

Symbol	Value	Unit
ρ	1.4×10^{-7} [146]	Ω·m
β	0.6 [13]	-
$l_{sf,\parallel}$, $l_{sf,\perp}$	5 [7], 0.8 [225]	nm
M_s	8×10^5 [51]	A·m^{-1}
A	1.3×10^{-11} [51]	joule·m^{-1}
α	0.007 [133]	-
l_{FM}, w_{FM}, t_{FM}	300, 20, 2	nm
l_{NM}, w_{NM}, t_{NM}	70, 20, 20	nm
$G_{\uparrow\uparrow}$, $G_{\downarrow\downarrow}$, $G_{\uparrow\downarrow}$	0.9, 0.1, 0.39 [13]	$10^{15}\Omega^{-1}$·m^{-2}

6.4.1 Logic Non-reciprocity

To maintain the device non-reciprocity, it is of importance to ensure that only the input can affect the output, not the other way around. Hence, in our proposed scheme based on SVs, the non-reciprocity is created as the magnetic response to STT of the input is much weaker than that of the output, which is realized by increasing the damping process at the end of the interconnect. Figure 54 shows the effect of damping coefficient at the end of the FM wire on the non-reciprocity as both input and output experience a strong STT. In Fig. 54, it can be seen that in the case of the damping coefficient being 0.18, the magnetization at the input is quite sensitive to the STT, and thus an inverter cannot be operated normally under positive bias current. However, as damping coefficient is increased to 0.5, the input's magnetization is almost unperturbed even under a strong STT, and in such a case, the output magnetization can be switched as expected. Note that the reversal of the average

magnetization in an FM wire implies the fact that a DW is created by a STT in the beginning of the wire, travels automatically using intrinsic shape anisotropy through the channel, and disappears at the end of the wire through the damping process. Although a large damping coefficient is desirable in the proposed scheme, so far the highest one demonstrated experimentally is only about 0.18 by intentionally doping Pd into Py [138]. Therefore, another efficient way to improve the non-reciprocity is to reduce the STT exerted on the input by sizing the contact areas of both input and output.

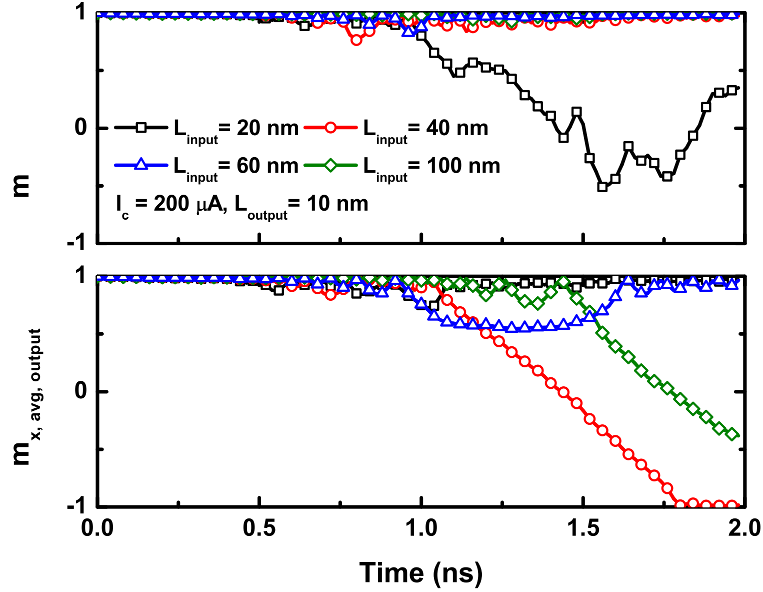

Figure 55: Time evolution of average magnetizations of FM wires for the input (top) and the output (bottom) in an SV inverter with different input contact lengths. The damping coefficient at the end of FM interconnect is set to be 0.18 for Figs. 55 to 63.

In Fig. 55, as the input contact length is increased from 20nm (black) to 40nm (red), the input's magnetization becomes less disturbed due to a weaker STT resulting from smaller current density flowing through the input. However, since the magnetization at the input is still affected by the STT due to the output, one can observe that input's and output's magnetizations still interact strongly with each other before the DW at the output is created. The input can become less sensitive to STTs

by further increasing the input contact length to 60nm (blue). In such a case, the coupling between the input and the output is significantly reduced, and a DW can be created faster. Note that there is no guarantee that a DW can definitely reach the end after creation, since a DW with $-x$ velocity may be created and then disappears in the beginning of the wire (e.g. blue in Fig. 55). If 100nm is used as the input contact length (olive), the input's magnetization is almost insensitive to the STT, similar to setting the damping coefficient as 0.5 as shown in Fig. 54. However, the time required to create a DW will become longer because the STT at the output is weakened as the charge current density at the input becomes smaller.

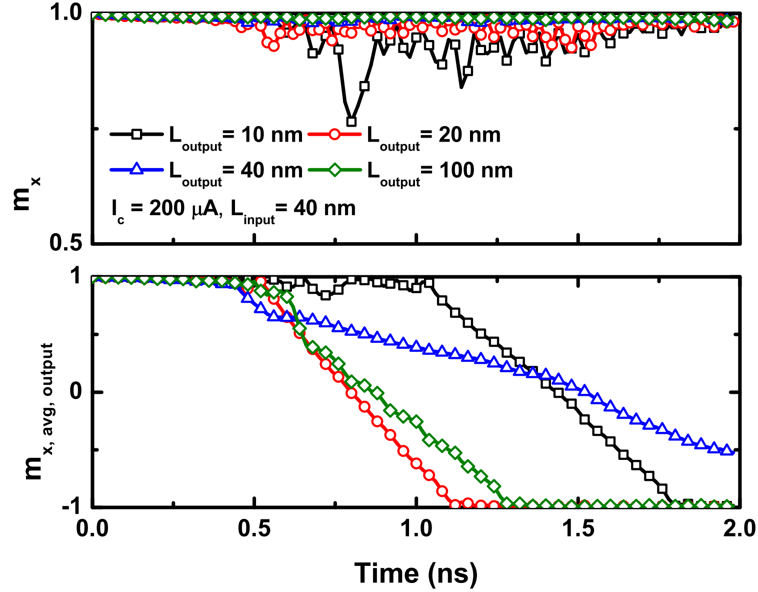

Figure 56: Time evolution of average magnetizations of FM wires for the input (top) and the output (bottom) in an SV inverter with different output contact lengths.

Since in SVs, the input and the output are closely coupled through STTs, the sensitivity of the input to the STT can also be reduced by increasing the output contact length. In Fig. 56, it is shown that by increasing the output contact length from 10nm (black) to 20nm (red), the time that a DW is created becomes faster. This is because the STT at the input is also reduced by lower current density at the

output. The output switching becomes more efficient as the input is less sensitive to STTs even though the output current density is reduced. As the length increases to 40nm (blue), the input's magnetization is almost unaffected by the output and thus an improvement in the speed of DW creation is also observed. However, as discussed in Ref. [25], a DW that is created faster may not reach the end of the wire earlier because of its slow DW velocity (e.g. blue in Fig. 56). The speed of DW creation is not further improved as the output contact length is increased to 100nm because the input's magnetization is already stable enough for efficient switching at smaller output contact lengths.

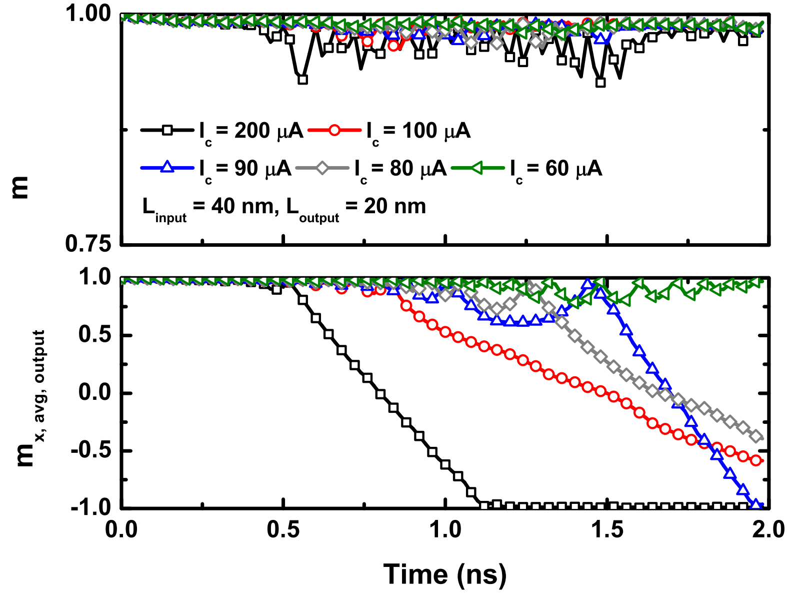

Figure 57: Time evolution of average magnetizations of FM wires for the input (top) and the output (bottom) in an SV inverter under different magnitudes of driving current.

In addition to the damping process and contact area, the device non-reciprocity can also be improved by smaller driving currents as shown in Fig. 57, where the input's magnetization becomes less disturbed as the applied current is reduced. However, the speed of DW creation becomes slower at smaller driving current since the current densities at both input and output are reduced. Note that a DW cannot be

created because of an insufficient STT if the driving current is too small (e.g. olive in Fig. 57).

6.4.2 Buffer, Inverter, 3-input Majority Gate, and DW/Spin current Transducer

As explained in Section 6.2, the proposed device prefers parallel and anti-parallel configurations under negative and positive driving currents, respectively, and a buffer as well as an inverter can be implemented based on that. Figs. 58 and 59 show that by properly sizing contact areas and using reasonable damping coefficient at the end ($\alpha = 0.18$) for the non-reciprocity, the device can act as an inverter (a buffer) as positive (negative) current is applied. Note that DW creation from the anti-parallel state is faster than that from the parallel one, which is consistent with a substantial asymmetry between the differential torque near parallel and anti-parallel alignment, predicted by all semiclassical calculations of transport and STTs in metallic multilayers [13, 206]. Fig. 60 also demonstrates that a 3-input majority gate can be operated normally under the proposed scheme. Note that the switching responses are different for the input patterns being 000 and 100 since the net STT at the output are different; thus, clocking a circuit with majority gates may be non-trivial.

In addition to logic gates, the proposed scheme can also be used as a transducer between the DW and spin current. As a result, a hybrid interconnect system combing the advantages of DW automotion and spin diffusion can be constructed to propagate spin information. For instance, the interconnect using automotion is energy-free, but it is difficult to bend a DW interconnect to have a 90° turn due to pinning sites at the corners. However, spin-diffusive interconnects can still work well at abrupt turning angles. Therefore, the wiring in spin circuits can become more flexible when this hybrid scheme is applied.

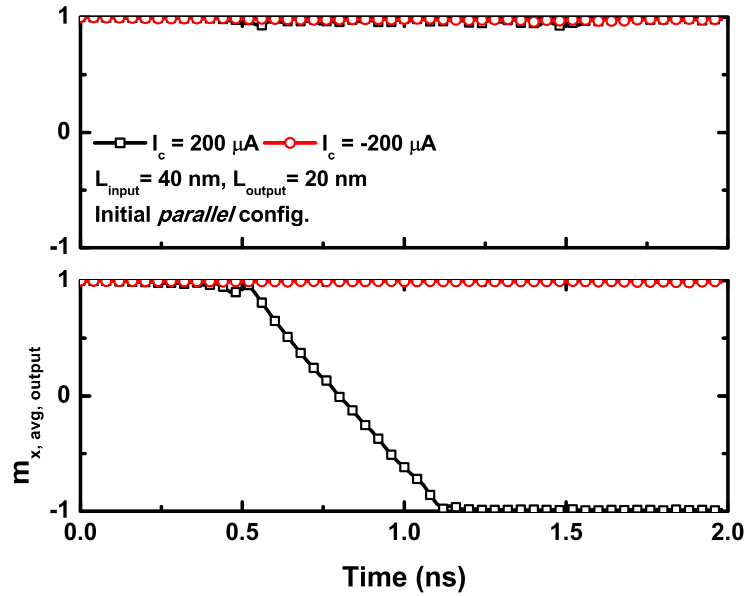

Figure 58: Time evolution of average magnetizations of FM wires for the input (top) and the output (bottom) in an SV device with initial parallel alignment under positive and negative driving currents.

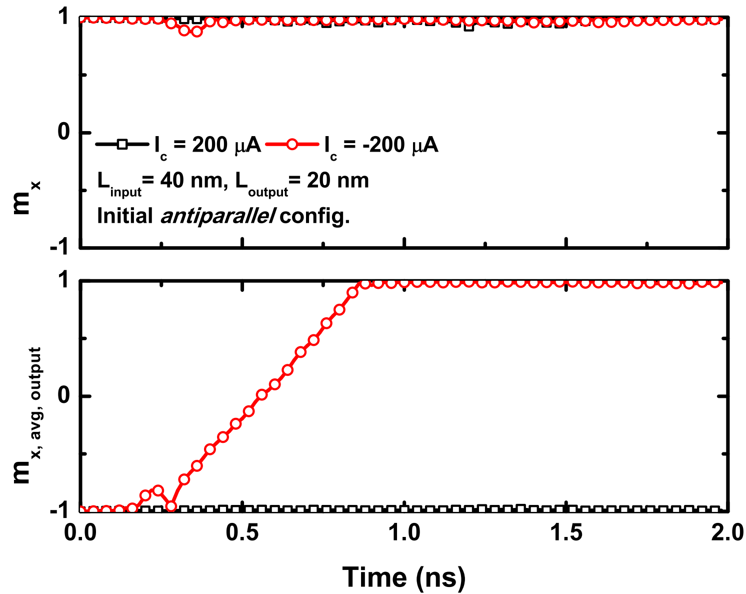

Figure 59: Time evolution of average magnetizations of FM wires for the input (top) and the output (bottom) in an SV device with initial anti-parallel alignment under positive and negative driving currents.

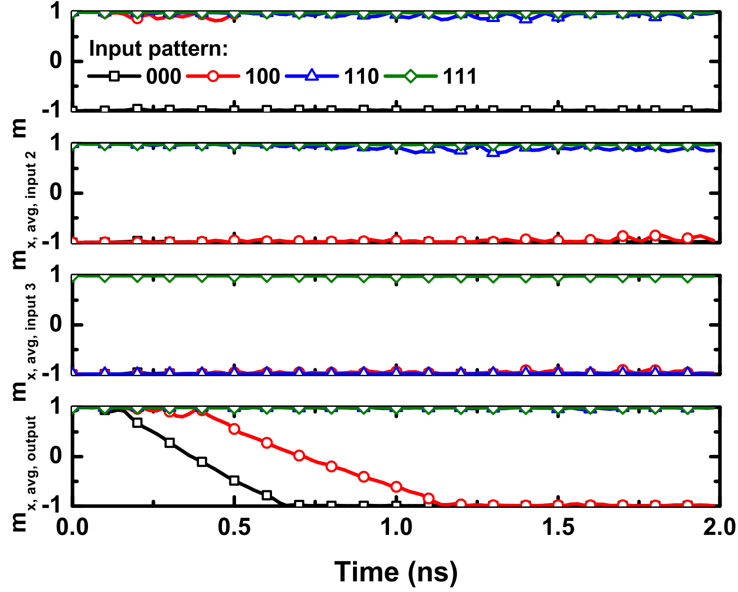

Figure 60: Time evolution of average magnetizations of FM wires in a 3-input majority gate based on SVs for the three inputs and the output (bottom). -100μA is applied at each input. The input and output contact lengths are 40 and 20nm, respectively.

6.4.3 Comparison to NLSVs and CMOS Circuits

To explore the real potential of the proposed scheme, it is required to compare the scheme based on NLSVs, which can also provide a complete set of Boolean functions [25]. However, to have a fair comparison between two schemes, here a performance optimization of NLSVs by engineering the contact areas is briefly discussed. The equivalent spin circuit for a single NLSV device can be found in Appendix B. Fig. 61 shows that as the output contact length increases, a DW is created slower with fixed injected spins at the input. This is because in NLSVs, the STT at the output only depends on injected spins at the input; therefore, a larger FM region needs longer time to be switched under the same amount of STT. If the input contact length is increased, meaning that both input current density and injected spins are reduced, the STT at the output is weakened and may not be strong enough to create a DW as shown in Fig. 62. As a result, based on Figs. 61 and 62, smaller input and output

contact lengths are desired in NLSVs to provide a strong STT exerted on the output. With the optimized contact size, Fig. 63 investigates the minimum driving current in NLSVs, and it is found that the minimum driving current in both schemes are similar (see Fig. 57); however, the current density in SVs is much smaller than that in NLSVs. This is mainly because in NLSVs, a significant part of injected spins are directly flowing into the ground, rather than contributing a STT at the output. In SVs, all the spins participate the switching process. Note that the non-reciprocity in NLSVs is realized by the asymmetry of the non-local structure, and sizing different input and output contact areas is only for performance optimization, which is very different from SVs.

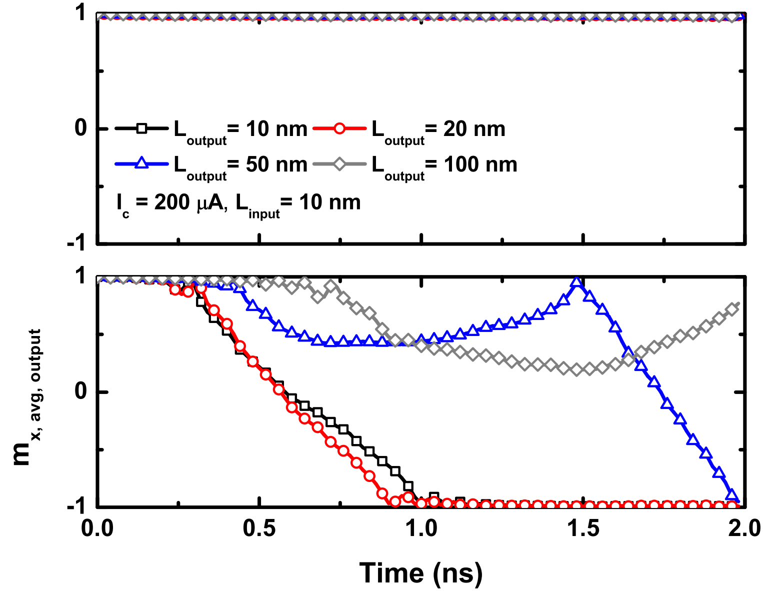

Figure 61: Time evolution of average magnetizations of FM wires for the input (top) and the output (bottom) in a NLSV inverter with different output contact lengths.

It is well known that the energy dissipation of current-driven STT logic devices is mainly due to the wiring network linked to the global power supply rather than the device itself [165]. Here 300Ω is assumed as the wiring resistance from the device to the global power supply for the contact length equal to 10nm, and the switching energy is

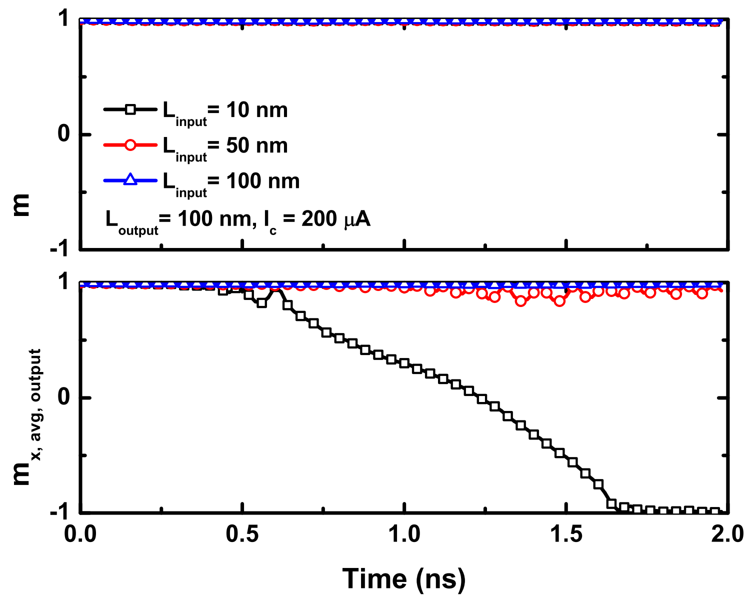

Figure 62: Time evolution of average magnetizations of FM wires for the input (top) and the output (bottom) in a NLSV inverter with different input contact lengths.

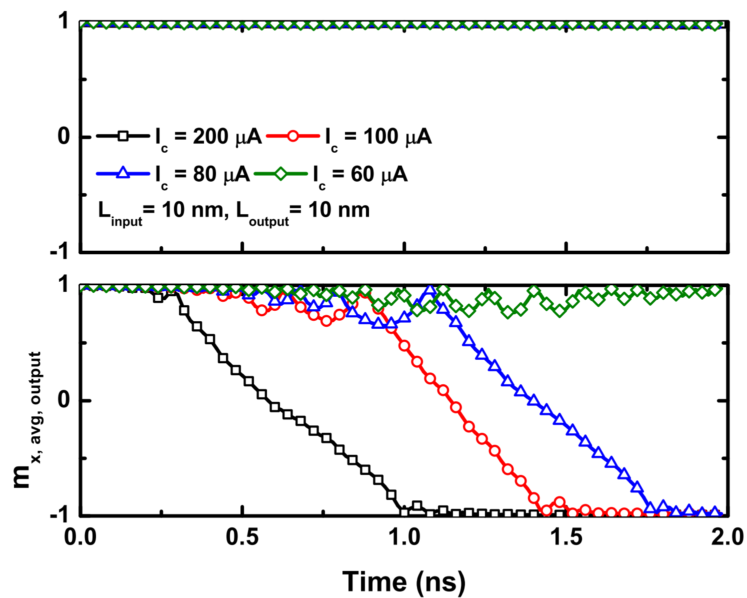

Figure 63: Time evolution of average magnetizations of FM wires for the input (top) and the output (bottom) in a NLSV inverter under different magnitudes of driving current.

calculated using $E = I^2 R\tau$, where E is the switching energy, I is the driving current, R is the wiring resistance, and τ is the current pulse duration. Using $I = 200\mu$A as an example, the corresponding energy for a single switching in a NLSV device is 18fJ (black in Fig. 63). Similarly, with the same driving current, an SV device only dissipates 6.7fJ due to lower resistance of the wiring network (black in Fig. 57), and thus provides a new low-power option for the STT-driven logic family. Since the proposed scheme can be operated at lower current density, electromigration induced by large current density in Cu-based NLSVs [209] can be significantly mitigated. Table. 9 summarizes the comparison between schemes based on SVs and NLSVs.

Table 9: A performance comparison between schemes based on SVs and NLSVs. 200μA is applied to both structures to simulate inverters, and the shunt path in the NLSV is 30nm. The delay (τ) is defined as the total time required for DW creation in the beginning of the FM wire and DW automotion to the end of the FM wire. E is the switching energy.

(L_{input}, L_{output})	I_c	E	τ
SV (40nm, 20nm)	200μA	6.7fJ	1.12ns
NLSV (10nm, 10nm)	200μA	18fJ	1ns

In addition to the non-volatility and the eliminating of static power in circuits, another major advantage of the proposed scheme is a straightforward implementation of a majority gate as shown in Fig. 52, which enables a significant reduction in the required circuit layout area. Table. 10 shows a performance comparison for a 3-input majority gate based on the proposed devices (Fig. 60) and low-power CMOS transistors [165]. From Table. 10, it is shown that even though the switching energy (or dynamic power) using the proposed scheme is still much higher than that using the CMOS counterpart due to a slow magnetic response of the FM metal to STTs, the circuit area under the proposed scheme is significantly reduced.

Table 10: A performance comparison for a majority gate using the proposed devices (Fig. 60) and the low-power (LP) CMOS switches (F=15nm, 2018 technology node in the 2013 edition of ITRS [165]). E, τ, and $Area$ are the switching energy, critical delay, and required circuit area, respectively. The spacing between FM interconnects is assumed to be 20nm. A 3-input majority gate function is given as $O = AB + BC + CA$, where A, B, C are the inputs and O is the output. In the CMOS implementation, a 3-input majority gate is composed of three 2-input NAND and one 3-input NAND gates, which require at least 18 CMOS digital switches with routing interconnects in different metal layers to minimize the area.

	E	τ	$Area$
This work	20.1fJ	1.14ns	0.01μm^2
LP CMOS [165]	0.069fJ	0.042ns	0.166μm^2

6.5 Summary

This chapter presents a novel scheme using SVs and FM wires to perform digital computation, and justifies the proposed concept through comprehensive simulations including spin transport in metallic multilayers and stochastic magnetization dynamics. The proposed scheme offers a new option to implement low-power logic using the current-driven STT due to removing the shunt path in NLSVs, and is more suitable in the path of scaling because of using FM wires to store bits, rather than single-domain FM metals. Furthermore, the proposed concept can also be viewed as a transducer between spin current and magnetic DW, which may significantly increase the flexibility in the wiring network of spin interconnects.

CHAPTER VII

ELECTRORESISTANCE IN FERROELECTRIC TUNNEL JUNCTIONS

7.1 Overview

In addition to the electron spin, in this chapter, our emphasis is switched to an emerging memory device based on switching electric polarization of an FE thin film, also known as an FTJ. As a result, this chapter presents a theoretical approach, comprising the NEGF method for electronic transport and Landau-Khalatnikov (LK) equation for electric polarization dynamics, to describe polarization-dependent TER in FTJs [31]. By using appropriate contact, interface, and FE parameters, the measured current-voltage characteristic curves in both inorganic (Co/$BaTiO_3$/$La_{0.67}Sr_{0.33}MnO_3$) and organic (Au/PVDF/W) FE tunnel junctions are well described by the proposed approach. Furthermore, under this theoretical framework, the controversy of opposite TER signs observed experimentally by different groups in Co/$BaTiO_3$/$La_{0.67}Sr_{0.33}MnO_3$ systems is addressed by considering the interface termination effects using the effective contact ratio, defined through the effective screening length and dielectric response at the metal/FE interfaces. Finally, our approach is extended to investigate the role of a CoO_x buffer layer at the Co/$BaTiO_3$ interface in an FE tunnel memristor. It is shown that, to have a significant memristor behavior, not only the interface oxygen vacancies but also the CoO_x layer thickness may vary with the applied bias.

7.2 Ferroelectric Tunnel Junctions

As the CMOS technology is down-scaled to the nanometer regime, the static power consumption plays a non-trivial role in total power dissipation due to a significant

amount of leakage currents in memory and logic devices [117]. As a consequence, recently, active research has also been underway in pursuit of low-power and non-volatile memory and logic circuits in the beyond-CMOS technologies [165], and the major advantages of the non-volatility in the microprocessor potentially are (i) the system speed improvement by eliminating the need of transferring data between volatile power-starving memories (i.e. static and dynamic random-access memories) and external non-volatile storage (i.e. hard disk drive) as well as (ii) the energy efficiency enhancement by removing the static power consumption.

Among many emerging non-volatile memory technologies, FE devices based on quantum-mechanical tunneling, also known as FTJs, have attracted significant attention due to the extremely high ON/OFF ratio, very low write power, and non-destructive read [92]. The concept of an FTJ has been demonstrated experimentally [75, 183, 32, 67, 218] thanks to improved technologies in fabricating high quality ultra-thin FE films by pulsed laser deposition or off-axis sputtering, which push the critical thickness of ferroelectricity down to a few unit cells [159, 118, 208, 62, 188]. Moreover, over the past decade, FE fabrication technologies have become mature and compatible to the back-end CMOS process [219], and therefore FTJ-CMOS circuits with additional microchip functionality may become a reality in the near future.

In an FTJ, the switching of resistance, also known as TER effect, is achieved by the polarization reversal in the FE barrier via applied voltage. The TER effect is fundamentally different from other resistive switching mechanisms such as the formation of conductive filaments within a metal-oxide insulator in an atomic switch [5], the oxygen-vacancy-assisted conduction in a resistive RAM [2], and the magnetization-dependent tunneling in an MTJ [215]. In particular, unlike TMR in the MTJ, which is typically only a few hundred percent [242, 173, 91], TER in an FTJ can easily reach 10^5% [67], offering a much more reliable *read* mechanism for the stored memory bits. While significant TER is achieved in FTJs, there still exists a controversy

in TER signs, particularly for $Co/BaTiO_3/La_{0.67}Sr_{0.33}MnO_3$ (Co/BTO/LSMO) systems [115, 32]; that is, TER signs observed experimentally from different groups are completely opposite. Note that the term "TER sign" is introduced here to specify the relation between the electric polarization direction and the resistance state. The TER sign is defined as "+" (positive) and "−" (negative) when the low (ON) resistance state is produced by the polarization pointing to the top and the bottom electrodes, respectively. Recent experimental work shows that these opposite TER signs can be attributed to the dead layers induced by either TiO_2 or BaO termination at the Co/BTO interface [236].

In addition to the promising progress in the FTJ experiments, lots of theoretical efforts have also been made in predicting or understanding TER in an FTJ. Inspired by the polar switch concept proposed by Leo Esaki in 1971 [55], the giant TER was predicted near the zero bias based on electron direct tunneling [224, 245]. Using a similar model, enhanced TER by inserting a non-polar dielectric layer at the metal/FE interface was also predicted near the equilibrium [246]. Furthermore, going beyond the equilibrium, polarization-dependent TER was predicted to be based either solely on direct tunneling [122] or on combination of several transport mechanisms including direct tunneling, Fowler-Nordheim tunneling, and thermionic emission [171]. Nevertheless, works on polarization-dependent TER were mainly based on the analytical models derived from the Wenzel-Kramer-Brillouin (WKB) approximation and did not include a realistic FE hysteresis loop. More importantly, most of the theoretical approaches describe the experimental data in the low-voltage range; so far, none of them has provided quantitative comparisons with current-voltage (I-V) characteristics measured from a full FE hysteresis sweep, which is extremely important in designing FTJs as memory elements, where both *read* and *write* operations need to be well-described. This chapter presents a comprehensive approach to (i) describe

the experimentally measured I-V relations for various types of FTJs, and (ii) to explain the discrepancy in the TER signs observed experimentally by different groups in the Co/BTO/LSMO layered structures. The developed approach includes the NEGF method for electronic transport under different bias conditions [46] and the thermodynamics-based LK equation for a complete ferroelectric hysteresis loop.

An FTJ structure is shown in Fig. 64(a), where the device is composed of an FE thin film sandwiched between two metal electrodes. In this chapter, TER is assumed to be induced by band structure modifications through the electrostatic effect due to polarization reversal (Fig. 66). Moreover, to explore the role of a CoO_x buffer layer in the Co/BTO/LSMO systems, reported to be an inevitable by-product while depositing the metallic electrode [115], an FTJ structure with a non-polar DE layer at the metal/FE interface is also considered as shown in Fig. 64(b).

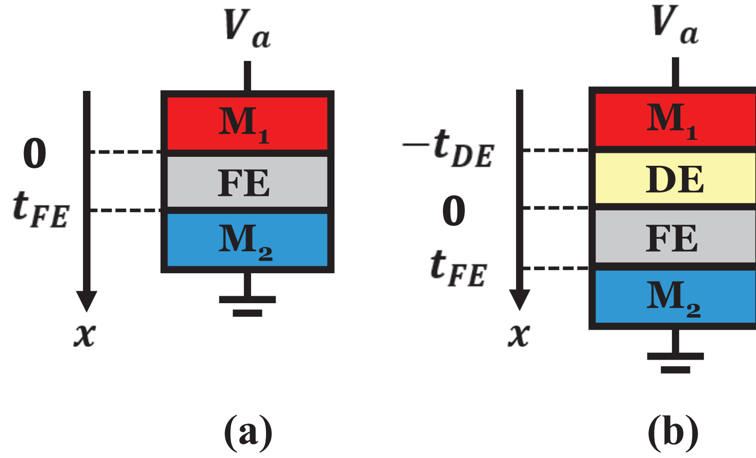

Figure 64: Schematics of FTJs in the (a) absence and (b) presence of a non-polar DE layer between the FE and metal electrode. M_1 and M_2 are top and bottom metal electrodes, respectively.

7.3 Mathematical Models

In this section, the mathematical details of the proposed approach for TER in an FTJ is presented.

7.3.1 FTJ without Non-polar Dielectric

To describe the polarization-dependent TER in an FTJ, the energy band diagram under the effects of the applied electric field, built-in field, and depolarization field is considered. In this chapter, the applied electric field is generated by a bias voltage across an FTJ, the built-in field is mainly due to the work function difference between layered materials [68, 211, 137], and the depolarization field is induced by the incomplete screening of the FE bound charge. Figs. 65(a), (b), and (c) illustrate electrostatic potential profiles induced by the applied electric field, built-in field, and depolarization field for FTJs in the presence and absence of a non-polar DE layer, respectively. Mathematically, for an FTJ without a non-polar DE layer, it is assumed that the potential profiles within metals (V_{M1} and V_{M2}) follow the Thomas-Fermi expression [174] and are given as (see Appendix C for detailed derivations)

$$V_{M1}(x) = \frac{-\rho_s \lambda_1}{\epsilon_1 \epsilon_0} e^{\frac{x}{\lambda_1}}, \tag{73}$$

$$V_{M2}(x) = \frac{\rho_s \lambda_2}{\epsilon_2 \epsilon_0} e^{\frac{-(x-t_{FE})}{\lambda_2}}, \tag{74}$$

where ρ_s is the screening charge density at the FE/metal interfaces (C/m^2), λ_1 and λ_2 are effecitve screening lengths of top and bottom FE/metal interfaces, respectively, ϵ_1 and ϵ_2 are relative dielectric constants of top and bottom FE/metal interfaces, respectively, and ϵ_0 is the vacuum dielectric constant. Note that the imperfect screening here is described by both effective screening length and dielectric constant, rather than Thomas-Fermi one, since it is generally accepted that the imperfect screening is determined not only by the metal, but also by the FE thin film and the specific interface geometry [105]. As a result, from Eqs. 73 and 74, the potential drop in top and bottom electrodes are $\frac{\rho_s \lambda_1}{\epsilon_1 \epsilon_0}$ and $\frac{\rho_s \lambda_2}{\epsilon_2 \epsilon_0}$, respectively. By assuming that the electric displacement is continuous throughout the FTJ, the following equation is held.

$$\rho_s = \epsilon_0 E_{FE} + P, \tag{75}$$

where P is the electric polarization of the FE and E_{FE} is the total electric field across the FE. Furthermore, due to the fact that the potential drop induced by the applied bias and built-in field has to be completely shared by both metal electrodes and the FE, the following equation is satisfied.

$$\frac{\rho_s \lambda_1}{\epsilon_1 \epsilon_0} + \frac{\rho_s \lambda_2}{\epsilon_2 \epsilon_0} + E_{FE} t_{FE} = V_a + V_{bi}, \tag{76}$$

where V_a is the applied voltage and V_{bi} is the voltage drop due to the built-in field, defined as $\frac{\phi_2 - \phi_1}{e}$ with ϕ_1 and ϕ_2 being conduction band discontinuities at the top and bottom FE/metal interfaces, respectively, and e being the elementary charge. From Eqs. 75 and 76, the total electric field across the FE is given as

$$E_{FE} = \frac{V_a + V_{bi} - P\left(\frac{\lambda_1}{\epsilon_1 \epsilon_0} + \frac{\lambda_2}{\epsilon_2 \epsilon_0}\right)}{t_{FE} + \frac{\lambda_1}{\epsilon_1} + \frac{\lambda_2}{\epsilon_2}}. \tag{77}$$

Note that the depolarization field, E_{dep}, is obtained by canceling the built-in field with the applied bias ($V_a + V_{bi} = 0$) and given as

$$E_{dep} = \frac{-P\left(\frac{\lambda_1}{\epsilon_1 \epsilon_0} + \frac{\lambda_2}{\epsilon_2 \epsilon_0}\right)}{t_{FE} + \frac{\lambda_1}{\epsilon_1} + \frac{\lambda_2}{\epsilon_2}}. \tag{78}$$

By replacing E_{FE} in Eq. 75 with Eq. 78, the screening charge density induced simply by the FE bound charge, $\rho_{s,p}$, is given as

$$\rho_{s,p} = \frac{P}{1 + \frac{\lambda_1}{t_{FE}\epsilon_1} + \frac{\lambda_2}{t_{FE}\epsilon_2}}, \tag{79}$$

which is consistent with the common expression shown in Ref. [245].

The energy band diagram is constructed by assuming that the bulk properties of metal electrodes remain the same under the applied bias; that is, the Fermi energy of the metal is fixed. Illustrated in Fig. 66(a) by setting the conduction band edge in the top metal contact as the zero energy reference, chemical potentials at top and bottom contacts (μ_1 and μ_2, respectively) have to satisfy the following equation:

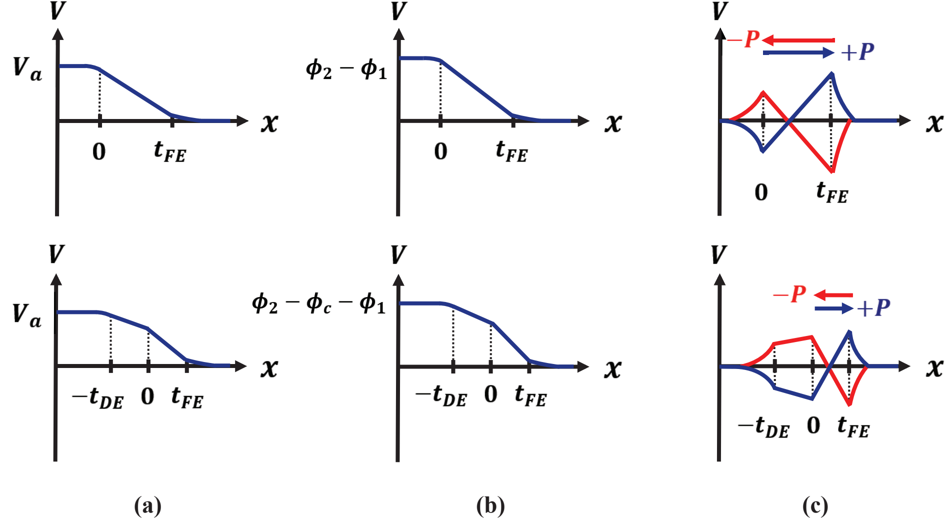

Figure 65: Schematics of electrostatic potential profiles due to (a) applied electric field, (b) built-in field, and (c) depolarization field for FTJs with (bottom panel) and without (top panel) a non-polar DE layer between the FE and top metal electrode.

$$\begin{aligned} eV_a &= \mu_2 - \mu_1 \\ &= \left(\frac{\rho_s \lambda_1}{\epsilon_1 \epsilon_0} + \phi_1 + E_{FE} t_{FE} - \phi_2 + \frac{\rho_s \lambda_2}{\epsilon_2 \epsilon_0} + E_{F2} \right) - E_{F1}, \end{aligned} \tag{80}$$

where E_{F1} and E_{F2} are Fermi energies of top and bottom metal electrodes, respectively.

7.3.2 FTJ with Non-polar Dielectric

As a non-polar DE layer is presented between the top electrode and the FE as shown in Fig. 64(b), similar procedures to Section 7.2.1 can be followed to obtain the electric fields and potential profiles in an FTJ. Again by assuming that the electric displacement is continuous at interfaces, and the net voltage drop has to be entirely

shared within the device, the following equations are satisfied.

$$\rho_s = \epsilon_0 E_{FE} + P = \epsilon_0 \epsilon_{DE} E_{DE}, \tag{81}$$

$$V_a + V_{bi} = \frac{\rho_s \lambda_1}{\epsilon_1 \epsilon_0} + \frac{\rho_s \lambda_2}{\epsilon_2 \epsilon_0} + E_{FE} t_{FE} + E_{DE} t_{DE}, \tag{82}$$

where E_{DE} is the electric field across the DE, and ϵ_{DE} is the dielectric constant of the non-polar layer. By solving Eqs. 81 and 82, the interface screening charge density and electric fields across the FE and the non-polar DE are given as

$$\rho_s = \frac{\frac{\epsilon_0}{t_{FE}}(V_a + V_{bi}) + P}{1 + \frac{t_{DE}}{\epsilon_{DE} t_{FE}} + \frac{\lambda_1}{\epsilon_1 t_{FE}} + \frac{\lambda_2}{\epsilon_2 t_{FE}}}, \tag{83}$$

$$E_{FE} = \frac{\rho_s - P}{\epsilon_0}, \tag{84}$$

$$E_{DE} = \frac{\rho_s}{\epsilon_{DE} \epsilon_0}, \tag{85}$$

where V_{bi} now is defined as $\frac{(\phi_2 + \phi_c - \phi_1)}{e}$ with ϕ_c being the band discontinuity at the FE/non-polar DE interface. Note that the screening charge density induced solely by the FE bound charge can be obtained by removing both V_a and V_{bi} in Eq. 83, and the resulting expression is consistent with that in Ref. [246]. After knowing the incomplete screening charge at the interface, the corresponding depolarization field can be calculated using Eq. 84 and is given as

$$E_{dep} = \frac{-P\left(\frac{t_{DE}}{\epsilon_{DE}} + \frac{\lambda_1}{\epsilon_1} + \frac{\lambda_2}{\epsilon_2}\right)}{\epsilon_0\left(t_{FE} + \frac{t_{DE}}{\epsilon_{DE}} + \frac{\lambda_1}{\epsilon_1} + \frac{\lambda_2}{\epsilon_2}\right)}. \tag{86}$$

As expected, Eq. 86 is reduced to Eq. 78 when t_{DE} is reduced to zero. Similarly, by using the same energy reference in the previous case, the FTJ energy band diagram with a non-polar DE layer, as shown in Fig. 66(b), is established by satisfying the following equation:

$$\begin{aligned} eV_a &= \mu_2 - \mu_1 \\ &= \left(\frac{\rho_s \lambda_1}{\epsilon_1 \epsilon_0} + \phi_1 + E_{DE} t_{DE} - \phi_c + E_{FE} t_{FE} \right. \\ &\quad \left. -\phi_2 + \frac{\rho_s \lambda_2}{\epsilon_2 \epsilon_0} + E_{F2}\right) - E_{F1}. \end{aligned} \tag{87}$$

7.3.3 FE Hysteresis Loop

To describe the electric polarization response of a FE thin film under applied bias, built-in field, and depolarization field, the LK equation is used and given as [214]

$$\gamma \frac{\partial P}{\partial t} = -\frac{\partial F}{\partial P}, \tag{88}$$

where γ is the viscosity coefficient and F is the FE free energy including the bulk and interactions with different types of electric fields, which can be in general expanded in terms of the thermodynamic order parameter based on the Landau theory and is written as

$$\begin{aligned} F &= \alpha_1 P^2 + \alpha_{11} P^4 + \alpha_{111} P^6 - \frac{1}{2} E_{dep} P \\ &- \left(E_{FE} - E_{dep}\right) P \end{aligned} \tag{89}$$

with α_1, α_{11}, and α_{111} being free energy expansion coefficients [229, 174, 27, 137]. The contribution from both built-in and applied electric fields is included in the last term in Eq. 89.

While Ref. [229] pointed out that Eq. 88 is particularly for the intrinsic single-domain FE switching, which typically requires a defect-free FE thin film with a very small cross-sectional area and is quite different from the extrinsic switching driven by FE domain nucleation and propagation, here for simplicity, we assume that the electric polarization in a FE thin film can be represented by an effective electric polarization, P, satisfying the LK equation, and the experimental FE hysteresis loops, characterized by the remanent polarization and coercive voltage, can be well described by adjusting expansion and viscosity coefficients. Furthermore, by using Eq. 88, the shift in a FE hysteresis loop due to a non-zero built-in field across a FTJ can also be easily captured [137]. Note that typically the electric displacement through the FE, D, is written as [152]

$$D = \epsilon_0 \left(1 + \chi\right) E_{FE} + P_d, \tag{90}$$

where χ accounts for the linear contribution of the polarization and P_d is the polarization due to switching dipoles. However, in the LK equation mentioned above, P accounts for the effects from both linear response and switching dipoles, and thus the electric displacement is simply written as $\epsilon_0 E_{FE} + P$.

7.3.4 Tunneling Currents

As shown in Fig. 66, based on Eqs. 80 and 87, the energy band diagram can be constructed for a given electric polarization obtained from the LK equation and is used as the electron potential energy in the NEGF method to calculate the transmission coefficient [46]. For the tunneling currents, the Landau formula is applied and given as [128]

$$J = -\sum_{k_y,k_z} \frac{2e}{Ah} \int dEt(E) \left\{ f_1(E) - f_2(E) \right\}, \tag{91}$$

where k_y and k_z are electron wave vectors in the transverse plane, e is the elementary charge, A is the cross-sectional area, E is the total electron energy, t is the transmission coefficient, and f_1 and f_2 are Fermi-Dirac distributions for top and bottom metal contacts, respectively, given as

$$f_{1(2)}(E) = \frac{1}{1 + e^{\frac{E-\mu_{1(2)}}{k_B T}}}, \tag{92}$$

where μ_1 and μ_2 are chemical potentials of top and bottom metal contacts with $\mu_2 - \mu_1 = eV_a$, k_B is the Boltzmann constant, and T is the temperature. The details of writing an alternative expression for currents using the electron wave vector in the spherical coordinate are shown in Appendix C. The transmission coefficient in Eq. 91 is calculated using the Green's function, $\mathbf{G}$, given as

$$t = trace\left(\mathbf{\Gamma^t G \Gamma^b G^\dagger}\right), \tag{93}$$

where $\mathbf{G}$ is defined as $(\mathbf{EI} - \mathbf{H} - \mathbf{\Sigma_t} - \mathbf{\Sigma_b})^{-1}$ with $\mathbf{I}$, $\mathbf{H}$, and $\mathbf{\Sigma}$ being the identity matrix, device Hamiltonian, and contact self-energy, respectively, and $\mathbf{\Gamma}$ is the broadening function defined as $i\left(\mathbf{\Sigma} - \mathbf{\Sigma}^\dagger\right)$. The detailed expression of the Hamiltonian and

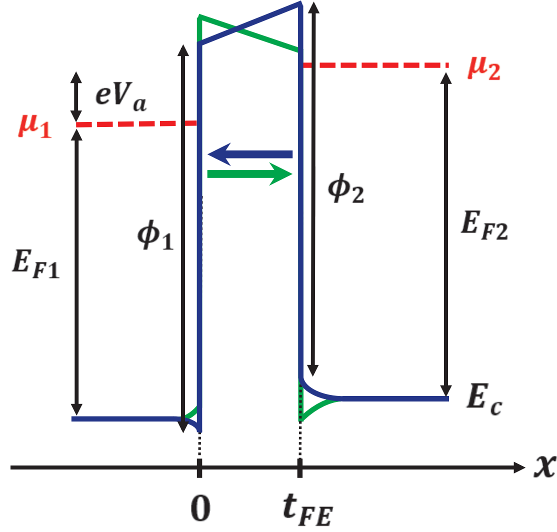

(a)

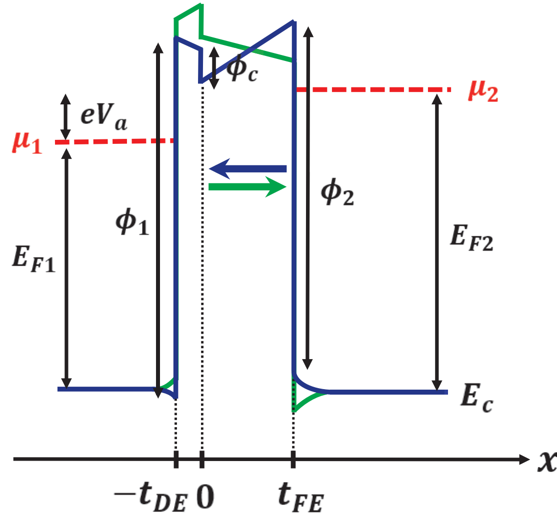

(b)

Figure 66: Schematics of energy band diagrams at a bias voltage V_a, satisfying $\mu_2 - \mu_1 = eV_a$, for FTJs (a) without and (b) with a non-polar DE layer between the FE and metal electrode. Arrows in the FE represent the direction of the electric polarization.

contact self-energy can be found in the Appendix C.

7.4 Results and Discussion

In this section, the theoretical framework presented above is used to explain existing experimental results [32, 115, 218]. First, to show the model captures key underlying physics behind FTJs, measured *I-V* characteristics for both inorganic and organic FTJs are fitted by using proper energy band diagram and LK parameters. Next, the concept of effective screening length and dielectric constant is applied to explain the opposite high/low resistance states observed in Co/BTO/LSMO systems [32, 115], which may result from interface termination effects [236]. Finally, the model is extended by including a CoO_x non-polar buffer layer at the Co/BTO interface, and it is shown that the voltage-dependent oxygen vacancies at the CoO_x/BTO interface may be partially responsible for the memristor behavior as mentioned in Ref. [115].

7.4.1 Comparison with Experimental *I-V* Characteristics

In this chapter, for an FTJ, it is assumed that TER is a main consequence of modifying the energy band diagram through depolarization fields induced by incomplete screening charge at FE/metal interfaces, and is expected to vary with the polarization. In other words, at a given voltage, a larger difference in two opposite polarization states leads to more pronounced TER. Hence, to describe measured FTJ *I-V* characteristics, it is required to accurately model FE hysteresis loops, which are also presented in the following comparisons with experiments. Note that, for simplicity, all the FE hysteresis loops in this work are simulated by applying a sinusoidal voltage signal with a period of 70 ps, and LK parameters are adjusted accordingly to obtain a reasonable FE response observed in experiments. In reality, FE thin films may have different dynamic responses with respect to an applied bias, depending on the quality, material, or size of the sample.

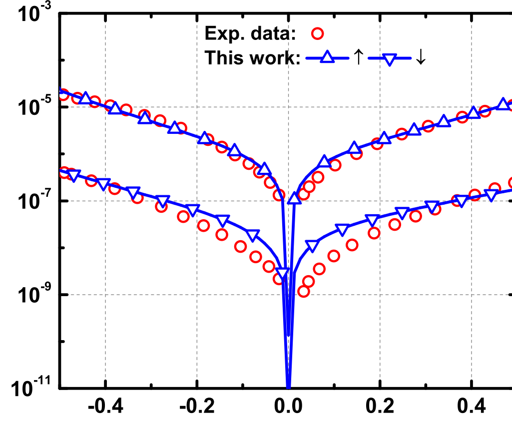

(a)

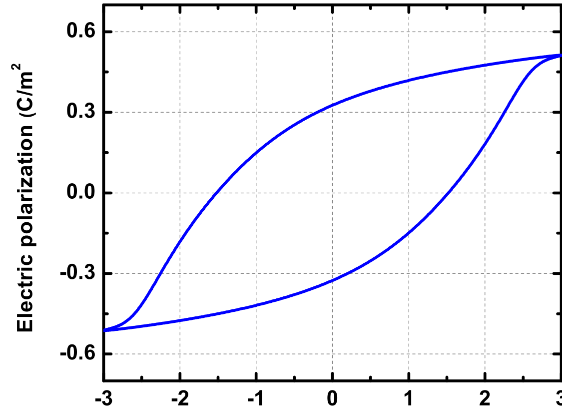

(b)

Figure 67: (a) Comparison between FTJ (Co/BTO/LSMO) experimental data [32] and simulation results using the following band diagram parameters: $t_{FE} = 2$ nm, $\phi_1 = \phi_2 = 7.15$ eV, $E_{F1} = E_{F2} = 6.5$ eV, $\epsilon_1 = 2.5$, $\epsilon_2 = 9.8$, $\lambda_1 = 0.5 \times 10^{-10}$ m [233], $\lambda_2 = 1 \times 10^{-10}$ m [233], $m^* = 0.8m_0$. (b) Simulated FE hysteresis loop for FTJ (Co/BTO/LSMO) experiments [32] ($V_c \sim \pm 3$ V, $\epsilon_{FE} \sim 15$, and $P_r \sim 0.3$ C/m^2) with the following LK parameters: $\gamma = 10^{-2}$ m sec/F, $\alpha_1 = -2.77 \times 10^7$ m/F, $\alpha_{11} = -5.35 \times 10^8$ m^5/C^{2}F, and $\alpha_{111} = 6.4 \times 10^9$ m^9/C^{4}F.

First, the measured FTJ I-V characteristics in a Co/BTO/LSMO layered structure [32] are used to justify our theoretical approach. Since there is no clear shift in hysteresis loops observed in experiments, it is assumed that a built-in field across

the junction is close to zero, which implies ϕ_1 is equal to ϕ_2 in our model. Next, LK parameters for BTO [174] are slightly varied so that the FE thin film exhibits a hysteresis loop with $V_c \sim \pm 3$ V, $\epsilon_{FE} \sim 15$, and $P_r \sim 0.3$ C/m^2 as shown in Fig. 67(b), where V_c, ϵ_{FE}, and P_r are the coercive voltage, the FE dielectric constant, and the remanent polarization, respectively. By assuming the following interface parameters: $\lambda_1 = 0.5 \times 10^{-10}$ m [233], and $\lambda_2 = 1 \times 10^{-10}$ m [233], ϕ_1, ϕ_2, ϵ_1, ϵ_2, and m^* are varied to obtain a good agreement with experimental data as shown in Fig. 67(a), which shows that in Co/BTO/LSMO systems, a depolarization field modifying the energy band diagram is the dominant driving force for TER, rather than the effects due to strain [122] or a FE polarization dependent complex band structure [228]. However, even though the experimental data can be well described by depolarization fields in Fig. 67, changes in FTJ energy band diagrams through polarization reversals is not a pure charge-mediated (or electrostatic) effect. This is mainly because the effective screening length and the dielectric response significantly depend on the specific interface geometry, which is a fully quantum-mechanical outcome and requires approaches in the microscopic level such as first-principles calculations [204].

In Fig. 67, since only the currents at low voltages are measured, the full dependence of tunneling currents on an FE hysteresis loop cannot be observed. As a result, an I-V characteristic curve reported in an Au/poly-vinylidene fluoride (PVDF)/W layered structure is used to justify our model for a complete FE sweep [218]. Again, to fit experimental data, a FE hysteresis loop of a monolayer PVDF film is generated by tuning LK parameters as shown in Fig. 68(b), in which the resulting V_c, ϵ_{FE}, and P_r are about 1 V, 4.4, and 0.18 C/m^2, respectively. By using the following interface parameters: $\epsilon_1 = 6.5$, $\lambda_1 = 0.75 \times 10^{-10}$ m [65], and $\lambda_2 = 0.45 \times 10^{-10}$ [94], ϕ_1, ϕ_2, ϵ_2, and m^* are adjusted to match experimental data as shown in Fig. 68(a), where a good agreement between the theoretical and experimental results is reached. Note that a weak built-in field, observed in the experiment [218] and leading to a small

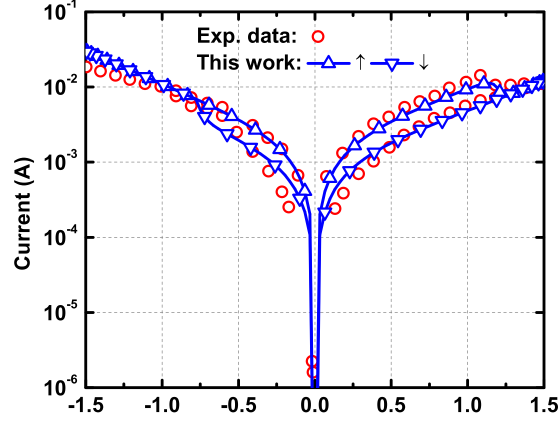

(a)

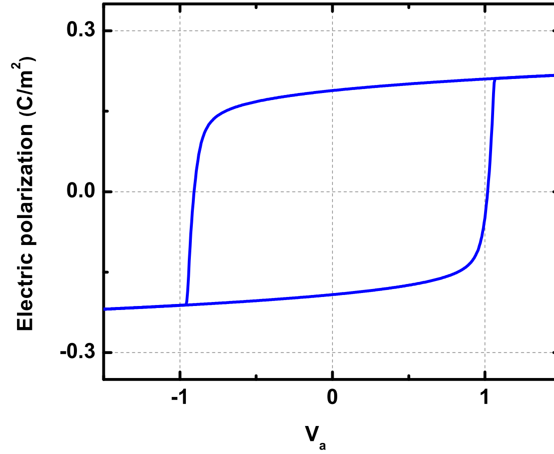

(b)

Figure 68: (a) Comparison between FTJ (Au/PVDF/W) experimental data [218] and simulation results using the following band diagram parameters: $t_{FE} = 2$ nm, $\phi_1 = 6.76$ eV, $\phi_2 = 6.7$ eV, $E_{F1} = E_{F2} = 6.5$ eV, $\epsilon_1 = 6.5$, $\epsilon_2 = 20$, $\lambda_1 = 0.75 \times 10^{-10}$ m [65], $\lambda_2 = 0.45 \times 10^{-10}$ m [94], $m^* = 0.1 m_0$. (b) Simulated FE hysteresis loop for FTJ (Au/PVDF/W) experiments [218] ($V_c \sim \pm 1$ V, $\epsilon_{FE} \sim 4.4$, and $P_r \sim 0.18$ C/m^2) with the following LK parameters: $\gamma = 1.5 \times 10^{-3}$ m sec/F, $\alpha_1 = -1.38 \times 10^9$ m/F, $\alpha_{11} = -2.67 \times 10^{10}$ m^5/C^{2}F, and $\alpha_{111} = 8 \times 10^{11}$ m^9/C^{4}F.

shift in the hysteresis loop as shown in Fig. 68(b), is included to obtain a better fit to the experimental data.

In Fig. 68(a), it can be seen that TER varies laregly with the electric polarization; that is, the difference between high and low resistance states is reduced as the voltage is close to or beyond the coercive voltage. Furthermore, since the interface parameters for Fig. 68(a) are closer to bulk values, it can also be concluded that TER in an Au/PVDF/W organic FTJ is more dominated by a pure electrostatic effect, rather than complex changes of interfacial bonds, which can be attributed to the fact that the electrodes are attached to PVDF thin films using mainly Van der Waals forces in an Au/PVDF/W structure [218].

7.4.2 Interface Termination Effects on TER

As shown in Figs. 67 and 68, in both experiments [32, 218], the low and high resistance states correspond to the electric polarizations pointing to the top (Co or Au) and the bottom (LSMO or W) electrodes, respectively. These experimental results can be explained by the energy band diagram shown Fig. 70(a), where a lower tunnel barrier is produced as the polarization is pointing to the top contact, which has larger changes in the interface potential energy. Note that as shown in Eqs. 73 and 74, a higher ratio of $\frac{\lambda}{\epsilon}$ leads to a larger change in the interface potential energy. From Fig. 70(a), it is found that since at low voltages, the energy slope on the FE barrier is mostly dominated by the depolarization field, whose direction is always opposite to that of the polarization, the top and bottom interfaces have opposite effects on the tunnel barrier. Using the polarization pointing to the top contact as an example, the top and bottom interface potential changes reduce and increase the FE barrier, respectively, and these contact effects on the barrier are reversed as the polarization is switched to the opposite direction. Consequently, if the interface energy change at the top is greater than that at the bottom, the FE barrier for the polarization pointing to the

top will be lower and thus a lower resistance state is generated. Therefore, as shown in Fig. 70(a), it seems that interface quantities play a significant role in determining the relation between the high/low resistance states and the polarization direction. Here a quantity called the effective contact ratio is defined as $\frac{\lambda_1\epsilon_2}{\lambda_2\epsilon_1}$ to distinguish the high/low resistance states in an FTJ. In Figs. 67 and 68, the effective contact ratios are 1.96 and 5.1, respectively, which are both larger than 1, implying that the resistance states are more dominated by the top interface. As a result, the lower resistance state is for the polarization pointing to the top contact (or the TER sign is "+"), consistent with experimental observations.

In Au/PVDF/W FTJs, it is believed that a depolarization field creates larger changes in the potential energy at the Au side [218], and so far, no experimental evidence has shown that high/low resistance states can be switched in the same FTJ structure, which is probably because contacts and an organic FE film are attached through Van der Waals forces, rather than complex interface bonds as mentioned previously [218]. However, in Co/BTO/LSMO layered structures, several groups have reported an opposite relation between the polarization direction and the resistance state [32, 115]. Recently, some groups have reported that the reversal of the high/low resistance states in Co/BTO/LSMO systems is attributed to either TiO_2 or BaO terminated at the Co/BTO interface [236]. To support this argument theoretically, our model provides an intuitive picture for the reversal of high/low resistance states induced by termination effects. As predicted by first-principles calculations, the screening length is almost zero at the Co/TiO_2-terminated BTO interface [204]. Therefore, in Fig. 69(b), the effective contact ratio is set to be less than 1 without adjusting $\frac{\lambda}{\epsilon}$ of the bottom interface, and it is shown that compared to Fig. 69(a), where the effective contact ratio is larger than 1, a lower tunneling barrier is generated by the polarization pointing the bottom electrode, rather than the top one, and thus the high/low resistance states are reversed.

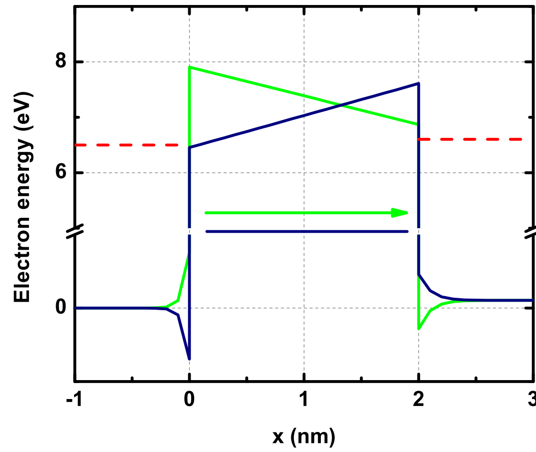

(a)

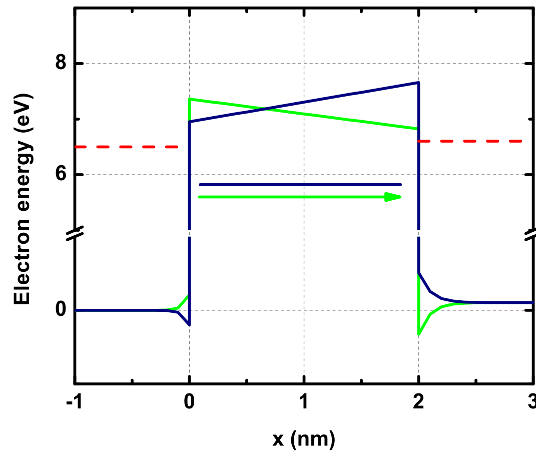

(b)

Figure 69: Energy band diagrams at 0.1 V for both polarization states with two different effective contact ratios: (a) 1.98 and (b) 0.49. The dark blue and the green correspond to the polarization states pointing to the top and bottom contacts, respectively. Red dash lines represent chemical potentials at both contacts.

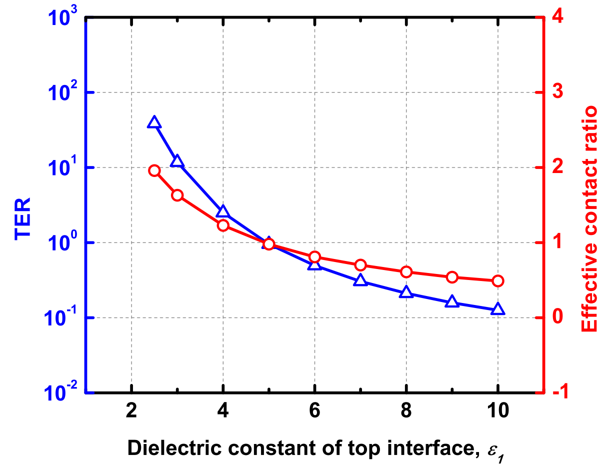

(a)

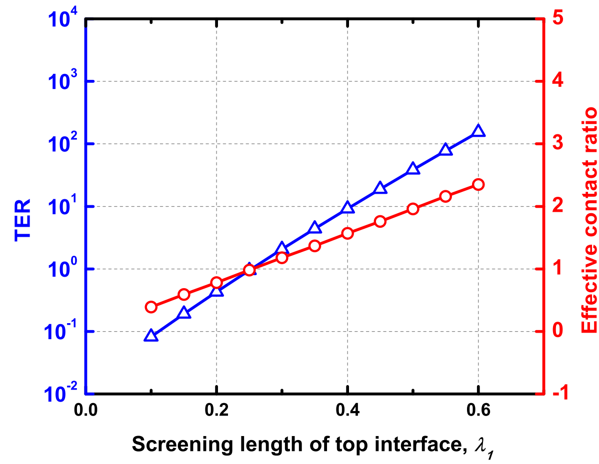

(b)

Figure 70: TER at $V_a = 0.1$ V and effective contact ratio versus top contact (a) dielectric constant and (b) screening length. TER and effective contact ratios are defined as $\frac{I_\uparrow}{I_\downarrow}$ and $\frac{\lambda_1 \epsilon_2}{\lambda_2 \epsilon_1}$, respectively.

Figs. 69(a) and (b) clearly indicate that rather than the individual interface properties, the effective contact ratio is the most essential factor to determine both sign and magnitude of TER, defined as $\frac{I_\uparrow}{I_\downarrow}$, where $I_\uparrow$ and $I_\downarrow$ are the currents corresponding to the polarizations pointing to the top and bottom electrodes, respectively. In Figs. 70(a) and (b), it is shown that a more pronounced TER can be produced as the top and the bottom interfaces become more distinct ($\frac{\lambda_1 \epsilon_2}{\lambda_2 \epsilon_1} \gg 1$ or $\ll 1$). Also, from the same figures, a lower resistance state is always produced by the polarization pointing to the interface with larger $\frac{\lambda}{\epsilon}$ as explained in Figs. 70(a) and (b). In other words, the sign of TER, as it is defined here, is switched from "+" to "−" as the effective contact ratio changes from the value larger than 1 to less than 1. As a result, if the effective contact ratio is equal to 1, meaning that the device is perfectly symmetric, the resulting TER will also be 1, and thus it is impossible to distinguish the polarization direction through tunneling resistance.

7.4.3 FTJs with CoO_x

From the previous section, it is shown that TER significantly depends on metal/BTO interface properties in an FTJ. Moreover, in addition to the termination effect, recently some experimental studies have reported that an inevitable CoO_x layer at the Co/BTO interface plays an important role for the memristor behavior of a Co/BTO/LSMO FTJ; that is, TER varies with the magnitude of the writing voltage [115]. Hence, in this section, our simple model is extended as shown in Figs. 64(b) and 66(b) to investigate the CoO_x effect on TER.

As mentioned in Ref. [115], a positive (negative) applied bias accumulates (dissipates) oxygen vacancies at the CoO_x/BTO interface, effectively reducing (increasing) ϕ_c. Therefore, as shown in the energy band diagrams of Fig. 71(a), which are constructed using Eq. 87, the low (high) resistance state corresponds to the polarization pointing to the bottom (top) contact with smaller (larger) ϕ_c. Note that as predicted

in Ref. [246], an unchanged ϕ_c in both polarization directions will result in a reversal of high/low resistance states, which haven't been observed in the experiment yet [115]. Furthermore, since no significant shift in the FE hysteresis loop was observed in the experiment [115], in our model, ϕ_1 is adjusted accordingly with ϕ_c so that the built-in field across the device is zero. In other words, $\phi_2 + \phi_c - \phi_1 = 0$, where ϕ_2 is fixed due to no change at the BTO/LSMO interface. Therefore, by using the same simulation parameters for the interfaces and the FE hysteresis loop as listed in Fig. 67, and assuming that part of BTO transforms into CoO_x ($t_{DE} = 0.6$ nm and $t_{FE} = 1$ nm), ϕ_c is adjusted to fit the experimental data as shown in Fig. 71(b), where a good agreement between the theory and the experiment is reached. As a result, Fig. 71(b) shows that it is possible to change TER through modifications of ϕ_c induced by voltage-dependent oxygen vacancies at the CoO_x/BTO interface. However, it seems that the required change in ϕ_c from off to on states may be too drastic for simply the charge-mediated effect (6.6 to 0.1eV). Therefore, the thickness of CoO_x may also be altered depending on the applied bias; that is, the CoO_x thickness may be reduced (increased) as the FTJ is switched from high (low) to low (high) resistance states. More experimental studies are required to confirm the possibility of the voltage-dependent CoO_x thickness in an FTJ.

7.5 Summary

This chapter presents a theoretical description of quantum-mechanical electronic transport and thermodynamic ferroelectric responses in both organic and inorganic FTJs. Inversed TER effect with respect to the polarization direction reported by different groups can also be explained by the proposed model through the effective contact ratio and termination effects. Finally, the role of a CoO_x buffer layer at the Co/BTO interface is also examined. It is found that the sizable memristive effects cannot be explained solely by the change in the barrier height due to charge-mediated

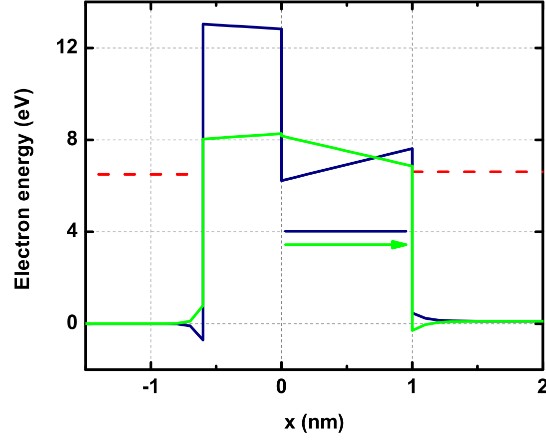

(a)

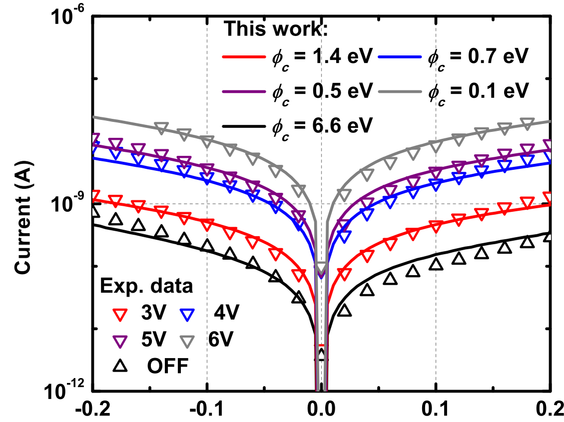

(b)

Figure 71: (a) Energy band diagrams at 0.1 V for high/low resistance states in an FTJ with a CoO_x buffer layer at the interface. ϕ_c for high and low resistance states are 6.6 and 0.1 eV, respectively. (b) Comparison with experimental data [115] using various ϕ_c for high and low resistance states and different writing voltages. In addition to $t_{DE} = 0.6$ nm, $t_{FE} = 1$nm, ϕ_1 and ϕ_c, the simulation parameters are the same as those in Fig. 67.

effects. It is suggested that the CoO_x layer thickness may also change as a result of electrically-induced Co oxidation/reduction at the Co/BTO interface. The proposed approach for description of the electroresistance effect in FTJs will provide a foundation for performance optimization of the core elements for nonvolatile memory and logic devices.

CHAPTER VIII

CONCLUSION AND OUTLOOK

8.1 Conclusion

8.1.1 Spintronic Logic

The first part of this thesis is to develop a computational scheme which minimizes the magnetization switching (or dynamic) energy in STT-driven devices and interconnects. In Chapter II, scaling limits on STT devices in the form of a non-local lateral SV (or ASL) is investigated theoretically. It is found that the dipolar coupling between the input and the output magnets, leakage currents due to the voltage driving the following stage, and the shunt path underneath the input for the non-reciprocity will significantly impair both performance and functionality of the device as its length scale is reduced to several tens of nanometers. As a result, to remove part of the currents leaking into the preceding stage, an SV with a tunnel barrier at the input is proposed as a potential interconnect option for ASL. Instead of the shunt path in an NLSV, the non-reciprocity of the interconnect is achieved by inserting a tunnel barrier at the input or an electric field across the channel. Hence, Chapters III and IV discuss the properties of these proposed interconnects using Si, Cu, and Al as channel materials, and also show the design rules for energy-efficient interconnects. The key result in Chapters III and IV is that for metallic interconnects, it is proven that an SV structure with a tunnel barrier saves more energy compared to a NLSV one because all the injected spins contribute the STT switching. However, as the interconnect length is increased to the μm scale, the semiconducting channel provides a more energy-efficient way for spin transport compared to the metallic one, since an electric field across the semiconducting channel significantly enhances the effective

spin relaxation length. However, even though the structure proposed in Chapters III and IV reduces the interconnect energy in ASL, a driving current is still required to inject spins or drive them from one end to another. Consequently, in Chapter V, a new concept for energy-free interconnects using automotion of magnetic DWs for ASL is presented, and the properties of this novel interconnect are discussed in detail. Since the DW velocity (or interconnect delay) depends significantly on the phase of a DW, properly choosing the bias current that excites a DW in the interconnect is extremely important to design this type of interconnect.

By combining all the advantages from the structures shown in Chapters III to V, Chapter VI presents a low-power computational scheme that combines SVs with DW automotion. The energy dissipation of this new scheme being superior to the previous proposals is mainly because all the spins can be fully used in STT-driven DW creation while a resistive tunnel barrier is removed. The non-reciprocity of both device and interconnect is realized by sizing different contact areas of the input and the output and also increasing the damping mechanism at the end of the interconnect through locally doping the impurities. Compared with the scheme based on the performance-optimized NLSVs, it is found that the dynamic energy of this proposed scheme can be three times lower and is more resistive to electromigration due to lower current density. Therefore, the proposed scheme introduced in Chapter VII provides a new low-power option in the current STT-driven logic family.

8.1.2 Ferroelectric Memory

The second part of this thesis is to construct a theoretical model that can describe I-V characteristics of an FTJ, which is one of the most promising candidates in the beyond CMOS memory technologies. As a result, Chapter VII presents a detailed theoretical derivation of the proposed model and shows that the measured data can be well described using the proposed formalism. Furthermore, under the proposed

model, a long-term controversy in the inconsistent TER sign measured by different groups has been resolved using surface termination effects. Finally, the model also predicts that the interface charge and DE thickness may vary with the applied bias to induce significant memristor behavior in an FTJ. Therefore, this new model can be served as an useful tool for design and optimization of the FTJ-based memory and logic systems.

8.2 Future Work

There are some interesting topics that can be directly extended by the concepts mentioned in this thesis. First, it is found that the switching energy of an STT-driven device is still much larger than that using CMOS switches for digital applications. Recently, based on the device and the model presented in Chapter II, it has been shown that some non-Boolean computing systems such as cellular neural network (CNN) based STT-driven devices can outperform CMOS-based CNN circuits [170]. Next, in Ref. [52], it has been shown that by applying a clocked voltage signal on the magnetostrictive cell, a weak magnetic signal such as spin waves can also provide a deterministic switching from a metastable state. As a result, a similar idea can also be applied in the device concept introduced in Chapter VI to further reduce the switching energy. Furthermore, a brief introduction on the devices based on the magnetoelectric (ME) effect and antiferromagnetism is also presented since they may also potentially provide a viable option in low-power beyond-CMOS technologies. Finally, some thoughts on modeling the polarization dynamics in an FE thin film are provided because both writing speed and state retention time are extremely important for the memory system design using FTJs. In the following, we particularly focus on magnetoelectric logic, STT logic with magnetostriction, antiferromagnetism, and switching dynamics in FE materials.

8.2.1 Magnetoelectric Logic

In Chapter VII, it has been shown that while all the injected spins participate in magnetization reversals in the proposed metallic structure, using simply the STT effect for digital logic still results in a much larger switching energy compared to CMOS switches. As a result, it is of interest to seek an alternative mechanism that can improve or even replace the STT-driven switching for higher energy efficiency, and one of the most promising mechanisms is the ME effect.

Recently, the ME coupling has been under active research due to the possibility of the voltage-controlled magnetization switching [60, 145]. The ME coupling is the interaction between the electric polarization and magnetization and has been observed in both a single material and a heteostructure [179]. However, a single material having the ME coupling is typically an anti-ferromagnet (e.g. Cr_2O_3), where the net magnetization is usually weak. Therefore, people typically focus on heterostructures showing the ME effect, which is defined as changing the magnetization by the electric polarization. The inverse ME effect is defined in a reverse order. Furthermore, in various material systems, the ME coupling can be induced by magnetostriction [37, 16, 126, 235, 61], charge transfer [143, 97, 22, 98, 144, 232, 196, 244, 4], or magnetic exchange bias [80, 83] at the interface. In particular, a successful ME magnetization reversal has been recently observed in a stack of multi-ferroic $BiFeO_3$ (BFO) and an FM metal [82]. In addition, a change in the electric polarization due to strain, induced by switching the magnetization through an external magnetic field, has been demonstrated in the layers of FE and FM films [56]. As a result, based on these unique relations between the electric polarization and the magnetization, some current-free spin-based logic devices are proposed [27]. For example, in Ref. [27], by using automotion of magnetic DWs mentioned in Chapters V, VI, and VII, a digital switch is composed of an FM wire with two FE capacitors as the input and the output as shown in Fig. 72(a), where logic 1 and 0 are defined in both magnetization and

voltage. The dominant mechanisms at the input and the output are ME and inverse ME effects, respectively, which are used to create and detect a magnetic DW. Due to no current flow in FM wires, automotion of the DW is in charge of propagating the magnetic signal from one end to another [34]. Using the inverse ME effect and a clocked switch, the voltage is established at the output when the magnetization of the wire is completely reversed. The output voltage can be used to drive the next stage by making the dimensions of connecting FE capacitors smaller as shown in Fig. 72(b). A 3-input majority gate can also be implemented as shown in Fig. 72(c). To realize Boolean functions correctly, initialization of magnetic states is required before every computation, and thus one of the possible circuits for initialization is also shown in Fig. 72(a). However, under this scheme, while the magnetization switching based on the exchange bias is much more energy-efficient than the STT effect, a few CMOS transistors are still required to make the device work normally. As a result, how to reduce the number of CMOS switches in this type of ME logic may be an interesting topic to work on.

8.2.2 Magnetostrictive Spin-transfer Torque Logic

In addition to the exchange-bias-driven ME effect, with the help of clocked signals, the ME effect induced by magnetostriction may further improve the energy efficiency in the STT-driven devices introduced in Chapter VII. Fig. 73 shows a possible device structure, in which the magnetostrictive cell drives the magnetization to the out-of-plane direction (or metastable state) before the STT is applied. Since it has been shown that a weak magnetic excitation such as spin waves can generate a deterministic switching when the magnetization is in the metastable state [52], it is also possible to switch the magnet with a much weaker STT compared to that shown in Chapter VII and simultaneously maintain the non-reciprocity. Note that a weak STT can be realized by reducing either the bias current or the pulse duration.

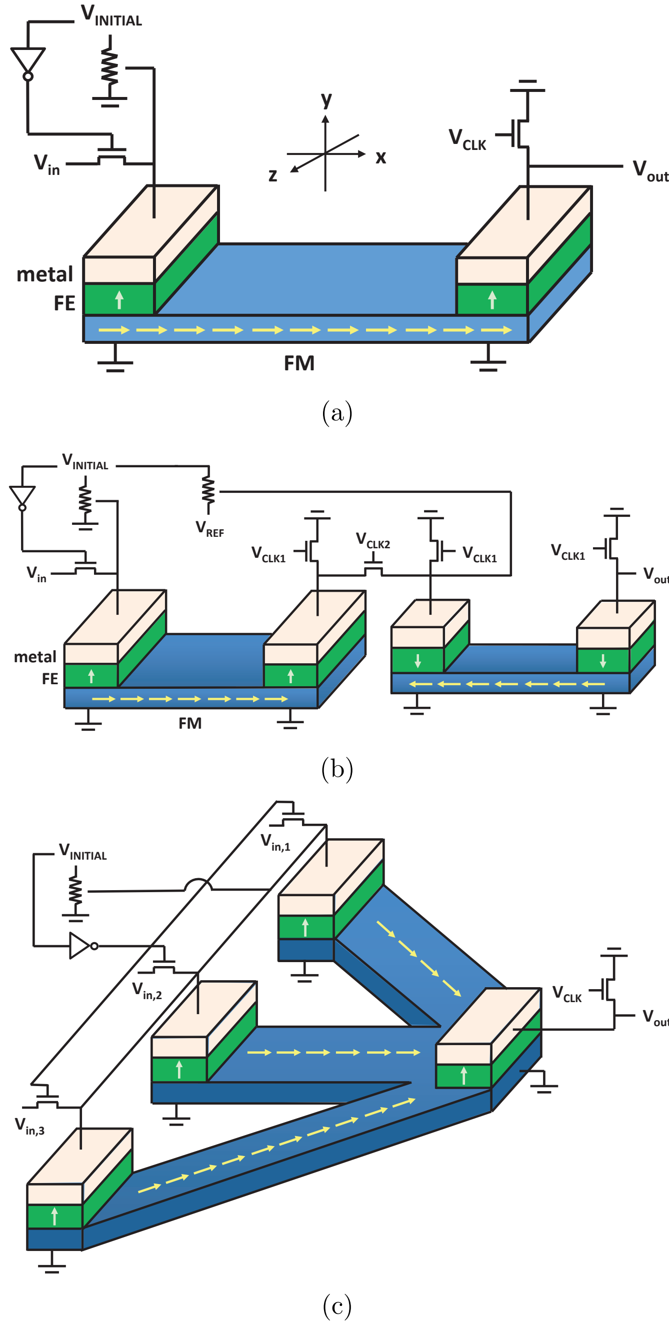

Figure 72: The proposed computational scheme using the magnetoelectric (ME) effects: (a) a single device, (b) two devices in cascade using a two-phase clocked circuit, and (c) a three-input majority gate [27]. The beige, green, and blue regions represent the metal contact, the ferroelectric (FE), and the ferromagnet (FM), respectively. The green and yellow arrows show the direction of the electric polarization of the FE and the magnetization of the FM, respectively. Under this scheme, logic 1 and 0 are represented by either voltage polarity or direction of the magnetization. A positive voltage and the magnetization pointing to the $+x$ direction stand for 1, and a negative voltage and the magnetization pointing to the $-x$ direction stand for -1. One of the possible setups for magnetization initialization is also shown.

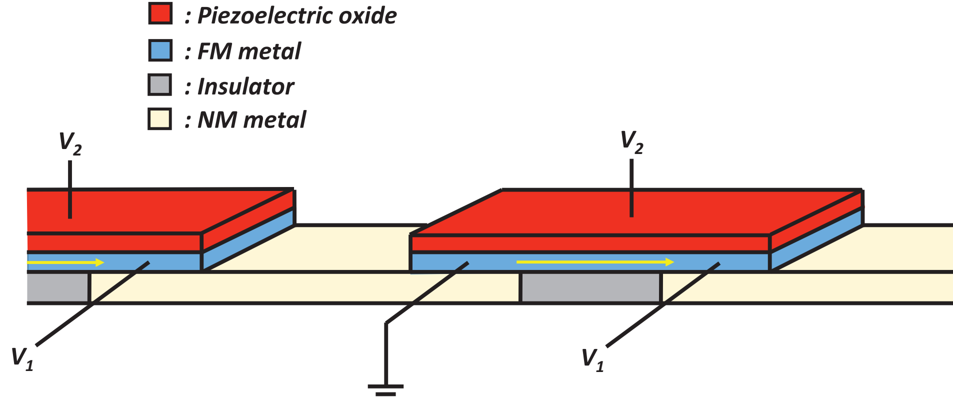

Figure 73: Schematic of clocked magnetostrictive STT logic, which may further reduce the STT switching energy with the help of magnetostriction. Red, blue, grey and yellow bars represent piezoelectric, FM, insulating, and NM materials, respectively. V_1 and V_2 are applied voltages with different clock cycles.

8.2.3 Antiferromagnetic Spintronics

In spintronics, antiferromagneic (AFM) materials are typically served as a passive component. Perhaps the most well-known spintronic application of AFM materials is an FM SV as magnetic field sensors or magnetic RAM, which is composed of a thin insulator or a thin non-magnetic metal sandwiched by a pair of fixed (or reference) and free FM layers. The fixed layer is typically achieved by increasing the magnetic hardness through the exchange coupling to the adjacent AFM layer [33]. Since the bits are represented by the magnetization of the FM layers, AFM materials simply play a supporting role in such devices. However, thanks to the recent experimental demonstrations of tunneling anisotropy magnetoresistance (TAMR) in AFM materials [172] and the spin-hall effect (SHE) in heavy non-magnetic materials [199], it becomes possible to write and read the magnetic state in AFM materials in the absence of FM materials. Note that AFM materials are insensitive to the applied magnetic field because the global magnetization is quite weak.

There are two main advantages in AFM spintronics. One is that there is no stray field produced by AFM materials. Consequently, the cross-talk in traditional FM

devices can be eliminated and thus one of the scaling limits discussed in Chapter II can also be removed. Another is that AFM materials generally is believed to have much faster magnetization dynamics than FM materials since the switching in AFM materials results from the canting of two anti-parallel sublattices, rather than coherent switching in FM materials [104].

In addition to the promising progress in reading and writing AFM materials, recently both experimental and theoretical work have shown that AFM insulators are suitable for efficient spin current transmitters [213, 231, 157] as illustrated conceptually in Fig. 74, where the input spin current is generated by the SHE from the left metal, and the output charge current (or voltage) is detected at the right metal through the inverse SHE. Theory has predicted that superfluid spin current transport can occur in AFM insulators, implying that the spin current can be lossless while flowing through the insulating AFM channel [213]. This unique feature is of great interest especially in the potential spin logic application, since the input and the output are electrically isolated but magnetically well-coupled.

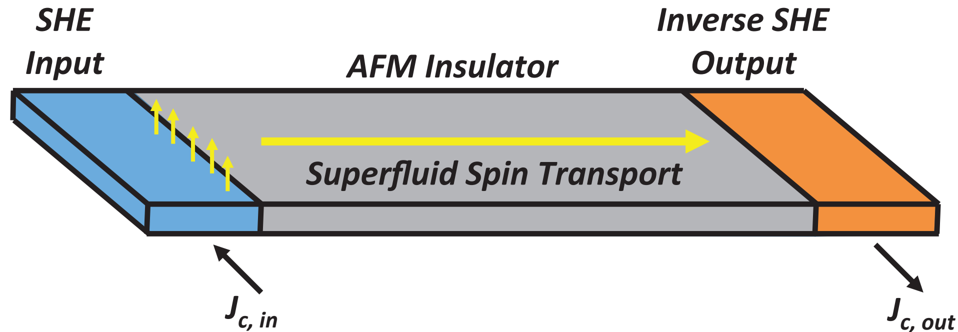

Figure 74: Schematic of superfluid spin transport through an AFM insulator predicted in Ref. [213], where the input and the output are electrically isolated but magnetically well coupled and may be potentially useful in the application of spin logic. Note that spin accumulation at the input/AFM insulator interface is generated by the SHE through $J_{c,in}$.

8.2.4 Switching Dynamics in Ferroelectric Tunnel Junctions

In Chapter VII, it has been shown that the proposed model can quantitatively describe the experimental I-V characteristics in an FTJ. However, the P-E hysteresis loop used in the model is generated by assuming that different FE thin films can follow the same applied AC voltage well, which is achieved by varying γ in the LK equation for different samples. In other words, the model presented in this thesis describes the static behavior of an FTJ since in reality, different FE thin films will have different dynamic responses depending on the size, quality, and material of the sample. As a result, it is of interest to modify the LK equation so that the polarization dynamics of an FE thin film can also be captured.

Typically, the polarization dynamics of an FE material can be well described by the so-called Kolmogorov-Avrami-Ishibashi (KAI) model, where the nucleation and propagation of an FE DW is responsible for the dynamic response to an applied electric field. In the KAI model, the fitting parameters are characterisitc times for the DW nucleation and propagation. The same dynamics can also be modeled by the LK equation shown in Chapter VII with a fitting parameter, γ, which can also be considered as a rate constant to describe how the net polarization varies with the applied field in the process of DW nucleation and propagation. However, as the FE material becomes thinner, a simple KAI model or the LK equation fails to describe the dynamic response since an FE thin film is highly disordered [99]. It has been shown that the polarization dynamics in a disordered sample is dominant by the nucleation-limited process, which can be described by assuming that a thin film is composed of several areas having different independent switching characteristics, and the change in polarization can be estimated by weighting all the possible characteristic time with a Lorentzian function under the KAI framework. Therefore, using the same concept from Ref. [99], it is of great interest to see if the polarization dynamics can also be described by summing over several independent LK equations, representing

independent FE domains, with different γ following the Lorentzian distribution, and thus a dynamic model for an FTJ can be established.

APPENDIX A

IMPORTANT DERIVATIONS AND JUSTIFICATION IN CHAPTER V

A.1 All-spin Logic Circuit Representation

For ASL equivalent circuit, a systematic nodal analysis is applied to obtain the conductance matrix, $\mathbf{G}$. The general idea behind this analysis is that the sum over current vectors at each node is equal to zero; that is,

$$0 = \sum_j I_{ij}. \tag{94}$$

Using the node A as an example, the current conservation yields the equation below

$$0 = -I_1 + I_{A0} + I_{AB} = -I_1 + G_{m,sh}V_A + G_{m,se}(V_A - V_B). \tag{95}$$

Similarly, the equations for current conservation at nodes B to F are given as

$$0 = G_{m,sh}V_B + G_{m,se}(V_B - V_A) + G_{f1}(V_B - V_C), \tag{96}$$

$$0 = G_{f1}(V_C - V_B) + G_{g,sh}V_C + G_{g,se}V_C + G_{c,sh}V_C + G_{c,se}(V_C - V_D), \tag{97}$$

$$0 = G_{c,sh}V_D + G_{c,se}(V_D - V_C) + \sum_{j=1}^{N}\left[G_{f2}(z_j)(V_D - V_E)\right], \tag{98}$$

$$0 = \sum_{j=1}^{N}\left[G_{f2}(z_j)(V_E - V_D)\right] + G_{m,sh}V_E + G_{m,se}(V_E - V_F), \tag{99}$$

$$0 = -I_2 + G_{m,sh}V_F + G_{m,se}(V_F - V_E). \tag{100}$$

Recall that in Chapter V, the conductance matrix, $\mathbf{G}$, is defined as follows:

$$\{V\} = \mathbf{G}^{-1}\{I\}, \tag{101}$$

where $\{V\}$ and $\{I\}$ are the voltage and current vectors representing charge and spin components at each node. Therefore, by re-writing the equations above into a matrix

expression, the conductance matrix for ASL with the interconnect where the STT is present is obtained and given as follows:

$$\mathbf{G} = \begin{bmatrix} G_{m,se}+G_{m,sh} & -G_{m,se} & Z & Z & Z & Z \\ -G_{m,se} & G_{m,se}+G_{m,sh}+G_{f1} & -G_{f1} & Z & Z & Z \\ Z & -G_{f1} & G_{f1}+G_{g,se}+G_{g,sh}+G_{c,se}+G_{c,sh} & -G_{c,se} & Z & Z \\ Z & Z & -G_{c,se} & G_{c,se}+G_{c,sh}+\sum_{j=1}^{N} G_{f2}(z_j) & -\sum_{j=1}^{N} G_{f2}(z_j) & Z \\ Z & Z & Z & -\sum_{j=1}^{N} G_{f2}(z_j) & \sum_{j=1}^{N} G_{f2}(z_j)+G_{m,se}+G_{m,sh} & -G_{m,se} \\ Z & Z & Z & Z & -G_{m,se} & G_{m,se}+G_{m,sh} \end{bmatrix} \quad (102)$$

where first subscripts for conductance components, m, f_1, g, c, and f_2, represent different regions in ASL including the metal contact, transmitting magnet, channel from the transmitter to ground, channel connecting two magnets, and receiving magnet, respectively, and the second subscripts, se and sh, mean series and shunt conductance, respectively, and the 1_{st} to 6_{th} rows in $\mathbf{G}$ represent laws of current conservation at nodes A to F, respectively. Since $\mathbf{G}$ is used to describe both charge and spin components (the latter includes x, y, and z directions), each conductance component is a 4×4 matrix, and Z here represents a 4×4 null matrix.

A.2 One-dimensional Landau-Lifshitz-Gilbert Equation

An one-dimensional (1-D) Landau-Lifshitz-Gilbert (LLG) equation is solved by rewriting it into a matrix form given as

$$
\begin{bmatrix} 1 & \alpha m_z & -\alpha m_y \\ -\alpha m_z & 1 & \alpha m_x \\ \alpha m_y & -\alpha m_x & 1 \end{bmatrix}
\begin{bmatrix} \frac{\partial m_x}{\partial t} \\ \frac{\partial m_y}{\partial t} \\ \frac{\partial m_z}{\partial t} \end{bmatrix} =
$$

$$
\left[\begin{array}{l}
-\frac{2\gamma A}{M_s}(m_y \frac{\partial^2 m_z}{\partial z^2} - m_z \frac{\partial^2 m_y}{\partial z^2}) - \gamma\mu_0(m_y H_{eff,z} - m_z H_{eff,y}) \\
-\frac{2\gamma A}{M_s}(m_z \frac{\partial^2 m_x}{\partial z^2} - m_x \frac{\partial^2 m_z}{\partial z^2}) - \gamma\mu_0(m_z H_{eff,x} - m_x H_{eff,z}) \\
-\frac{2\gamma A}{M_s}(m_x \frac{\partial^2 m_y}{\partial z^2} - m_y \frac{\partial^2 m_x}{\partial z^2}) - \gamma\mu_0(m_x H_{eff,y} - m_y H_{eff,x})
\end{array} \right.
$$

$$
\begin{array}{l}
-\gamma a_J[m_x(m_y p_y + m_z p_z) - p_x(m_y^2 + m_z^2)] - u_J \frac{\partial m_x}{\partial z} \\
-\gamma a_J[m_y(m_z p_z + m_x p_x) - p_y(m_x^2 + m_z^2)] - u_J \frac{\partial m_y}{\partial z} \\
-\gamma a_J[m_z(m_x p_x + m_y p_y) - p_z(m_x^2 + m_y^2)] - u_J \frac{\partial m_z}{\partial z}
\end{array}
$$

$$
\left. \begin{array}{l}
+\beta u_J(m_y \frac{\partial m_z}{\partial z} - m_z \frac{\partial m_y}{\partial z}) - \frac{\gamma\mu_0\nu}{\Delta t}(m_y dW_z - m_z dW_y) \\
+\beta u_J(m_z \frac{\partial m_x}{\partial z} - m_x \frac{\partial m_z}{\partial z}) - \frac{\gamma\mu_0\nu}{\Delta t}(m_z dW_x - m_x dW_z) \\
+\beta u_J(m_x \frac{\partial m_y}{\partial z} - m_y \frac{\partial m_x}{\partial z}) - \frac{\gamma\mu_0\nu}{\Delta t}(m_x dW_y - m_y dW_x)
\end{array} \right], \tag{103}
$$

where ν is the magnitude of the thermal noise field and first- and second-order derivatives are calculated using four-nearest-neighbors approximation given as

$$
\left.\frac{\partial m_i}{\partial z}\right|_{z_j} = \frac{m_i(z_{j-2}) - 8m_i(z_{j-1}) + 8m_i(z_{j+1}) - m_i(z_{j+2})}{12\Delta z} \tag{104}
$$

$$
\left.\frac{\partial^2 m_i}{\partial z^2}\right|_{z_j} = \frac{-m_i(z_{j-2}) + 16m_i(z_{j-1}) - 30m_i(z_j) + 16m_i(z_{j+1}) - m_i(z_{j+2})}{12(\Delta z)^2}, \tag{105}
$$

where i represents x, y, or z components of the magnetization and Δz is the distance between the nearest domains. Note that Eq. 104 and 105 are not valid anymore when the domain becomes closest or next-to-closest to the boundary of the wire; therefore, here the free boundary condition ($\partial m_{x,y,z}/\partial z = 0$) is implemented, and the corresponding first- and second-order derivatives closest and next-to-closest to the

left and right ends are given as follows:

$$\left.\frac{\partial m_i}{\partial z}\right|_{z_{c,L(R)}} = \frac{\mp 37 m_i(z_c) \pm 44 m_i(z_{c\pm 1}) \mp 7 m_i(z_{c\pm 2})}{46\Delta z}, \tag{106}$$

$$\left.\frac{\partial^2 m_i}{\partial z^2}\right|_{z_{c,L(R)}} = \frac{-25 m_i(z_c) + 26 m_i(z_{c\pm 1}) - m_i(z_{c\pm 2})}{23(\Delta z)^2}, \tag{107}$$

$$\left.\frac{\partial m_i}{\partial z}\right|_{z_{nc,L(R)}} = \frac{\mp 53 m_i(z_{nc\mp 1}) \pm 3 m_i(z_{nc}) \pm 57 m_i(z_{nc\pm 1}) \mp 7 m_i(z_{nc\pm 2})}{88\Delta z}, \tag{108}$$

$$\left.\frac{\partial^2 m_i}{\partial z^2}\right|_{z_{nc,L(R)}} = \frac{335 m_i(z_{nc\mp 1}) - 669 m_i(z_{nc}) + 357 m_i(z_{nc\pm 1}) - 23 m_i(z_{nc\pm 2})}{264(\Delta z)^2}, \tag{109}$$

where the subscripts c and nc denote the domain closest and next-closest to the left (L) or right (R) boundary, respectively.

To control the convergence of stochastic LLG in a sense of Stratonovich calculus, the predictor-corrector (Heun) scheme is used and given as

$$\vec{m_p} = \vec{m}(t_n) + \frac{\partial \vec{m}(t_n)}{\partial t}\Delta t, \tag{110}$$

$$\vec{m_c} = \vec{m}(t_n) + \frac{1}{2}\left(\frac{\partial \vec{m}(t_n)}{\partial t} + \frac{\partial \vec{m_p}}{\partial t}\right), \tag{111}$$

$$\vec{m_p} = \vec{m_c}, \tag{112}$$

where $\vec{m_p}$ and $\vec{m_c}$ are the predictor and corrector, respectively, and t_n denotes the time step. Note that Eq. 112 can be done more than once to make sure the result is converged.

A.3 Equations of Motion for Domain Wall Transport

To derive equations of motion for DW transport, the standard approach is followed, and the starting point is to write the 1-D LLG equation in the spherical coordinate

as follows:

$$\begin{aligned}
\frac{\partial\theta}{\partial t}+\alpha\sin\theta\frac{\partial\phi}{\partial t} &= \frac{2\gamma A}{M_s}(2\cos\theta\frac{\partial\theta}{\partial z}\frac{\partial\phi}{\partial z}+\sin\theta\frac{\partial^2\theta}{\partial z^2})-\frac{\gamma}{M_s}(K_x-K_y)\sin 2\phi\sin\theta \\
&\quad -u_J(\frac{\partial\theta}{\partial z}+\beta\sin\theta\frac{\partial\phi}{\partial z})-\gamma a_J p\sin\theta \qquad (113)\\
\sin\theta\frac{\partial\phi}{\partial t}-\alpha\frac{\partial\theta}{\partial t} &= \gamma\mu_0 H_{ex}\sin\theta+\frac{2\gamma A}{M_s}(-\frac{\partial^2\theta}{\partial z^2}+\sin\theta cos\theta(\frac{\partial\phi}{\partial z})^2) \\
&\quad -\frac{\gamma}{M_s}K_{eff}\sin 2\theta-u_J(\sin\theta\frac{\partial\phi}{\partial z}-\beta\frac{\partial\theta}{\partial z}), \qquad (114)
\end{aligned}$$

where θ and ϕ are the polar and azimuthal angles in the spherical coordinate, H_{ex} is the magnitude of an applied magnetic field in the z direction, p is either 1 or -1, representing z or -z spin polarization, respectively, and K_{eff} is equal to $K_x\cos^2\phi+K_y\sin^2\phi-K_z$, in which K_i includes uniaxial and shape anisotropy and is written as $\frac{1}{2}\mu_0 M_s^2 N_i-K_{u,i}$. As mentioned in the main paper, an important assumption here is that the demagnetization tensor, N_i, is independent of the space and only determined by the geometry. Here we also introduce the Walker's trial solutions as follows:

$$\begin{aligned}
\theta(z,t) &= 2\tan^{-1}\left[e^{Qc(t)(z-\int_0^{\tau}v(\tau)d\tau)}\right] \qquad (115)\\
\phi(z,t) &= \phi(t), \qquad (116)
\end{aligned}$$

where Q is the topological charge distinguishing the type of the DW (+1: head-to-head and -1: tail-to-tail), v is the DW velocity, and c is defined as $1/\Delta$, in which Δ is the thickness of the DW.

The next step is to replace θ and ϕ in Eq. 10 and Eq. 7 using the trial solutions and assume the DW thickness does not change with time too much. The resulting set of equations are given as

$$\begin{aligned}
-Qc(t)v(t)+\alpha\frac{\partial\phi}{\partial t} &= \frac{\gamma}{M_s}(K_x-K_y)\sin 2\phi-Qc(t)u_J-\gamma a_J p \qquad (117)\\
\frac{-2\gamma\cos\theta}{M_s}(Ac^2(t)-K_{eff}) &= \frac{\partial\phi}{\partial t}+Q\alpha c(t)v(t)-\gamma\mu_0 H_{ex}-u_J\beta Qc(t). \qquad (118)
\end{aligned}$$

Note that the left-hand side of Eq. **??** has z-dependence, but the right-hand side is

independent of z; thus, the DW thickness, Δ, can be written as

$$\Delta(t) = \frac{1}{c(t)} = \sqrt{\frac{A}{K_{eff}}}, \tag{119}$$

and here we express the DW velocity in terms of the DW displacement as $\frac{\partial \chi}{\partial t}$. After collecting all the terms mentioned above, the compact expressions for DW transport are given as

$$\left(1+\alpha^2\right)\frac{\partial \chi}{\partial t} = \frac{-\gamma\Delta(K_x - K_y)\sin 2\phi}{QM_s} + (1+\alpha\beta)\,\mu_J + \frac{\gamma\Delta p a_J}{Q} + \frac{\gamma\Delta\alpha\mu_0 H_{ex}}{Q} \tag{120}$$

$$\left(1+\alpha^2\right)\frac{\partial \phi}{\partial t} = \frac{\alpha\gamma(K_x - K_y)\sin 2\phi}{M_s} + \frac{(\beta-\alpha)\,Q}{\Delta}\mu_J - \gamma p\alpha a_J + \gamma\mu_0 H_{ex}. \tag{121}$$

A.4 Justification of Eq. 67

The validation of using Eq. 67 as the simplified demagnetization tensor for the DW transport is given in Fig. 75, where the demagnetization fields for a given DW profile using Eq. 58 and Eq. 67 in Chapter V are shown. From Fig. 75, we can see that the space-independent demagnetization tensor gives us correct fields in the transverse direction over the DW region; however, it fails to estimate the field in the z direction, especially for the field at the edges where the magnetic poles are accumulated. Later we will show that this deviation of the demagnetization field in the z direction does not affect the accuracy too much since (i) instead of the fields near the boundary, only those over the DW region affect transport, (ii) the internal field in the z direction over the DW region is dominated by the material anisotropy field rather than shape anisotropy, and (iii) transverse demagnetization fields, which are essential especially for DW automotion, are well-described by the space-independent demagnetization tensor.

Note that the analytical equations for DW transport are derived by assuming the DW follows the Walker's trial form during transport; thus, only specific driving forces such as an applied field in the z direction or z spin-polarized out-of-plane currents can be included; otherwise, m_z in the wire will not perfectly be $+1$ or -1

as z goes to positive or negative infinity, and in those cases, i.e. a magnetic field in the transverse plane, the higher-order correction terms are needed to describe the DW [72]. Furthermore, the analytical forms are only valid when the DW exists in the wire; thus, the driving force such as out-of-plane spin currents can not be too large since it may either destroy the DW or excite spin waves [114]. In Fig. 76, a DW with given phase and displacement is plugged into both numerical solver for the 1-D LLG equation and analytical expressions. It is shown that the results from the analytical expressions are quite close to those from the numerical solver. The small difference is due to the deviated demagnetization field in the z direction calculated by the space-independent tensor as mentioned previously; therefore, from Fig. 76, the compact expressions give us a fairly accurate description on DW transport without going through complicated numerical simulations.

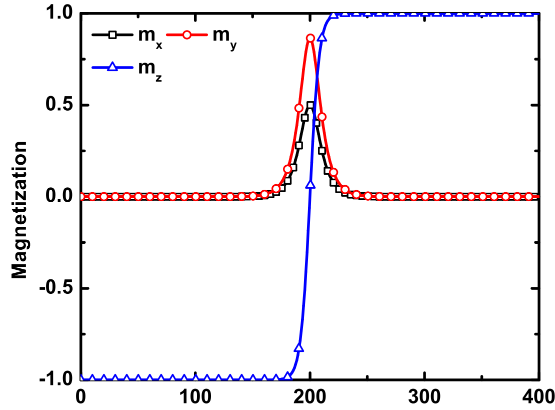

(a)

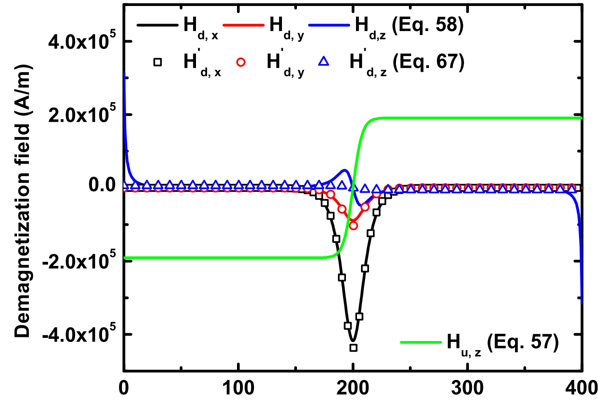

(b)

Figure 75: (a) The magnetization profile for a DW in a wire. (b) The corresponding demagnetization field using Eq. 58 and Eq. 67 and material anisotropy field using Eq. 57. The wire dimension is $400 \times 20 \times 2$ nm^3 with $M_s = 1 \times 10^6$ A/m and $K_{u,z} = 1.2 \times 10^5$ joule/m^3.

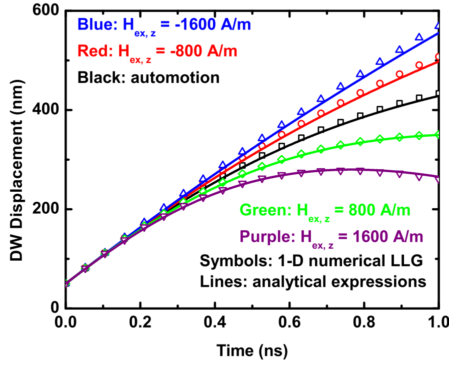

(a)

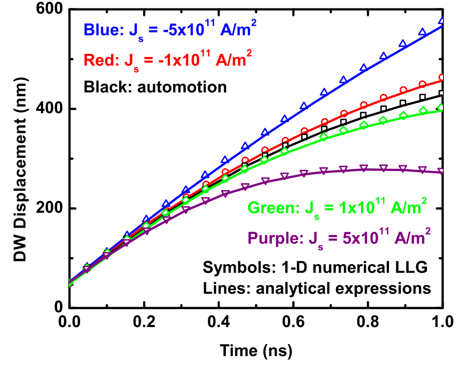

(b)

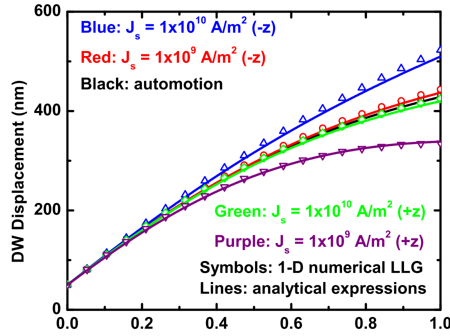

(c)

Figure 76: Comparisons between the numerical solver for the 1-D LLG equation and the analytical expressions for DW transport in Chapter V. C under (a) an external magnetic field, (b) in-plane spin currents, and (c) out-of-plane spin currents. The DW motion due to transverse shape anisotropy (automotion) is included in all the figures above as a reference. Note that for (c), the out-of-plane spin currents cannot be too large since in such a case, either the DW is destroyed or spin waves are created, and the analytical models fail to describe the transport. ±z in (c) represents ±z spin polarization of currents.

APPENDIX B

IMPORTANT DERIVATIONS AND EQUIVALENT SPIN CIRCUITS IN CHAPTER VI

B.1 Analytical Expression between Charge Current Density and Spin Current in Spin Valves

Fig. 77 shows the structure of a simple SV that is used to derive the analytical expression for the relation between charge current density at both input and output and spin current. From Ref. [226], spin accumulation (μ_s) and current (J_s) in FM metals are described by the differential equations as follows.

$$\frac{\partial^2 \mu_s(x)}{\partial x^2} = \frac{\mu_s(x)}{L_{sf,F}^2} \tag{122}$$

$$J_s(x) = P_\sigma J_c + \frac{4\sigma_\uparrow \sigma_\downarrow}{e\sigma_F}\frac{\partial \mu_s(x)}{\partial x}, \tag{123}$$

where $L_{sf,F}$ is the spin relaxation length of FM metal, P_σ is the polarization of conductivity, J_c is charge current flowing through the FM metal, and σ_F, $\sigma_\uparrow$, as well as $\sigma_\downarrow$ are total, up-spin, and down-spin conductivity of FM metals, respectively. For the NM metal, the differential equations are given as

$$\frac{\partial^2 \mu_s(x)}{\partial x^2} = \frac{\mu_s(x)}{L_{sf,N}^2} \tag{124}$$

$$J_s(x) = \frac{\sigma_N}{e}\frac{\partial \mu_s(x)}{\partial x}, \tag{125}$$

where σ_N is conductivity of NM metals. The general solutions of these differential equations in each region are given as

$$\mu_s(x) = Ae^{\frac{x}{L_{sf,F}}} + Be^{\frac{-x}{L_{sf,F}}}, -t_F \le x \le 0 \tag{126}$$

$$J_s(x) = P_\sigma J_{c,1} + \frac{4\sigma_\uparrow\sigma_\downarrow}{e\sigma_F L_{sf,F}}\left(Ae^{\frac{x}{L_{sf,F}}} - Be^{\frac{-x}{L_{sf,F}}}\right), -t_F \le x \le 0 \tag{127}$$

$$\mu_s(x) = Ce^{\frac{x}{L_{sf,N}}} + De^{\frac{-x}{L_{sf,N}}}, 0 \le x \le L_c \tag{128}$$

$$J_s(x) = \frac{\sigma_N}{eL_{sf,N}}\left(Ce^{\frac{x}{L_{sf,N}}} - De^{\frac{-x}{L_{sf,N}}}\right), 0 \le x \le L_c \tag{129}$$

$$\mu_s(x) = Ee^{\frac{x}{L_{sf,F}}} + Fe^{\frac{-x}{L_{sf,F}}}, L_c \le x \le L_c + t_F \tag{130}$$

$$J_s(x) = P_\sigma J_{c,2} + \frac{4\sigma_\uparrow\sigma_\downarrow}{e\sigma_F L_{sf,F}}\left(Ee^{\frac{x}{L_{sf,F}}} - Fe^{\frac{-x}{L_{sf,F}}}\right), L_c \le x \le L_c + t_F \tag{131}$$

with A, B, C, D, E, and F being the coefficients determined by specifying the boundary conditions. Hence, the following boundary conditions are applied by assuming that both spin accumulation and current are continuous at the FM/NM interface, and no spin accumulation at the terminal connected to the bias voltage or ground.

$$\mu_s(-t_{FM}) = \mu_s(L_c + t_{FM}) = 0 \tag{132}$$

$$\mu_s\left(0^+\right) = \mu_s\left(0^-\right) \tag{133}$$

$$\mu_s\left(L_c^+\right) = \mu_s\left(L_c^-\right) \tag{134}$$

$$J_s\left(0^+\right) = J_s\left(0^-\right) \tag{135}$$

$$J_s\left(L_c^+\right) = J_s\left(L_c^-\right) \tag{136}$$

A set of equations are then obtained by plugging these boundary conditions into the general solutions of the differential equations of spin accumulation and current, and

given as

$$Ae^{\frac{-t_F}{L_{sf,F}}} + Be^{\frac{t_F}{L_{sf,F}}} = Ee^{\frac{(L_c+t_F)}{L_{sf,F}}} + Fe^{\frac{-(L_c+t_F)}{L_{sf,F}}} = 0 \quad (137)$$

$$A + B = C + D \quad (138)$$

$$Ce^{\frac{L_c}{L_{sf,N}}} + De^{\frac{-L_c}{L_{sf,N}}} = Ee^{\frac{L_c}{L_{sf,F}}} + Fe^{\frac{-L_c}{L_{sf,F}}} \quad (139)$$

$$P_\sigma J_{c,1} + \frac{4\sigma_\uparrow\sigma_\downarrow}{e\sigma_F L_{sf,F}}(A - B) = \frac{\sigma_N}{eL_{sf,N}}(C - D) \quad (140)$$

$$\frac{\sigma_N}{eL_{sf,N}}\left(Ce^{\frac{L_c}{L_{sf,N}}} - De^{\frac{-L_c}{L_{sf,N}}}\right) = P_\sigma J_{c,2} + \frac{4\sigma_\uparrow\sigma_\downarrow}{e\sigma_F L_{sf,F}}\left(Ee^{\frac{L_c}{L_{sf,F}}} - Fe^{\frac{-L_c}{L_{sf,F}}}\right) \quad (141)$$

By solving Eq. 134 to Eq. 138, the spin current along the NM channel is given as

$$J_s(x) = \frac{\sigma_N}{eL_{sf,N}}\left(\frac{P_\sigma J_{c,1}\left(\alpha e^{\frac{x-L_c}{L_{sf,N}}} + \beta e^{\frac{-(x-L_c)}{L_{sf,N}}}\right) + P_\sigma J_{c,2}\left(\alpha e^{\frac{-x}{L_{sf,N}}} + \beta e^{\frac{x}{L_{sf,N}}}\right)}{\beta^2 e^{\frac{L_c}{L_{sf,N}}} - \alpha^2 e^{\frac{-L_c}{L_{sf,N}}}}\right) \quad (142)$$

with α and β being $\left(\frac{4\sigma_\uparrow\sigma_\downarrow}{e\sigma_F L_{sf,F}}\right)\coth\left(\frac{t_F}{L_{sf,F}}\right) - \frac{\sigma_N}{eL_{sf,N}}$ and $\left(\frac{4\sigma_\uparrow\sigma_\downarrow}{e\sigma_F L_{sf,F}}\right)\coth\left(\frac{t_F}{L_{sf,F}}\right) + \frac{\sigma_N}{eL_{sf,N}}$, respectively. From Eq. 142, it can be seen that spin current in the NM channel increases with charge current density flowing through the FM metals. Thus, since a STT is in general proportional to spin current, the non-reciprocity of a spin valve can be realized by modifying spin current at both input and output through sizing contact areas as simulated in the main text.

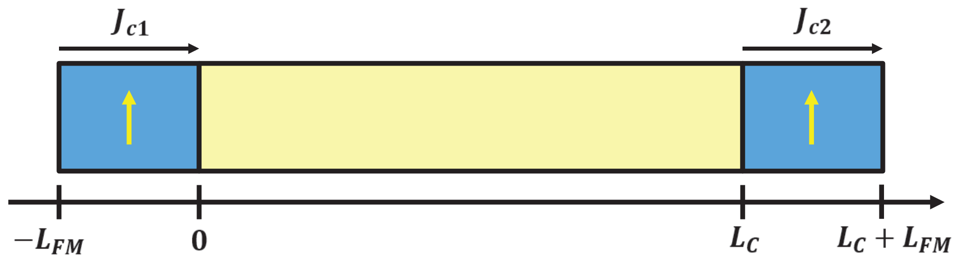

Figure 77: A simple SV structure that is used to derive Eq. 142.

B.2 Equivalent Spin Circuits for a 3-input Majority Gate using Spin Valves

Fig. 78 shows a 3-input majority gate equivalent spin circuit, which is calculated with stochastic LLG equations to generate Fig. 60 in the main text.

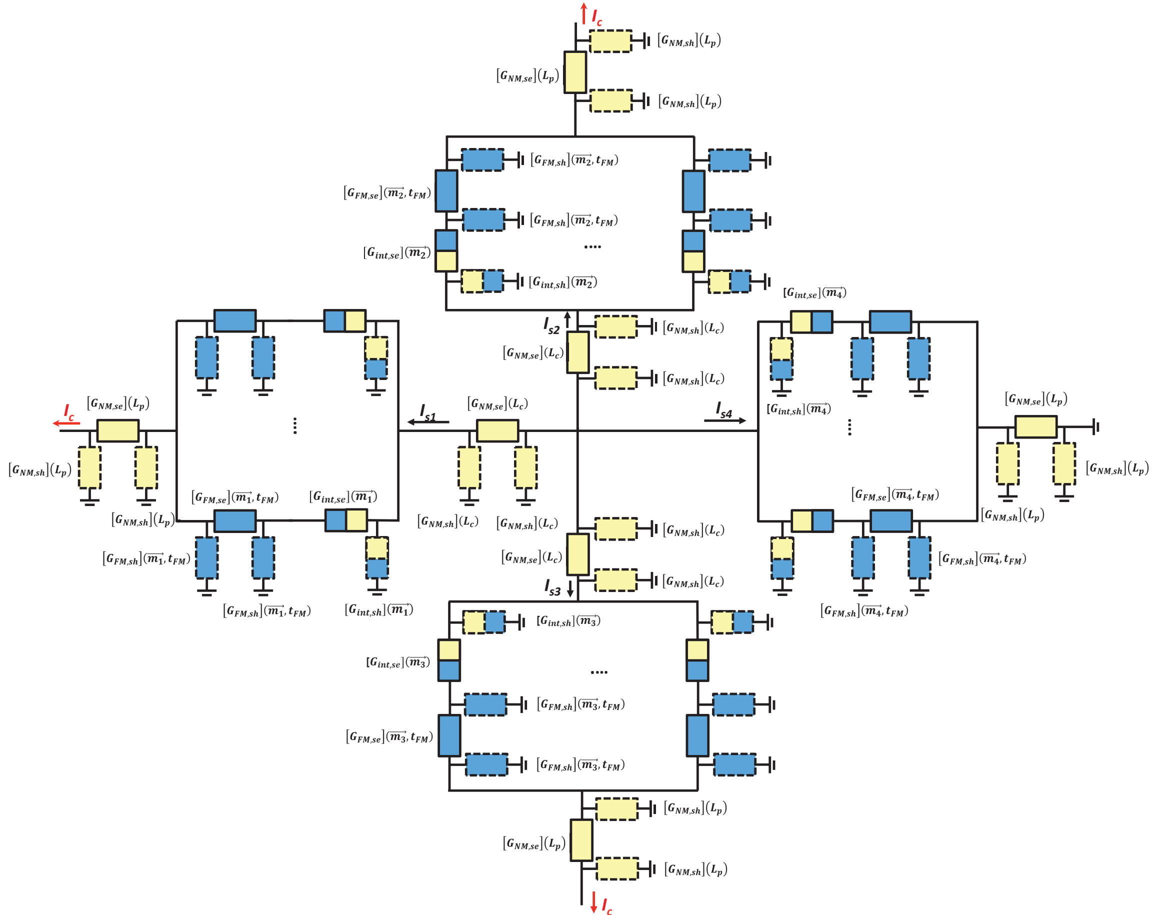

Figure 78: An equivalent spin circuit for a 3-input majority gate. The color definition is the same as that shown in the main text.

B.3 Equivalent Spin Circuits for a Non-local Spin Valve

Fig. 79 shows the equivalent spin circuit of a NLSV that is used to generate Figs. 61 to 63 in the main text.

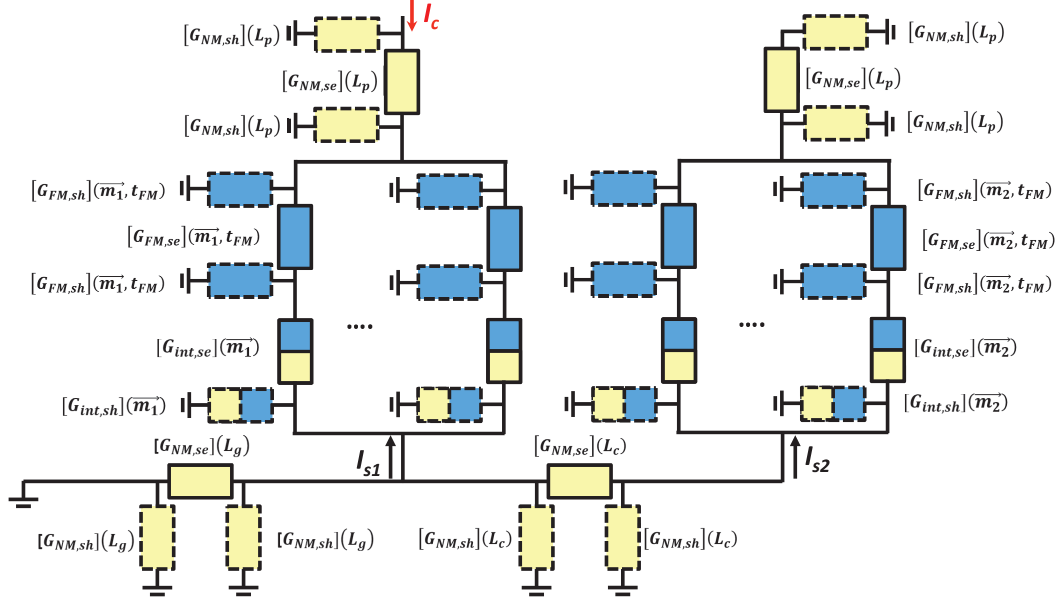

Figure 79: An equivalent spin circuit for a NLSV. The color definition is the same as that shown in the main text.

APPENDIX C

IMPORTANT DERIVATIONS IN CHAPTER VII

C.1 Derivations of Eqs. 73 and 74

The relation between charge (Q) and electric field (E) in the metal can be described by the Poisson's equation given as

$$\frac{\partial E(x)}{\partial x} = \frac{Q}{\epsilon_m \epsilon_0} = \frac{-e(n - n_0)}{\epsilon_m \epsilon_0}, \tag{143}$$

where ϵ_m is the dielectric constant of the metal, n is the electron density, and n_0 is the electron density in the neutral metal electrode. In the metal, the electrons can be treated as a free fermi gas, and thus the local potential (V) and electron density can be related as [120]

$$V = \frac{\hbar^2}{2m_0}\left(3\pi^2 n\right)^{\frac{2}{3}} \tag{144}$$

with $\hbar$ being the reduced Planck constant, and m_0 being the free electron mass. By using $-\frac{\partial V}{\partial x} = E$, the derivative of the electron density with respect to x can be expressed as

$$\frac{\partial n}{\partial x} = -\frac{E}{\frac{\hbar^2}{3m_0}\left(3\pi^2\right)^{\frac{2}{3}} n^{\frac{-1}{3}}}, \tag{145}$$

and therefore the derivative of Eq. 143 with respect to x becomes

$$\frac{\partial^2 E}{\partial x^2} = \frac{-e}{\epsilon_m \epsilon_0}\frac{\partial n}{\partial x} = \frac{E}{\lambda^2}, \tag{146}$$

where the metal Thomas-Fermi screening length, λ, is defined as $\frac{\hbar^2 \epsilon_m \epsilon_0}{3em_0}\left(3\pi^2\right)^{\frac{2}{3}} n^{\frac{-1}{3}}$. The general solution of Eq. 146 is $Ae^{\frac{x}{\lambda}} + Be^{\frac{-x}{\lambda}}$ with A and B being coefficients determined by the boundary conditions, which are, using the top electrode as an

example, $E(-\infty) = 0$ and $E(0) = \frac{\rho_s}{\epsilon_1 \epsilon_0}$. Therefore, the corresponding electric field (E_1) and potential profile (V_1) ($-\infty < x \leq 0$) are given as

$$E_1 = \frac{\rho_s}{\epsilon_1 \epsilon_0} e^{\frac{x}{\lambda_1}}, \tag{147}$$

$$V_1 = -\int_{-\infty}^{x} dx' E(x') = \frac{-\rho_s \lambda_1}{\epsilon_1 \epsilon_0} e^{\frac{x}{\lambda_1}}. \tag{148}$$

Similarly, by using $E(\infty) = 0$ and $E(t_{FE}) = \frac{-\rho_s}{\epsilon_2 \epsilon_0}$ as boundary conditions, the potential profile (V_2) of the bottom electrode ($t_{FE} \leq x < \infty$) is given as

$$V_2 = \frac{\rho_s \lambda_2}{\epsilon_2 \epsilon_0} e^{\frac{-(x - t_{FE})}{\lambda_2}}. \tag{149}$$

Eqs. 148 and 149 are identical to Eqs. 73 and 74. Note that as mentioned in the main text, for some FTJs with complex interfacial bonds, the potential drop near the interface is described by the effective screening length and dielectric response, rather than the Thomas-Fermi one [105].

C.2 Alternative Expression of Eq. 90

The electron wave vector can be represented in the spherical coordinate as shown in Fig. 80. To rewrite Eq. 90, the first step is to convert the summation into the integral using periodic boundary conditions ($\sum_k = \frac{L}{2\pi} \int dk$), and the resulting expression is given as

$$J = \frac{-e}{2\pi^2 h} \int_{-\infty}^{\infty} \int_{-\infty}^{\infty} dk_y dk_z \int dE t (f_1 - f_2). \tag{150}$$

Note that t, f_1, and f_2 are all energy-dependent. Under the spherical coordinate, $dk_y dk_z$ can be written as $k^2 \sin\theta d\phi d\theta$. For electrons coming from $+x$ with total energy, E, equal to $E = \frac{\hbar^2 k^2}{2m^*} + U_0$, where m^* is the effective mass and U_0 is the potential energy, the current equation becomes

$$\begin{aligned} J &= \frac{-e}{2\pi^2 h} \int_0^{2\pi} \int_0^{\frac{\pi}{2}} d\phi d\theta k^2 \sin\theta \int dE t (f_1 - f_2) \\ &= \frac{-em}{\pi^2 \hbar^3} \int_0^{\frac{\pi}{2}} d\theta \sin\theta \int_{U_0}^{\infty} dE (E - U_0) t (f_1 - f_2). \end{aligned} \tag{151}$$

It can be seen from Eq. 151 that the tunneling currents account for all the contribution of electrons from different energy levels and injection angles in the metal contact.

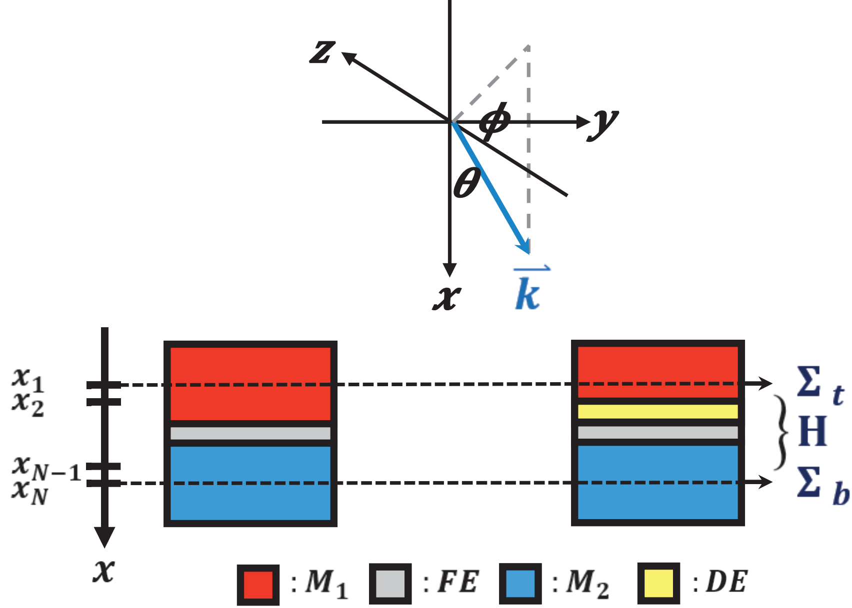

Figure 80: Schematics of illustrating the electron wave vector in the spherical coordinate and the NEGF approach to FTJs without and with a non-polar DE layer between the FE and metal electrode.

C.3 Device Hamiltonian and Contact Self-energy

The device Hamiltonian, **H**, is constructed based on a single-band effective mass Hamiltonian operator of an electron given as

$$\hat{H} = \frac{-\hbar^2}{2m^*}\frac{\partial^2}{\partial x^2} + \frac{\hbar^2\left(k_y^2 + k_z^2\right)}{2m^*} + U\left(x\right), \tag{152}$$

where $U\left(x\right)$ is the energy band diagram of an FTJ. Note that in this approach, a space-independent effective mass, m^*, is used to characterize the quantum-mechanical tunneling process in the thin-film device. Therefore, by considering an electron coming from $+x$ with total energy, E, equal to $E = \frac{\hbar^2 k^2}{2m^*} + U_0$, the operator can be

rewritten using Fig. 80 and is given as

$$
\begin{aligned}
\hat{H} &= \frac{-\hbar^2}{2m^*}\frac{\partial^2}{\partial x^2} + (E - U_0)\sin^2\theta + U(x) \\
&= \frac{-\hbar^2}{2m^*}\frac{\partial^2}{\partial x^2} + E_\perp(\theta) + U(x),
\end{aligned}
\tag{153}
$$

where $E_\perp$ is the transverse energy of the electron, which depends on the injection angle, θ. The device Hamiltonian can be obtained by simply converting $\hat{H}$ into a matrix using the finite difference method and is given as

$$
\mathbf{H} = \begin{bmatrix}
2t + E_\perp(\theta) + U(x_1) & -t & 0 & \cdots & \cdots & 0 & 0 & 0 \\
-t & 2t + E_\perp(\theta) + U(x_2) & -t & 0 & \cdots & \cdots & 0 & 0 \\
\vdots & \vdots & \ddots & \ddots & \ddots & \ddots & \vdots & \vdots \\
0 & 0 & \cdots & \cdots & 0 & -t & 2t + E_\perp(\theta) + U(x_{N-1}) & -t \\
0 & 0 & 0 & \cdots & \cdots & 0 & -t & 2t + E_\perp(\theta) + U(x_N),
\end{bmatrix},
\tag{154}
$$

where the x axis is divided into N mesh points, x_1, x_2, $\cdots$, x_{N-1}, and x_N, and t is the coupling strength between the nearest neighbors defined as $t = \frac{\hbar^2}{2m^* a^2}$ with a being the distance between two nearest mesh points, which is set as 0.1 nm in the main text. Under the open boundary condition, the self-energies of top and bottom

contacts are given as

$$\mathbf{\Sigma_t} = \begin{bmatrix} -te^{ik_{x,t}a} & 0 & \cdots \\ 0 & 0 & \\ \vdots & & \ddots \end{bmatrix},$$
$$\mathbf{\Sigma_b} = \begin{bmatrix} \ddots & & \vdots \\ & 0 & 0 \\ \cdots & 0 & -te^{ik_{x,b}a} \end{bmatrix}, \tag{155}$$

where $k_{x,t}$ and $k_{x,b}$ are longitudinal electron wave vectors inside top and bottom electrodes, respectively, given as

$$k_{x,t} = \frac{\cos^{-1}\left\{1 - \frac{E-U(x_1)-E_\perp(\theta)}{2t}\right\}}{a}, \tag{156}$$
$$k_{x,b} = \frac{\cos^{-1}\left\{1 - \frac{E-U(x_N)-E_\perp(\theta)}{2t}\right\}}{a}. \tag{157}$$

In addition to TER in FTJs, the same approach can also be applied to other problems such as spin injection from a ferromagnet into a semiconductor or a metal [28, 29], as long as the energy band diagram is known.

REFERENCES

[1] Acremann, Y., Strachan, J. P., Chembrolu, V., Andrews, S. D., Tyliszczak, T., Katine, J. A., Carey, M. J., Clemens, B. M., Siegmann, H. C., and Stöhr, J., “Time-resolved imaging of spin transfer switching: Beyond the macrospin concept,” *Phys. Rev. Lett.*, vol. 96, p. 217202, May 2006.

[2] Akinaga, H. and Shima, H., “Resistive random access memory (reram) based on metal oxides,” *Proceedings of the IEEE*, vol. 98, pp. 2237–2251, Dec 2010.

[3] Alijani, V., Winterlik, J., Fecher, G. H., and Felser, C., “Tuning the magnetism of the heusler alloys mn3-xcoxga from soft and half-metallic to hard-magnetic for spin-transfer torque applications,” *Applied Physics Letters*, vol. 99, no. 22, pp. –, 2011.

[4] Alzate, J., Amiri, P., Upadhyaya, P., Cherepov, S., Zhu, J., Lewis, M., Dorrance, R., Katine, J., Langer, J., Galatsis, K., Markovic, D., Krivorotov, I., and Wang, K., “Voltage-induced switching of nanoscale magnetic tunnel junctions,” in *Electron Devices Meeting (IEDM), 2012 IEEE International*, pp. 29.5.1–29.5.4, Dec 2012.

[5] Aono, M. and Hasegawa, T., “The atomic switch,” *Proceedings of the IEEE*, vol. 98, pp. 2228–2236, Dec 2010.

[6] Avci, U. E., Morris, D. H., and Young, I. A., “Tunnel field-effect transistors: Prospects and challenges,” *IEEE Journal of the Electron Devices Society*, vol. 3, pp. 88–95, May 2015.

[7] Bass, J. and Jr., W. P., “Current-perpendicular (cpp) magnetoresistance in magnetic metallic multilayers,” *Journal of Magnetism and Magnetic Materials*, vol. 200, no. 13, pp. 274 – 289, 1999.

[8] Behin-Aein, B., Datta, D., Salahuddin, S., and Datta, S., “Proposal for an all-spin logic device with built-in memory,” *Nature Nanotechnology*, vol. 5, pp. 266–270, 2010.

[9] Behin-Aein, B., Sarkar, A., Srinivasan, S., and Datta, S., “Switching energy-delay of all spin logic devices,” *Applied Physics Letters*, vol. 98, no. 12, 2011.

[10] Beleggia, M., Graef, M. D., and Millev, Y. T., “The equivalent ellipsoid of a magnetized body,” *Journal of Physics D: Applied Physics*, vol. 39, no. 5, p. 891, 2006.

[11] Berger, L., "Exchange interaction between ferromagnetic domain wall and electric current in very thin metallic films," *Journal of Applied Physics*, vol. 55, no. 6, pp. 1954–1956, 1984.

[12] Bonhomme, P., Manipatruni, S., Iraei, R. M., Rakheja, S., Chang, S. C., Nikonov, D. E., Young, I. A., and Naeemi, A., "Circuit simulation of magnetization dynamics and spin transport," *IEEE Transactions on Electron Devices*, vol. 61, pp. 1553–1560, May 2014.

[13] Brataas, A., Bauer, G. E., and Kelly, P. J., "Non-collinear magnetoelectronics," *Physics Reports*, vol. 427, no. 4, pp. 157 – 255, 2006.

[14] Bratkovsky, A. M., "Tunneling of electrons in conventional and half-metallic systems: Towards very large magnetoresistance," *Phys. Rev. B*, vol. 56, pp. 2344–2347, Aug 1997.

[15] Bratkovsky, A. M., "Spintronic effects in metallic, semiconductor, metaloxide and metalsemiconductor heterostructures," *Reports on Progress in Physics*, vol. 71, no. 2, p. 026502, 2008.

[16] Brintlinger, T., Lim, S.-H., Baloch, K. H., Alexander, P., Qi, Y., Barry, J., Melngailis, J., Salamanca-Riba, L., Takeuchi, I., and Cumings, J., "In situ observation of reversible nanomagnetic switching induced by electric fields," *Nano Letters*, vol. 10, no. 4, pp. 1219–1223, 2010. PMID: 20199031.

[17] Bromberg, D., Morris, D., Pileggi, L., and Zhu, J.-G., "Novel stt-mtj device enabling all-metallic logic circuits," *Magnetics, IEEE Transactions on*, vol. 48, pp. 3215–3218, Nov 2012.

[18] Brown, W., *Micromagnetics*. Interscience tracts on physics and astronomy, Interscience Publishers, 1963.

[19] Brown, W. F., "Thermal fluctuations of a single-domain particle," *Phys. Rev.*, vol. 130, pp. 1677–1686, Jun 1963.

[20] Brown, W. F., "Thermal fluctuations of a singledomain particle," *Journal of Applied Physics*, vol. 34, no. 4, pp. 1319–1320, 1963.

[21] Butler, W. H., Zhang, X.-G., Schulthess, T. C., and MacLaren, J. M., "Spin-dependent tunneling conductance of Fe|MgO|Fe sandwiches," *Phys. Rev. B*, vol. 63, p. 054416, Jan 2001.

[22] Cai, T., Ju, S., Lee, J., Sai, N., Demkov, A. A., Niu, Q., Li, Z., Shi, J., and Wang, E., "Magnetoelectric coupling and electric control of magnetization in ferromagnet/ferroelectric/normal-metal superlattices," *Phys. Rev. B*, vol. 80, p. 140415, Oct 2009.

[23] Calayir, V., Nikonov, D., Manipatruni, S., and Young, I., "Static and clocked spintronic circuit design and simulation with performance analysis relative to cmos," *Circuits and Systems I: Regular Papers, IEEE Transactions on*, vol. 61, pp. 393–406, Feb 2014.

[24] Camsari, K. Y., Ganguly, S., and Datta, S., "Modular approach to spintronics," *Scientific Reports*, vol. 5, pp. 10571 EP –, Jun 2015. Article.

[25] Chang, S., Dutta, S., Manipatruni, S., Nikonov, D., Young, I., and Naeemi, A., "Interconnects for all-spin logic using automotion of domain walls," *Exploratory Solid-State Computational Devices and Circuits, IEEE Journal on*, vol. PP, no. 99, pp. 1–1, 2015.

[26] Chang, S. C., Kani, N., Manipatruni, S., Nikonov, D. E., Young, I. A., and Naeemi, A., "Scaling limits on all-spin logic," *IEEE Transactions on Magnetics*, vol. 52, pp. 1–4, July 2016.

[27] Chang, S. C., Manipatruni, S., Nikonov, D., and Young, I., "Clocked domain wall logic using magnetoelectric effects," *IEEE Journal on Exploratory Solid-State Computational Devices and Circuits*, vol. PP, no. 99, pp. 1–1, 2016.

[28] Chang, S.-C., Iraei, R., Manipatruni, S., Nikonov, D., Young, I., and Naeemi, A., "Design and analysis of copper and aluminum interconnects for all-spin logic," *Electron Devices, IEEE Transactions on*, vol. 61, pp. 2905–2911, Aug 2014.

[29] Chang, S.-C., Manipatruni, S., Nikonov, D., Young, I., and Naeemi, A., "Design and analysis of si interconnects for all-spin logic," *Magnetics, IEEE Transactions on*, vol. 50, pp. 1–13, Sept 2014.

[30] Chang, S.-C. C., Manipatruni, S., E. Nikonov, D., A. Young, I., and Naeemi, A., "Low-power spin valve logic using spin-transfer torque with automotion of domain walls," *arXiv:1609.06281*, 2016.

[31] Chang, S.-C. C., Naeemi, A., Dmitri, E. N., and Gruverman, A., "Theoretical approach to electroresistance in ferroelectric tunnel junctions," *arXiv:1609.02991*, 2016.

[32] Chanthbouala, A., Crassous, A., Garcia, V., Bouzehouane, K., Fusil, S., Moya, X., Allibe, J., Dlubak, B., Grollier, J., Xavier, S., Deranlot, C., Moshar, A., Proksch, R., Mathur, N. D., Bibes, M., and Barthelemy, A., "Solid-state memories based on ferroelectric tunnel junctions," *Nat Nano*, vol. 7, pp. 101–104, Feb 2012.

[33] Chappert, C., Fert, A., and Van Dau, F. N., "The emergence of spin electronics in data storage," *Nat Mater*, vol. 6, pp. 813–823, Nov 2007.

[34] Chauleau, J.-Y., Weil, R., Thiaville, A., and Miltat, J., "Magnetic domain walls displacement: Automotion versus spin-transfer torque," *Phys. Rev. B*, vol. 82, p. 214414, Dec 2010.

[35] Chen, M. J., Chang, L. M., Kuang, S. J., Lee, C. W., Hsieh, S. H., Wang, C. A., Chang, S. C., and Lee, C. C., "Temperature-oriented mobility measurement and simulation to assess surface roughness in ultrathin-gate-oxide (1 nm) nmosfets and its tem evidence," *IEEE Transactions on Electron Devices*, vol. 59, pp. 949–955, April 2012.

[36] Chen, M. J., Chang, S. C., Kuang, S. J., Lee, C. C., Lee, W. H., Cheng, K. H., and Zhan, Y. H., "Temperature-dependent remote-coulomb-limited electron mobility in n+ -polysilicon ultrathin gate oxide nmosfets," *IEEE Transactions on Electron Devices*, vol. 58, pp. 1038–1044, April 2011.

[37] Chen, Y., Fitchorov, T., Vittoria, C., and Harris, V. G., "Electrically controlled magnetization switching in a multiferroic heterostructure," *Applied Physics Letters*, vol. 97, no. 5, pp. –, 2010.

[38] Chern, J.-H., Huang, J., Arledge, L., Li, P.-C., and Ping Yang, B., "Multilevel metal capacitance models for cad design synthesis systems," *Electron Device Letters, IEEE*, vol. 13, pp. 32–34, Jan 1992.

[39] Chung, N. L., Jalil, M. B. A., and Tan, S. G., "The effects of schottky barrier profile on spin dependent tunneling in a ferromagnet-insulator-semiconductor system," *Journal of Applied Physics*, vol. 108, no. 3, 2010.

[40] Cohen, R. E., "Origin of ferroelectricity in perovskite oxides," *Nature*, vol. 358, pp. 136–138, Jul 1992.

[41] Cowburn, R. P. and Welland, M. E., "Room temperature magnetic quantum cellular automata," *Science*, vol. 287, no. 5457, pp. 1466–1468, 2000.

[42] Currivan, J., Jang, Y., Mascaro, M., Baldo, M., and Ross, C., "Low energy magnetic domain wall logic in short, narrow, ferromagnetic wires," *Magnetics Letters, IEEE*, vol. 3, pp. 3000104–3000104, 2012.

[43] dAquino, M., Serpico, C., Coppola, G., Mayergoyz, I. D., and Bertotti, G., "Midpoint numerical technique for stochastic landau-lifshitz-gilbert dynamics," *Journal of Applied Physics*, vol. 99, no. 8, 2006.

[44] Dash, S. P., Sharma, S., Patel, R. S., de Jong, M. P., and Jansen, R., "Electrical creation of spin polarization in silicon at room temperature," *Nature*, vol. 462, pp. 491–494, Nov 2009.

[45] Datta, D., Behin-Aein, B., Datta, S., and Salahuddin, S., "Voltage asymmetry of spin-transfer torques," *IEEE Transactions on Nanotechnology*, vol. 11, pp. 261–272, March 2012.

[46] Datta, S., *Quantum transport: atom to transistor.* Cambridge University Press, 2005.

[47] Datta, S., Salahuddin, S., and Behin-Aein, B., "Non-volatile spin switch for boolean and non-boolean logic," *Applied Physics Letters*, vol. 101, no. 25, pp. –, 2012.

[48] Dawber, M., Rabe, K. M., and Scott, J. F., "Physics of thin-film ferroelectric oxides," *Rev. Mod. Phys.*, vol. 77, pp. 1083–1130, Oct 2005.

[49] Dennard, R. H., Gaensslen, F. H., Kuhn, L., and Yu, H. N., "Design of micron mos switching devices," in *Electron Devices Meeting, 1972 International*, vol. 18, pp. 168–170, 1972.

[50] Dery, H., Song, Y., Li, P., and Zuti, I., "Silicon spin communication," *Applied Physics Letters*, vol. 99, no. 8, 2011.

[51] Donahue, M. J. and Porter, D. G., "Oommf users guide," *National Institute of Standards and Technology Interagency*, 1999.

[52] Dutta, S., Chang, S.-C., Kani, N., Nikonov, D. E., Manipatruni, S., Young, I. A., and Naeemi, A., "Non-volatile clocked spin wave interconnect for beyond-cmos nanomagnet pipelines," *Scientific Reports*, vol. 5, pp. 9861 EP –, May 2015. Article.

[53] Elliott, R. J., "Theory of the effect of spin-orbit coupling on magnetic resonance in some semiconductors," *Phys. Rev.*, vol. 96, pp. 266–279, Oct 1954.

[54] Eltschka, M., Wötzel, M., Rhensius, J., Krzyk, S., Nowak, U., Kläui, M., Kasama, T., Dunin-Borkowski, R. E., Heyderman, L. J., van Driel, H. J., and Duine, R. A., "Nonadiabatic spin torque investigated using thermally activated magnetic domain wall dynamics," *Phys. Rev. Lett.*, vol. 105, p. 056601, Jul 2010.

[55] Esaki, L., Laibowitz, R. B., and Stiles, P. J., "Polar switch," *IBM Tech. Discl. Bull.*, 1971.

[56] Feng, M., Wang, J.-j., Hu, J.-M., Wang, J., Ma, J., Li, H.-B., Shen, Y., Lin, Y.-H., Chen, L.-Q., and Nan, C.-W., "Optimizing direct magnetoelectric coupling in pb(zr,ti)o3/ni multiferroic film heterostructures," *Applied Physics Letters*, vol. 106, no. 7, pp. –, 2015.

[57] Fert, A., George, J. M., Jaffres, H., and Mattana, R., "Semiconductors between spin-polarized sources and drains," *IEEE Transactions on Electron Devices*, vol. 54, pp. 921–932, May 2007.

[58] Fert, A. and Jaffrès, H., "Conditions for efficient spin injection from a ferromagnetic metal into a semiconductor," *Phys. Rev. B*, vol. 64, p. 184420, Oct 2001.

[59] FIDLER, J. and SCHREFL, T., "Micromagnetic modelling - the current state of the art," *Journal of Physics D: Applied Physics*, vol. 33, no. 15, p. R135, 2000.

[60] FIEBIG, M., "Revival of the magnetoelectric effect," *Journal of Physics D: Applied Physics*, vol. 38, no. 8, p. R123, 2005.

[61] FITCHOROV, T., CHEN, Y., HU, B., GILLETTE, S. M., GEILER, A., VITTORIA, C., and HARRIS, V. G., "Tunable fringe magnetic fields induced by converse magnetoelectric coupling in a fega/pmn-pt multiferroic heterostructure," *Journal of Applied Physics*, vol. 110, no. 12, pp. –, 2011.

[62] FONG, D. D., STEPHENSON, G. B., STREIFFER, S. K., EASTMAN, J. A., AUCIELLO, O., FUOSS, P. H., and THOMPSON, C., "Ferroelectricity in ultrathin perovskite films," *Science*, vol. 304, no. 5677, pp. 1650–1653, 2004.

[63] FRANK, D. J., "Power-constrained cmos scaling limits," *IBM Journal of Research and Development*, vol. 46, pp. 235–244, March 2002.

[64] GADEKAR, S. N. and RAMAKRISHNAN, T. V., "Why does devonshire's theory work so well," *Ferroelectrics*, vol. 35, no. 1, pp. 249–249, 1981.

[65] GAJEK, M., BIBES, M., FUSIL, S., BOUZEHOUANE, K., FONTCUBERTA, J., BARTHELEMY, A., and FERT, A., "Tunnel junctions with multiferroic barriers," *Nat Mater*, vol. 6, pp. 296–302, Apr 2007.

[66] GARANIN, D. A., "Fokker-planck and landau-lifshitz-bloch equations for classical ferromagnets," *Phys. Rev. B*, vol. 55, pp. 3050–3057, Feb 1997.

[67] GARCIA, V. and BIBES, M., "Ferroelectric tunnel junctions for information storage and processing," *Nat Commun*, vol. 5, Jul 2014. Review.

[68] GERRA, G., TAGANTSEV, A. K., and SETTER, N., "Ferroelectricity in asymmetric metal-ferroelectric-metal heterostructures: A combined first-principles˘phenomenological approach," *Phys. Rev. Lett.*, vol. 98, p. 207601, May 2007.

[69] GERRA, G., TAGANTSEV, A. K., SETTER, N., and PARLINSKI, K., "Ionic polarizability of conductive metal oxides and critical thickness for ferroelectricity in batio$_3$," *Phys. Rev. Lett.*, vol. 96, p. 107603, Mar 2006.

[70] GILBERT, T. L., "A phenomenological theory of damping in ferromagnetic materials," *IEEE Transactions on Magnetics*, vol. 40, pp. 3443–3449, Nov 2004.

[71] GILMORE, K., IDZERDA, Y. U., and STILES, M. D., "Identification of the dominant precession-damping mechanism in fe, co, and ni by first-principles calculations," *Phys. Rev. Lett.*, vol. 99, p. 027204, Jul 2007.

[72] GOUSSEV, A., LUND, R. G., ROBBINS, J. M., SLASTIKOV, V., and SONNENBERG, C., "Fast domain-wall propagation in uniaxial nanowires with transverse fields," *Phys. Rev. B*, vol. 88, p. 024425, Jul 2013.

[73] Graf, T., Parkin, S. S., and Felser, C., "Heusler compounds – a material class with exceptional properties," *Magnetics, IEEE Transactions on*, vol. 47, pp. 367–373, Feb 2011.

[74] Grenet, L., Jamet, M., No, P., Calvo, V., Hartmann, J.-M., Nistor, L. E., Rodmacq, B., Auffret, S., Warin, P., and Samson, Y., "Spin injection in silicon at zero magnetic field," *Applied Physics Letters*, vol. 94, no. 3, 2009.

[75] Gruverman, A., Wu, D., Lu, H., Wang, Y., Jang, H. W., Folkman, C. M., Zhuravlev, M. Y., Felker, D., Rzchowski, M., Eom, C.-B., and Tsymbal, E. Y., "Tunneling electroresistance effect in ferroelectric tunnel junctions at the nanoscale," *Nano Letters*, vol. 9, no. 10, pp. 3539–3543, 2009.

[76] Gunnarsson, O. and Lundqvist, B. I., "Exchange and correlation in atoms, molecules, and solids by the spin-density-functional formalism," *Phys. Rev. B*, vol. 13, pp. 4274–4298, May 1976.

[77] Gupta, P. and Kahng, A. B., "Manufacturing-aware physical design," in *Proceedings of the 2003 IEEE/ACM International Conference on Computer-aided Design*, ICCAD '03, (Washington, DC, USA), pp. 681–, IEEE Computer Society, 2003.

[78] Haney, P., Duine, R., Nez, A., and MacDonald, A., "Current-induced torques in magnetic metals: Beyond spin-transfer," *Journal of Magnetism and Magnetic Materials*, vol. 320, no. 7, pp. 1300 – 1311, 2008.

[79] Haron, N. Z. and Hamdioui, S., "Why is cmos scaling coming to an end?," in *2008 3rd International Design and Test Workshop*, pp. 98–103, Dec 2008.

[80] He, X., Wang, Y., Wu, N., Caruso, A. N., Vescovo, E., Belashchenko, K. D., Dowben, P. A., and Binek, C., "Robust isothermal electric control of exchange bias at room temperature," *Nat Mater*, vol. 9, pp. 579–585, Jul 2010.

[81] Heinrich, B., Tserkovnyak, Y., Woltersdorf, G., Brataas, A., Urban, R., and Bauer, G. E. W., "Dynamic exchange coupling in magnetic bilayers," *Phys. Rev. Lett.*, vol. 90, p. 187601, May 2003.

[82] Heron, J. T., Bosse, J. L., He, Q., Gao, Y., Trassin, M., Ye, L., Clarkson, J. D., Wang, C., Liu, J., Salahuddin, S., Ralph, D. C., Schlom, D. G., Iniguez, J., Huey, B. D., and Ramesh, R., "Deterministic switching of ferromagnetism at room temperature using an electric field," *Nature*, vol. 516, pp. 370–373, Dec 2014. Letter.

[83] Heron, J. T., Trassin, M., Ashraf, K., Gajek, M., He, Q., Yang, S. Y., Nikonov, D. E., Chu, Y.-H., Salahuddin, S., and Ramesh, R., "Electric-field-induced magnetization reversal in a ferromagnet-multiferroic heterostructure," *Phys. Rev. Lett.*, vol. 107, p. 217202, Nov 2011.

[84] Hickey, M. C. and Moodera, J. S., “Origin of intrinsic gilbert damping,” *Phys. Rev. Lett.*, vol. 102, p. 137601, Mar 2009.

[85] Hisamoto, D., Lee, W.-C., Kedzierski, J., Takeuchi, H., Asano, K., Kuo, C., Anderson, E., King, T.-J., Bokor, J., and Hu, C., “Finfet-a self-aligned double-gate mosfet scalable to 20 nm,” *IEEE Transactions on Electron Devices*, vol. 47, pp. 2320–2325, Dec 2000.

[86] Hlinka, J. and Márton, P., “Phenomenological model of a 90 degree domain wall in $BaTio_3$-type ferroelectrics,” *Phys. Rev. B*, vol. 74, p. 104104, Sep 2006.

[87] Hoffmann, A. and Bader, S. D., “Opportunities at the frontiers of spintronics,” *Phys. Rev. Applied*, vol. 4, p. 047001, Oct 2015.

[88] Hong, J. and Fang, D., “Size-dependent ferroelectric behaviors of batio3 nanowires,” *Applied Physics Letters*, vol. 92, no. 1, pp. –, 2008.

[89] Horley, P. P., Sukhov, A., Jia, C., Martínez, E., and Berakdar, J., “Influence of magnetoelectric coupling on electric field induced magnetization reversal in a composite unstrained multiferroic chain,” *Phys. Rev. B*, vol. 85, p. 054401, Feb 2012.

[90] Hu, J., Haratipour, N., and Koester, S. J., “The effect of output-input isolation on the scaling and energy consumption of all-spin logic devices,” *Journal of Applied Physics*, vol. 117, no. 17, pp. –, 2015.

[91] Ikeda, S., Hayakawa, J., Ashizawa, Y., Lee, Y. M., Miura, K., Hasegawa, H., Tsunoda, M., Matsukura, F., and Ohno, H., “Tunnel magnetoresistance of 604ta diffusion in cofeb-mgo-cofeb pseudo-spin-valves annealed at high temperature,” *Applied Physics Letters*, vol. 93, no. 8, 2008.

[92] Ionescu, A. M., “Nanoelectronics: Ferroelectric devices show potential,” *Nat Nano*, vol. 7, pp. 83–85, Feb 2012.

[93] Jain, A., Rojas-Sanchez, J.-C., Cubukcu, M., Peiro, J., Le Breton, J. C., Prestat, E., Vergnaud, C., Louahadj, L., Portemont, C., Ducruet, C., Baltz, V., Barski, A., Bayle-Guillemaud, P., Vila, L., Attané, J.-P., Augendre, E., Desfonds, G., Gambarelli, S., Jaffrès, H., George, J.-M., and Jamet, M., “Crossover from spin accumulation into interface states to spin injection in the germanium conduction band,” *Phys. Rev. Lett.*, vol. 109, p. 106603, Sep 2012.

[94] Jamal Berakdar, J. K., ed., *Correlation Spectroscopy of Surfaces, Thin Films, and Nanostructures.* Wiley Online Library, 2005.

[95] Jansen, R., Dash, S. P., Sharma, S., and Min, B. C., “Silicon spintronics with ferromagnetic tunnel devices,” *Semiconductor Science and Technology*, vol. 27, no. 8, p. 083001, 2012.

[96] Jansen, R., Min, B. C., Dash, S. P., Sharma, S., Kioseoglou, G., Hanbicki, A. T., van 't Erve, O. M. J., Thompson, P. E., and Jonker, B. T., "Electrical spin injection into moderately doped silicon enabled by tailored interfaces," *Phys. Rev. B*, vol. 82, p. 241305, Dec 2010.

[97] Jia, C.-L., Wei, T.-L., Jiang, C.-J., Xue, D.-S., Sukhov, A., and Berakdar, J., "Mechanism of interfacial magnetoelectric coupling in composite multiferroics," *Phys. Rev. B*, vol. 90, p. 054423, Aug 2014.

[98] Jia, C., Wang, F., Jiang, C., Berakdar, J., and Xue, D., "Electric tuning of magnetization dynamics and electric field-induced negative magnetic permeability in nanoscale composite multiferroics," *Scientific Reports*, vol. 5, pp. 11111 EP –, Jun 2015. Article.

[99] Jo, J. Y., Han, H. S., Yoon, J.-G., Song, T. K., Kim, S.-H., and Noh, T. W., "Domain switching kinetics in disordered ferroelectric thin films," *Phys. Rev. Lett.*, vol. 99, p. 267602, Dec 2007.

[100] Johnson, M. and Silsbee, R. H., "Thermodynamic analysis of interfacial transport and of the thermomagnetoelectric system," *Phys. Rev. B*, vol. 35, pp. 4959–4972, Apr 1987.

[101] Jones, R. O. and Gunnarsson, O., "The density functional formalism, its applications and prospects," *Rev. Mod. Phys.*, vol. 61, pp. 689–746, Jul 1989.

[102] Jonker, B. T., Kioseoglou, G., Hanbicki, A. T., Li, C. H., and Thompson, P. E., "Electrical spin-injection into silicon from a ferromagnetic metal/tunnel barrier contact," *Nat Phys*, vol. 3, pp. 542–546, Aug 2007.

[103] Joyce, W. B. and Dixon, R. W., "Analytic approximations for the fermi energy of an ideal fermi gas," *Applied Physics Letters*, vol. 31, no. 5, pp. 354–356, 1977.

[104] Jungwirth, T., Marti, X., Wadley, P., and Wunderlich, J., "Antiferromagnetic spintronics," *Nat Nano*, vol. 11, pp. 231–241, Mar 2016. Review.

[105] Junquera, J. and Ghosez, P., "First-principles study of ferroelectric oxide epitaxial thin films and superlattices: Role of the mechanical and electrical boundary conditions," *Journal of Computational and Theoretical Nanoscience*, vol. 5, no. 11, pp. 2071–2088, 2008.

[106] Kahng, A. B., Park, C.-H., Xu, X., and Yao, H., "Layout decomposition for double patterning lithography," in *Proceedings of the 2008 IEEE/ACM International Conference on Computer-Aided Design*, ICCAD '08, (Piscataway, NJ, USA), pp. 465–472, IEEE Press, 2008.

[107] Kamberský, V., "On ferromagnetic resonance damping in metals," *Czechoslovak Journal of Physics B*, vol. 26, no. 12, pp. 1366–1383, 1976.

[108] Kani, N., Chang, S.-C., Dutta, S., and Naeemi, A., "A model study of an error-free magnetization reversal through dipolar coupling in a two-magnet system," *Magnetics, IEEE Transactions on*, vol. PP, no. 99, pp. 1–1, 2015.

[109] Karin M. Rabe, Charles H. Ahn, J.-M. T., ed., *Physics of Ferroelectrics*. Springer, 2007.

[110] Kawahara, T., Ito, K., Takemura, R., and Ohno, H., "Spin-transfer torque {RAM} technology: Review and prospect," *Microelectronics Reliability*, vol. 52, no. 4, pp. 613 – 627, 2012. Advances in non-volatile memory technology.

[111] Kawaura, H., Sakamoto, T., and Baba, T., "Observation of source-to-drain direct tunneling current in 8 nm gate electrically variable shallow junction metaloxidesemiconductor field-effect transistors," *Applied Physics Letters*, vol. 76, no. 25, pp. 3810–3812, 2000.

[112] Kepler, R. G., "Piezoelectricity, pyroelectricity, and ferroelectricity in organic materials," *Annual Review of Physical Chemistry*, vol. 29, no. 1, pp. 497–518, 1978.

[113] Khitun, A., Nikonov, D. E., and Wang, K. L., "Magnetoelectric spin wave amplifier for spin wave logic circuits," *Journal of Applied Physics*, vol. 106, no. 12, 2009.

[114] Khvalkovskiy, A. V., Zvezdin, K. A., Gorbunov, Y. V., Cros, V., Grollier, J., Fert, A., and Zvezdin, A. K., "High domain wall velocities due to spin currents perpendicular to the plane," *Phys. Rev. Lett.*, vol. 102, p. 067206, Feb 2009.

[115] Kim, D. J., Lu, H., Ryu, S., Bark, C.-W., Eom, C.-B., Tsymbal, E. Y., and Gruverman, A., "Ferroelectric tunnel memristor," *Nano Letters*, vol. 12, no. 11, pp. 5697–5702, 2012. PMID: 23039785.

[116] Kim, J., Paul, A., Crowell, P., Koester, S., Sapatnekar, S., Wang, J.-P., and Kim, C., "Spin-based computing: Device concepts, current status, and a case study on a high-performance microprocessor," *Proceedings of the IEEE*, vol. 103, pp. 106–130, Jan 2015.

[117] Kim, N. S., Austin, T., Baauw, D., Mudge, T., Flautner, K., Hu, J. S., Irwin, M. J., Kandemir, M., and Narayanan, V., "Leakage current: Moore's law meets static power," *Computer*, vol. 36, pp. 68–75, Dec 2003.

[118] Kim, Y. S., Kim, D. H., Kim, J. D., Chang, Y. J., Noh, T. W., Kong, J. H., Char, K., Park, Y. D., Bu, S. D., Yoon, J.-G., and Chung, J.-S., "Critical thickness of ultrathin ferroelectric batio3 films," *Applied Physics Letters*, vol. 86, no. 10, 2005.

[119] Kioseoglou, G., Hanbicki, A. T., Goswami, R., van t Erve, O. M. J., Li, C. H., Spanos, G., Thompson, P. E., and Jonker, B. T., "Electrical spin injection into si: A comparison between fe/si schottky and fe/al2o3 tunnel contacts," *Applied Physics Letters*, vol. 94, no. 12, 2009.

[120] Kittel, C., *Introduction to Solid State Physics*. New York: John Wiley & Sons, Inc., 6th ed., 1986.

[121] Kodera, H., "Effect of doping on the electron spin resonance in phosphorus doped silicon. iii. absorption intensity," *Journal of the Physical Society of Japan*, vol. 26, no. 2, pp. 377–380, 1969.

[122] Kohlstedt, H., Pertsev, N. A., Rodríguez Contreras, J., and Waser, R., "Theoretical current-voltage characteristics of ferroelectric tunnel junctions," *Phys. Rev. B*, vol. 72, p. 125341, Sep 2005.

[123] Kohn, W. and Sham, L. J., "Self-consistent equations including exchange and correlation effects," *Phys. Rev.*, vol. 140, pp. A1133–A1138, Nov 1965.

[124] Kovalev, A. A., Bauer, G. E. W., and Brataas, A., "Perpendicular spin valves with ultrathin ferromagnetic layers: Magnetoelectronic circuit investigation of finite-size effects," *Phys. Rev. B*, vol. 73, p. 054407, Feb 2006.

[125] Kovalev, A. A., Brataas, A., and Bauer, G. E. W., "Spin transfer in diffusive ferromagnet˘normal metal systems with spin-flip scattering," *Phys. Rev. B*, vol. 66, p. 224424, Dec 2002.

[126] Lahtinen, T., Tuomi, J., and Van Dijken, S., "Electrical writing of magnetic domain patterns in ferromagnetic/ferroelectric heterostructures," *Magnetics, IEEE Transactions on*, vol. 47, pp. 3768–3771, Oct 2011.

[127] Lancaster, G., van Wyk, J. A., and Schneider, E. E., "Spin-lattice relaxation of conduction electrons in silicon," *Proceedings of the Physical Society*, vol. 84, no. 1, p. 19, 1964.

[128] Landauer, R., "Spatial variation of currents and fields due to localized scatterers in metallic conduction," *IBM Journal of Research and Development*, vol. 1, pp. 223–231, July 1957.

[129] Lee, D., Raghunathan, S., Wilson, R. J., Nikonov, D. E., Saraswat, K., and Wang, S. X., "The influence of fermi level pinning/depinning on the schottky barrier height and contact resistance in ge/cofeb and ge/mgo/cofeb structures," *Applied Physics Letters*, vol. 96, no. 5, 2010.

[130] Lee, H., Alzate, J., Dorrance, R., Cai, X. Q., Markovic, D., Khalili Amiri, P., and Wang, K., "Design of a fast and low-power sense amplifier and writing circuit for high-speed mram," *Magnetics, IEEE Transactions on*, vol. 51, pp. 1–7, May 2015.

[131] Lépine, D. J., "Spin resonance of localized and delocalized electrons in phosphorus-doped silicon between 20 and 30 k," *Phys. Rev. B*, vol. 2, pp. 2429–2439, Oct 1970.

[132] Li, C. H., van 't Erve, O. M. J., and Jonker, B. T., "Electrical injection and detection of spin accumulation in silicon at 500 k with magnetic metal/silicon dioxide contacts," *Nature Communications*, vol. 2, pp. 245 EP –, Mar 2011. Article.

[133] Li, Y., Barra, A.-L., Auffret, S., Ebels, U., and Bailey, W. E., "Inertial terms to magnetization dynamics in ferromagnetic thin films," *Phys. Rev. B*, vol. 92, p. 140413, Oct 2015.

[134] Li, Z. and Zhang, S., "Domain-wall dynamics and spin-wave excitations with spin-transfer torques," *Phys. Rev. Lett.*, vol. 92, p. 207203, May 2004.

[135] Lichtensteiger, C., Triscone, J.-M., Junquera, J., and Ghosez, P., "Ferroelectricity and tetragonality in ultrathin $pbtio_3$ films," *Phys. Rev. Lett.*, vol. 94, p. 047603, Feb 2005.

[136] Liu, M., Cai, M., and Taur, Y., "Scaling limit of cmos supply voltage from noise margin considerations," in *2006 International Conference on Simulation of Semiconductor Processes and Devices*, pp. 287–289, Sept 2006.

[137] Liu, Y., Lou, X., Bibes, M., and Dkhil, B., "Effect of a built-in electric field in asymmetric ferroelectric tunnel junctions," *Phys. Rev. B*, vol. 88, p. 024106, Jul 2013.

[138] Luo, C., Feng, Z., Fu, Y., Zhang, W., Wong, P. K. J., Kou, Z. X., Zhai, Y., Ding, H. F., Farle, M., Du, J., and Zhai, H. R., "Enhancement of magnetization damping coefficient of permalloy thin films with dilute nd dopants," *Phys. Rev. B*, vol. 89, p. 184412, May 2014.

[139] Magen, N., Kolodny, A., Weiser, U., and Shamir, N., "Interconnect-power dissipation in a microprocessor," in *Proceedings of the 2004 International Workshop on System Level Interconnect Prediction*, SLIP '04, (New York, NY, USA), pp. 7–13, ACM, 2004.

[140] Malozemoff, A. and Slonczewski, J., *Magnetic domain walls in bubble materials*. Applied solid state science: Supplement, Academic Press, 1979.

[141] Manipatruni, S., Nikonov, D., and Young, I., "Modeling and design of spintronic integrated circuits," *Circuits and Systems I: Regular Papers, IEEE Transactions on*, vol. 59, pp. 2801–2814, Dec 2012.

[142] Manipatruni, S., Nikonov, D. E., and Young, I. A., "Material targets for scaling all-spin logic," *Phys. Rev. Applied*, vol. 5, p. 014002, Jan 2016.

[143] Mardana, A., Ducharme, S., and Adenwalla, S., "Ferroelectric control of magnetic anisotropy," *Nano Letters*, vol. 11, no. 9, pp. 3862–3867, 2011. PMID: 21823660.

[144] MaruyamaT., ShiotaY., NozakiT., OhtaK., TodaN., MizuguchiM., A., T., ShinjoT., ShiraishiM., MizukamiS., AndoY., and SuzukiY., "Large voltage-induced magnetic anisotropy change in a few atomic layers of iron," *Nat Nano*, vol. 4, pp. 158–161, Mar 2009.

[145] Matsukura, F., Tokura, Y., and Ohno, H., "Control of magnetism by electric fields," *Nat Nano*, vol. 10, pp. 209–220, Mar 2015. Review.

[146] Mayadas, A. F., Janak, J. F., and Gangulee, A., "Resistivity of permalloy thin films," *Journal of Applied Physics*, vol. 45, no. 6, pp. 2780–2781, 1974.

[147] McMichael, R. D. and Donahue, M. J., "Head to head domain wall structures in thin magnetic strips," *IEEE Transactions on Magnetics*, vol. 33, pp. 4167–4169, Sep 1997.

[148] McMichael, R. D., Twisselmann, D. J., and Kunz, A., "Localized ferromagnetic resonance in inhomogeneous thin films," *Phys. Rev. Lett.*, vol. 90, p. 227601, Jun 2003.

[149] Meir, Y. and Wingreen, N. S., "Landauer formula for the current through an interacting electron region," *Phys. Rev. Lett.*, vol. 68, pp. 2512–2515, Apr 1992.

[150] Merz, W. J., "Switching time in ferroelectric batio3 and its dependence on crystal thickness," *Journal of Applied Physics*, vol. 27, no. 8, pp. 938–943, 1956.

[151] Meservey, R., Tedrow, P. M., and Fulde, P., "Magnetic field splitting of the quasiparticle states in superconducting aluminum films," *Phys. Rev. Lett.*, vol. 25, pp. 1270–1272, Nov 1970.

[152] Miller, S. L. and McWhorter, P. J., "Physics of the ferroelectric nonvolatile memory field effect transistor," *Journal of Applied Physics*, vol. 72, no. 12, pp. 5999–6010, 1992.

[153] Miltat, J. E. and Donahue, M. J., *Numerical Micromagnetics: Finite Difference Methods*. John Wiley & Sons, Ltd, 2007.

[154] Min, B.-C., Motohashi, K., Lodder, C., and Jansen, R., "Tunable spin-tunnel contacts to silicon using low-work-function ferromagnets," *Nat Mater*, vol. 5, pp. 817–822, Oct 2006.

[155] Mizukami, S., Ando, Y., and Miyazaki, T., "Effect of spin diffusion on gilbert damping for a very thin permalloy layer in cu/permalloy/cu/pt films," *Phys. Rev. B*, vol. 66, p. 104413, Sep 2002.

[156] Moore, G. E., "Cramming more components onto integrated circuits," *Electronics*, vol. 38, pp. 114–117, Apr. 1965.

[157] Moriyama, T., Takei, S., Nagata, M., Yoshimura, Y., Matsuzaki, N., Terashima, T., Tserkovnyak, Y., and Ono, T., "Anti-damping spin transfer torque through epitaxial nickel oxide," *Applied Physics Letters*, vol. 106, no. 16, 2015.

[158] Myers, E. B., Ralph, D. C., Katine, J. A., Louie, R. N., and Buhrman, R. A., "Current-induced switching of domains in magnetic multilayer devices," *Science*, vol. 285, no. 5429, pp. 867–870, 1999.

[159] Nagarajan, V., Prasertchoung, S., Zhao, T., Zheng, H., Ouyang, J., Ramesh, R., Tian, W., Pan, X. Q., Kim, D. M., Eom, C. B., Kohlstedt, H., and Waser, R., "Size effects in ultrathin epitaxial ferroelectric heterostructures," *Applied Physics Letters*, vol. 84, no. 25, pp. 5225–5227, 2004.

[160] Nara, Y., Ootsuka, F., Inumiya, S., and Ohji, Y., "High-k/metal gate stack technology for advanced cmos," in *2006 8th International Conference on Solid-State and Integrated Circuit Technology Proceedings*, pp. 360–363, Oct 2006.

[161] Narendra, S. G., "Challenges and design choices in nanoscale cmos," *J. Emerg. Technol. Comput. Syst.*, vol. 1, pp. 7–49, Mar. 2005.

[162] Newell, A. J., Williams, W., and Dunlop, D. J., "A generalization of the demagnetizing tensor for nonuniform magnetization," *Journal of Geophysical Research: Solid Earth*, vol. 98, no. B6, pp. 9551–9555, 1993.

[163] Nikonov, D., Bourianoff, G., and Ghani, T., "Proposal of a spin torque majority gate logic," *Electron Device Letters, IEEE*, vol. 32, pp. 1128–1130, Aug 2011.

[164] Nikonov, D. and Young, I., "Overview of beyond-cmos devices and a uniform methodology for their benchmarking," *Proceedings of the IEEE*, vol. 101, pp. 2498–2533, Dec 2013.

[165] Nikonov, D. and Young, I., "Benchmarking of beyond-cmos exploratory devices for logic integrated circuits," *Exploratory Solid-State Computational Devices and Circuits, IEEE Journal on*, vol. 1, pp. 3–11, Dec 2015.

[166] Nikonov, D. E., Bourianoff, G. I., Rowlands, G., and Krivorotov, I. N., "Strategies and tolerances of spin transfer torque switching," *Journal of Applied Physics*, vol. 107, no. 11, 2010.

[167] Nikonov, D. E., Manipatruni, S., and Young, I. A., "Automotion of domain walls for spintronic interconnects," *Journal of Applied Physics*, vol. 115, no. 21, pp. –, 2014.

[168] Nikonov, D. E. and Young, I. A., "Benchmarking spintronic logic devices based on magnetoelectric oxides," *Journal of Materials Research*, vol. 29, pp. 2109–2115, 2014.

[169] Nowak, E. J., "Maintaining the benefits of cmos scaling when scaling bogs down," *IBM Journal of Research and Development*, vol. 46, pp. 169–180, March 2002.

[170] Pan, C. and Naeemi, A., "A proposal for energy-efficient cellular neural network based on spintronic devices," *IEEE Transactions on Nanotechnology*, vol. PP, no. 99, pp. 1–1, 2016.

[171] Pantel, D. and Alexe, M., "Electroresistance effects in ferroelectric tunnel barriers," *Phys. Rev. B*, vol. 82, p. 134105, Oct 2010.

[172] Park, B. G., Wunderlich, J., Martí, X., Holý, V., Kurosaki, Y., Yamada, M., Yamamoto, H., Nishide, A., Hayakawa, J., Takahashi, H., Shick, A. B., and Jungwirth, T., "A spin-valve-like magnetoresistance of an antiferromagnet-based tunnel junction," *Nat Mater*, vol. 10, pp. 347–351, May 2011.

[173] Parkin, S. S. P., Kaiser, C., Panchula, A., Rice, P. M., Hughes, B., Samant, M., and Yang, S.-H., "Giant tunnelling magnetoresistance at room temperature with mgo (100) tunnel barriers," *Nat Mater*, vol. 3, pp. 862–867, Dec 2004.

[174] Qi, Y. and Rappe, A. M., "Designing ferroelectric field-effect transistors based on the polarization-rotation effect for low operating voltage and fast switching," *Phys. Rev. Applied*, vol. 4, p. 044014, Oct 2015.

[175] Ragusa, C., d'Aquino, M., Serpico, C., Xie, B., Repetto, M., Bertotti, G., and Ansalone, D., "Full micromagnetic numerical simulations of thermal fluctuations," *Magnetics, IEEE Transactions on*, vol. 45, pp. 3919–3922, Oct 2009.

[176] Rakheja, S., Chang, S.-C., and Naeemi, A., "Impact of dimensional scaling and size effects on spin transport in copper and aluminum interconnects," *Electron Devices, IEEE Transactions on*, vol. 60, pp. 3913–3919, Nov 2013.

[177] Rakheja, S. and Naeemi, A., "Roles of doping, temperature, and electric field on spin transport through semiconducting channels in spin valves," *IEEE Transactions on Nanotechnology*, vol. 12, pp. 796–805, Sept 2013.

[178] Ralph, D. and Stiles, M., "Spin transfer torques," *Journal of Magnetism and Magnetic Materials*, vol. 320, no. 7, pp. 1190 – 1216, 2008.

[179] Ramesh, R. and Spaldin, N. A., "Multiferroics: progress and prospects in thin films," *Nat Mater*, vol. 6, pp. 21–29, Jan 2007.

[180] RASHBA, E. I., "Theory of electrical spin injection: Tunnel contacts as a solution of the conductivity mismatch problem," *Phys. Rev. B*, vol. 62, pp. R16267–R16270, Dec 2000.

[181] RIPPARD, W. H., PUFALL, M. R., KAKA, S., RUSSEK, S. E., and SILVA, T. J., "Direct-current induced dynamics in $co_{90}fe_{10}/ni_{80}fe_{20}$ point contacts," *Phys. Rev. Lett.*, vol. 92, p. 027201, Jan 2004.

[182] RIPPARD, W. H., PUFALL, M. R., KAKA, S., SILVA, T. J., and RUSSEK, S. E., "Current-driven microwave dynamics in magnetic point contacts as a function of applied field angle," *Phys. Rev. B*, vol. 70, p. 100406, Sep 2004.

[183] RODRIGUEZ CONTRERAS, J., KOHLSTEDT, H., POPPE, U., WASER, R., BUCHAL, C., and PERTSEV, N. A., "Resistive switching in metal-ferroelectricmetal junctions," *Applied Physics Letters*, vol. 83, no. 22, pp. 4595–4597, 2003.

[184] ROJAS-SÁNCHEZ, J.-C., CUBUKCU, M., JAIN, A., VERGNAUD, C., PORTEMONT, C., DUCRUET, C., BARSKI, A., MARTY, A., VILA, L., ATTANÉ, J.-P., AUGENDRE, E., DESFONDS, G., GAMBARELLI, S., JAFFRÈS, H., GEORGE, J.-M., and JAMET, M., "Spin pumping and inverse spin hall effect in germanium," *Phys. Rev. B*, vol. 88, p. 064403, Aug 2013.

[185] ROSSI, E., HEINONEN, O. G., and MACDONALD, A. H., "Dynamics of magnetization coupled to a thermal bath of elastic modes," *Phys. Rev. B*, vol. 72, p. 174412, Nov 2005.

[186] ROY, A. M., NIKONOV, D. E., and SARASWAT, K. C., "Conductivity mismatch and voltage dependence of magnetoresistance in a semiconductor spin injection device," *Journal of Applied Physics*, vol. 107, no. 6, 2010.

[187] ROY, A. M., NIKONOV, D. E., and YOUNG, I. A., "Atomistic simulation of tunneling magnetoresistance using extended hckel theory," *Journal of Applied Physics*, vol. 112, no. 10, 2012.

[188] SAI, N., KOLPAK, A. M., and RAPPE, A. M., "Ferroelectricity in ultra-thin perovskite films," *Phys. Rev. B*, vol. 72, p. 020101, Jul 2005.

[189] SANKEY, J. C., CUI, Y. T., SUN, J., SLONCZEWSKI, J. C., BUHRMAN, R. A., and RALPH, D. C., "Measurement of the spin-transfer-torque vector in magnetic tunnel junction," *Nature Physics*, vol. 4, p. 67, 2008.

[190] SARPESHKAR, R., *Ultra low power bioelectronics: fundamentals, biomedical applications, and bio-inspired systems.* Cambridge: Cambridge Univ. Press, 2010.

[191] SASAKI, T., OIKAWA, T., SUZUKI, T., SHIRAISHI, M., SUZUKI, Y., and NOGUCHI, K., "Evidence of electrical spin injection into silicon using mgo

tunnel barrier," *IEEE Transactions on Magnetics*, vol. 46, pp. 1436–1439, June 2010.

[192] Schmidt, G., Ferrand, D., Molenkamp, L. W., Filip, A. T., and van Wees, B. J., "Fundamental obstacle for electrical spin injection from a ferromagnetic metal into a diffusive semiconductor," *Phys. Rev. B*, vol. 62, pp. R4790–R4793, Aug 2000.

[193] Schmidt, G., Richter, G., Grabs, P., Gould, C., Ferrand, D., and Molenkamp, L. W., "Large magnetoresistance effect due to spin injection into a nonmagnetic semiconductor," *Phys. Rev. Lett.*, vol. 87, p. 227203, Nov 2001.

[194] Scholz, W., Schrefl, T., and Fidler, J., "Micromagnetic simulation of thermally activated switching in fine particles," *Journal of Magnetism and Magnetic Materials*, vol. 233, no. 3, pp. 296 – 304, 2001.

[195] Schryer, N. L. and Walker, L. R., "The motion of 180 domain walls in uniform dc magnetic fields," *Journal of Applied Physics*, vol. 45, no. 12, pp. 5406–5421, 1974.

[196] Shiota, Y., Nozaki, T., Bonell, F., Murakami, S., Shinjo, T., and Suzuki, Y., "Induction of coherent magnetization switching in a few atomic layers of feco using voltage pulses," *Nat Mater*, vol. 11, pp. 39–43, Jan 2012.

[197] Shiraishi, M., Honda, Y., Shikoh, E., Suzuki, Y., Shinjo, T., Sasaki, T., Oikawa, T., Noguchi, K., and Suzuki, T., "Spin transport properties in silicon in a nonlocal geometry," *Phys. Rev. B*, vol. 83, p. 241204, Jun 2011.

[198] Sinova, J., Jungwirth, T., Liu, X., Sasaki, Y., Furdyna, J. K., Atkinson, W. A., and MacDonald, A. H., "Magnetization relaxation in (ga,mn)as ferromagnetic semiconductors," *Phys. Rev. B*, vol. 69, p. 085209, Feb 2004.

[199] Sinova, J., Valenzuela, S. O., Wunderlich, J., Back, C. H., and Jungwirth, T., "Spin hall effects," *Rev. Mod. Phys.*, vol. 87, pp. 1213–1260, Oct 2015.

[200] SIVASUBRAMANIAN, S., WIDOM, A., and SRIVASTAVA, Y. N., "Physical kinetics of ferroelectric hysteresis," *Ferroelectrics*, vol. 300, no. 1, pp. 43–55, 2004.

[201] Slonczewski, J., "Current-driven excitation of magnetic multilayers," *Journal of Magnetism and Magnetic Materials*, vol. 159, no. 12, pp. L1 – L7, 1996.

[202] Srinivasan, S., Sarkar, A., Behin-Aein, B., and Datta, S., "All-spin logic device with inbuilt nonreciprocity," *IEEE Transactions on Magnetics*, vol. 47, pp. 4026–4032, Oct 2011.

[203] Srinivasan, S., Diep, V., Behin-Aein, B., Sarkar, A., and Datta, S., *Modeling Multi-Magnet Networks Interacting via Spin Currents*, pp. 1–49. Springer Netherlands, 2014.

[204] Stengel, M., Vanderbilt, D., and Spaldin, N. A., "Enhancement of ferroelectricity at metal-oxide interfaces," *Nat Mater*, vol. 8, pp. 392–397, May 2009.

[205] Stiles, M. D. and Zangwill, A., "Anatomy of spin-transfer torque," *Phys. Rev. B*, vol. 66, p. 014407, Jun 2002.

[206] Stiles, M. D. and Miltat, J., *Spin-Transfer Torque and Dynamics*, pp. 225–308. Berlin, Heidelberg: Springer Berlin Heidelberg, 2006.

[207] Stirniman, J. P. and Rieger, M. L., "Fast proximity correction with zone sampling," 1994.

[208] Streiffer, S. K., Eastman, J. A., Fong, D. D., Thompson, C., Munkholm, A., Ramana Murty, M. V., Auciello, O., Bai, G. R., and Stephenson, G. B., "Observation of nanoscale 180° stripe domains in ferroelectric $pbtio_3$ thin films," *Phys. Rev. Lett.*, vol. 89, p. 067601, Jul 2002.

[209] Su, L., Zhang, Y., Klein, J.-O., Zhang, Y., Bournel, A., Fert, A., and Zhao, W., "Current-limiting challenges for all-spin logic devices," *Scientific Reports*, vol. 5, pp. 14905 EP –, Oct 2015. Article.

[210] Sun, J. Z., "Spin-current interaction with a monodomain magnetic body: A model study," *Phys. Rev. B*, vol. 62, pp. 570–578, Jul 2000.

[211] Tagantsev, A. K., Gerra, G., and Setter, N., "Short-range and long-range contributions to the size effect in metal-ferroelectric-metal heterostructures," *Phys. Rev. B*, vol. 77, p. 174111, May 2008.

[212] "Newly launched activity in jmmmcurrent perspectives," *Journal of Magnetism and Magnetic Materials*, vol. 320, no. 7, pp. 1189 –, 2008.

[213] Takei, S., Halperin, B. I., Yacoby, A., and Tserkovnyak, Y., "Superfluid spin transport through antiferromagnetic insulators," *Phys. Rev. B*, vol. 90, p. 094408, Sep 2014.

[214] Tan, E.-K., Osman, J., and Tilley, D., "Theory of switching in bulk first-order ferroelectric materials," *physica status solidi (b)*, vol. 228, no. 3, pp. 765–776, 2001.

[215] Tehrani, S., Slaughter, J. M., DeHerrera, M., Engel, B., Rizzo, N., Salter, J., Durlam, M., Dave, R., Janesky, J., Butcher, B., Smith, K., and Grynkewich, G., "Magnetoresistive random access memory using magnetic tunnel junctions," *Proceedings of the IEEE*, vol. 91, pp. 703–714, May 2003.

[216] Tenne, D. A., Bruchhausen, A., Lanzillotti-Kimura, N. D., Fainstein, A., Katiyar, R. S., Cantarero, A., Soukiassian, A., Vaithyanathan, V., Haeni, J. H., Tian, W., Schlom, D. G., Choi, K. J., Kim, D. M., Eom, C. B., Sun, H. P., Pan, X. Q., Li, Y. L., Chen, L. Q., Jia, Q. X., Nakhmanson, S. M., Rabe, K. M., and Xi, X. X., "Probing nanoscale ferroelectricity by ultraviolet raman spectroscopy," *Science*, vol. 313, no. 5793, pp. 1614–1616, 2006.

[217] Thiaville, A., Garcia, J., and Miltat, J., "Domain wall dynamics in nanowires," *Journal of Magnetism and Magnetic Materials*, vol. 242 - 245, no. 0, pp. 1061 – 1063, 2002. Proceedings of the Joint European Magnetic Symposia (JEMS'01).

[218] Tian, B. B., Wang, J. L., Fusil, S., Liu, Y., Zhao, X. L., Sun, S., Shen, H., Lin, T., Sun, J. L., Duan, C. G., Bibes, M., Barthelemy, A., Dkhil, B., Garcia, V., Meng, X. J., and Chu, J. H., "Tunnel electroresistance through organic ferroelectrics," *Nat Commun*, vol. 7, May 2016. Article.

[219] Toyoshima, H., Kobayashi, S., Yamada, J., Miwa, T., Koike, H., Takeuchi, H., Mori, H., Kasai, N., Maejima, Y., Tanabe, N., Tatsumi, T., and Hada, H., "Feram device and circuit technologies fully compatible with advanced cmos," in *Custom Integrated Circuits, 2001, IEEE Conference on.*, pp. 171–178, 2001.

[220] Tran, M., Jaffrès, H., Deranlot, C., George, J.-M., Fert, A., Miard, A., and Lemaître, A., "Enhancement of the spin accumulation at the interface between a spin-polarized tunnel junction and a semiconductor," *Phys. Rev. Lett.*, vol. 102, p. 036601, Jan 2009.

[221] Tserkovnyak, Y., Brataas, A., Bauer, G. E. W., and Halperin, B. I., "Nonlocal magnetization dynamics in ferromagnetic heterostructures," *Rev. Mod. Phys.*, vol. 77, pp. 1375–1421, Dec 2005.

[222] Tsu, R. and Esaki, L., "Tunneling in a finite superlattice," *Applied Physics Letters*, vol. 22, no. 11, pp. 562–564, 1973.

[223] Tsu-Jae King Liu, K. K., ed., *CMOS and Beyond Logic Switches for Terascale Integrated Circuits*. Cambridge Univ. Press, 2015.

[224] Tsymbal, E. Y. and Kohlstedt, H., "Tunneling across a ferroelectric," *Science*, vol. 313, no. 5784, pp. 181–183, 2006.

[225] Urazhdin, S., Loloee, R., and Pratt, W. P., "Noncollinear spin transport in magnetic multilayers," *Phys. Rev. B*, vol. 71, p. 100401, Mar 2005.

[226] Valet, T. and Fert, A., "Theory of the perpendicular magnetoresistance in magnetic multilayers," *Phys. Rev. B*, vol. 48, pp. 7099–7113, Sep 1993.

[227] van 't Erve, O. M. J., Awo-Affouda, C., Hanbicki, A. T., Li, C. H., Thompson, P. E., and Jonker, B. T., "Information processing with pure spin currents in silicon: Spin injection, extraction, manipulation, and detection," *IEEE Transactions on Electron Devices*, vol. 56, pp. 2343–2347, Oct 2009.

[228] Velev, J. P., Duan, C.-G., Belashchenko, K. D., Jaswal, S. S., and Tsymbal, E. Y., "Effect of ferroelectricity on electron transport in Pt/batio$_3$/Pt tunnel junctions," *Phys. Rev. Lett.*, vol. 98, p. 137201, Mar 2007.

[229] Vizdrik, G., Ducharme, S., Fridkin, V. M., and Yudin, S. G., "Kinetics of ferroelectric switching in ultrathin films," *Phys. Rev. B*, vol. 68, p. 094113, Sep 2003.

[230] Vouille, C., Barthélémy, A., Elokan Mpondo, F., Fert, A., Schroeder, P. A., Hsu, S. Y., Reilly, A., and Loloee, R., "Microscopic mechanisms of giant magnetoresistance," *Phys. Rev. B*, vol. 60, pp. 6710–6722, Sep 1999.

[231] Wang, H., Du, C., Hammel, P. C., and Yang, F., "Antiferromagnonic spin transport from y$_3$fe$_5$o$_{12}$ into nio," *Phys. Rev. Lett.*, vol. 113, p. 097202, Aug 2014.

[232] Wang, W.-G., Li, M., Hageman, S., and Chien, C. L., "Electric-field-assisted switching in magnetic tunnel?junctions," *Nat Mater*, vol. 11, pp. 64–68, Jan 2012.

[233] Wang, Z., Zhao, W., Kang, W., Bouchenak-Khelladi, A., Zhang, Y., Zhang, Y., Klein, J.-O., Ravelosona, D., and Chappert, C., "A physics-based compact model of ferroelectric tunnel junction for memory and logic design," *Journal of Physics D: Applied Physics*, vol. 47, no. 4, p. 045001, 2014.

[234] Worledge, D. C., Hu, G., Abraham, D. W., Sun, J. Z., Trouilloud, P. L., Nowak, J., Brown, S., Gaidis, M. C., OSullivan, E. J., and Robertazzi, R. P., "Spin torque switching of perpendicular ta—cofeb—mgo-based magnetic tunnel junctions," *Applied Physics Letters*, vol. 98, no. 2, pp. –, 2011.

[235] Wu, T., Bur, A., Zhao, P., Mohanchandra, K. P., Wong, K., Wang, K. L., Lynch, C. S., and Carman, G. P., "Giant electric-field-induced reversible and permanent magnetization reorientation on magnetoelectric ni/(011) [pb(mg1/3nb2/3)o3](1?x)[pbtio3]x heterostructure," *Applied Physics Letters*, vol. 98, no. 1, pp. –, 2011.

[236] Yamada, H., Tsurumaki-Fukuchi, A., Kobayashi, M., Nagai, T., Toyosaki, Y., Kumigashira, H., and Sawa, A., "Strong surface-termination effect on electroresistance in ferroelectric tunnel junctions," *Advanced Functional Materials*, vol. 25, no. 18, pp. 2708–2714, 2015.

[237] Yamaguchi, A., Ono, T., Nasu, S., Miyake, K., Mibu, K., and Shinjo, T., "Real-space observation of current-driven domain wall motion in submicron magnetic wires," *Phys. Rev. Lett.*, vol. 92, p. 077205, Feb 2004.

[238] Yu, B., Yuan, K., Ding, D., and Pan, D. Z., "Layout decomposition for triple patterning lithography," *IEEE Transactions on Computer-Aided Design of Integrated Circuits and Systems*, vol. 34, pp. 433–446, March 2015.

[239] Yu, Z. G. and Flatté, M. E., "Electric-field dependent spin diffusion and spin injection into semiconductors," *Phys. Rev. B*, vol. 66, p. 201202, Nov 2002.

[240] Yu, Z. G. and Flatté, M. E., "Spin diffusion and injection in semiconductor structures: Electric field effects," *Phys. Rev. B*, vol. 66, p. 235302, Dec 2002.

[241] Yuasa, S. and Djayaprawira, D. D., "Giant tunnel magnetoresistance in magnetic tunnel junctions with a crystalline mgo(0????) barrier," *Journal of Physics D: Applied Physics*, vol. 40, no. 21, p. R337, 2007.

[242] Yuasa, S., Nagahama, T., Fukushima, A., Suzuki, Y., and Ando, K., "Giant room-temperature magnetoresistance in single-crystal fe/mgo/fe magnetic tunnel junctions," *Nat Mater*, vol. 3, pp. 868–871, Dec 2004.

[243] Zhang, S. and Li, Z., "Roles of nonequilibrium conduction electrons on the magnetization dynamics of ferromagnets," *Phys. Rev. Lett.*, vol. 93, p. 127204, Sep 2004.

[244] Zhu, J., Katine, J. A., Rowlands, G. E., Chen, Y.-J., Duan, Z., Alzate, J. G., Upadhyaya, P., Langer, J., Amiri, P. K., Wang, K. L., and Krivorotov, I. N., "Voltage-induced ferromagnetic resonance in magnetic tunnel junctions," *Phys. Rev. Lett.*, vol. 108, p. 197203, May 2012.

[245] Zhuravlev, M. Y., Sabirianov, R. F., Jaswal, S. S., and Tsymbal, E. Y., "Giant electroresistance in ferroelectric tunnel junctions," *Phys. Rev. Lett.*, vol. 94, p. 246802, Jun 2005.

[246] Zhuravlev, M. Y., Wang, Y., Maekawa, S., and Tsymbal, E. Y., "Tunneling electroresistance in ferroelectric tunnel junctions with a composite barrier," *Applied Physics Letters*, vol. 95, no. 5, 2009.

[247] Zutic, I. and Fuhrer, M., "Spintronics: A path to spin logic," *Nat Phys*, vol. 1, pp. 85–86, Nov 2005.

[248] Zwierzycki, M., Tserkovnyak, Y., Kelly, P. J., Brataas, A., and Bauer, G. E. W., "First-principles study of magnetization relaxation enhancement and spin transfer in thin magnetic films," *Phys. Rev. B*, vol. 71, p. 064420, Feb 2005.